Cranfield UNIVERSITY

Defence College of Management & Technology
Department of Aerospace, Power & Sensors

PhD Thesis
2006

Russell Kenneth Strachan

The Aerodynamic Interference Effects of Side Wall Proximity on a Generic Car Model

Supervisors: Dr. K. Knowles
Dr. N. Lawson

Presented on 31st July, 2006

Page Intentionally Left Blank

Abstract

The flow around a generic car model both in isolation and in proximity to a near side wall has been investigated utilising experimental and computational methods.

Phase one of this investigation tested a range of Ahmed generic road vehicle models with varying backlight angles in isolation, employing laser-Doppler anemometry, static pressure and aerodynamic force and moment measurements in the experimental section. Additionally, numerical simulations were conducted using a commercial Reynolds-averaged Navier Stokes (RANS) code with the RNG k-ε turbulence model. This phase served both to extend the previous knowledge of the flow around the Ahmed model, and analyse the effects of both the supporting strut and rolling road. Phase two then used similar methods to investigate the Ahmed model in proximity to a non-moving side wall.

Results from phase two are compared with previous near-wall studies in order that an understanding of the effects of wall proximity can be presented, an area lacking in the existing literature.

It is found that the flow on the isolated model must be understood before the effects of side wall proximity can be assessed. There is though, in general, a breakdown of any longitudinal vortices on the near-wall side of the model as model-to-wall distance reduces, with an increase in longitudinal vortex strength on the model side away from the wall. There also exists a large pressure drop on the near-wall model side, which increases in magnitude as model-to-wall distance reduces, before dissipating at separations where the boundary layer restricts the flow.

Additionally, there is found to be a pressure drop on the top and bottom of the model with decreasing wall distance, with the relative magnitudes of these dependent on model geometry.

To Mum

Acknowledgements

To all of those who helped with this thesis, either directly or simply by lending support when needed, I can only say thank you.

I must thank my supervisors, Dr Knowles and Dr Lawson, for their guidance and support throughout the project, and especially for Dr Knowles' seemingly limitless patience concerning the wind tunnel testing.

I would also like to thank Dr Mark Finnis for his help with the wind tunnel, and Mark Eyles for teaching me the delicate art of technical drawing. Without their help the experiments would never have been started.

Thanks also to Dr Salman Ansari and Dr Simon Ritchie. Their help with both the experiments and subsequent analysis of the data was invaluable. Without them the diagrams in this thesis simply would not exist.

Finally, I must give a special thanks to Dr Robin Knowles. The time he took to explain and help set up the test rig, in addition to the help he gave when it all broke down again, is very gratefully acknowledged.

Contents

List of Figures

•

•

Notation

α	Backlight Angle (°)
ε	Turbulent kinetic energy dissipation rate (m^2s^{-3})
ν	Kinematic viscosity (m^2s^{-1})
ρ	Air density (kgm^{-3})
ζ_x	Vorticity (s^{-1})
CART	Championship Auto Racing Teams
CFD	Computational Fluid Dynamics
C^*_R	Viscous drag coefficient in Figure 2.4
C^*_K	Pressure drag coefficient on front end in Figure 2.4
C^*_B	Pressure drag coefficient on back end in Figure 2.4
C^*_S	Pressure drag coefficient on angled section in Figure 2.4
C^*_W	Drag coefficient in Figure 2.4
c	Support strut chord (m)
C_D	Drag Coefficient = Drag Force (N) /qS
C_L	Lift Coefficient = Lift Force (N) /qS
C_M	Pitching Moment Coefficient = Pitching Moment (Nm) /qSL
C_p	Pressure Coefficient = Pressure (Pa) /q
C_R	Rolling Moment Coefficient = Rolling Moment (Nm) /qSL
C_Z	Side Force Coefficient = Side Force (N) /qS
C_N	Yawing Moment Coefficient = Yawing Moment (Nm) /qSL
k	Specific turbulent kinetic energy (m^2s^{-2})
L	Model length (m)
LDA	Laser Doppler Anemometry
LIC	Line Integral Convolution
NASCAR	National Association for Stock Car Auto Racing
q	Dynamic Pressure (Pa)
Re	Reynolds Number (based on L)
S	Frontal area of model (m^2)
t	Support strut thickness (m)

u_∞	Freestream velocity (ms^{-1})
u,v,w	Velocity components aligned with X, Y and Z axis respectively (ms^{-1})
X	Streamwise co-ordinate (see Figure 2.1)
Y	Vertical co-ordinate (see Figure 2.1)
y_H	Non-dimensionalised height above model surface
Z	Transverse co-ordinate (see Figure 2.1)
z_w	Distance between model and side wall (m)

1. Introduction

"Aerodynamics are for people who can't build proper engines"

Enzo Ferrari (1898 - 1988)

The vast sums of money currently being invested in the field of motorsport aerodynamic development serve only to highlight the extent to which this area of science has advanced since Enzo Ferrari made the above statement. The original primary goal of drag reduction has long since yielded to the efficient creation of downforce, achieved through a multitude of varying techniques.

The performance of a racing car in isolation has formed the basis for the vast majority of this research. This is to be expected as it is in this state that the vehicle would most commonly be required to operate. There also exists a body of literature in which the aerodynamic effects of both slipstreaming (drafting) and of one car passing another have been investigated. To date, however, the interference effects between a car and a retaining wall, to which it is often running in very close proximity, have not been the subject of equal scrutiny.

There are a number of classes of motor racing in which the track is bounded by a retaining wall. These include NASCAR and CART, and an example of the former can be seen in Figure 1.1. In an environment where fractions of a second are of paramount importance, the advantages gained from understanding the aerodynamic effects of side-wall proximity become abundantly clear. Not only will any effects on overall drag be of importance, but the relative front and rear downforce contributions when in wall proximity must also be taken into consideration. The ability to assess and understand both the aerodynamic forces and subsequent stability of a car when in proximity to a side wall may yield a previously unknown competitive advantage.

The present work aims to address this apparent gap in the literature by considering a generic car-like bluff body in wall proximity. No attempt is made to model any particular automobile

shape, as it is considered that the current understanding of side wall effects are such that a generic model study will provide both greater insight and less ambiguity in the results.

Chapter 2 will provide a detailed overview of the current level of literature, followed by the specific aims of the current investigation. The experimental and computational methods used will be outlined in Chapters 3 and 4 respectively. Chapters 5, 6 and 7 will present results from both the experimental and computational methods used to investigate the flow over the generic car model in isolation (Chapter 5) and in wall proximity (Chapters 6 and 7). The generality of the effects observed will then be assessed with reference to previous work in Chapter 8. Finally, the resulting conclusions and recommendations for further investigation will be given in Chapter 9.

Figure 1.1 - NASCARs in proximity to a retaining side wall

2. Review of Literature

2.1 Ahmed Model

2.1.1 Overview

S.R. Ahmed developed the "Ahmed Body" standard automobile shape in 1984 for a study into time-averaged vehicle wakes [Ahmed et al. 1984]. It is a bluff body with a curved front, straight centre section, and an angled backlight (the specific angle of which is variable), and is an adaptation of the model used previously by Morel [1978]. A diagram of the Ahmed reference model with the axis system used in the current investigation is shown in Figure 2.1. The model is approximately 1m long, 400mm wide, and 300mm in height, and represents a highly simplified ¼ scale lower-medium size hatchback vehicle. It includes 10 interchangeable rear ends, ranging from a backlight angle of 0° to 40° in 5° increments in addition to a further 12.5° angled backlight. In each case the length of the angled rear section remains constant. The body was designed to have a separation-free flow over the front, and to exhibit many of the flow features of an automobile with its variable backlight geometry. This body shape was also designed to ensure that an experiment could be conducted with reference to only one significant aerodynamic feature, namely the angled backlight, as flow would remain attached over the other sections. This greatly simplifies experiments as aerodynamic influences from separate areas, which must be accounted for when using a complex car geometry, need not be considered. It is also for this reason that the Ahmed reference model has been used extensively in computational fluid dynamics (CFD) validations.

2.1.2 Experimental Investigations

A great deal of experimental data has been acquired concerning the flow around the Ahmed model, most notably from experiments conducted by Ahmed et al [1984], Graysmith et al [1994], Lienhart and Becker [2002], Bayraktar et al [2001] and Sims-Williams and Duncan [2003]. During Ahmed's original investigation (and all subsequent experiments) the model has been mounted 50mm above the ground, in order to simulate the standard driving height of a road car. In his original investigation Ahmed used four cylindrical struts to support the body

from underneath. Pressure readings were taken at various points over the model, in addition to force data and measurements taken by a ten-hole directional probe, used to acquire information in the near-wake region. Oil flow visualisations over the model backlight were also taken to investigate separation and vortex generation in this region.

Graysmith et al. [1994] supported the model from above by means of an aerodynamic strut in the centre of its upper surface, in order that it could be tested above a moving ground plane. In addition lift coefficient data, not published in Ahmed's work, were recorded.

Lienhart and Becker [2002] tested only models with the 25° and 35° backlight angles. They recorded LDA flow data for these two angles, which are either side of the 2nd critical angle (30° - see section 2.1.3). The investigation's aim was to provide a detailed data set against which CFD simulations could be validated.

Bayraktar et al. [2001] investigated the effect of Reynolds Number on the flow around the Ahmed model with 0°, 12.5° and 25° backlight angles. In addition, the effects of yaw angle on the model drag force were recorded. Although the model was yawed by Ahmed in his original experiment this was to check the symmetry of the flow, rather than an integral part of the investigation, and as such no results concerning the effect of yaw angle had been published before Bayraktar et al.

Sims-Williams and Duncan [2003] published time resolved experimental results for the 25° Ahmed model. Probe measurements were made in the model wake using a single element hot-wire probe and a 5-hole probe, with all measurements recorded at 800Hz.This added to the existing literature as previous studies had only presented time-averaged data.

2.1.3. Flow Structure

A general description of the flow over the Ahmed body, as presented by Ahmed et al. [1984], is given below.

The flow stagnates at the bluff front end of the model, and then accelerates over the rounded front edges. The air velocity is nearly constant over the upper surface and is accelerated locally near the front edge of the backlight. As such the pressure coefficient (C_p) over the model varies from a maximum at the front of the body, to minima at the local suction peaks at both the rounded front edges and at the leading edge of the backlight.

The flow over the angled back section of the model is dependent on the specific angle being investigated. Two critical angles at which there is a significant change in the flow regime over

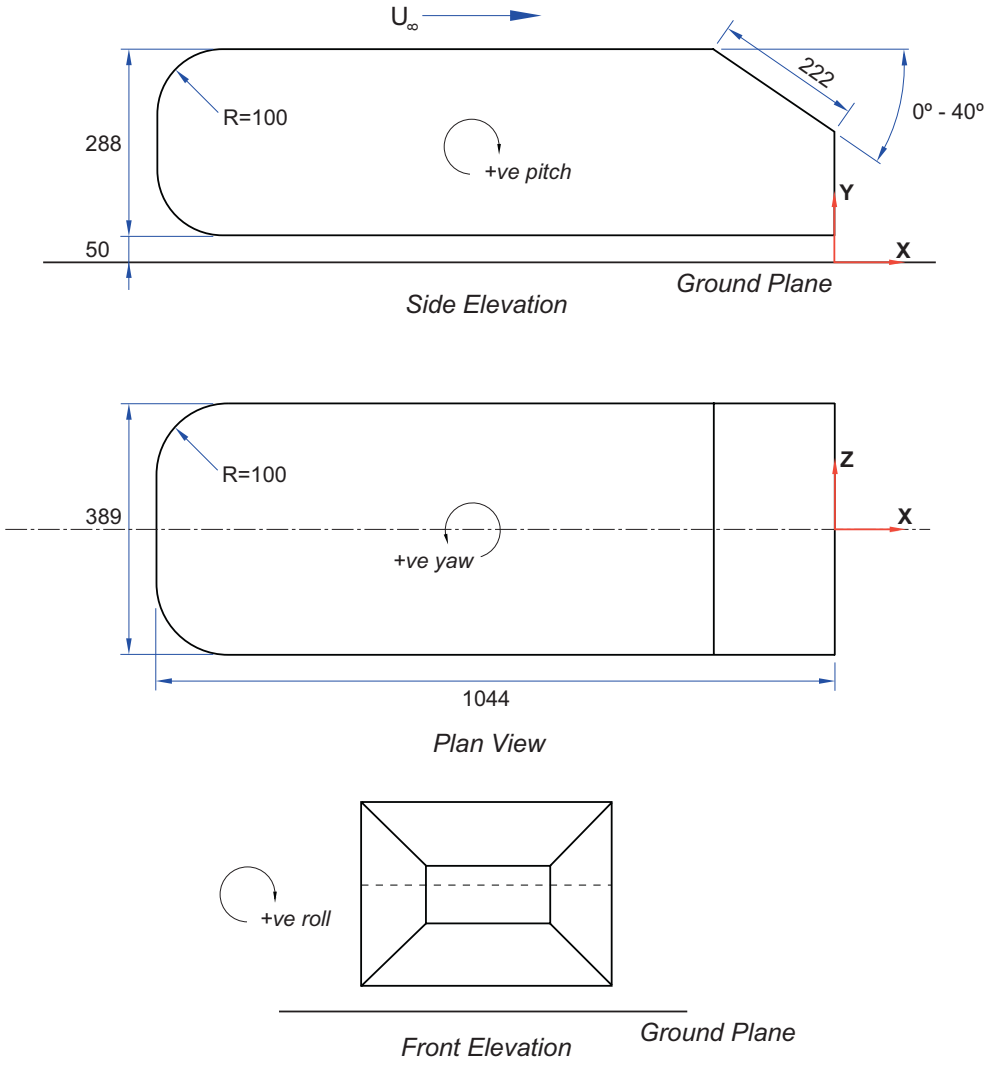

Figure 2.1 - Schematic Diagram of Ahmed Reference Model. Coordinate system used for current study is shown (all dimensions in mm)

this section were reported by Ahmed to be 12.5° (the 1st critical angle) and 30° (the 2nd critical angle). Therefore the three flow structures exhibited over the range of backlight angles (α) as described below:

$0° < \alpha < 12.5°$

Below the first critical angle, the airflow over the angled section of the back end remains fully attached. The shear layer rolls up at the top and bottom edges of the vertical base to form two recirculatory regions marked A and B in Figure 2.2(a). At a backlight angle of 5° these two regions are of comparable orders of magnitude, but the upper recirculatory region (A) becomes more dominant with increasing backlight angle (α). The shear layer from the sides of the angled back section rolls up to form two longitudinal vortices marked C in Figure 2.2(a). Except in the vicinity of the side edges, where the flow is affected by these longitudinal vortices, the flow over the angled surface appears to be two-dimensional.

12.5° < α < 30°

Between the two critical angles, the flow over the angled section becomes highly three dimensional. The two counter-rotating longitudinal vortices shed from the sides of the angled back section are larger than those formed below the 1st critical angle, as shown schematically in Figure 2.2(b). This increased vortex size affects the flow over the whole backlight, causing the three-dimensional flow. These vortices are also responsible for maintaining attached flow over a section of the backlight up to an angle of approximately 30°. Close to the 2nd critical angle a separation bubble (marked D in Figure 2.2(b)) is formed over the backlight. The flow separates from the body, but re-attaches before reaching the vertical base. At this point the flow again separates to form the previously-described two recirculatory regions A and B, which can again be seen in Figure 2.2(b).

α > 30°

For all back angles above this 2nd critical angle, the flow over the angled section is fully separated. Again, two recirculatory regions A and B are formed over the back end, but in this case the upper region is formed from the flow separation from the top of the model, instead of from the top of the vertical base. In effect, the two previous separated regions A and D are no longer distinct and can now be regarded as being a single larger region. When the flow is in this state a near-constant pressure is found across the backlight.

Flow Structure in Wake

Figure 2.3 plots time-averaged LDA data (from Lienhart and Becker [2002]) for the wakes of the 25° and 35° Ahmed models. Plotted are the v and w velocity vectors (vector magnitude represented by length), with contours of vertical velocity. The vortices marked C in Figure 2.2 can clearly be seen in the x/L=0.077 25° case, whilst their absence is equally evident in the corresponding 35° diagram. As a result of this, the counter-rotating longitudinal vortex system formed in the wake of both back angles is found to be stronger in the 25° case. This wake structure is symptomatic of the higher drag coefficient experienced by the 25° backlight.

a) $\alpha<12.5°$

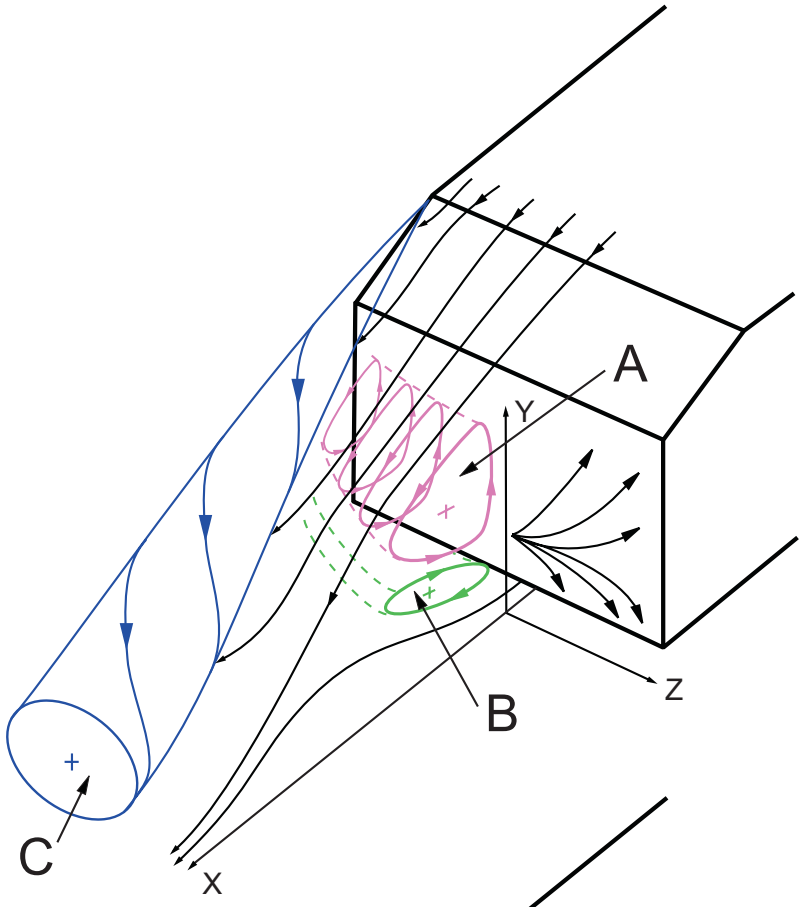

b) $12.5< \alpha<30°$

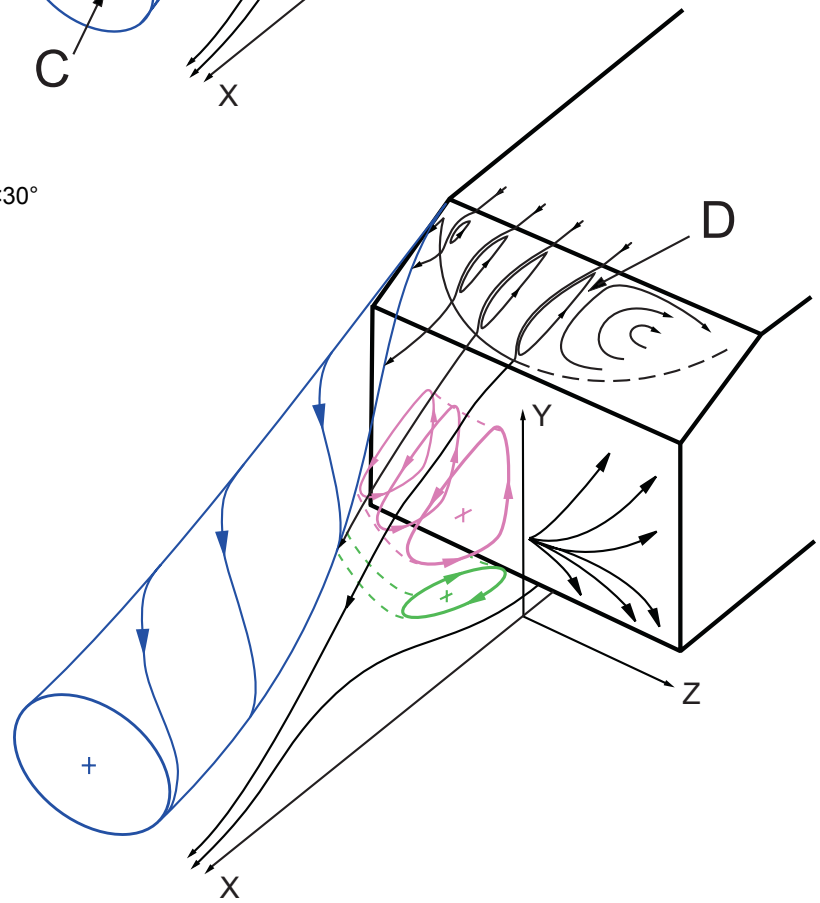

Figure 2.2 - Schematic Diagram of vortex system in the wake of the Ahmed model - After Ahmed et al. [1984]

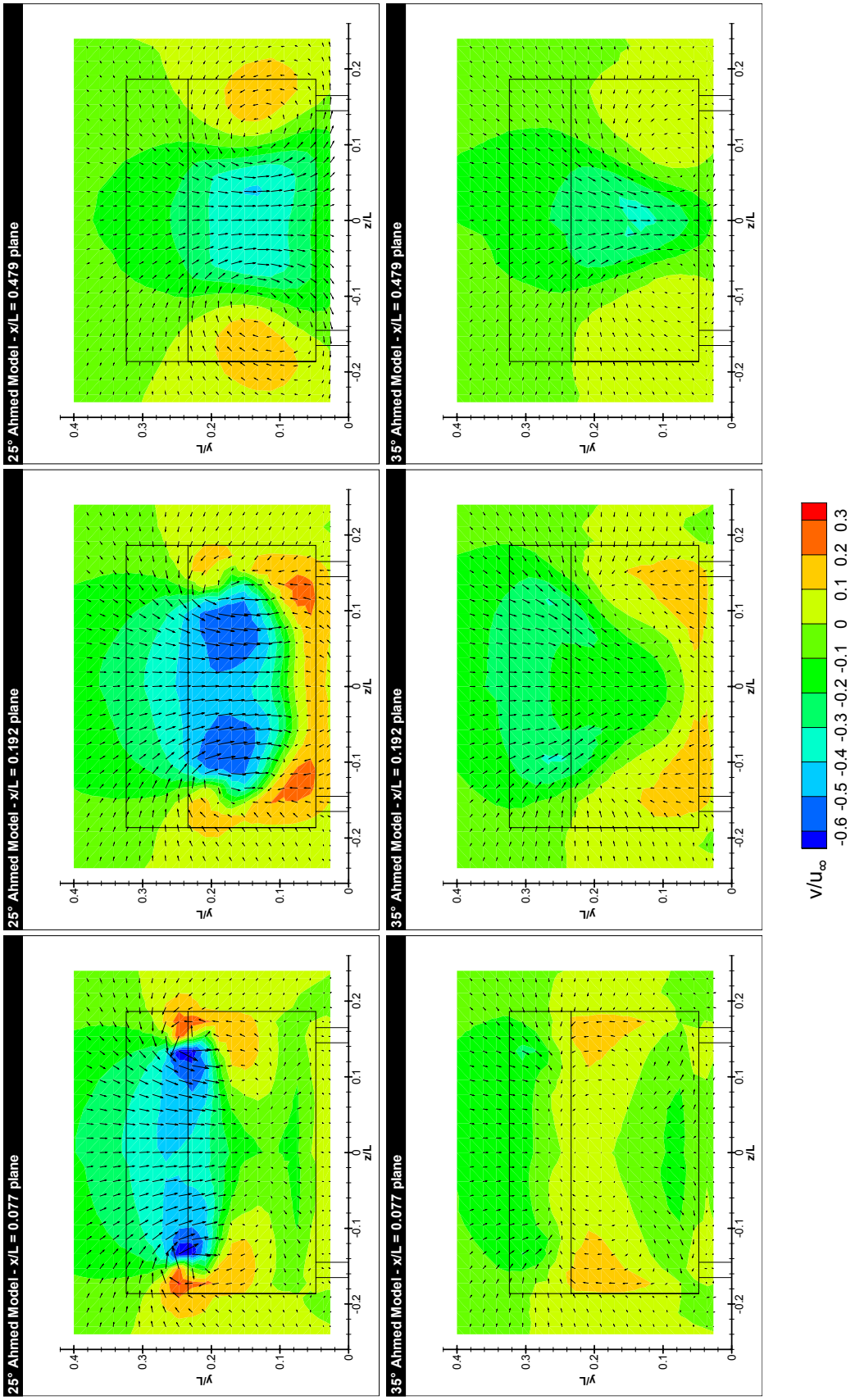

Figure 2.3 - Near wake of Ahmed Model - 25° and 35° back angles. Contours of v velocity and in-plane velocity vectors scaled by magnitude. Data from Lienhart and Becker [2002]

2.1.4 Lift and Drag Coefficients

Drag Breakdown

From Figure 2.4 the effect on the drag coefficient of the flow structure changes at the critical angles is evident. Total C_D decreases from its value of 0.250 at a 0° back angle to its minimum value (0.230) at the first critical angle (12.5°). After this point, C_D increases until its highest recorded value (0.378) at the second critical angle (30°). Beyond this angle C_D drops dramatically, returning to values close to the 0° case. There are two recorded values of C_D for the 30° case as Ahmed tested both the attached backlight flow (high drag) and separated backlight flow conditions, with the latter being produced by the introduction of a vertical splitter plate behind the model.

From Figure 2.4 it can also be seen that the relative contributions to the overall C_D from each model section varies significantly with changing back angle. The relative percentage of the overall pressure drag contributed by the angled section increases to 66.4%, for a corresponding increase of 38.5% of model front area between 0° (when the pressure drag contribution from the backlight is zero) to a maximum value at 30°. Clearly part of this can be

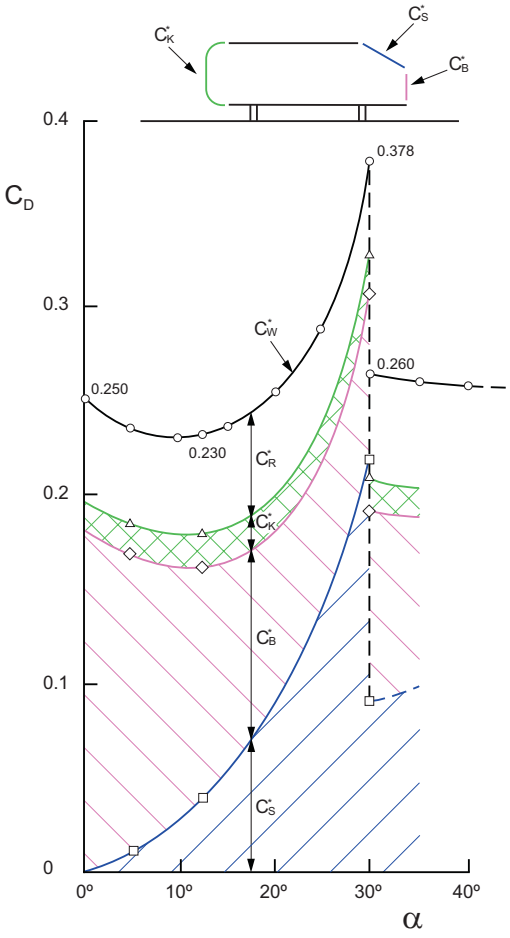

Figure 2.4 - Variation of Ahmed Reference Model drag with base slant angle - After Ahmed et al. [1984]

attributed to the model's altered geometry causing a larger component of the pressure force parallel to the freestream flow. However, the rapid increase evident in Figure 2.4 in C^*_S as α approaches the 2nd critical angle (30°) would suggest that the separation bubble formed in this region creates a significant pressure drop over the backlight. After this separation bubble has burst (α > 30°) this component of the drag force drops dramatically, as the backlight no longer exhibits attached flow. Beyond this critical angle pressure over the backlight remains constant as a result of the separated flow and further variations in the relative pressure drag components of the back end are due mainly to the change in projected frontal area of the backlight.

The pressure drag contribution of the front end of the model does not appear to have any significant relationship to the back angle, remaining at a near-constant level throughout. It is probable that the relatively long middle section of the model does not allow for any influence of the backlight flow on the front end.

The absolute value of friction drag is also not significantly altered by changing back angle. Thus its percentage contribution to the overall drag varies from 15% to 24% between the highest and lowest recorded drag results respectively.

Lift Coefficient

From Fig 2.5 there appears to be an almost linear increase in overall lift coefficient between back angles of 0° and 30°. After this point, there is a large change to a slight negative C_L. The negative lift at a backlight angle of 0° is a result of the proximity of the ground plane increasing the flow velocity under the model, with the subsequent decrease in pressure. As backlight angle increases, increasing the camber of the model, the lift coefficient also increases. The large drop in pressure with increasing α over the model backlight close to 30°, seen from the

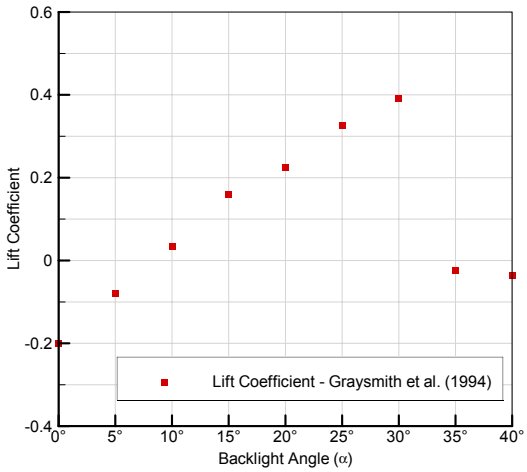

Figure 2.5 - Lift Coefficient on the Ahmed Reference Model - After Graysmith et al. [1994]

increased contribution to model drag from this section in Figure 2.4, would also be expected to cause this increase in model lift. The increase in C_L continues until the separation bubble bursts (at 30°) and there is no longer any drop in backlight pressure. At this point the C_L returns to a negative value.

Reynolds Number Effects

As previous experimental studies had tested at Reynolds Numbers (based on model length) ranging from $1.8x10^6$ to $4.29x10^6$, the effect of Re on the lift and drag coefficient of the Ahmed model was investigated by Bayraktar et al. [2001]. They tested at six separate Reynolds Numbers between $2.2x10^6$ and $13.2x10^6$. It was found that even over this wide range of Re, C_D was altered by only around 3.5%, whilst C_L varied by approximately 2.0%.

Yaw Effects

Bayraktar et al. [2001] also examined the effect of yaw angle on the C_D of the Ahmed model. The results from these experiments are shown in Figure 2.6. Despite some asymmetry in these results it is apparent that at small angles (±3°) the 0° backlight model experiences greater sensitivity to variations in yaw than in the cases of either the 12.5° or 25° backlight models. There is found to be a variation in C_D of 0.016 between yaw angles of 0° and -3° on the 0° model, with corresponding variations of 0.009 and 0.006 on the 12.5° and 25° models respectively.

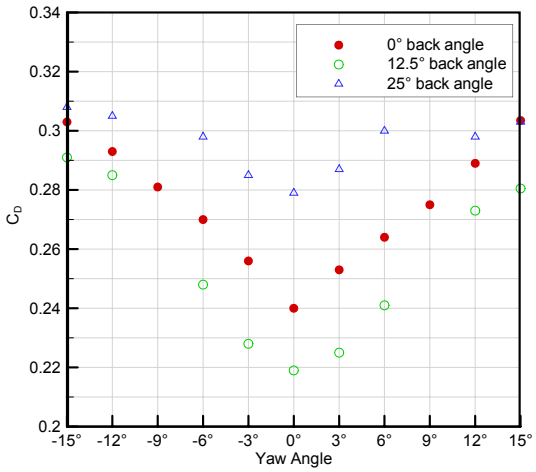

Figure 2.6 - Variation of drag coefficient with changing yaw angle on the Ahmed Reference Model - After Bayraktar et al. [2001]

2.1.5 Computational Investigations

As stated previously, the Ahmed model lends itself well to CFD studies as a result of both its simplicity and the large body of experimental data available. Having only one significant aerodynamic feature (the angled backlight) has allowed CFD codes to be validated with a reduced likelihood of errors from separate parts of the model cancelling each other out overall. An investigation conducted on the flows round a separate simplified car model (Aider et al. [2000]) concluded that a significant difficulty in accurately predicting the lift and drag of automobile shapes with numerical simulation was accurate modelling of the wake behind the wheels. As the Ahmed body has no wheels this should theoretically allow for more accurate results whilst simultaneously reducing necessary areas of grid refinement. It has been standard practice to model only half of the Ahmed model when performing CFD, due to the model symmetry and the need to reduce computational cost.

In general, the data produced by Lienhart and Becker [2002] have subsequently been used as the main CFD source, due both to their comprehensiveness and their well-defined inlet conditions. These are imperative to successful CFD validation. Prior to this Ahmed's original experiment was used as a comparison.

Graysmith et al [1994] employed commercial RANS CFD codes to compute steady-state results for all backlight angles tested by Ahmed, except the 12.5° case. Both the standard k-ε model and the renormalization group methods (RNG) k-ε model were used on grids of up to 250000 cells. Unlike Graysmith's experimental set-up, run in parallel with the computational investigation, the CFD simulation did not include a supporting strut. The model was instead assumed to be 'floating' in mid air. In both cases, however, a moving ground simulation was used, unlike Ahmed's case. Figure 2.7 compares the lift and drag coefficients measured by

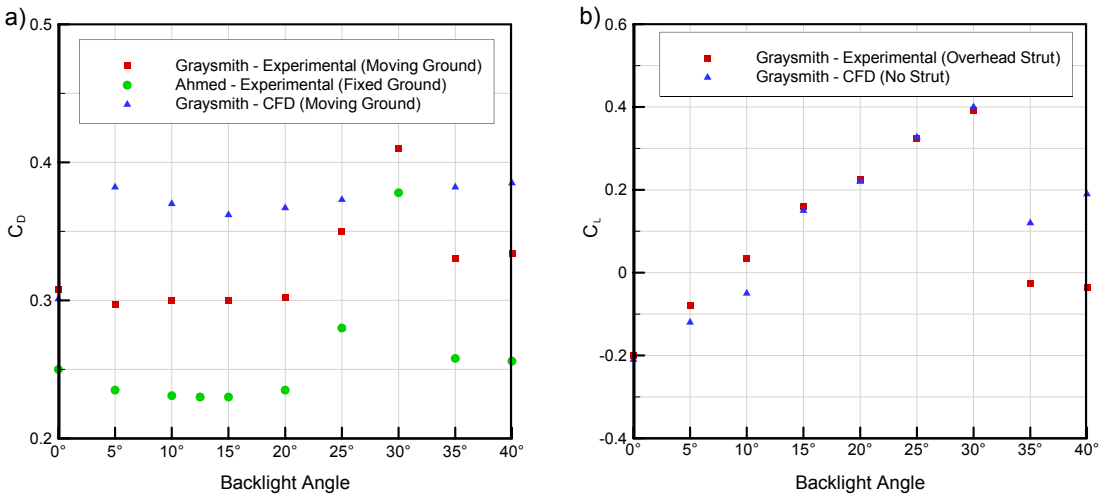

Figure 2.7 - (a) Lift and (b) Drag Coefficients on the Ahmed Reference Model - Experimental and Computational results

Graysmith in both his experimental investigation and computational simulation of the Ahmed model.

Initial inspection of Figure 2.7 shows that the drag coefficients measured experimentally by Graysmith are larger than those measured by Ahmed by approximately 25% in each case. In addition, it shows that Graysmith's computed coefficients are greater even than his own experimental values by around a further 20%. The change in experimental C_D from Ahmed is to be expected as the inclusion of ground simulation normally raises the drag coefficient of an automotive model (Howell & Hickman [1997]). The large difference in C_D between Graysmith's experimental and computational results is also expected due to the turbulence models used. As the Ahmed body has a large frontal area in comparison to its overall dimensions, the calculation of C_D is largely dependent on the correct prediction of the stagnation pressure over this surface. The k-ε turbulence model tends to over-predict the turbulent viscosity near stagnation points (Makowski and Kim [2000]), subsequently leading to an over-prediction of stagnation pressure. This appears to be one of the main reasons for the excessive drag results predicted by Graysmith's CFD calculations.

Although the drag coefficients predicted by Graysmith were only accurate to within 20% of the experimental value, as can be seen from Figure 2.7 (b) the lift coefficients predicted by the same computation are generally within experimental error. This is certainly the case for backlight angles of 30° or less. After the critical angle (30°) has been passed, the CFD is no longer able to predict C_L accurately, suggesting that this simulation is less accurate at modelling fully separated flow.

Gillieron and Chometon [1999] conducted a similar investigation to Graysmith, again using the RNG k-ε turbulence model, this time on a mesh of around 450,000 cells (approximately twice

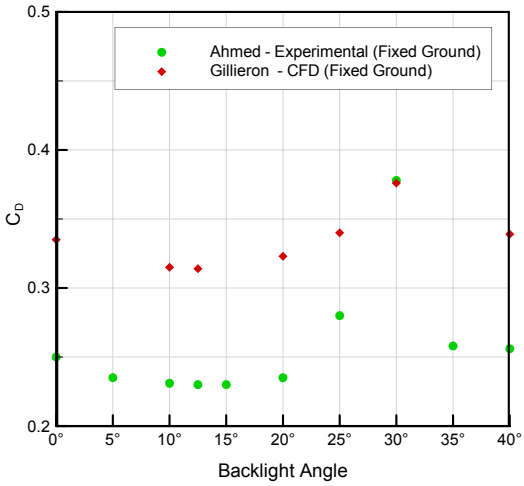

Figure 2.8 - Drag Coefficients on the Ahmed Reference Model - Experimental and Computational results

the size of Graysmith's mesh). Drag coefficient results from this investigation are shown in Figure 2.8, and are compared to the experiments of Ahmed. These results are on average around ΔC_D=0.08 (approximately 25%) greater than Ahmed's original experiment. However, the results for the 30° case are very accurate, though this appears likely to be as a result of an inability of the model to accurately represent the change in C_D with changing back angle, as the mesh was the same for all the angles considered. Once again the excessive drag prediction can be attributed to the use of the k-ε turbulence model over-predicting the front end pressure drag. Comparing FIgures 2.7 and 2.8, however, shows that the general trend in C_D does appear to be better predicted by Gillieron and Chometon [1999] than by Graysmith et al [1994]. Thus the greater mesh refinement has conceivably increased the accuracy of the flow prediction over the backlight.

Large Eddy Simulation (LES) was performed by Krajnovic and Davidson [2002 and 2004] on both the 0° and 25° Ahmed models. These studies were performed at low Re ($2x10^5$) in order to facilitate the use of LES, because to do a similar study at a Re of $5x10^6$, approximately $6x10^8$ cells would be required in the near-wall region alone. This study was validated against data from Lienhart and Becker [2002] and found that the flow structure around the model was very well predicted, despite the lower Re. It was concluded, therefore, that the model geometry, rather than viscosity, dictates the separation points. This would tend to agree with the experimental results from Bayraktar et al. [2001].

Detached Eddy Simulation (DES) was used by Kapadia and Roy [2003], employing a RANS-based model in the near-wall region, and an LES model in the remainder of the flow. This study was performed only on the 25° back angle of the Ahmed body, using the flow solver COBALT. The unsteady flow around the model was calculated for 4.5 seconds, and the averages of C_D compared extremely well with those of the Ahmed experiment (within 4%). The grid employed for this unsteady calculation had 1,714,106 cells, four times larger than that of Gillieron. Kapadia and Roy also performed an unsteady calculation employing the RNG k-ε turbulence modelling, which yielded very similar drag results to those of Gillieron (within 3%), notwithstanding the more refined mesh. Thus, these results suggest that large eddy simulation in the wake of the Ahmed model gives a much more accurate representation of this region than a RANS-based approach. Kapadia notes, though, that general flow features are predicted similarly by both numerical models.

2.2 Wall Proximity Investigations

There has been a great deal of research performed into discovering the effects of cars running in a slipstream and into the interference effects experienced when a car is passed by another. To date, however, the interference effects between a car and the retaining wall in which it is often running in very close proximity have not been the subject of equal scrutiny. To the author's knowledge, there have been only two experimental investigations (Wallis and Quinlan [1988] and Brown [2005]) and one computational study (Advantage CFD [2001]) performed into the aerodynamic effects experienced by a car when travelling in close proximity to a side wall. This will be discussed in more detail in the following sections.

2.2.1 Experimental Investigations

Type C Racecar Investigation Set-up

Brown [2005] conducted a wall proximity study employing a simplified Type C racecar model, a schematic of which can be seen in Figure 2.9. The tests were conducted in a closed-section wind tunnel without boundary layer control on the model wall. Ground simulation in the form of a rolling road was employed with suction upstream of the rolling road leading edge used to remove the tunnel boundary layer. Despite the model's simplicity, it did include both a front splitter plate, rear wing and underbody diffuser, each of which produce significant downforce.

The model was tested at side-wall separations ranging from approximately z_w=0.14L to z_w=0.01L at various ride heights. The model was also tested with various rear wing angles of attack and at a range of Reynolds numbers.

NASCAR Investigation set-up

An experimental wall proximity investigation was conducted by Wallis and Quinlan [Wallis & Quinlan, 1988]. A 3/8-scale generic NASCAR model was tested in proximity to a 1.37m high (0.29L) scale wall. The experiment was performed in a closed-section wind tunnel, without moving ground simulation and no boundary layer control employed on either the test section floor or the wall itself.

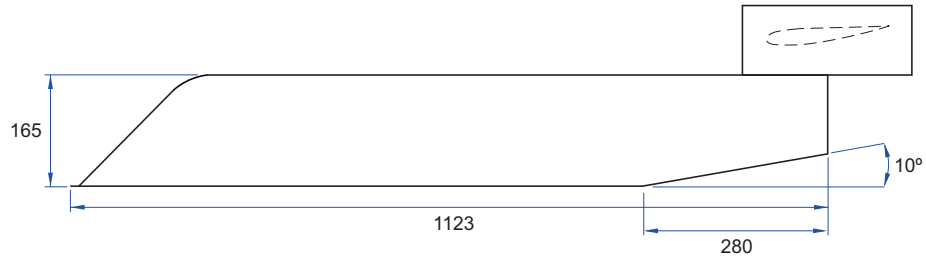

Figure 2.9 - Schematic diagram of Type C model (dimensions in mm) - after Brown [2005]

The NASCAR model was tested at various distances from the wall, ranging from an equivalent full size distance of 52" (z_w=0.74L) from the near-side car door to the car virtually touching the wall. Each case was also tested at car yaw angles between ± 4° in 2° increments, in order to simulate a car either skidding or set up at a non-zero track angle. Finally, the model wall was also inclined at angles of 10°, 20° and 30° away from the car. As in NASCAR racing, the driver's side window was modelled as being open, and a rear spoiler was included. A diagram of Wallis and Quinlan's experimental set up is shown in Figure 2.10.

Type C Racecar Results

Figure 2.11 plots the variation in front lift from the isolated case (without a near side wall) on the Type C model with changing ride heights and wall separation. Variations in rear wing angle were not found to have a significant effect on this parameter and thus have not been included. In all cases positive lift is upwards.

Initial inspection of Figure 2.11 shows firstly that the overall decrease in C_{Lf} (corresponding to an increase in front end downforce) is smaller with decreasing ride height. Indeed for the lowest height tested (11mm) there is actually an increase in C_{Lf} (loss of front end downforce in comparison to the isolated case) for all but the farthest point measured from the wall. It also appears that the point of minimum C_{Lf} moves closer to the wall for increasing ride height. Following this minimum point there is a sharp increase in C_{Lf} for all ride heights measured (except the 39mm case).

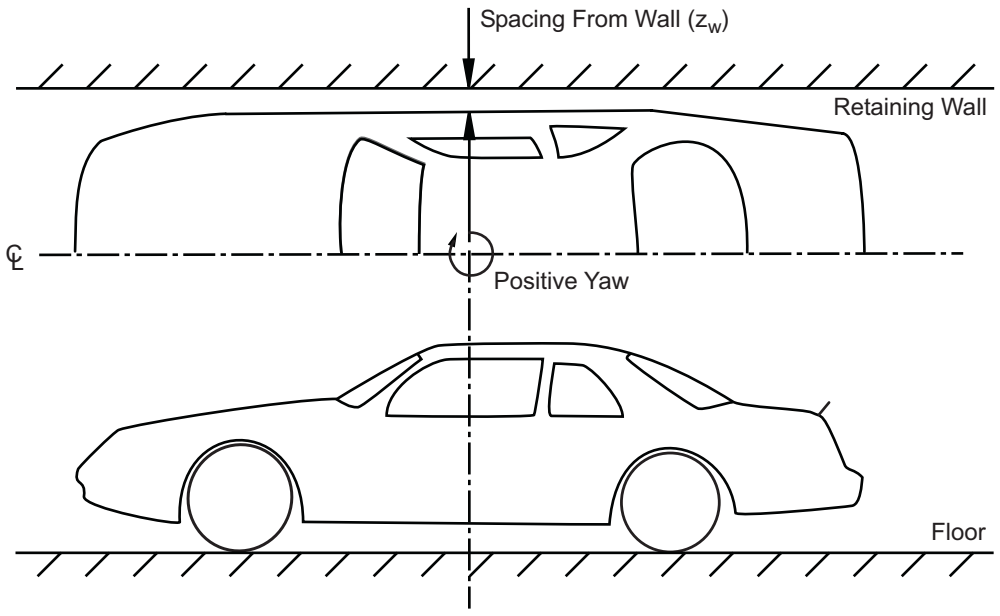

Figure 2.10 - Experimental set-up for NASCAR near wall investigation - after Wallis and Quinlan [1984]

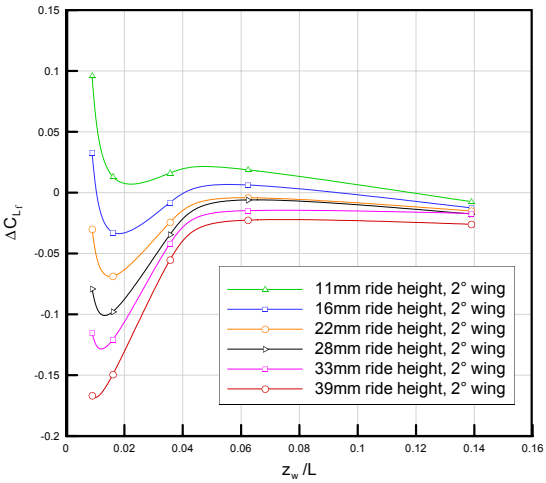

Figure 2.11 - Front lift coefficient variation with changing wall separation - data from Brown [2005]

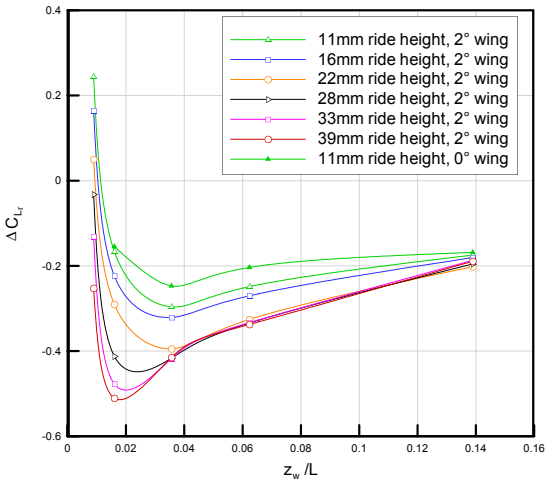

Figure 2.12 - Rear lift coefficient variation with changing wall separation and rear wing angle - data from Brown [2005]

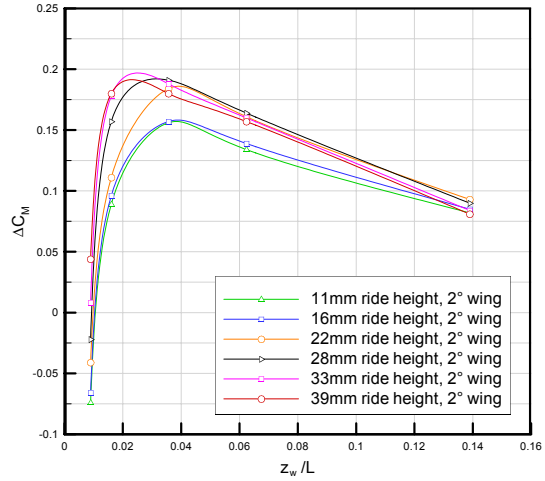

Figure 2.13 - Pitching moment coefficient variation with changing wall separation - data from Brown [2005]

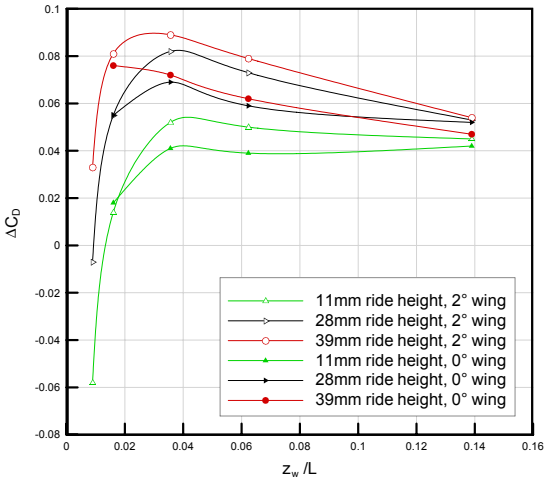

Figure 2.14 - Drag coefficient variation with changing wall separation and rear wing angle - data from Brown [2005]

Figure 2.12 plots the variation in rear lift from the isolated case with changing ride heights, wall separation and rear wing angle (for 11mm ride height). Like C_{Lf}, C_{Lr} exhibits an increase in downforce with decreasing wall separation followed by a sharp decline, once again with the maximum decrease in C_{Lr} being greater for increasing ride height. In addition, the point of minimum C_{Lr} is again moved closer to the wall for increasing ride height, however this point appears to be approximately double the distance from the wall as the corresponding points of minimum C_{Lf}. The maximum variations in C_{Lr} in comparison to C_{Lf} are perhaps expected due to the rear end of the model producing between three and four times (depending on the ground clearance) as much downforce as the front end when not in wall proximity.

Figure 2.12 also plots the variation in rear lift for the 0° rear wing, 11mm ride height case. It is

clear that for the 0° case the drop in C_{Lr} is less than for the 2° case. Brown suggests this could be because when the model is closer to the wall the constrained flow forces more air over the rear wing making the near-wall side work more efficiently, increasing the change in C_{Lr} for the case of the inclined wing. Data for a 0° rear wing angle at other ride heights follow a similar pattern to this, and are omitted here for clarity.

Figure 2.13 plots the change in pitching moment with wall distance. It can be seen that there is an increase in C_M (nose up pitching moment) with decreasing wall separation, which then falls rapidly once past a maximum point. This follows a very similar trend to the rear lift graph (Figure 2.12) owing to the larger changes in C_{Lr} in comparison to C_{Lf}. Indeed the maximum C_M for each ride height is at almost the same distance from the wall as the point of maximum C_{Lr}, although more near-wall readings would be required for this to be verified.

From Figure 2.14 it is evident that C_D increases with decreasing wall separation, before falling rapidly past a maximum point. It can also be seen that this maximum point is again moved closer to the wall with increasing ride height. Also plotted are the corresponding C_D changes for a 0° wing, showing both that the overall drag increase is lower than with a 2° wing, and that the subsequent fall is less severe. These effects are readily understood when combined with those of the Figure 2.12, which showed that the rear wing at a 2° angle produced significant extra downforce when in wall proximity. This increase in downforce is accompanied by an increase in drag on the wing, shown in the difference in C_D between the 0° and 2° wing angles.

As can be seen from Figure 2.15 the side force on the model increases (attracted towards the wall) until a point at approximately z_w=0.02L is reached. This point appears to be independent of both ride height and rear wing angle. The overall increase in C_Z though does appear to be approximately 3% lower for the 0° wing angle, with Brown attributing this discrepancy to “being caused by the increased strength of the vortex interacting more strongly with the retaining wall” in the 2° case. No further explanation of the nature of this interaction is presented however.

Figure 2.16 shows how the yawing moment coefficient varies with wall proximity, ride height and wing angle. In this case a negative yaw is rotating the model nose away from wall. Ride heights between the highest and lowest cases are omitted from this diagram for clarity. The yawing moment is maximised at a wall separation of approximately z_w=0.02L, as was the side force (Figure 2.15). It is clear, therefore, that the side force attracting the model to the wall acts aft of the model centreline. At wall separation less than approximately z_w=0.02L the side force falls causing a corresponding increase in C_N (nose towards wall).

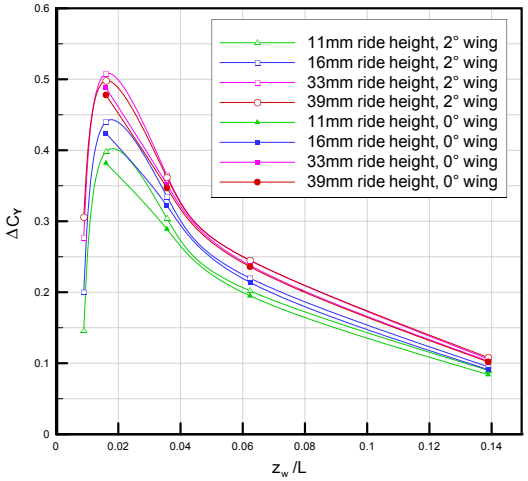

Figure 2.15 - Side force coefficient variation with changing wall separation and rear wing angle - data from Brown [2005]

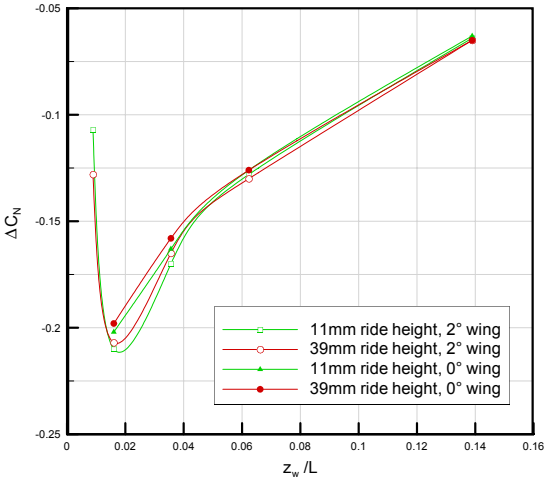

Figure 2.16 - Yawing moment coefficient variation with changing wall separation and rear wing angle - data from Brown [2005]

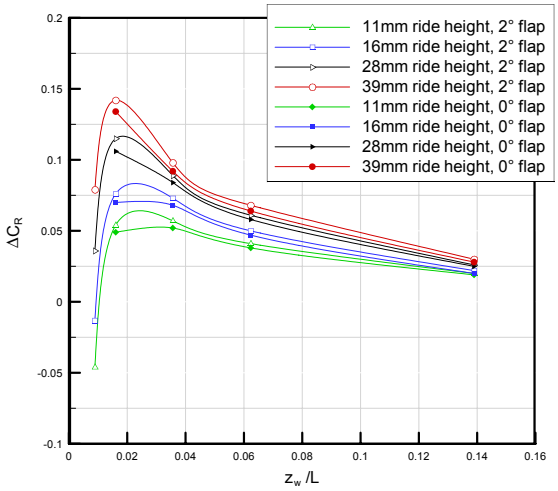

Figure 2.17 - Rolling moment coefficient variation with changing wall separation and rear wing angle - data from Brown [2005]

Rolling moment, like front lift and rear lift increases to a maximum point which is moved closer to the wall for increasing ride height. The similarity of Figures 2.17, 2.11 and 2.12 suggests that the increase in C_R (top of the model towards the wall) is due to an asymmetrical lift produced at both ends of the model. It is also evident from Figure 2.17 that the 2° wing angle cases create a larger overall rolling moment than the 0° cases by approximately 7%. Brown suggests that "this would be due to the stronger vortex for the two degree wing angle interacting with the wall". Again, however, no further explanation of this interaction is presented.

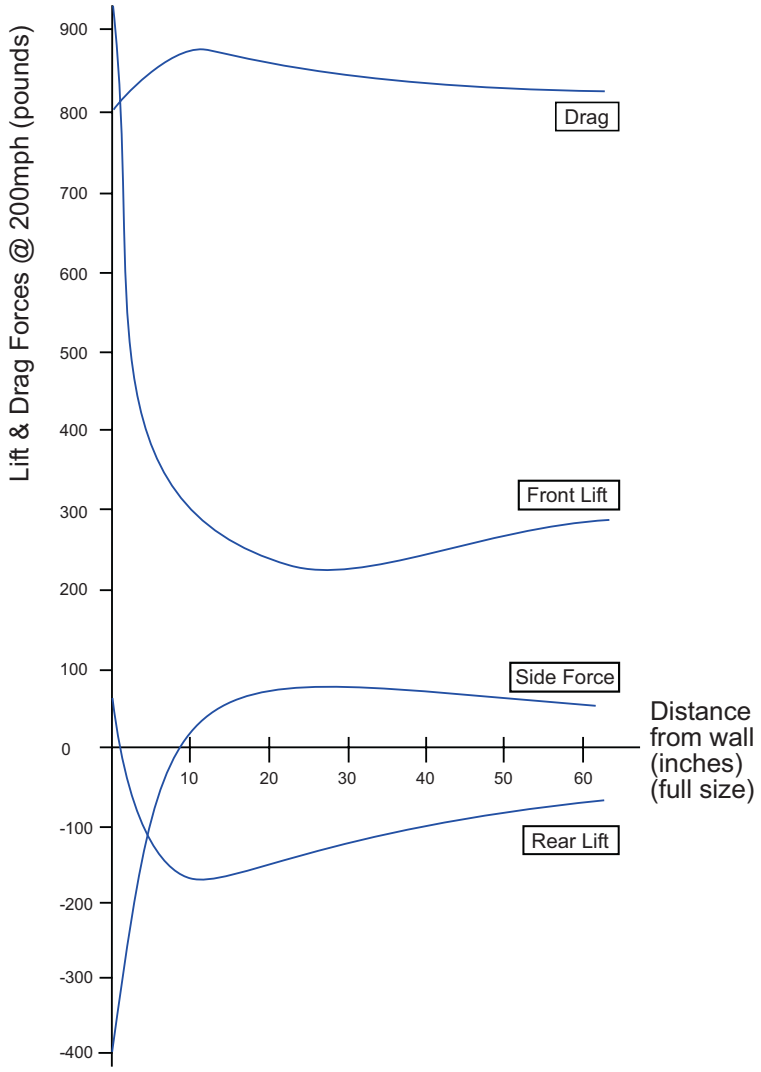

Figure 2.18 - Variation in front and rear lift, side force and drag with changing wall separation - after Wallis and Quinlan [1988]

NASCAR Near-Wall Results

Figure 2.18 shows firstly that the drag force on Wallis and Quinlan's model increases to a maximum point before falling rapidly as wall separation distance reduces. This trend is consistent with the drag results measured by Brown, plotted in Figure 2.13. In addition, it can be seen that Wallis and Quinlan's front lift force falls to a minimum point, before rising almost exponentially as the wall separation tends towards zero. This must be compared with the trend shown by Brown in Figure 2.11. This also shows the rapid increase in C_{Lf} as wall separation falls below a certain point, with a comparatively small drop in C_{Lf} evident for most ride heights in the region z_w>0.06L. However, the large drop in C_{Lf} particularly evident for the higher ride heights plotted in Figure 2.11 is not reproduced by Wallis and Quinlan.

The rear lift trends from both experiments do, however, show a high degree of similarity.

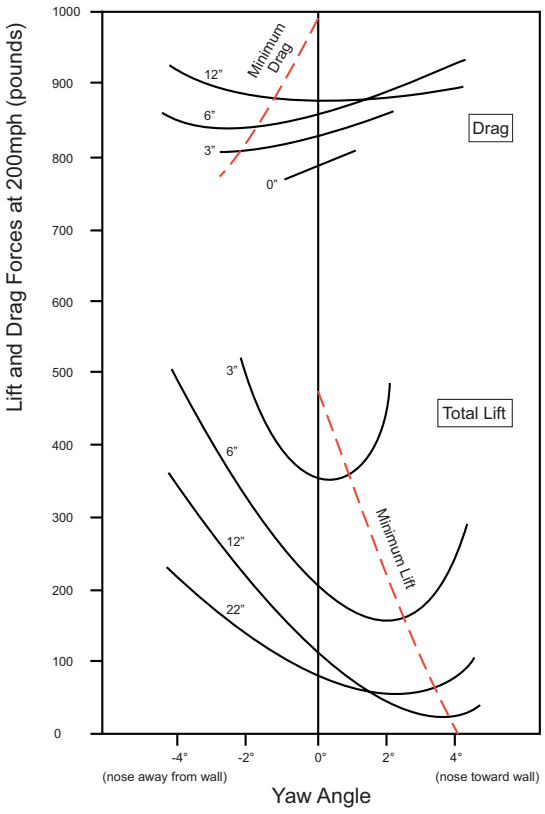

Figure 2.19 - Variation in C_L and C_D with changing wall separation and vehicle yaw angle - after Wallis and Quinlan [1988]

Brown's data (Figure 2.12) shows a gradual decline in C_{Lr} before exhibiting a large increase once the model moves closer to the wall. This mirrors the trend in Wallis and Quinlan's results, shown in Figure 2.18.

The side force measured by Wallis and Quinlan exhibits a very slight increase in magnitude (force towards the wall) as wall separation falls, before dropping quickly and becoming negative (force away from wall) in the very near wall region. This trend is consistent with Brown's results, shown in Figure 2.15.

Figure 2.19 plots total lift and drag for the various model yaw angles measured by Wallis and Quinlan. These data cannot be compared with that of Brown as the model was not yawed in that investigation. It can be seen from Wallis and Quinlan's data that the points of minimum drag occur as the model is yawed negatively (nose away from the wall), whereas points of minimum total lift occur at positive yaw angles. In both the lift and drag cases the minimum value yaw angle fell as wall separation decreased.

2.2.2 NASCAR Near-Wall CFD Investigation

A separate investigation into the aerodynamic effects of a NASCAR running in close proximity to a retaining wall was conducted by a commercial company, Advantage CFD [2001]. This was an entirely computational investigation, and was performed for only one configuration. The car was modelled as being ¼ of the car's width (≈0.1L) from a 1.28m (0.27L) high wall. As in Wallis and Quinlan's study the driver's side window was modelled as being open and a rear spoiler was included. Data from this case were compared to baseline data from an initial study into the NASCAR running in isolation, and the change in static pressure on the near-wall side of the car is shown in Figure 2.20.

No quantitative force data has been presented by Advantage CFD for this investigation, but it is stated that the overall drag force was slightly increased, as was the overall downforce. Despite this overall downforce increase it was found that front end lift actually increased, whilst rear end lift decreased. The increase in overall drag can be readily explained by the increase in near-wall side front-end pressure shown in Figure 2.20. It was also found that at this wall separation the computation predicted a side force attracting the car to the wall. This is again easily understood from Figure 2.20 by the drop in pressure over the near-wall side.

The wall height used in this case was slightly lower than that used by Wallis and Quinlan [1988] - 0.27L compared to 0.29L. Also, in this case the exact distance between the car and the wall was specified as being one quarter of the car's overall width. This distance was

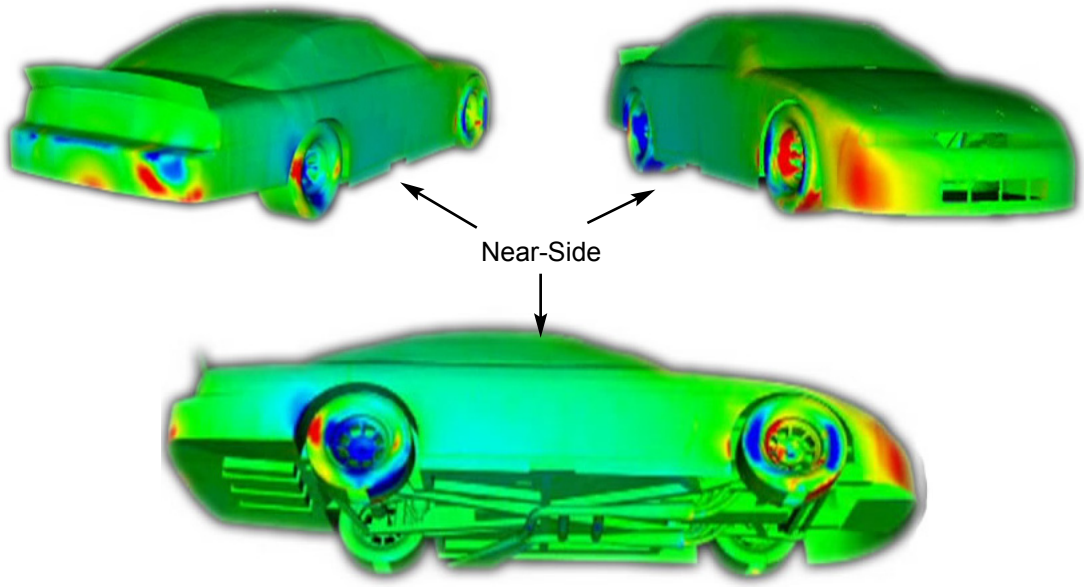

Figure 2.20 - ΔCp between isolated and near-wall (z_w≈0.1L) cases on the near-side of a NASCAR. Yellow and red indicate a rise in C_p, blue indicates a drop. Green indicates no C_p change - after Advantage CFD [2001]

therefore found to be approximately z/L = 0.1. At this distance from the wall in Wallis and Quinlan's investigation the car exhibited almost a doubling of rear downforce, a slight decrease in front downforce (approximately 15%), and a slight increase in overall vehicle drag (5%). Although both the increase in rear-end downforce and the rise in overall drag were both predicted by these two studies, they differ in their respective predictions of front end lift. The computational model predicts a rise in front end lift force at this distance from the wall, whilst the experiments predicted a drop. This is a significant discrepancy as the front end lift dictates, to a large extent, the handling characteristics of the car. No significant differences of this type would be expected between Wallis and Quinlan's and Advantage CFD's results, due to the almost identical geometry of the models used in each investigation.

2.2.3 Overview of Previous Near Wall Studies

The previous studies described above are summarised in Table 2.1. An overview of their main findings is given below.

Front Lift

Wallis and Quinlan's data reveal that front lift force falls to a minimum point, before rising almost exponentially as the wall separation tends towards zero. Brown's data mirror the rapid increase in C_{Lf} as wall separation falls below a certain point. However, the sudden large drop in C_{Lf} particularly evident for the higher ride heights tested by Brown is not reproduced by Wallis and Quinlan. Advantage CFD's study predicts a rise in C_{Lf} at the one wall separation computed, whilst both Wallis and Quinlan's and Brown's results predict a drop in C_{Lf} at this point.

Rear Lift

The rear lift trends from both experiments show a high degree of similarity. Brown's data (Figure 2.12) show a gradual decline in C_{Lr} before exhibiting a large increase once the model moves closer to the wall. This is in agreement with the trend shown in Figure 2.18. Advantage CFD's study predicts a slight drop in C_{Lr} at the one wall separation computed, in agreement with the experimental data.

Drag

Figure 2.18 shows that the drag force on Wallis and Quinlan's model increases to a maximum point before falling rapidly as wall separation in further reduced, a trend consistent with Brown's data. Advantage CFD's study is also in agreement, predicting a slight fall at the one wall separation computed.

Side Force

The side force measured by Wallis and Quinlan exhibits an increase in magnitude (force

towards the wall) as wall separation falls, before dropping rapidly in the very near wall region. This trend is consistent with Brown's results and with Advantage CFD's for its single wall separation.

2.3 Aims and Objectives of the Current Research

It is clear that there exists a significant gap in the literature as far as the understanding of the aerodynamic effects of side-wall proximity is concerned. Although two experimental studies have been reported in the literature recording the variation in forces with wall separation, no attempt has as yet been made to analyse the induced flow structure alterations.

Aims

To investigate the flow structure around a generic car body in ground effect and in the influence of a side wall.

Objectives

i) To provide a greater understanding of the flow around an isolated Ahmed model, with particular reference to the effects of a rolling road and overhead supporting strut.
ii) To provide an understanding of the effects of wall proximity on an Ahmed model.
iii) To determine the generality of these near-wall effects, and how this knowledge could be utilised in assessing the effects of wall proximity on other body shapes.
iv) To determine the validity and usefulness of the RANS simulations in predicting the above effects

Author(s)	Experimental or CFD	Reynolds Number(s)	Model Type	Variable(s) Tested	Measurements Presented
Wallis and Quinlan	Experimental	$5.9x10^6$	NASCAR	Wall separation; Vehicle yaw angle; Wall inclination	6-Component Forces and Moments, Pressure on side wall
Advantage CFD	CFD	$2.2x10^7$	NASCAR	None - only one case computed	Pressure contour changes on car
Brown	Experimental	$1.46x10^6$, $1.77x10^6$, $2.54x10^6$	Type C model	Wall separation; Ride height; Rear wing angle; Re	6-Component Forces and Moments

Table 2.1 - Summary of near side-wall aerodynamics literature

3. Experimentation

The investigation incorporated two distinct experimental phases. Phase one was concerned with analysis of the flow around an isolated Ahmed model, whilst the second phase studied the flow with the inclusion of a near side-wall. The major components of the test set-up used in the isolated case will be described here, with variations facilitating the inclusion of the side-wall detailed at the end of the chapter. Detailed test parameters and error analysis can be found in Appendices A and F respectively.

3.1 Wind Tunnel

The testing was conducted in the D.S. Houghton wind tunnel, a schematic of which can be seen in Figure 3.1. The tunnel is of closed-return, ¾ open-jet type, and employs ground

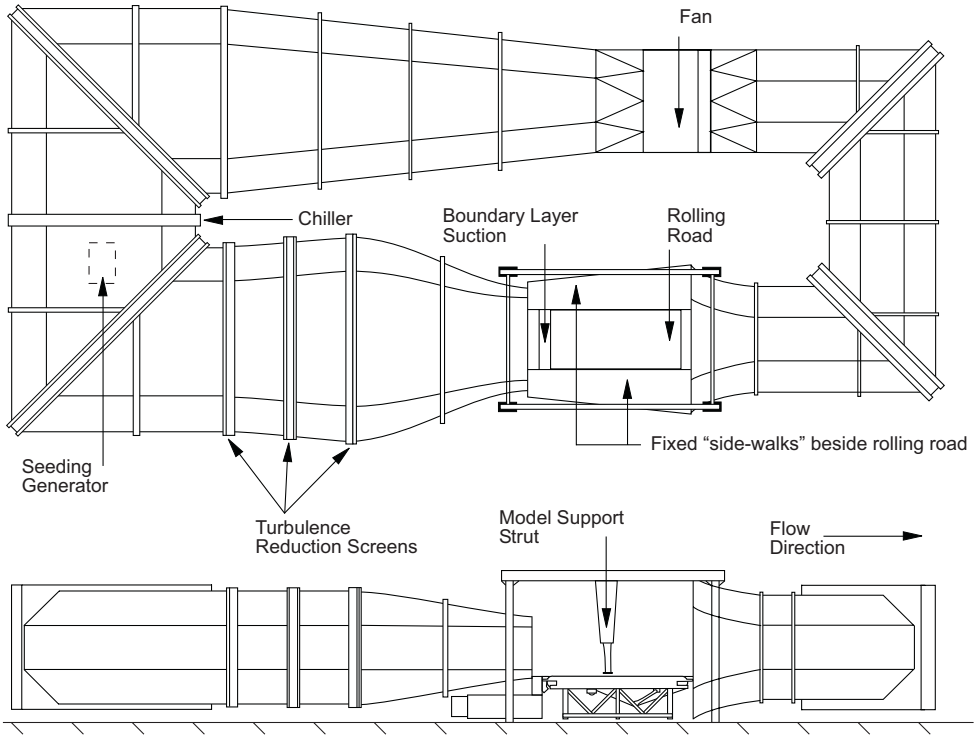

Figure 3.1 - Schematic Diagram of D.S. Houghton Wind Tunnel

simulation in the form of a rolling road, synchronised with the freestream velocity. Suction applied through the tunnel floor and a knife-edge transition to the rolling road are used to remove the tunnel boundary layer. Distributed suction is also applied to the underside of the rolling road to prevent belt lifting caused by aerodynamic effects. The air and road temperatures were held constant throughout testing at 25°C by chiller units. Further detailed specifications of the wind tunnel can be found in Appendix B.

An Ahmed model was constructed with dimensions as shown in Figure 2.1. This was made of aluminium sheet on an aluminium frame with interchangeable sections to create the required nine backlight angles. The overhead strut on which the model was supported in the wind tunnel was attached on an internally mounted force balance.

Experiments were conducted at a freestream velocity of 25ms^{-1}, equating to a Reynolds number of 1.7x10^{6} based on model length. The model blockage was 3%, based on the frontal area of the model and the wind-tunnel nozzle.

3.2 Laser Doppler Anemometry

3.2.1 Overview

Figure 3.2 outlines the important features of the laser Doppler anemometry set-up employed.

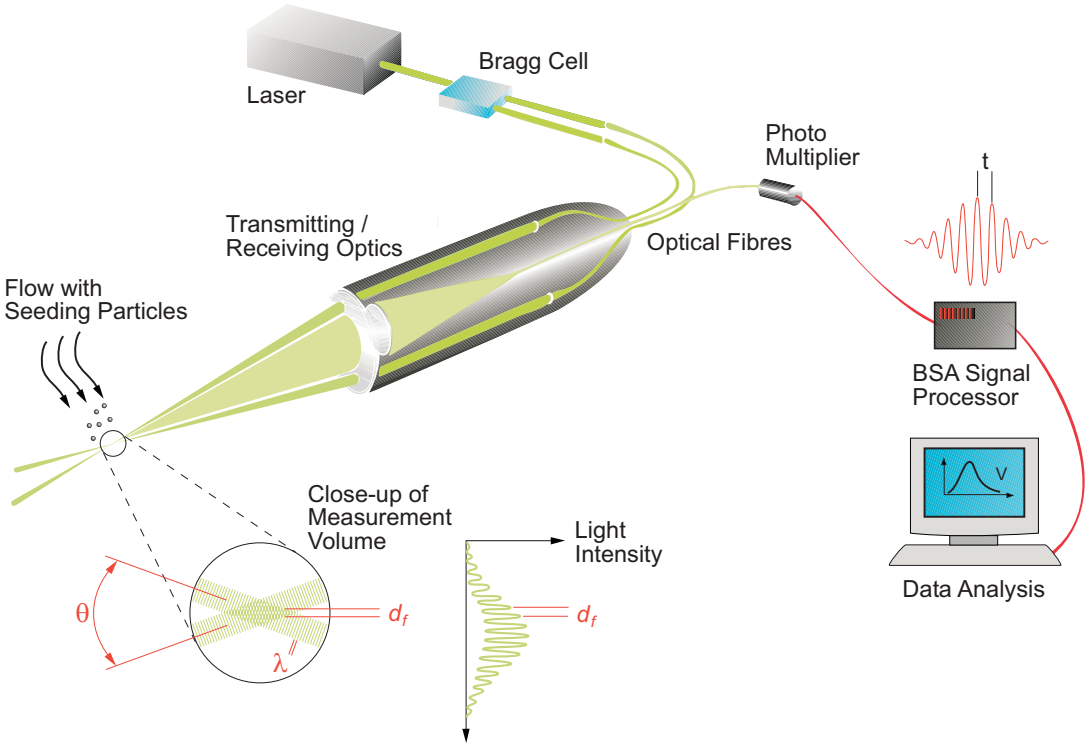

Figure 3.2 - Schematic Diagram of LDA set-up - after DANTEC

Two intersecting beams of laser light are used per component of velocity to be measured, which are focused by the transmitting optics to intersect in the measurement volume. Two velocity components can be measured by the same probe where two pairs of beams are aligned so that the respective planes which they occupy are perpendicular to one another. In order to record the third velocity component either a third single component probe aligned with the third velocity direction is required, or a two-component probe aligned at a sufficient angle from the first probe to allow resolution of the velocities.

The main advantages of this method of flow measurement are its non-intrusive nature (apart from the need to introduce seeding particles), high spatial and temporal resolution and the absence of any required calibration.

3.2.2 Experimental LDA Set-up

Due to the size of the wind tunnel working section a LDA system with a focal length of over 2m was required. The transmitting and receiving optics would otherwise have caused disturbances in the flow and induced errors in the positioning of the system due to vibrations. The LDA system available has only one 2.5m focal length lens and therefore only two velocity components measurements could be measured simultaneously. The probe was mounted on a 3-component traverse aligned with the tunnel working section. The signal from each beam pair was processed by a dedicated Burst Spectrum Analyser (BSA), and all equipment was controlled by Dantec BSA Flow software v.1.4.

A JEM Hydrosonic 2000 fog generator was used to seed the flow with a water/glycerol seeding mixture. This system produced high volumes of ambient temperature seeding, with a

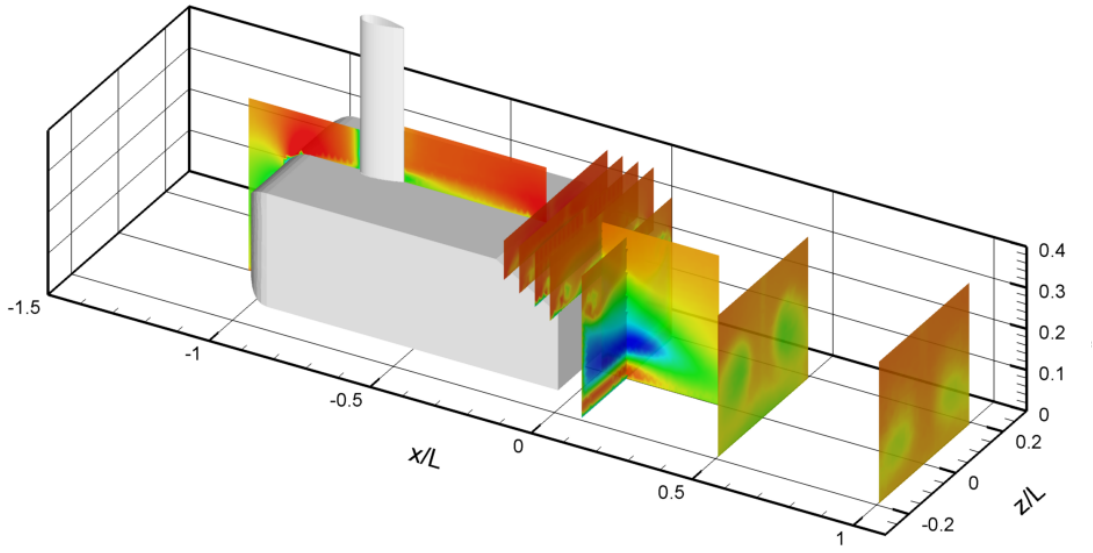

Figure 3.3 - Example LDA planes of data taken for the 25° isolated Ahmed model

constant mean particle size of 1.3μm. The generator ran continuously throughout the tests, positioned upstream of the first set of turning vanes, as can be seen in Figure 3.1. A previous investigation was conducted to determine the effect of the seeder wake on the flow in the working section [Knowles, 2005]. It was found that with the seeder in the position indicated in Figure 3.1 the presence of a set of cascades and the turbulence-reduction screens effectively redistributed the seeder wake so that it had no discernable effect on the model.

The LDA measurement volume was 0.024mm x 0.024mm x 10.01mm in the x, y and z directions respectively. As a result, the spatial resolution of the measurement plane was dictated by the length of the measurement volume in the z-direction, and the grid was spaced to ensure the measurement volume at each point was unique, and did not overlap that of other points. Planes of data were taken both around and downstream of the model, a number of which (taken for the 25° case) are shown in Figure 3.3. A full list of the planes taken for each backlight angle can be found in Appendix A.

For all LDA tests the model was mounted 50mm above the moving ground plane, in agreement with previous Ahmed model studies.

3.3 Force and Moment Measurements

A PC-controlled six-component force balance was mounted inside the model, and calibrated with known forces prior to testing. The balance was attached to the overhead supporting strut shown in Figure 3.1. This aerodynamic strut (t/c=0.25) was positioned at x/L=0.25 (strut leading edge) downstream of the model leading edge, and was controlled by the central wind

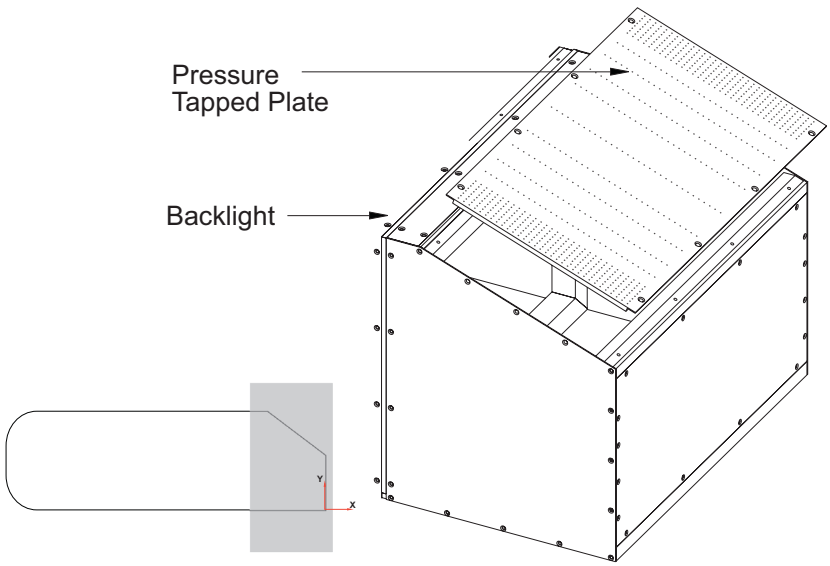

Figure 3.4 - Pressure tappings on the Ahmed model backlight

tunnel control system, allowing alteration of ride height during testing. The effect of ride height was investigated only during experiments recording the forces and moments on the model, as to conduct all LDA tests for changing model ride heights in addition to backlight angles would have proved prohibitively time consuming.

3.4 Static Pressure Measurements

The backlight of the model was designed so as to be interchangeable with a plate containing a number of pressure tappings. This set-up can be seen in Figure 3.4. A greater concentration of tappings was placed close to the edges of the model in order to investigate both the vortex structure in this area and the effects on this structure due to wall interference. The exact positions of the tappings can be found in Appendix A. The tappings were read sequentially, each averaged over a period of 16 seconds at a rate of 500Hz. Pressure measurements were conducted only for the 25° case, both for the isolated model and in wall proximity.

3.5 Wall Model

The wall was mounted from the side of the rolling road on the “side-walks” marked on Figure 3.1. This set-up can be seen in Figure 3.5. The wall was made from perspex so as to minimise any reflections during the acquisition of the LDA data. The model wall extended 0.5L upstream and 0.5L downstream of the leading and trailing edges of the Ahmed model respectively, and extended to a height of 0.63L above the top edge of the model. An aerodynamic leading edge

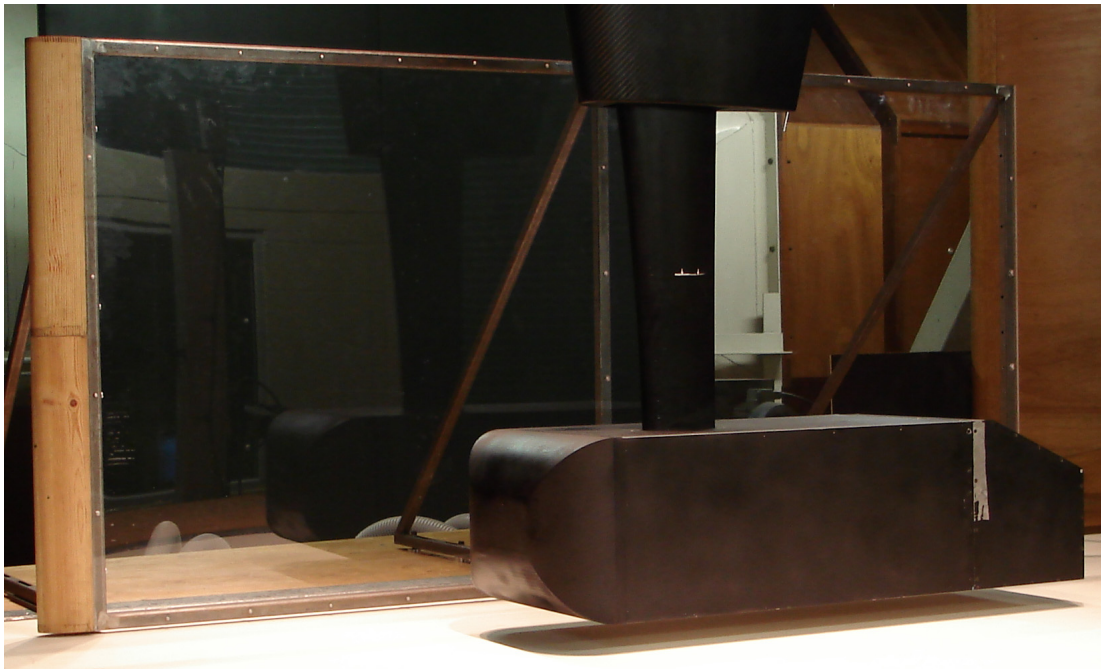

Figure 3.5 - Experimental near-wall wind tunnel set-up

was fitted to the wall model in order to reduce the boundary layer thickness on the wall itself. For each test case, the gap required between the rolling road and the wall was kept at 2mm in order to allow for any vertical flapping of the rolling road, whilst minimising any flow escaping at this junction. During near-wall testing all other parameters of the experiments were kept consistent with the isolated tests.

4 Computational Method

The computational work, like the experiments, was split into two separate phases, the first investigating the isolated model case and the second analysing the effects of the side-wall. First performing computations on an isolated model would allow comparison of the data with those previous experimental and computational studies described in Chapter 2. In addition, this isolated investigation would provide baseline data with which to compare near-wall computations. The following outlines the procedure used for the isolated CFD cases, with the alterations required for the near-wall cases described at the end of this chapter. Commercially -available software was employed for each of the four main stages of the CFD process.

1. Initial pre-processing using GAMBIT
2. Secondary pre-processing using TGrid
3. Processing using FLUENT
4. Post-processing using FLUENT

These stages will described in the following sections, while detailed solver parameters for each test case can be found in Appendix D.

4.1 Computational Pre-Processing

Gambit Pre-Processing

GAMBIT is FLUENT's pre-processing software used for building and meshing models for subsequent solving. Its graphical user interface allows the user to input the geometry of the model to be studied, before meshing and exporting the model. In this case, the Ahmed model and domain boundaries were created, their surfaces meshed and subsequently exported for generation of the 3D volume mesh. A viscous hybrid meshing scheme was employed, whereby sections of flow where boundary layers are formed are solved using prismatic cells, with the remainder of the flow meshed with tetrahedral cells. This approach was used owing to its ability to solve flow gradients more accurately than could be achieved with a mesh of

equal size consisting entirely of tetrahedral cells. The mesh size had to be limited to approximately $2x10^6$ cells due to available computing power and the time needed to run each simulation.

Model Generation

An Ahmed model shape was generated and adjustments made as required for each of the nine separate back angles. The extent of the computational domain around the Ahmed model forms a virtual wind tunnel, and as such possible wall effects had to be considered when determining these wall boundaries. The computational domain was therefore created 8L in length, 2L in height, and 2L in width, with the model leading edge positioned 2L downstream of the fluid inlet, 50mm above the ground plane and centrally between the side walls. These dimensions give a blockage ratio of 2.8%. The longitudinal gradients of static pressure produced by this blockage ratio are very small in comparison to the gradients of static pressure on the Ahmed body, and as such can be considered negligible in the calculations. It has also been shown previously that these dimensions chosen for the simulated wall boundaries should ensure insignificant effects on the airflow around the Ahmed model [Gillieron and Chometon, 1999].

It is of paramount importance that both the upstream and downstream boundaries of the domain extend a sufficient distance from the leading and trailing edges respectively of the Ahmed model. In particular, the Ahmed body has a large frontal area in comparison to its overall dimensions, and therefore C_D calculation is largely dependent on the correct prediction of the stagnation pressure over this surface. This has proved to be problematic in the past [Graysmith et al. 1994], and incorrect stagnation pressure prediction over this area has been one of the main reasons for the discrepancy in the drag results from previous CFD

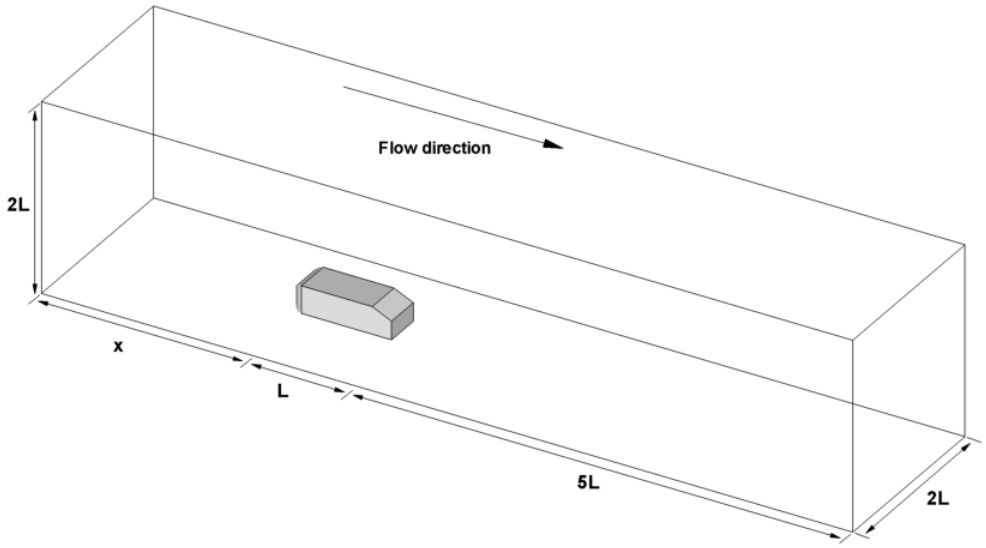

Figure 4.1 - Schematic of Computational Domain

calculations. For this reason, it is necessary not only to have a highly refined mesh at the front of the CFD modelled body, but also for this mesh to extend far upstream. A study was performed whereby the distance of the inlet boundary upstream of the model was varied and the effect on C_D investigated. The complete results of this study can be found in Appendix E, but it was found that approximately two model lengths is a sufficient inlet distance from the model leading edge. Further increasing this distance has little effect on the C_D prediction and serves only to increase the size of the computational domain. The domain used for the current CFD calculations was therefore extended to the required two model lengths upstream of the model leading edge.

The downstream computational boundary must extend far enough to capture the entire wake flow, and be at a point where the flow static pressure has returned to its undisturbed value. It has been shown [Gillieron and Chometon, 1999] that a refined mesh 5 car lengths downstream is sufficient to achieve this, and as such the domain used extended this distance downstream.

Mesh Generation

The first stage of meshing the resulting computational domain is to mesh the various surfaces on the domain boundaries. Meshing is the spatial discretisation of these surfaces into a grid of individual points. It is on these points and these points only that the solver will perform the required calculations, and as a result of this there must be a higher concentration of points (i.e. a finer mesh) in the sections of flow which experience significant pressure gradients (e.g. flow separation). For the Ahmed model, as has been shown previously, the most significant aerodynamic phenomenon is the separation of the flow over the back end of the model, and as such this region requires greater mesh refinement. A surface meshing system similar to that of Gillieron and Chometon [1999] was employed. This involved meshing those faces of the Ahmed model not experiencing flow separation with a mesh spacing of $2x10^{-2}$m, and meshing those faces which do with a spacing of $5x10^{-3}$m.

TGrid Pre-Processing

TGrid is another FLUENT pre-processor, designed specifically to create unstructured meshes. TGrid works by importing either a surface mesh (in 3D) or meshed edges (in 2D) and creating an unstructured mesh to fill in the intervening space. TGrid is also used to create prisms on a surface mesh which are used to solve the boundary layer close to that surface, when a viscous hybrid meshing scheme is employed. It is for this ability that TGrid was used for the current computations. Details of the size and composition of each mesh used in both the isolated and near-wall computations can be found in Appendix D.

Supporting Strut

The supporting strut used in the experiments was not modelled in the present computations. A preliminary computational study was performed with the inclusion of the strut, but it was found that a large number of cells were required to resolve its boundary layer and wake. As a result of the available computing power, the strut's inclusion limited the number of cells available to resolve the backlight flow. The resulting resolution of the flow on the body and in the wake therefore gave poorer results than without the strut. Details of the computations performed with the strut can be found in Appendix E.

4.2 Processing

Boundary Conditions

The boundary conditions on the faces of the domain, shown in Figure 4.1, were as follows. At the velocity inlet, a freestream velocity of 25ms^{-1} was specified in order that the results could be compared with current experimental work and that of Graysmith [Graysmith et al. 1994]. At the downstream face a pressure outlet condition was set to atmospheric pressure. Symmetry conditions were set on the walls, roof and the floor underneath the model. It was found that the computationally more expensive method of modelling the floor as a wall moving at the freestream velocity has no effect on the prediction of the flow, and therefore was not used.

Turbulence Modelling

It has been shown previously that the RNG k-ε model is superior to the standard k-ε model in both its prediction of aerodynamic coefficients and the prediction of pressure distribution over the Ahmed model [Graysmith et al. 1994], due to its ability to predict better types of flow which exhibit large regions of flow separation. In addition, it has been shown that for the 30° case the Reynolds Stress model (RSM) provides a more accurate prediction of the separation over the backlight [Makowski and Kim, 2000]. As all back angles were to be tested in the current investigation however, both these viscous models and the k-ω model were tested to ascertain which would be the most accurate. Both the RNG k-ε and Reynold Stress models were found to be comparatively accurate over the range of backlights, but with the RSM proving to be unstable in some cases. As such the RNG k-ε model was employed throughout the majority of the computational investigations. The use of more advanced models such as LES and DES was not possible due to insufficient computing power being available.

Convergence

As the grid was not aligned with the flow due to the unstructured mesh, it was necessary to use second-order discretisation, as first-order discretisation greatly increases the numerical

diffusion. Although first-order iterations are more likely to converge quickly, the solution would be less accurate. In order to ensure convergence, however, a number of first-order iterations were performed in each calculation before switching to second-order iterations.

Plots of the residuals from the governing equations, as well as plots of both the total lift and drag on the Ahmed model were used to ascertain convergence. The computation was terminated when it appeared the force measurements had stopped fluctuating. It was thought that this method would prove more accurate than using the default convergence settings as this would not take account of the force measurements, which were considered to be of greater importance.

Mesh Refinement

After convergence of the solution the mesh was refined in FLUENT. FLUENT gives the option to increase the number of cells in a specific region of the flow, depending on user defined criteria. In this case the mesh was refined in cells where the gradient of static pressure over the cell was greater than a specified threshold value. This value was dependent on both the model geometry being investigated and the number of previous refinements already performed. The total number of cells had still to be kept to a level where the computing power available could continue the iterations. After each mesh refinement approximately 200 iterations were necessary in order to converge the solution, this relatively small required number being expected from previous work [Makowski and Kim, 2000].

4.3 Post - processing

Once all calculations on each of the cases were completed, a number of graphical plots of the flow were created. These included contour, vector and line integral convolution (LIC) plots. In addition force, pressure and turbulence data were extracted from the flow solution. This information was used to compare the CFD simulation with the current experimental work and previous investigations into the Ahmed model.

4.4 Inclusion of Side-Wall

The side-wall model used in the experiments was not modelled directly in the CFD. To include accurate geometry of the wall would have taken an excessively large portion of the available cells, and therefore the simulation would have been less accurate in other regions of the flow. This would also have made comparisons between the isolated and near-wall CFD cases problematic due to the different mesh densities employed. Instead the Ahmed model was moved closer to one side of the computational domain, effectively rendering that side an

infinite wall. A higher mesh density was used on the section of this wall directly beside the Ahmed model, but all other parameters remained identical to the isolated cases. The computationally more expensive method of modelling the side-wall as a solid boundary was found during a preliminary computational investigation not to alter the flow over the model at the smallest computed wall separations.

5. Isolated Model Results and Discussion

The following analysis of the isolated Ahmed model results is split into two distinct sections. The first will be concerned with the forces, pressures and flow structure measured throughout the current experimental programme. Particular attention will be paid both to the flow over each of the angled backlights and the near wake of the model. This will aim to provide a fuller understanding of the flow than has been published previously in the literature, in addition to encompassing a wider range of backlight geometries than it has become common practice to investigate. This understanding of the flow regimes formed will be vital for these isolated case results to be used as a baseline against which to assess accurately the effects of side wall proximity.

The current data will, where appropriate, be compared with those of Lienhart and Becker [2000], and Ahmed et al. [1984]. The variations in experimental method between the investigations and their effects on the flow will be analysed. Quantification of these variations is necessary in order to assess accurately the effects of the current experimental set-up on the flow.

Secondly, the current computational results will be compared to experimental data for validation and verification purposes. The flow structure, pressures and forces on the model will be used for this purpose.

5.1 Experimental Results

5.1.1 Force Results

Figure 5.1 shows the force measurements taken during the current experiments compared with previously-published experimental data. Lift coefficient data were not presented by Ahmed et al. [1984]. It can be seen that two overall drag coefficients were recorded by Ahmed for the 30° backlight angle. These represented high drag and low drag cases, the latter being

achieved by fixing a vertical splitter plate behind the model. It is clear from Figure 5.1 that Graysmith et al. [1994] tested only the high drag case. For the current experiments, it appears from the results that at the critical 30° angle the flow has already separated over the backlight, causing only the low drag case to be measured. In all the results outlined the trends for both lift and drag follow those expected from the flow regimes outlined earlier. The shifting of this trend - an evident increase in drag coefficient in both the investigations employing a moving ground plane - is likely to be caused by both the effect of the rolling road itself and the relocation of the supporting struts from underneath to on top of the model. The current data show an increase in C_D of approximately 5% at each point measured in comparison to Ahmed, whilst data from Graysmith exhibit a shift of approximately 25%. A previous investigation [Howell and Hickman, 1997] reported that rolling road simulation caused an increase in C_D of around 3% for a typical road car at ground clearances comparable to those used here. As such this variation in experimental procedure cannot account for the differences in C_D reported by Graysmith.

The C_L values from the current experiments are generally within 0.04 of Graysmith's values, aside from the 30° case due to the flow variations stated above. Due to the large discrepancies in Graysmith's C_D values however, it is difficult to assess accurately the validity of his lift data. The trends in C_L though are what would be expected from the previously recorded flow structure changes on the model throughout the backlight angle range.

5.1.2 Time-Averaged Velocity Results

Front End

We chose to begin the analysis of the flow upstream of the model leading edge and progress

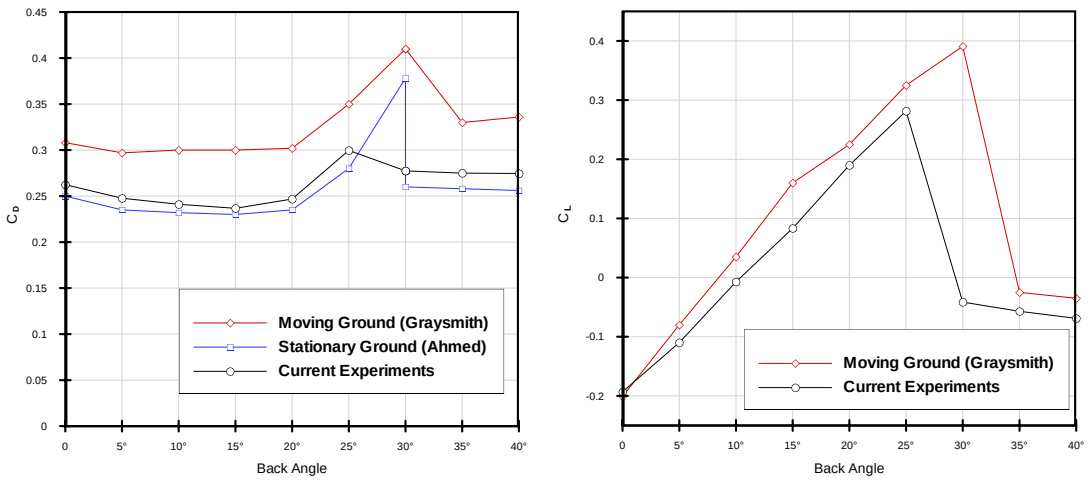

Figure 5.1 - Ahmed Model Experimentally Measured Lift and Drag coefficients

downstream. Ahmed previously reported that the backlight angle had little effect on the flow around the front end, owing to the long central section. To investigate this a model centreline (z/L = 0) plane of LDA data was taken around and upstream of the leading edge for both the 10° and 25° backlights. These angles were chosen as they have been shown previously to have dissimilar flow over their respective back ends. Figures 5.2 - 5.4 show lines of data extracted from both these planes in order that any differences in flow structure over the model front end can be distinguished. Wherever possible, data from Lienhart and Becker [2000] have been included in order that comparison between the experimental results can be made.

Figure 5.2 shows the variation in flow velocity in the freestream direction for the 10° and 25° cases with the y/L positions chosen corresponding to 0.025L above and below the model.
It is evident that downstream of the suction peaks on the top and bottom of the curved front there is found a higher velocity on the model underside. This is expected due to ground proximity, and subsequent lower pressure on the model underside is the cause of the downforce experienced by the symmetrical model configuration (0° back angle).

Inspection of the u velocity plot of Figures 5.2 also shows very little variation in the streamwise velocities measured between the two back angles tested. Indeed the maximum variation measured in this plot is less than $0.01u_{\infty}$, which is within experimental error. There is a larger variation between the 10° and 25° backlights in the v velocity plot of Figure 5.2, the maximum variation found to be approximately $0.03u_{\infty}$. This suggests that although the effects of the backlight geometry on the front end flow are minor, the increased suction over the back end of the 25° model appears to have the effect of moving the stagnation point on the front end upwards in comparison to the 10° case. This would account for the marginally higher v velocity over the top of the model at 10°.

Data from the 25° and 35° cases tested by Lienhart are plotted along with current data in Figure 5.3. Again it can be seen that although these two angles tested by Lienhart exhibit quite different flow structures over the back end, the velocity profiles shown at x/L=-1.02 show differences which are within experimental error. This reinforces the assumption that for a given test set-up the angle of the backlight has little effect on the front end flow. It can also be seen from Figure 5.3 that the velocity in the freestream direction over the top of the model is higher by approximately 5% in Lienhart’s experiments in comparison to the current 25° case. This is confirmed by data taken slightly further downstream of the front end for both the current and Lienhart cases, omitted here for brevity. It seems reasonable to assume that this is an effect of the flow slowing due to the blockage created by the supporting strut. As the data shown in Figures 5.2 - 5.4 were extracted from the model centreline (z/L=0), this is the position where the strut will have the greatest upstream effect. As this overhead blockage does not exist in Lienhart's experiments, a higher flow velocity is experienced over the top of the model.

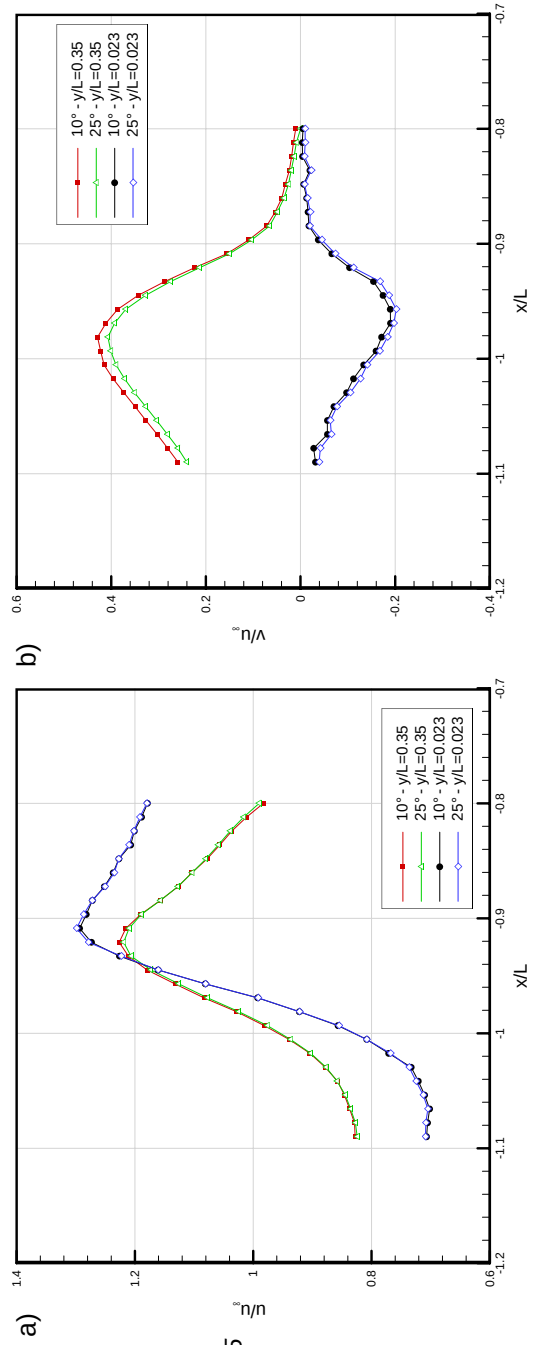

Figure 5.2 - Streamwise profiles of normalised u and v velocity at y/L=0.35 and 0.023 around Ahmed model front end for 10° and 25° backlight angles

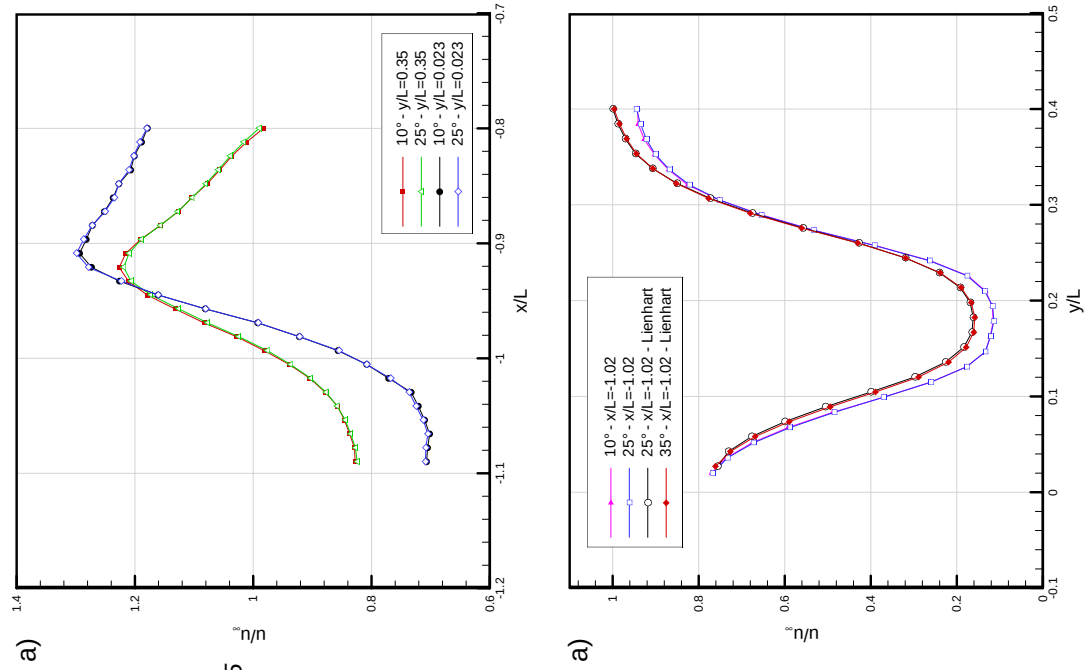

Figure 5.3 - Vertical profiles of normalised u and v velocity at x/L=-1.02 around Ahmed model front end for 10° and 25° backlight angles

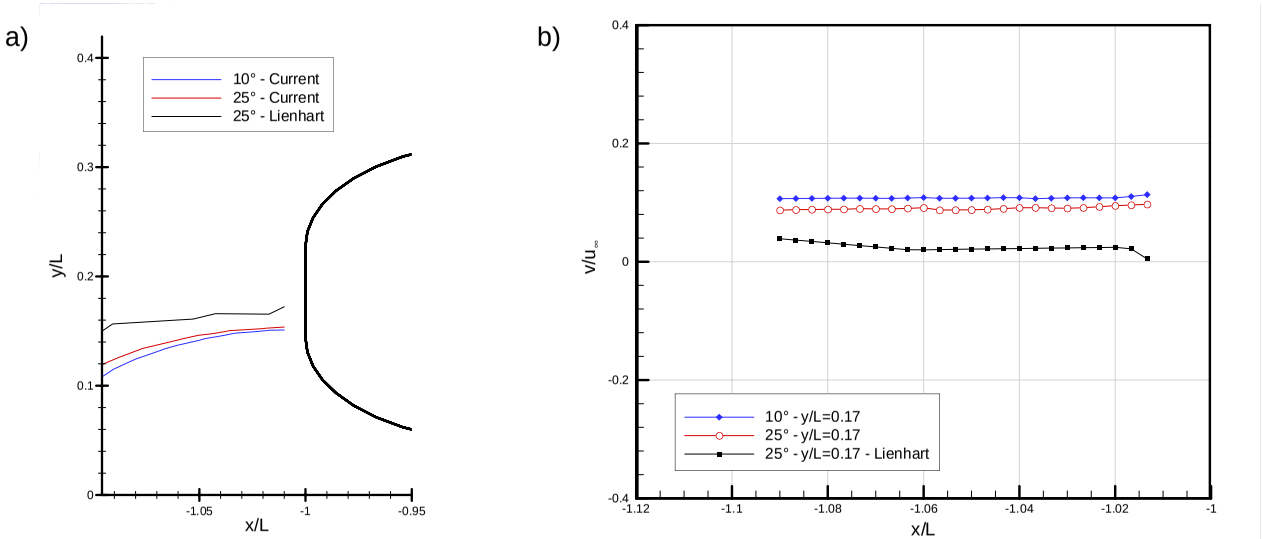

Figure 5.4 - (a) Contours of v=0 and (b) streamwise profiles of normalised v velocity at y/L=0.17 around Ahmed model front end for 10° and 25° backlight angles

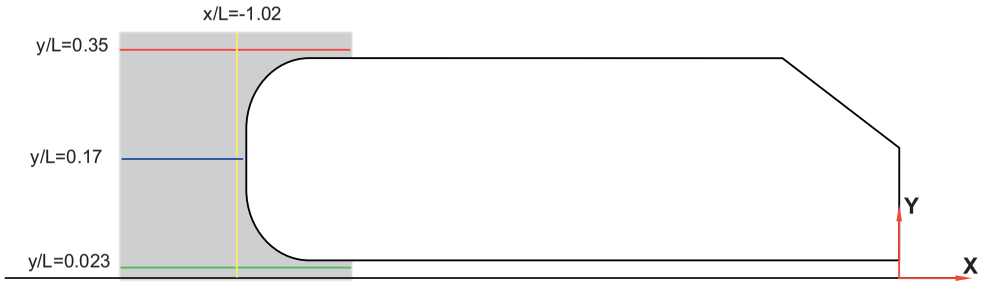

Figure 5.5 - Schematic diagram of model centreline plane investigated and positions of extracted data in Figures 5.2 - 5.4

The subsequent increased suction over the top of the model front end in Lienhart's experiments has the effect of relocating the stagnation point nearer the the top of the model, accounting for the lower v velocity component measured by Lienhart in comparison to the current experiments evident in the v velocity plot of Figure 5.3.

In order to confirm the above reasoning, Figure 5.4 plots contours of v=0 near the model front end (illustrating the positions of the stagnation points), in addition to a line of data taken at y/L=0.17. It can be seen that the increased suction over the backlight between the 10° and 25° current cases does indeed have the effect of relocating the stagnation point closer to the top of the model. Similarly the effective removal of the overhead strut and subsequent absence of blockage in Lienhart's data also increases the suction over the top of the model causing further movement of the stagnation point nearer the model top end. The subsequent expected variation in v velocity at y/L=0.17 can clearly be seen in the velocity plot of Figure 5.4.

Mention must also be made of the support system employed by Lienhart. The four cylindrical struts underneath the model would be expected to cause lower flow velocity under the model and force more flow above and round the sides. It is not, however, possible to make judgements on their effects from the data presented here as they are positioned at z/L=±0.16 (centre of strut), and therefore would not be expected to have any discernable effect in the model centreline plane presented.

Strut Wake

Planes of data were taken directly behind the supporting strut for both the 10° and 25° backlight angles. It was expected that the dissimilar flows over these two backlights would allow any effects the backlight flow may have on the strut wake to be quantified by investigation of this region. In addition, the 25° data could be compared directly with previous experimental work which did not include this overhead support system.

Inspection of the contour plots in Figure 5.6 show that the wake of the supporting strut in the two cases appears similar in formation, though with the 10° case causing a velocity deficit in more of the surrounding flow in the plane shown. This is confirmed by Figure 5.7 (a), which shows that the u velocity has returned to freestream values by approximately z/L= ±0.03 at the plotted downstream position (x/L=0.4) for the 25° case. This distance is approximately double the width of the strut itself. For the 10° case the u velocity does not recover to freestream within the traverse area.

To investigate the effect of the support strut wake on the backlight flow, Figure 5.7 (b) plots

model centreline data at y/L=0.345 for both the current investigation and that of Lienhart, where the model was instead supported from underneath. The small decrease in v velocity recorded in the immediate wake of the strut is caused by the downwash from the horseshoe vortex formed at the strut-body junction. This effect has dissipated and v velocities returned to values within $0.02u_\infty$ of those of Lienhart by x/L=-0.35, 0.16L upstream of the backlight. Therefore although some induced downwash over the backlight can be assumed to be created by the strut, this effect should prove to be minor.

The u velocity component, however, exhibits a larger drop in the strut's wake. It is also evident that the velocity recovery is greater for the 25° case than the 10°. This is due to the larger suction over the 25° backlight causing a larger increase in local flow velocity at the backlight. This effect can also be seen in Lienhart's data as an increase in u velocity after x/L= -0.55. The steeper gradient of the u velocity in the cases with the strut is due to the combined effects of this suction and recovery in the strut wake. It seems reasonable to assume that it is this suction difference between the two cases which causes the greater dispersion of the strut wake in the z direction in the 10° case.

At the leading edge of the 25° backlight (x/L = -0.19), the difference in u velocity between the strut / no strut cases is approximately $0.15u_\infty$. It was shown in Figure 5.3 (a) that upstream of the strut this difference was approximately $0.1u_\infty$. Therefore the velocity deficit caused by the strut wake would appear to have only an effect of around $0.05u_\infty$ at the point where the flow reaches the backlight.

In comparing the measured v velocities in Figure 5.8 the downwash caused by the vortices formed at the strut/model junction can be seen. This downwash dissipates rapidly downstream, and at y/L=-0.3 a difference of only $0.01u_\infty$ between the current 25° experiments and those of Lienhart is reported. As such, although there will be some downward deflection of the flow due to this interaction, it would not be expected to have a significant effect on the backlight flow.

To investigate the strut wake further, boundary layer profiles on the 0° Ahmed model at two separate distances upstream of the trailing edge are shown in Figure 5.8. Profiles are shown both for the model centreline (where the strut wake would have greatest effect) and at z/L=±0.1. In comparison the strut extends to z/L=±0.033. The 0° case was chosen due to the two-dimensional flow and lack of suction peak over the backlight. It is clear that losses from the wake are still evident at the trailing edge (x/L=0), varying from approximately $0.1u_\infty$ at y_H=0.02 to only around $0.03u_\infty$ at y_H=0.07. This suggests that the effects of the strut over the backlight cannot be neglected, and analysis of the flow structure in this area, and indeed in the model wake, will have to account for this influence which, with the lowered u and v velocity

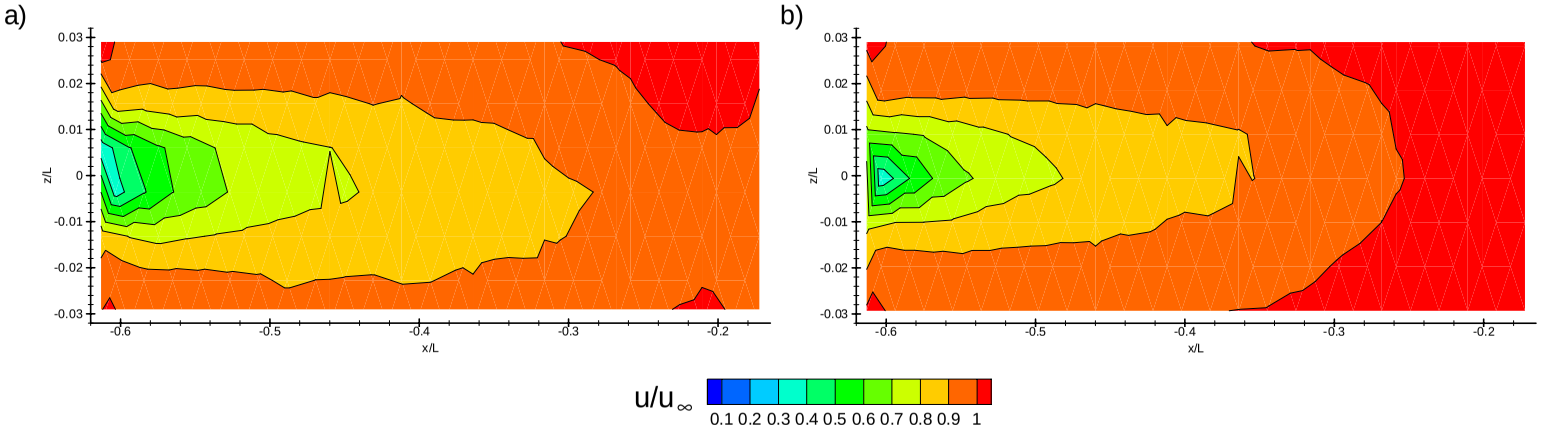

Figure 5.6 - Contours of normalised u velocity in the wake of the supporting strut at y/L=0.345 - (a) 10° backlight (b) 25° backlight

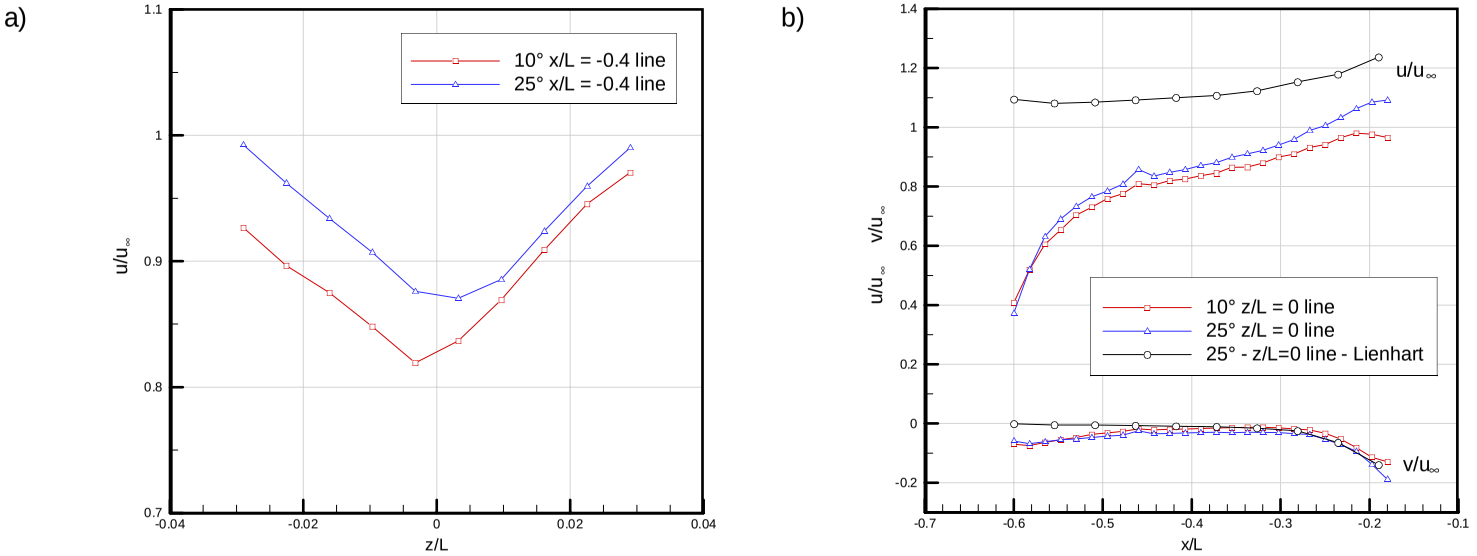

Figure 5.7 - (a) Horizontal (b) streamwise profiles of normalised u and v velocity in the wake of the supporting strut - 10° and 25° Ahmed models

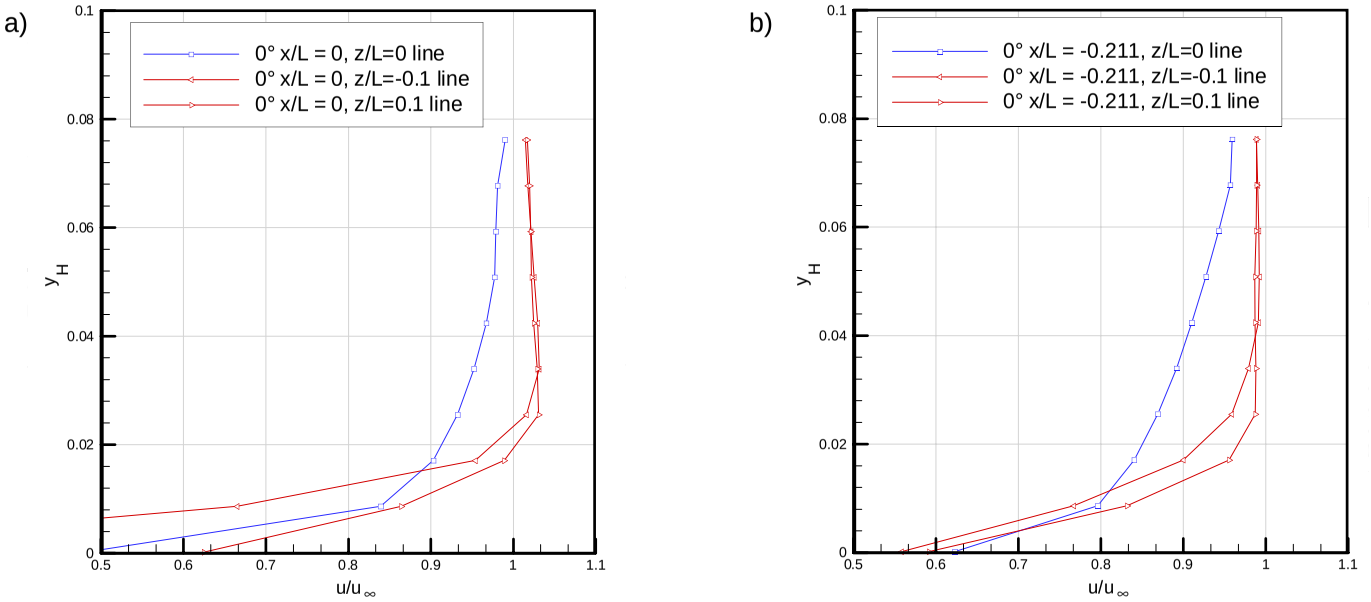

Figure 5.8 - vertical profiles of normalised u velocity in the wake of the supporting strut - 0° Ahmed model

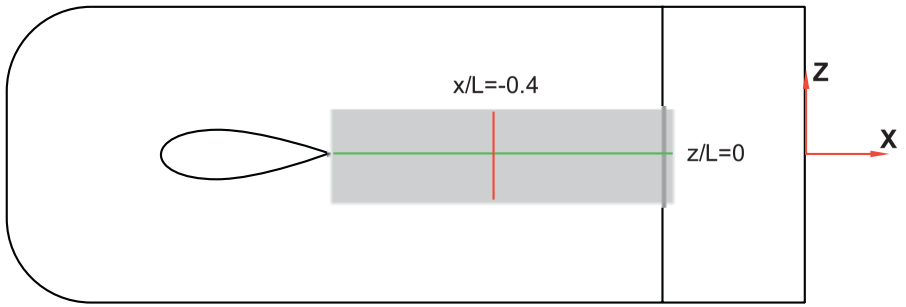

Figure 5.9 - Schematic diagram of supporting strut wake plane investigated and positions of extracted data in Figures 5.6 and 5.7

components, would be a downward deflection of the velocity vector over the central section of the backlight.

Backlight Flow

Figure 5.10 shows both contours of u velocity and streamlines calculated from the current LDA data. As expected from Ahmed's flow description, there is an increase in suction at the upstream edge of the angled section with increasing back angle, in addition to a local increase in flow velocity over the backlight. This is due to an effective increase in curvature of the model, responsible for the rise in both lift and drag shown in Figure 5.1. Most noticeable from Figure 5.10 though are the two counter-rotating regions formed over the backlight in the two separated cases (30° and 40°). This flow structure differs from that recorded by Ahmed, where the single separated region A in Figure 2.2 encompassed both the immediate wake of the model and the volume above the backlight once flow separation had occurred. Lienhart's results do suggest formation of the lower region, although as these results were skewed towards measurement of the boundary layer the existence of both upper and lower regions in this work is ultimately inconclusive.

It appears that, in the current data, the lower of the two new circulating regions becomes larger with increasing back angle. This is most likely due to the reduced downward deflection of the flow separated from the backlight upstream edge at 40° (in comparison to the 30° case) and the increased space due to the increased back angle allowing the lower region to develop more fully. The upper region in comparison appears to be little affected by changing back angle. It is, in fact, an extension of the upper region which dominates the near wake of the model for all backlights, as reported by Ahmed and marked as A in Figure 2.2. Lienhart's LDA is, as before, inconclusive regarding the existence of the separate upper recirculation region shown.

Figure 5.11 shows similar plots to Figure 5.10, this time for the 10°, 25° and 40° backlight angles at positions away from the model centreline. For the 10° case the prediction of essentially two-dimensional flow over most of the backlight has been confirmed, with very little variation in flow structure between $z/L=\pm0.077$, aside from the slight suction increase away from the central strut wake. In the 25° case the effect of the two longitudinal vortices can clearly be seen in the streamlines at both $z/L=\pm0.144$. The 40° plots show almost identical structure of the backlight flow at $z/L=\pm0.077$ as on the model centreline, suggesting little variation in the size and structure of these separated regions with transverse position.

To quantify further the effect of α on the flow structure, boundary layer profiles have been extracted at 5 distinct upstream positions on each backlight. These are shown in Figure 5.12, and are all plotted as heights above the model surface at the point they were taken (y_H). The

increase in suction with increasing α can be quantitatively assessed here as at the furthest upstream positions extracted the maximum u velocity rises from $1.02u_\infty$ (0°) to $1.17u_\infty$ (25°).

From the trailing edge profiles it can be seen that the maximum velocity at 0° was found to be $1u_\infty$, whereas at 25° this has dropped to $0.9u_\infty$. This is naturally an effect of the increasing adverse pressure gradient which ultimately results in the separated boundary layers shown for the 30° and 40° cases. It is noticeable that at the furthest upstream positions measured for the 30° and 40° cases the flow had not yet separated. Clearly the flow is able to negotiate a section of the backlight prior to separation, in contrast to the predictions of Ahmed.

Figures 5.13 and 5.14 show contours of u and v velocities respectively, at the trailing edge of each model configuration. It is again clear that the flow is two dimensional away from the influence of the longitudinal vortices for configurations both below the 1st (12.5°) and above the 2nd (30°) critical angles. In particular the reversed flow region formed at 40° shows almost no variation in height between z/L=±0.15, again suggesting that the rotating regions shown previously maintain their size to this point. From the v velocity plots the increased vortex strength up to 25° can be seen. To assess this increase, lines of data as close as possible through the maximum and minimum v velocity points have been extracted from the trailing edge of each back angle, and are shown in Figure 5.15 with the attached (0° - 25°) and separated (>25°) cases shown separately.

The increased suction up to 25° back angle causes an increase in the strength of the two longitudinal vortices formed at the backlight edges. It can be seen from Figure 5.15 that the maximum plotted v velocity rises from $v/u_\infty=0.02$ (0°) to $v/u_\infty=0.23$ (25°). Although the highest value of v/u_∞ in Figure 5.15 is found to occur over the 20° backlight, this is in fact found to be a result of the inability of a single transverse profile to capture the exact maximum and minimum v velocity values in the 25° backlight case. The maximum v velocity measured over the 25° backlight trailing edge is found to be approximately $0.34u_\infty$, greater then the $0.325u_\infty$ measured in the 20° case. The downwash formed increases the minimum v velocity from $v/u_\infty= -0.02$ (0°) to $v/u_\infty= -0.7$ (25°). The effects of the strong vortices formed at 25° were noted by Ahmed to have significant effects beyond 0.5L downstream of the trailing edge, and the rapid increase in C_D as the backlight approaches the 2nd critical angle (30°) is in part a result of the resultant vortex drag. There is still a weak tendency of the flow to turn around the side edges of the model visible at 30° and 40°, although as expected the strong vortices produced prior to separation are not formed.

Figure 5.16 compares both the current u and v velocities over the 25° trailing edge against those of Lienhart. It can be seen that the maximum positive and negative v velocities recorded by Lienhart were approximately $0.1u_\infty$ higher and $0.12u_\infty$ lower respectively than the current

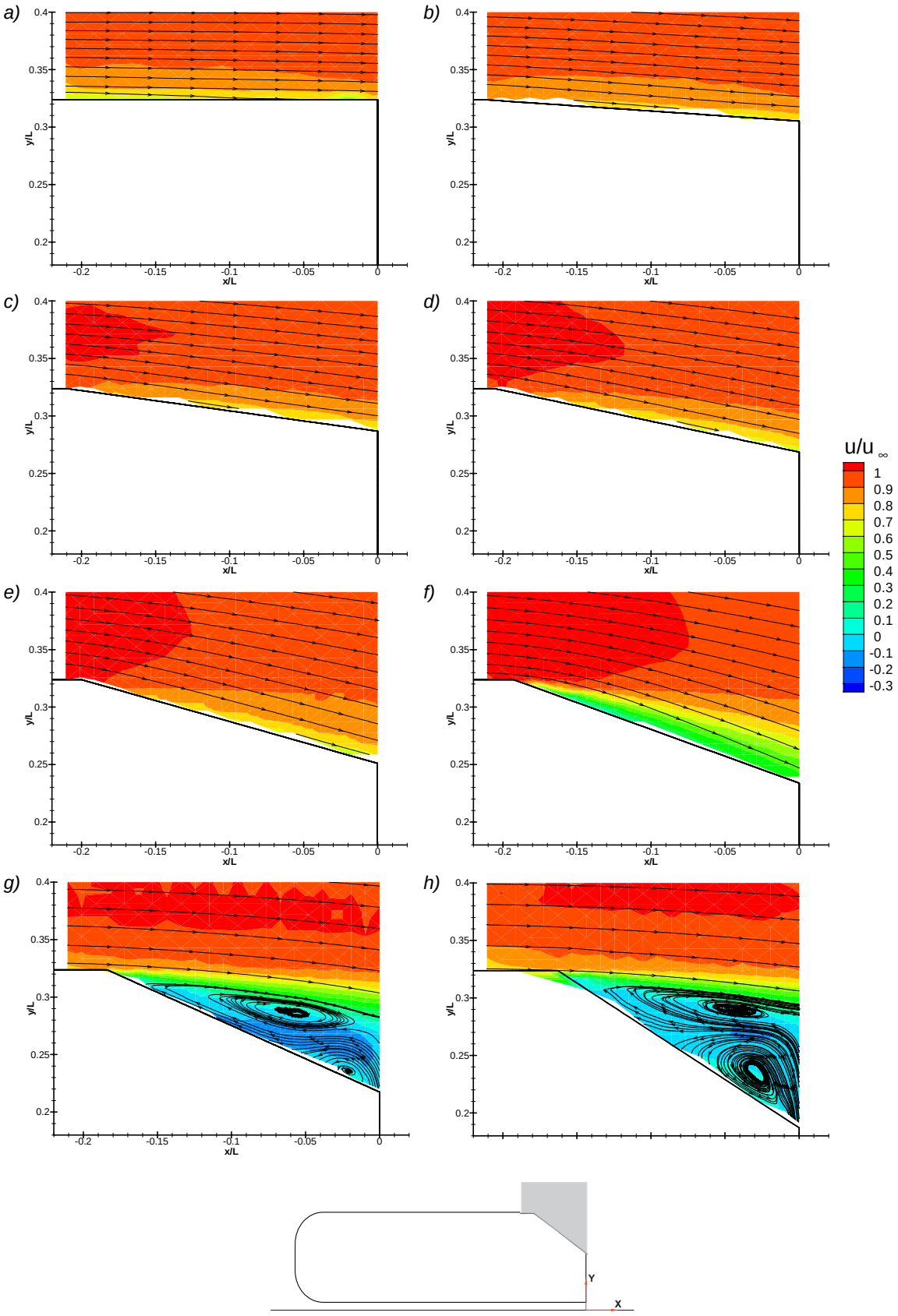

Figure 5.10 - Contours of normalised u velocity and in-plane streamlines at z/L=0 for a)0° b)5° c)10° d)15° e)20° f)25° g)30° h)40° backlight angles

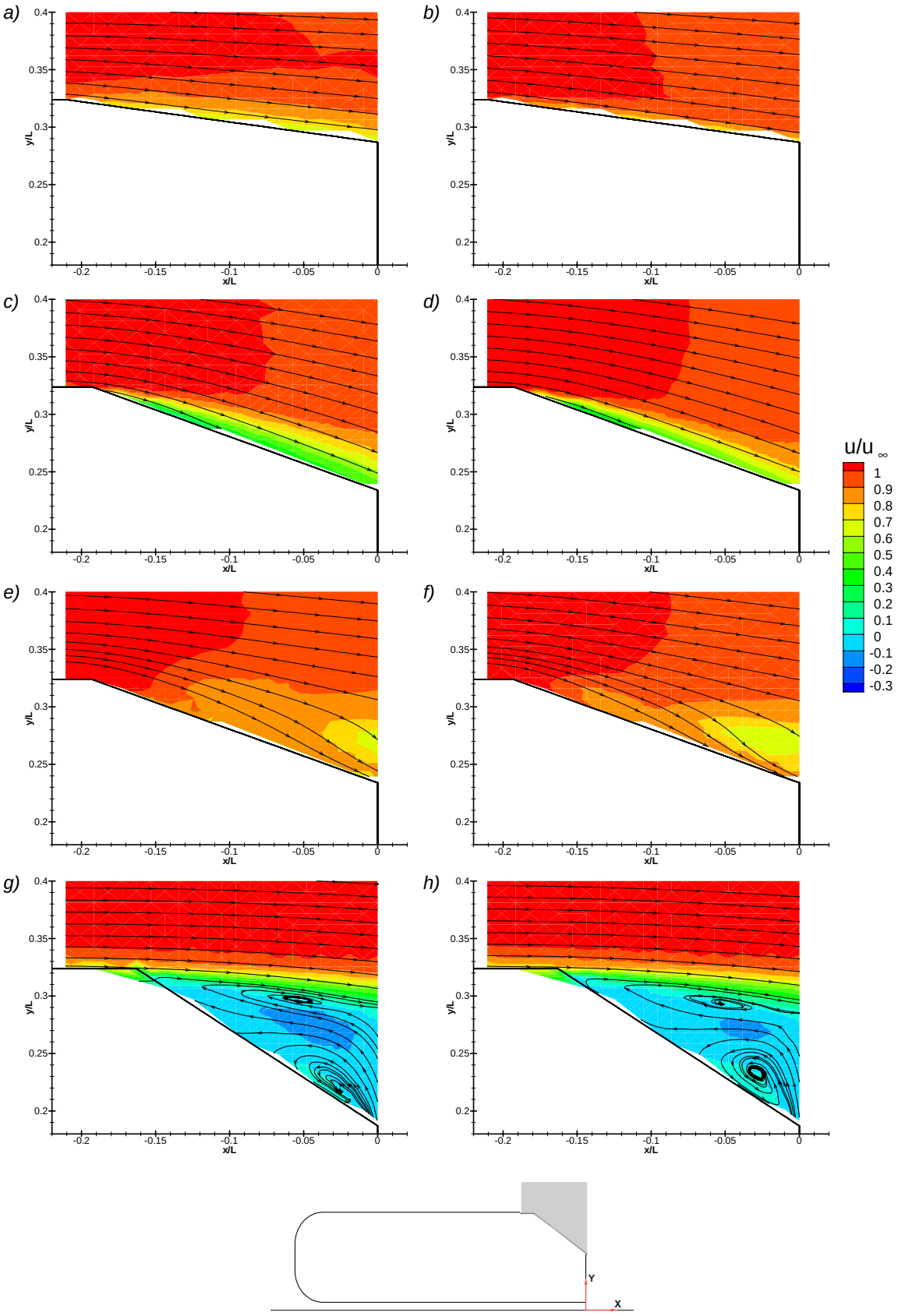

Figure 5.11 - Contours of normalised u velocity and in-plane streamlines over 10° backlight at a)z/L=0.077 and b)z/L=-0.077, 25° backlight at c)z/L=0.077 d)z/L=-0.077 e)z/L=0.144 f)z/L=-0.144 and 40° backlight at g)z/L=0.077 h)z/L=-0.077

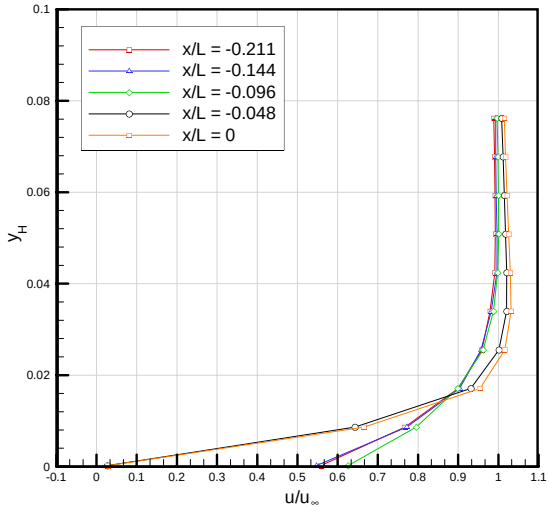

a) 0° backlight angle

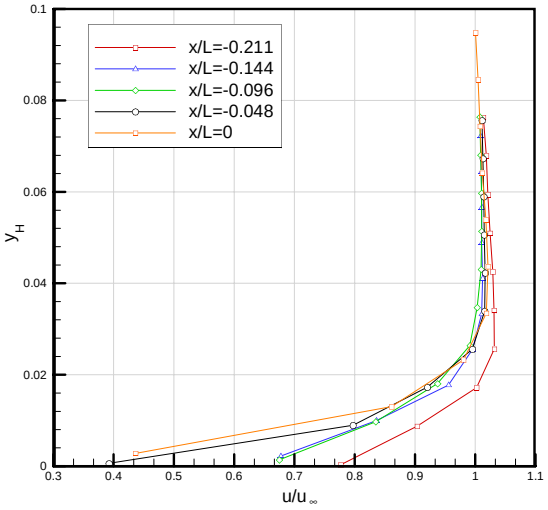

b) 5° backlight angle

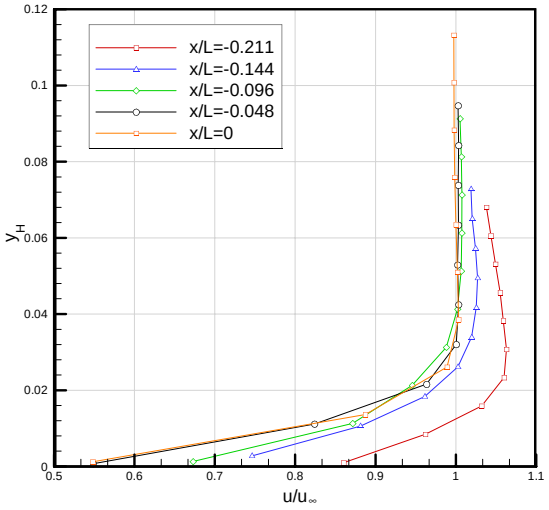

c) 10° backlight angle

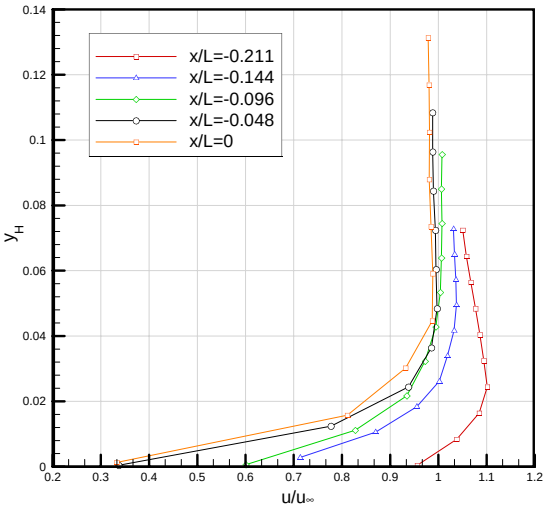

d) 15° backlight angle

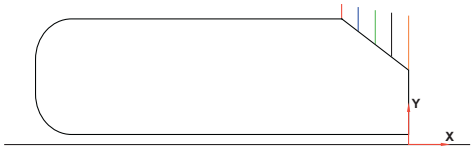

Figure 5.12 - Boundary Layer profiles over Ahmed model backlights at z/L=-0.1

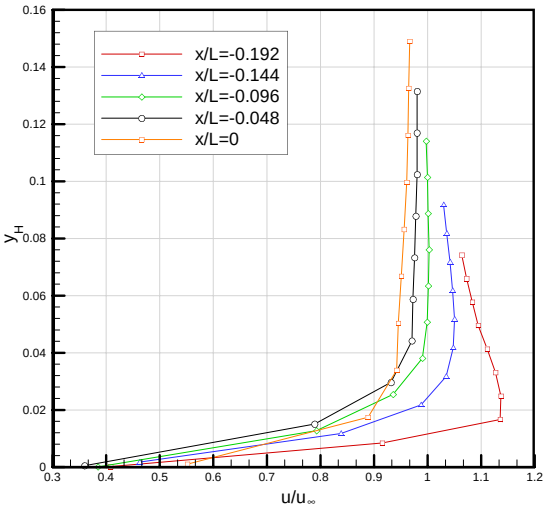

e) 20° backlight angle

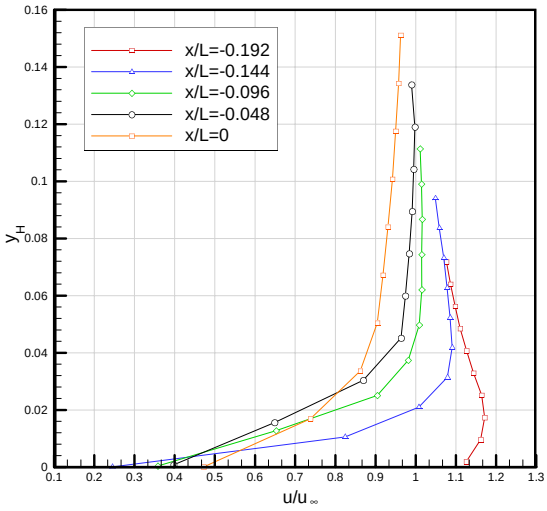

f) 25° backlight angle

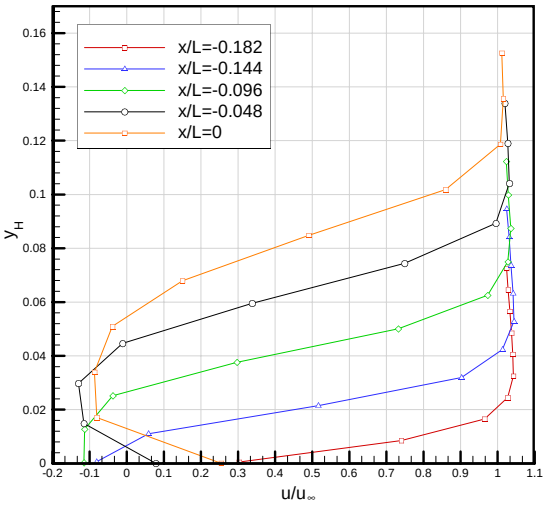

g) 30° backlight angle

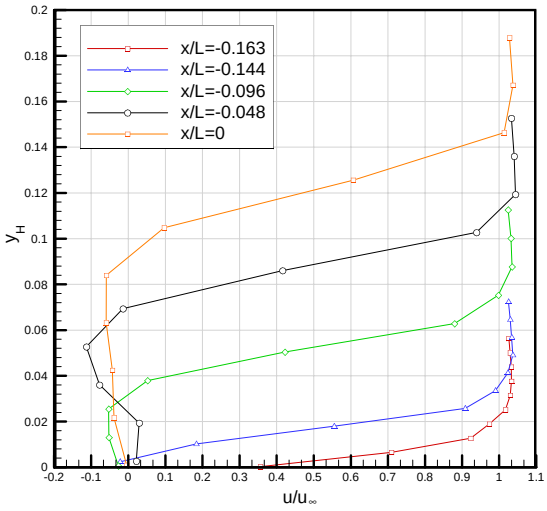

h) 40° backlight angle

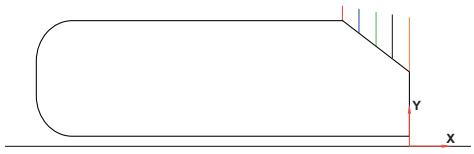

Figure 5.12 (cont) - Boundary Layer profiles over Ahmed model backlights at z/L=-0.1

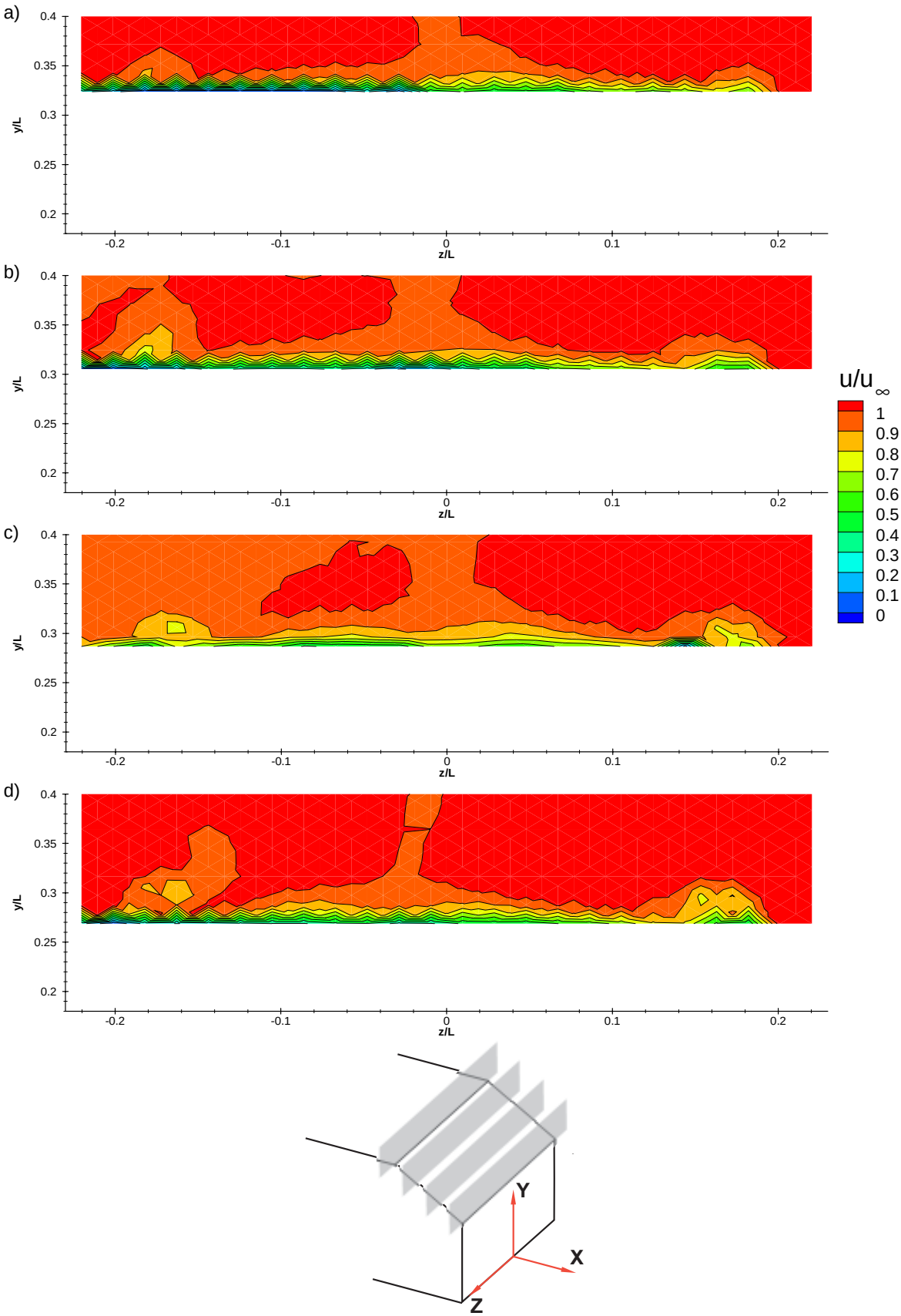

Figure 5.13 - Contour plots of normalised u velocity above the a)0° b)5° c)10° d)15° backlight Ahmed model trailing edge

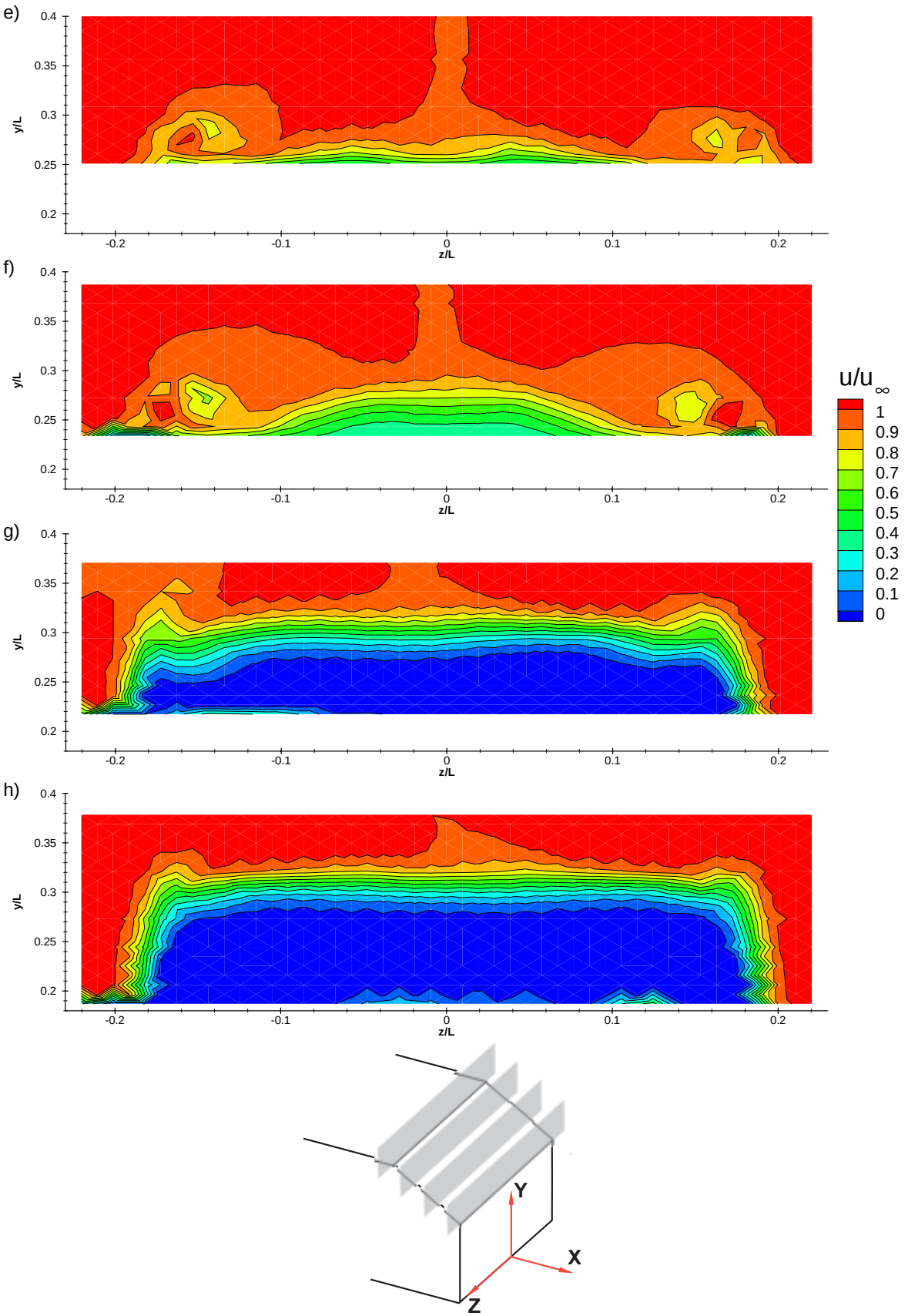

Figure 5.13 (cont) - Contour plots of normalised u velocity above the e)20° f)25° g)30° h)40° backlight Ahmed model trailing edge

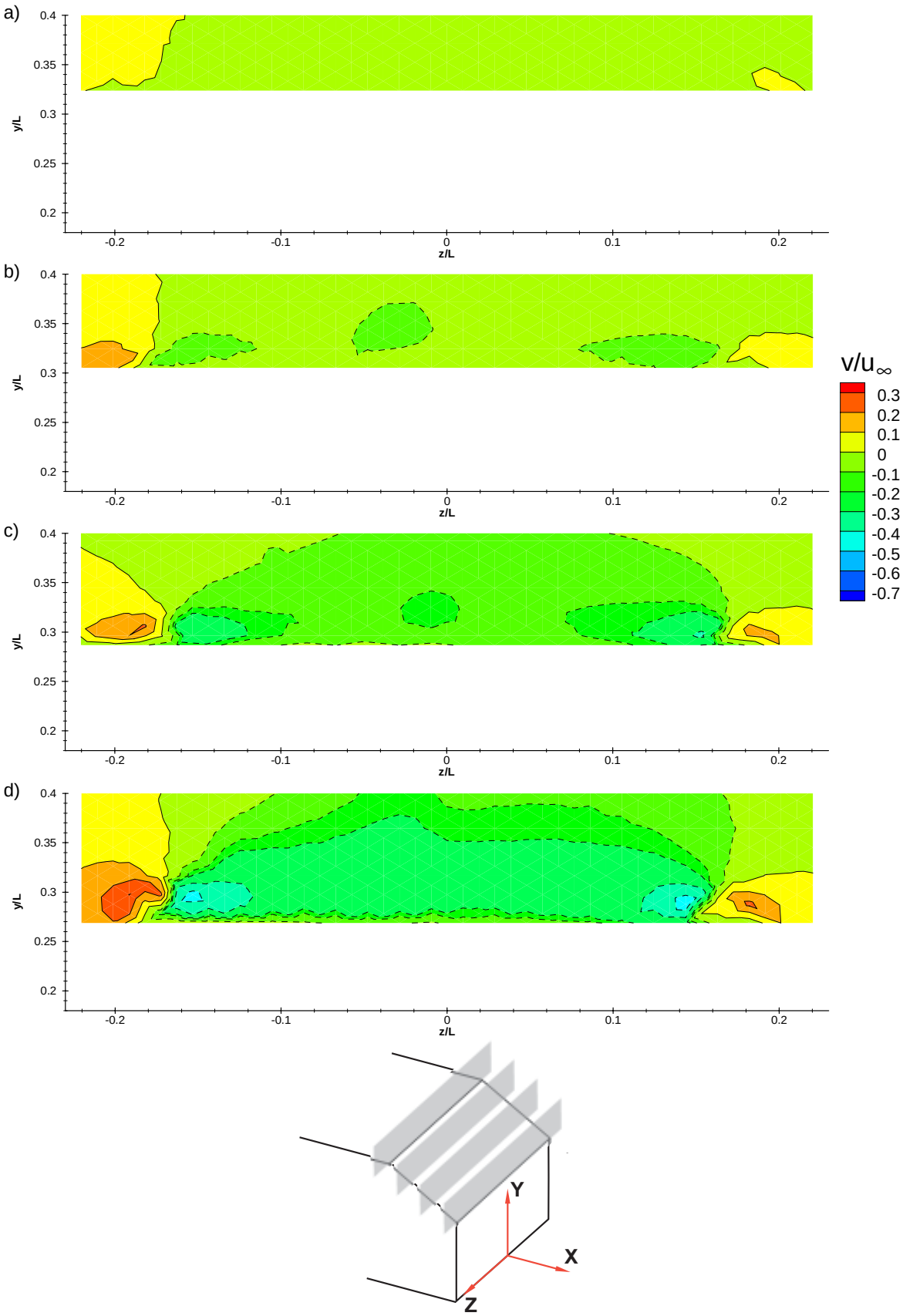

Figure 5.14 - Contour plots of normalised v velocity above the a)0° b)5° c)10° d)15° backlight Ahmed model trailing edge

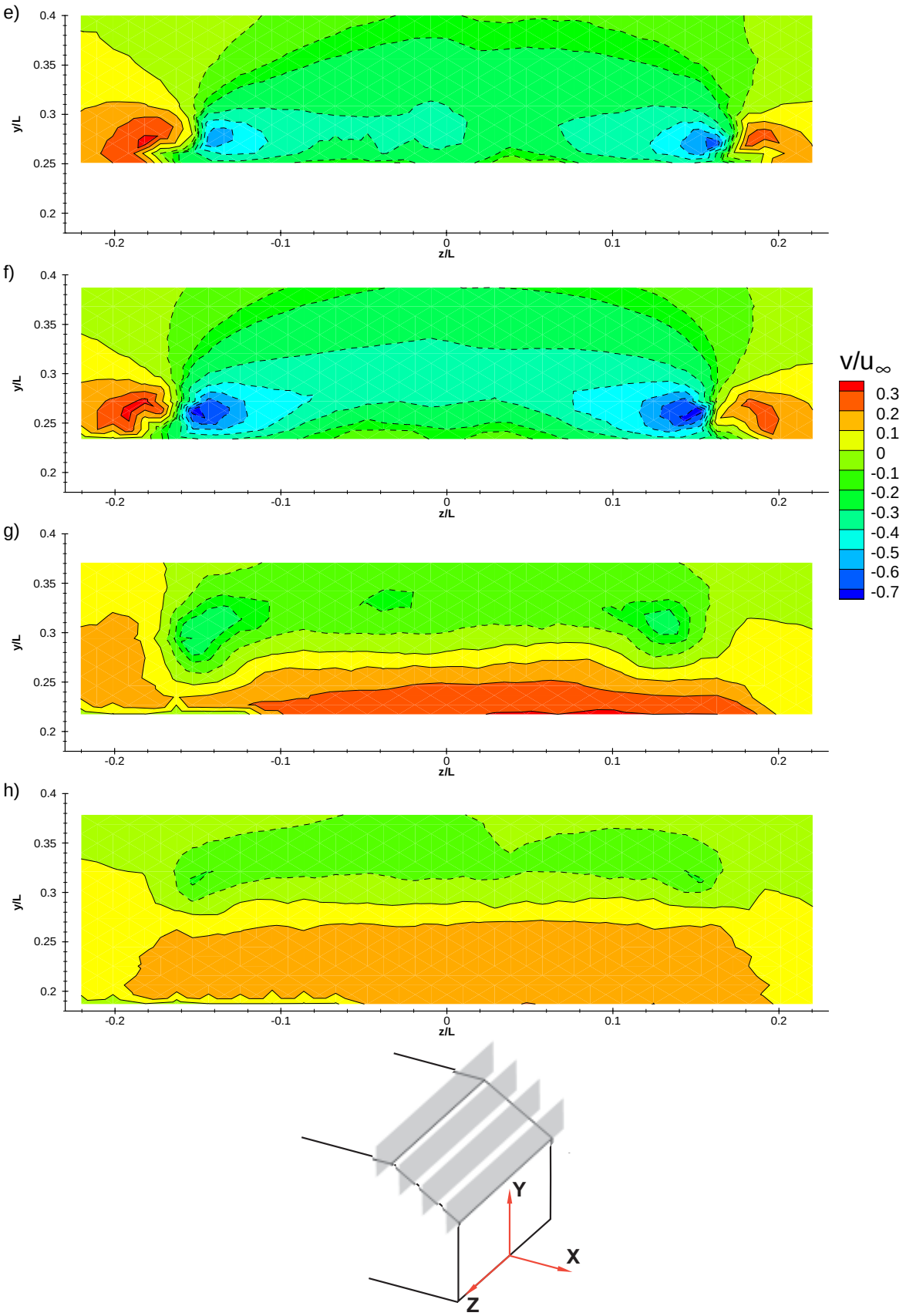

Figure 5.14 (cont) - Contour plots of normalised v velocity above the e)20° f)25° g)30° h)40° backlight Ahmed model trailing edge

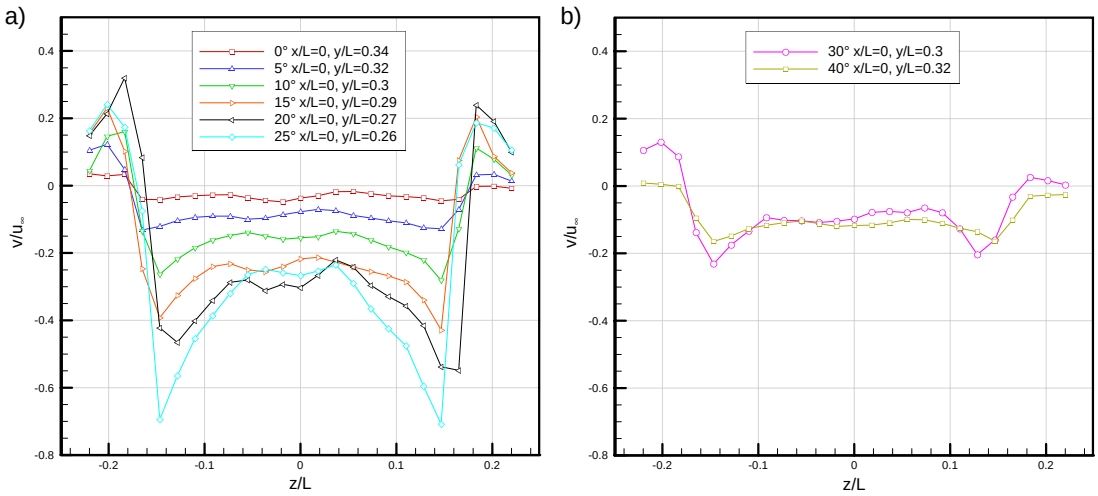

Figure 5.15 - Transverse profiles of v velocity at Ahmed model trailing edge

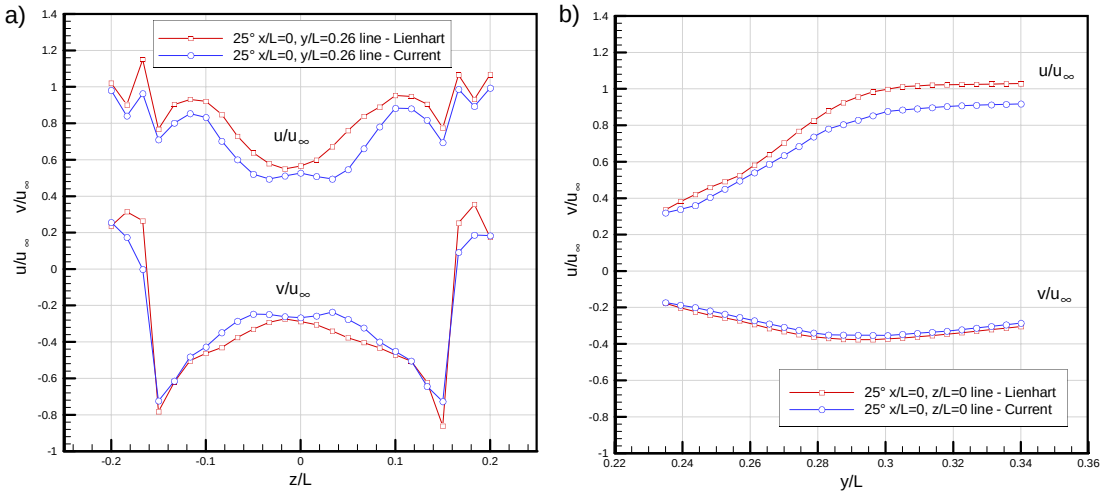

Figure 5.16 - (a) Transverse and (b) vertical profiles of u and v velocities at model trailing edge - 25° case - current and Lienhart data

experiments. This suggests the vortices shed from the trailing edge in Lienhart's tests were more energetic, resulting in the increased downwash evident over the central section of the backlight. This effect is likely to be a result of increased flow over the side sections of the model in Lienhart's experiments due to the under body blockage caused by the cylindrical struts, in addition to the increased suction caused by the higher flow velocity over the backlight, owing to the upstream effects outlined previously. There is, however, a section of the flow close to the model centreline (z/L=±0.02) where the current data displays a drop in the downward velocity not found in Lienhart's data. It can be assumed from the previous analysis that this is due to the interference of the supporting strut altering the flow in this region.

Variation in u velocity between the two sets of results generally remains at approximately $0.1u_\infty$, consistent with upstream results. Again though this is not the case between z/L=±0.02, where the u velocity in the current experiments exhibits a rise not consistent with Lienhart's

data. This inconsistency is most likely a result of the strut-induced downwash preventing a full development of the boundary layer over this section, in the same way that the downwash from the side vortices do over the outboard sections of the backlight. Figure 5.12 gives the best illustration of the flow in this region.

Lower Vortices

In addition to the top longitudinal vortices observed previously over the Ahmed model backlight, the current experiments demonstrated the existence of two further vortices shed from the model underside. These were not found either in Ahmed's original experiment, or in Lienhart's results. Although the grid spacing for the LDA was finer in the current study, it would still be expected that some evidence of these lower vortices would have been found by Lienhart. As analysis of those results shows no trace, and as no report of these vortices' existence was given in Ahmed's analysis of the wake flow, it must be assumed that the inclusion of the cylindrical struts suppresses their formation. As such no direct comparison can be given with other experimental data. Throughout the following analysis data is presented only for the lower left vortex (looking from behind the model) due to model symmetry.

In order to ascertain what effect the back angle has on these lower vortices, data were taken at a number of downstream distances for both of the extreme back angle cases (0° and 40°). Figure 5.18 shows a comparison between these angles for a y-z plane 50mm (0.048L) downstream of the trailing edge. It is clear that both the 0° and 40° cases produce lower vortices which are visible downstream of the trailing edge, therefore suggesting that they are produced at all intervening back angles. There is, however, a significant change in the flow structure between the 1st and 2nd critical angles for which no lower vortex data have been taken, and as such further work will be required to prove that these vortices are also formed for these back angles.

It is also evident from Figure 5.18 that these vortices exhibit a number of structural differences. In order that these differences can be quantified, data have been extracted at a height of y/L=0.06 for both cases, which can be seen in Fig 5.19(a). For the 40° case, where there is fully separated flow over the back end, the maximum negative v velocity is approximately double that of the 0° case - a difference of approximately $0.04u_\infty$. The maximum positive v velocity is also found to be greater by around $0.02u_\infty$. In addition, the centre of the vortex, identified in this case as the point where the v velocity component is zero, is found to be located at z/L=-0.204 for the 0° case, and at z/L=-0.19 for the 40° case.

It is clear, therefore, that where the flow over the trailing edge is fully separated, the lower vortex produced is both stronger and located further from the side of the model than when the flow remains fully attached. Thus, it appears that the tendency of the flow to turn over the top

of the model in the 40° case has the effect of forcing more of the flow from the underside upwards than in the 0° case, resulting in the formation of a pair of stronger lower vortices.

Figures 5.19(a) - (f) show how these vortices propagate downstream of the trailing edge. At each distance downstream data have been extracted at y/L=0.06 from both 0° and 40° cases. This is the centre of the visible vortices at every recorded downstream position, as they do not appear to alter position in the y-axis.

The plots of data at 100mm and 150mm (0.096L and 0.144L) downstream show a trailing lower vortex, with the 40° case exhibiting a more energetic vortex than its 0° counterpart (Figures 5.19(b) and 5.19(c)). At 0.19L downstream, however, both 0° and 40° plots show the

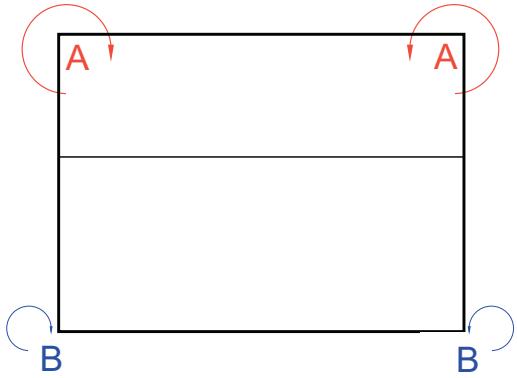

Figure 5.17 - Schematic diagram of position and mode of rotation of upper (A) and lower (B) longitudinal vortices evident at Ahmed model trailing edge

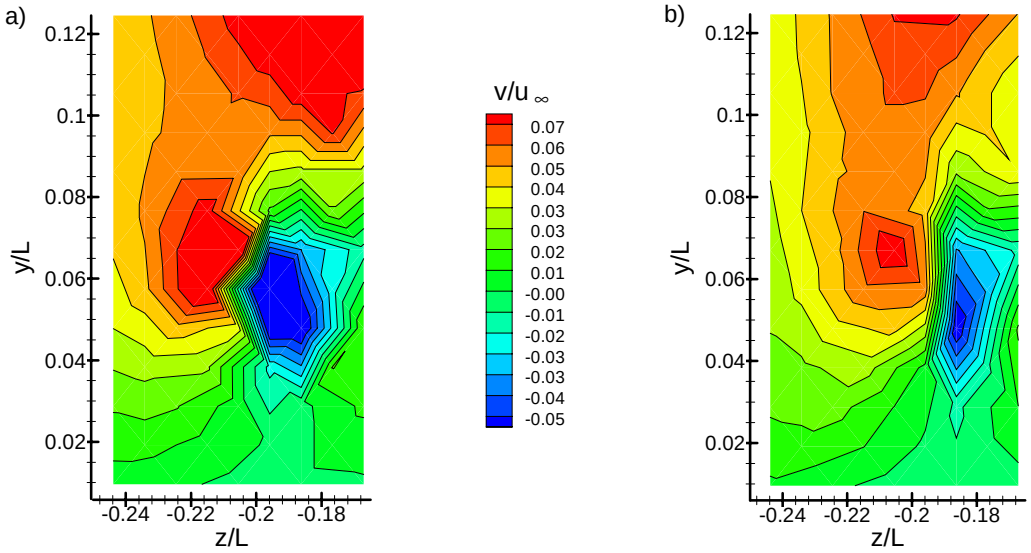

Figure 5.18 - Contours of normalised vertical velocity at x/L=0.048 behind Ahmed model (a) 40° backlight (b) 0° backlight - LDA data

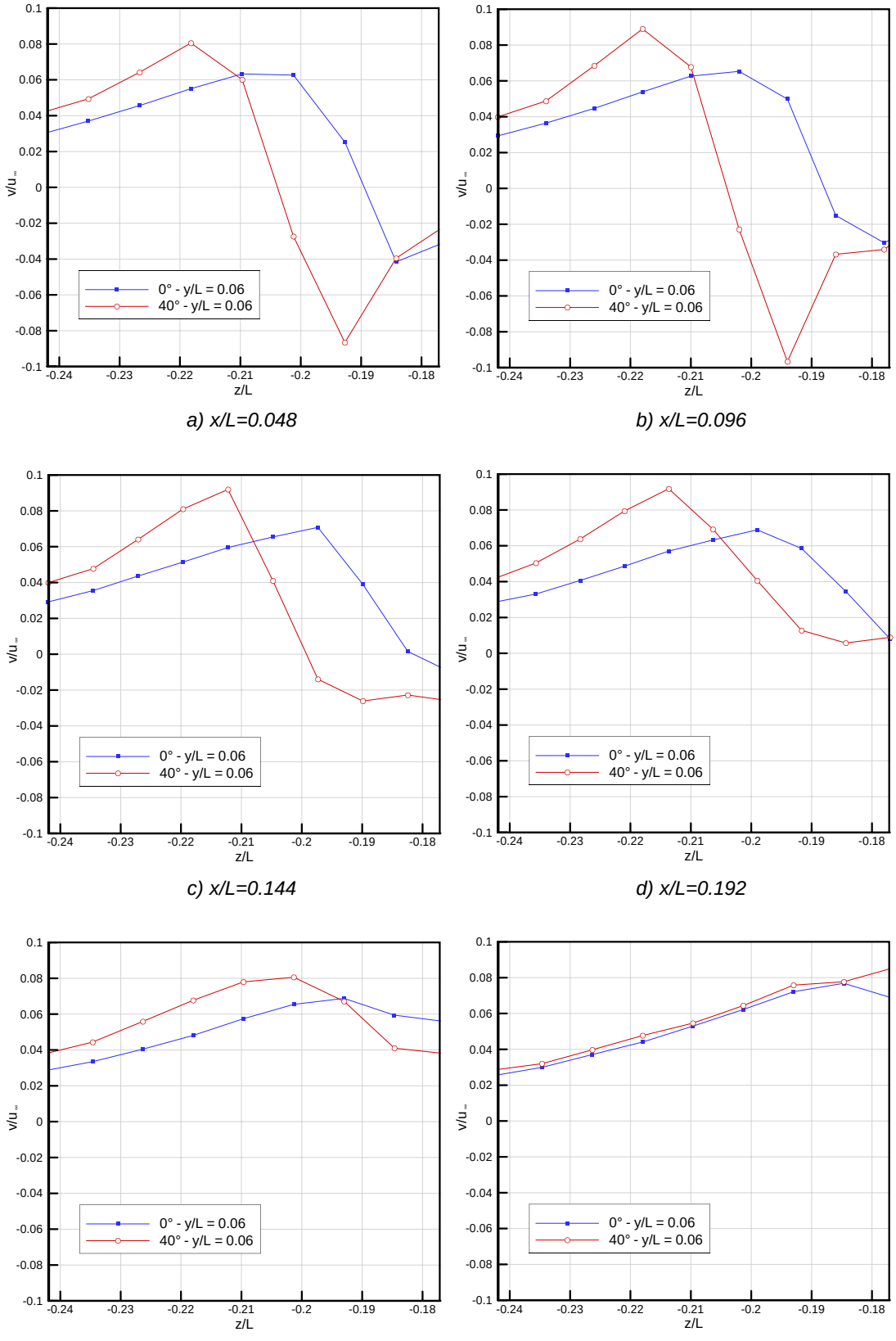

a) x/L=0.048

b) x/L=0.096

c) x/L=0.144

d) x/L=0.192

e) x/L=0.24

f) x/L=0.287

Figure 5.19 - Profiles of vertical velocity at y/L=0.06, 10° and 40° Ahmed models

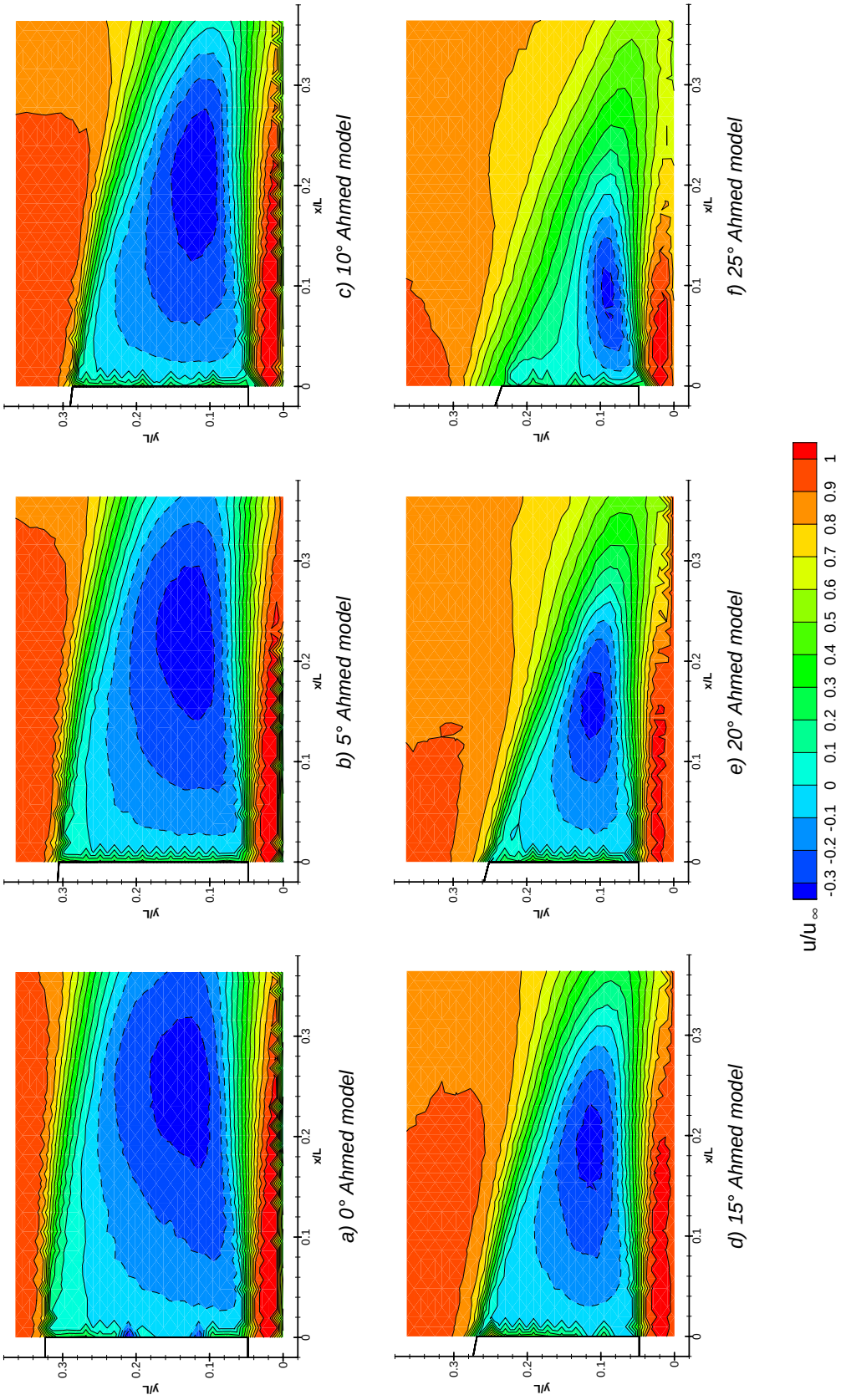

Figure 5.20 - Isolated Ahmed Model - contours of normalised streamwise velocity on centreline (z/L = 0) behind model - LDA data

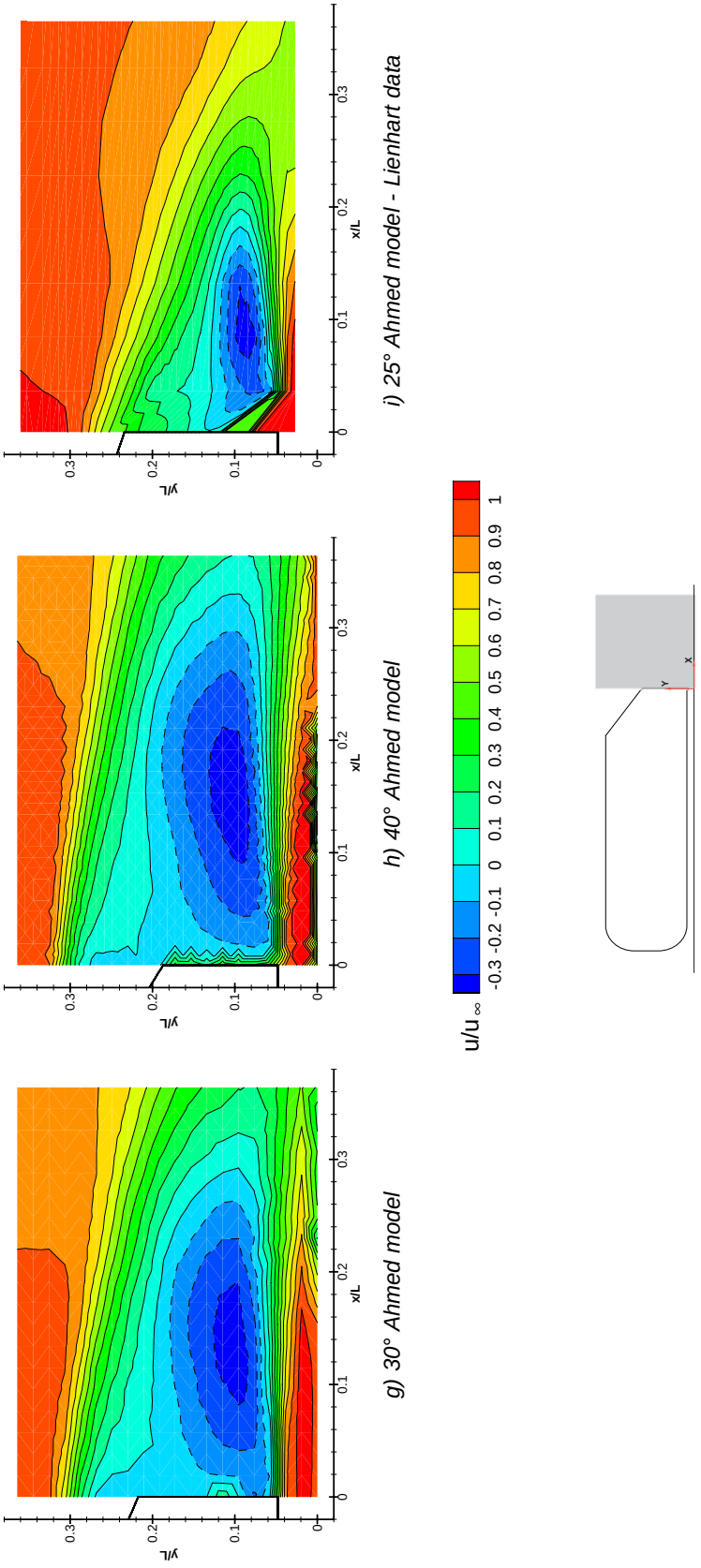

Figure 5.20 (cont) - Isolated Ahmed Model - contours of normalised streamwise velocity on centreline (z/L = 0) behind model - LDA data

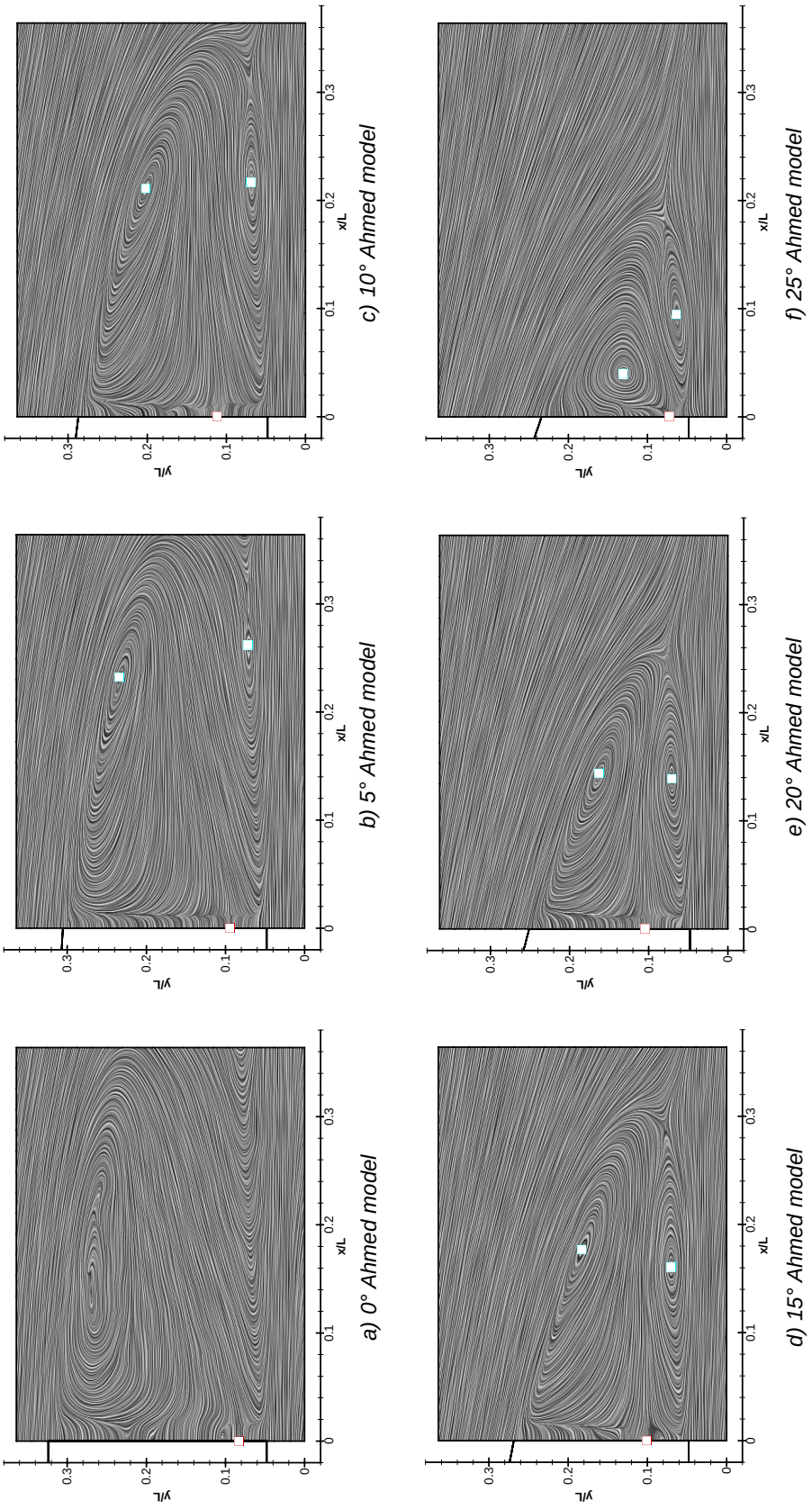

Figure 5.21 - Isolated Ahmed Model - Line Integral Convolution plots of LDA data on model centreline (z/L=0) behind model. Red squares mark attachment nodes; blue squares mark vortex centres

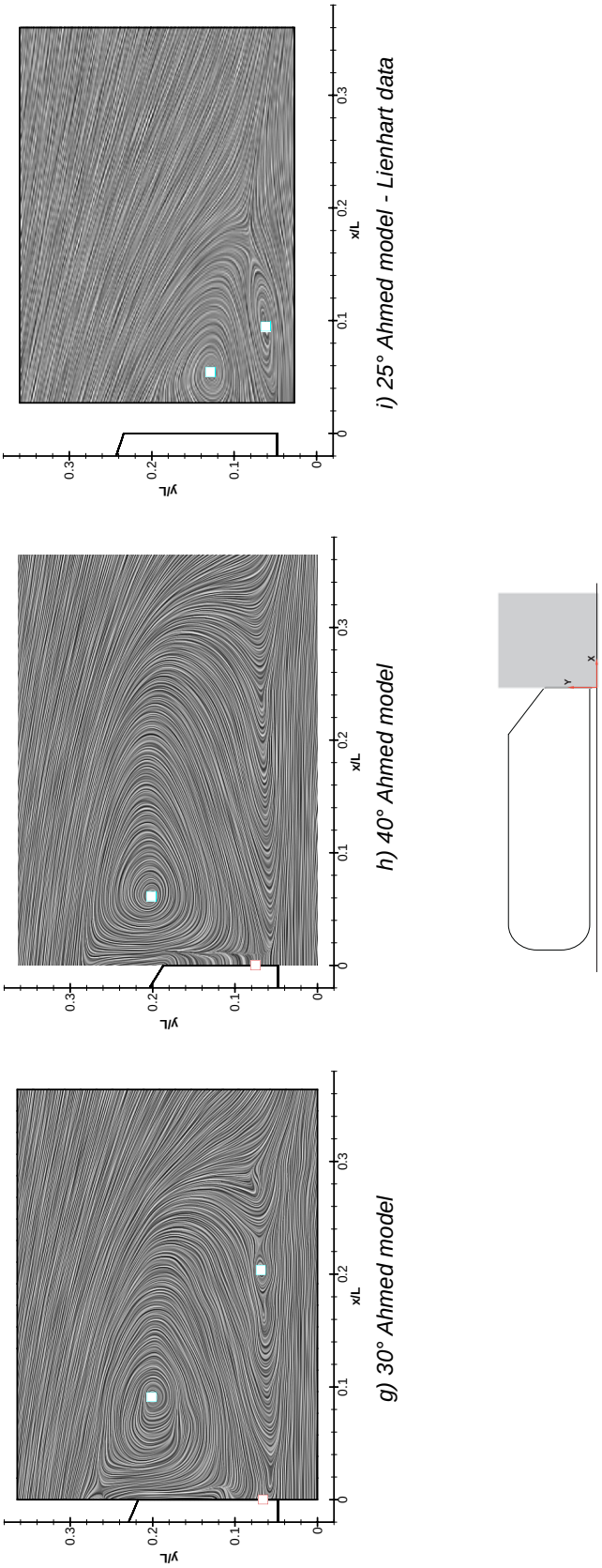

Figure 5.21 - Isolated Ahmed Model - Line Integral Convolution plots of LDA data on model centreline (z/L=0) behind model. Red squares mark attachment nodes; blue squares mark vortex centres

vortex has already dissipated (Fig 5.19(d)). The effects of the vortices can still be seen up to 0.24L downstream, as shown in the plots by the line of data following the same general pattern as before (Fig 5.19(e)), but there appears to be no vortex or spiral flow downstream of x/L=0.14.

A computational investigation into the 25° Ahmed body, and employing an advanced LES turbulence model was performed by Krajnovic and Davidson [2004]. In this study the model was assumed to be sitting in mid-air, with neither underneath or overhead struts to alter the flow. Similar lower trailing vortices were found in this case and extended from 800mm (0.77L) upstream to 100mm (0.096L) downstream of the trailing edge. At the two backlight angles tested in the current experimental programme the lower vortices were still clearly visible at 150mm (0.14L) downstream, which would suggest that this may well also be the case for the intermediate angles. As such Krajnovic's results may well under-predict the distance downstream which these vortices travel. This may be due to the lower Reynolds number at which this computation was performed, as the stronger influence of viscous forces may be the cause of the earlier vortex breakdown

Near Wake Flow

x-y planes

Figure 5.20 plots contours of velocity in the freestream direction for model centreline planes immediately downstream of the trailing edge, with regions of negative streamwise flow bound by dashed lines. Lienhart's data for the 25° backlight are also included for comparison, although it must be noted that due to a far lower number of data points taken in the near wake in Lienhart's experiments (390 against the 761 taken in the current investigation), more interpolation was required and subsequently less accuracy was possible. This was most problematic in the region between $0<x/L<0.025$. In order to visualise the flow structure the equivalent LIC plots with both vortex centres and singular attachment nodes marked are shown in Figure 5.21.

From Figure 5.20 the evidence of the decreased flow velocity at the model trailing edge up to 25° back angle can be seen, in this instance presented as a smaller region of higher velocity flow at the top of each plot. This trend is reversed once the flow has become separated over the backlight.

Evident in the 20°, 25° and Lienhart's 25° data is the effect of the longitudinal vortices causing retardation of the flow at the model centreline. This can be seen by the increase in height from the ground plane of the lower streamwise velocity wake flow in the respective contour plots. As would be expected by the nature of the vortices and their relative strengths (outlined previously), their effect is more pronounced for the 25° case than for the 20° one. Indeed, their

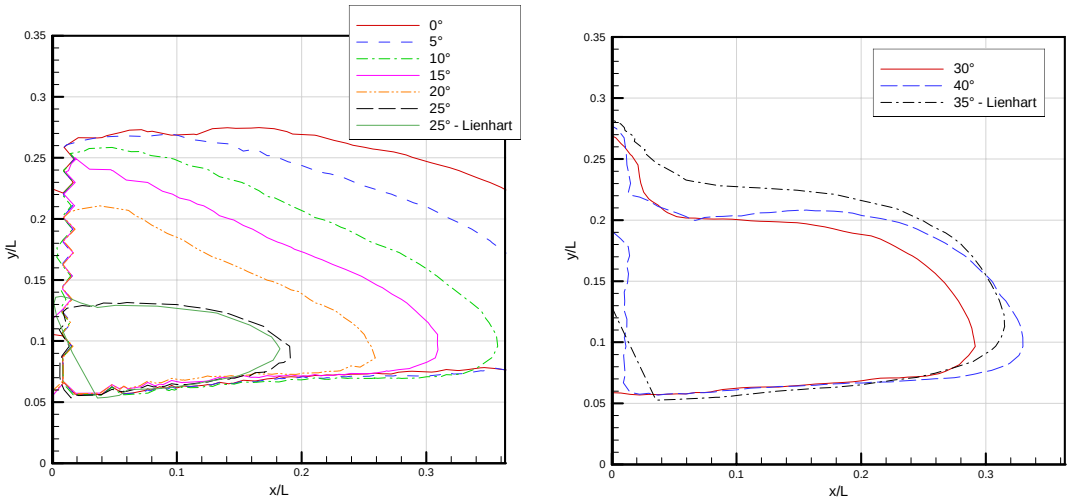

Figure 5.22 - Contours of u/u_∞=0 in near wake of Ahmed model on centreline (z/L=0) - all angles

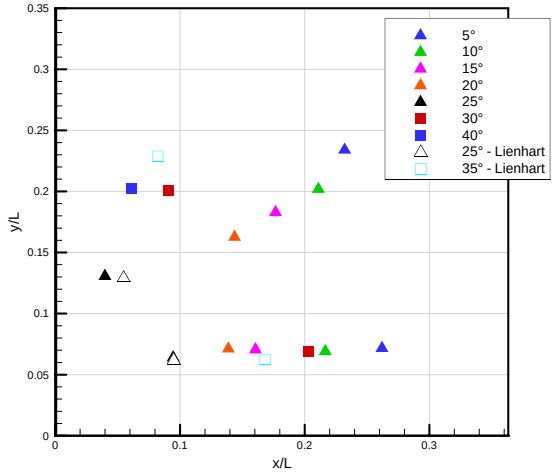

Figure 5.23 - Vortex centres in near wake of Ahmed model on centreline (z/L=0) - all angles

Backlight Angle (α)	Maximum streamwise extent of reversed flow region (x/L)
10°	0.36
15°	0.31
20°	0.26
25°	0.19
25° Lienhart	0.18
30°	0.29
35° Lienhart	0.315
40°	0.33

Table 5.1 - Streamwise extent of reversed flow region on model centreline (z/L=0) in near wake of Ahmed model - LDA data

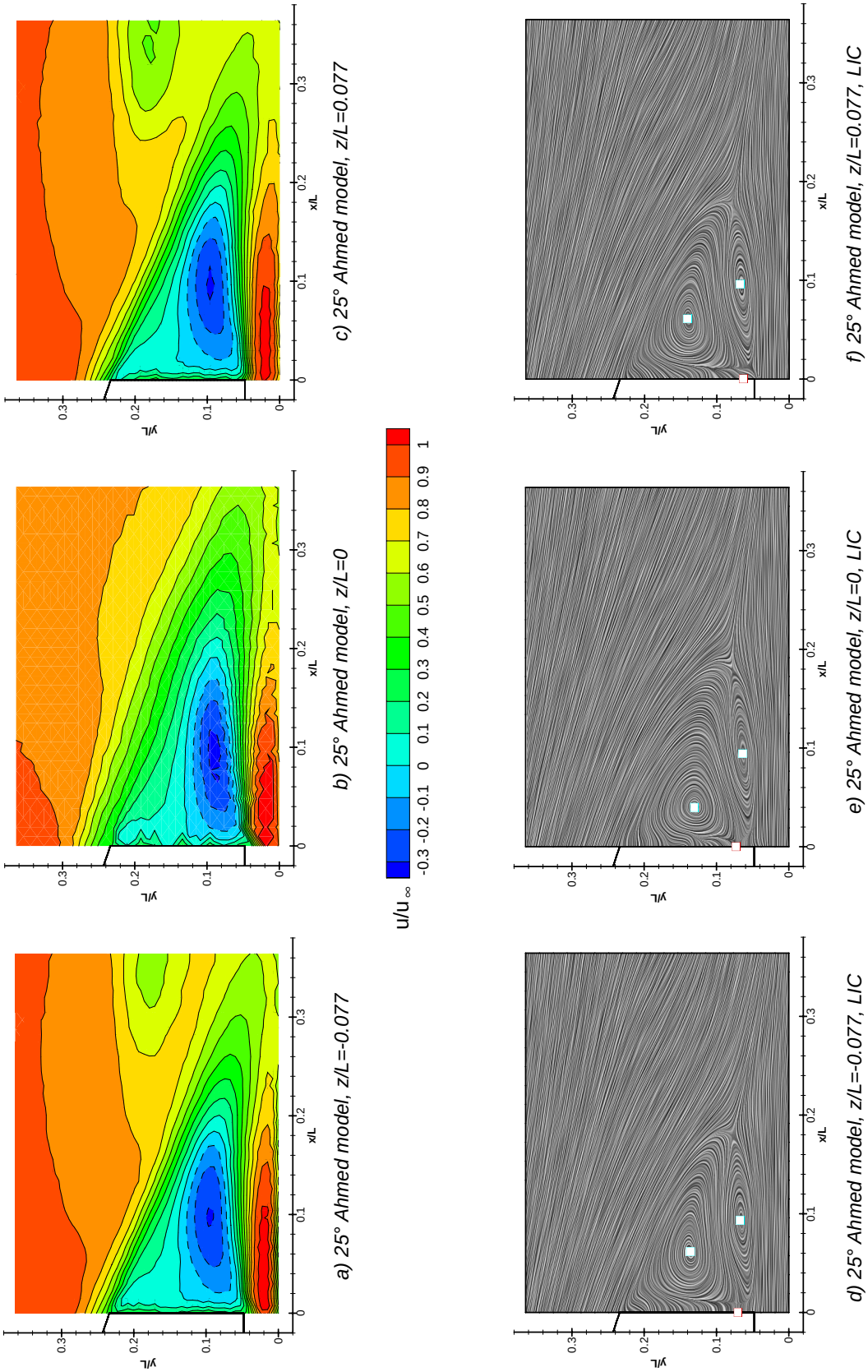

Figure 5.24 - 25° Isolated Ahmed Model - z/L = 0, 0.77 and -0.77 behind model planes - LDA data - contour and LIC plots. Red squares mark attachment nodes; blue squares mark vortex centres

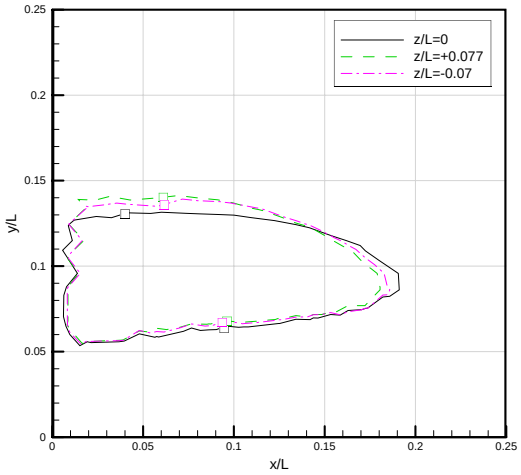

Figure 5.25 - Contours of u/u_∞=0 and vortex centres in near wake of Ahmed model at z/L=0 and ±0.077 - 25° backlight

effects can be seen at approximately x/L=0.22 downstream at 20° and at x/L=0.16 downstream for both the current and Lienhart's 25° case.

It can also be seen that as α approaches 25° the reversed flow region decreases dramatically in size. This is explained by the LIC plots (Fig 5.21) which show that the upper recirculation region in the separation bubble dominates the flow for angles greater than 10° in accordance with Ahmed [1984]. As the size of this upper region drops with increasing α, due to the downwash produced over the backlight, the overall effect is a decrease in the distance to which the separation bubble extends downstream.

For comparison purposes the regions of flow reversal, vortex centres and singular attachment nodes for all angles are plotted in Figures 5.22 and 5.23. Clearly the region of flow reversal extends beyond the measurement plane for both the 0° and 5° backlights. The distances downstream to which these regions extend for the other angles are shown in Table 5.1. The lower left section of Lienhart's 25° and 35° reversed flow regions do not follow the same trend as all other cases due to insufficient data in this area.

In the 30° and 40° cases the reversed flow regions extend up on top of the backlight. At this point they join with the upper recirculation regions shown in Figure 5.10. As stated previously Ahmed's original experiment predicted the extension of the reversed flow above the backlight, but not the additional circulatory regions shown in Figure 5.10.

The relative positions of the upper vortices at each back angle were also expected from the previous studies. The shortening of the overall length of the separation bubble is caused by the increased downwash moving the upper vortex downward and closer to the model rear end as α tends towards 25°. The lower vortex centre also tends towards the model rear end due

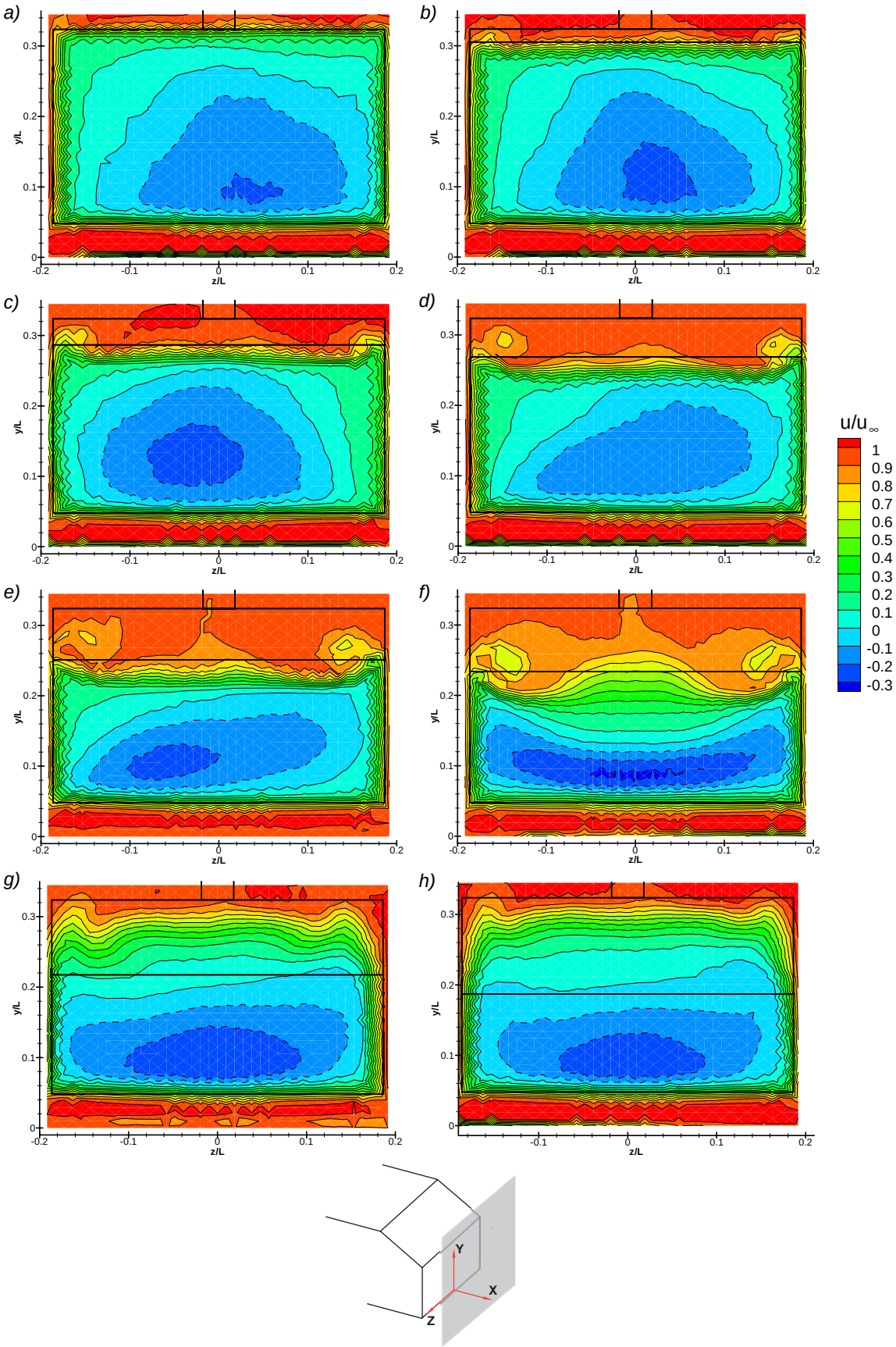

Figure 5.26 - Isolated Ahmed Model - contours of normalised streamwise velocity at x/L = 0.077 behind a)0° b)5° c)10° d)15° e)20° f)25° g)30° h)40° models - LDA data

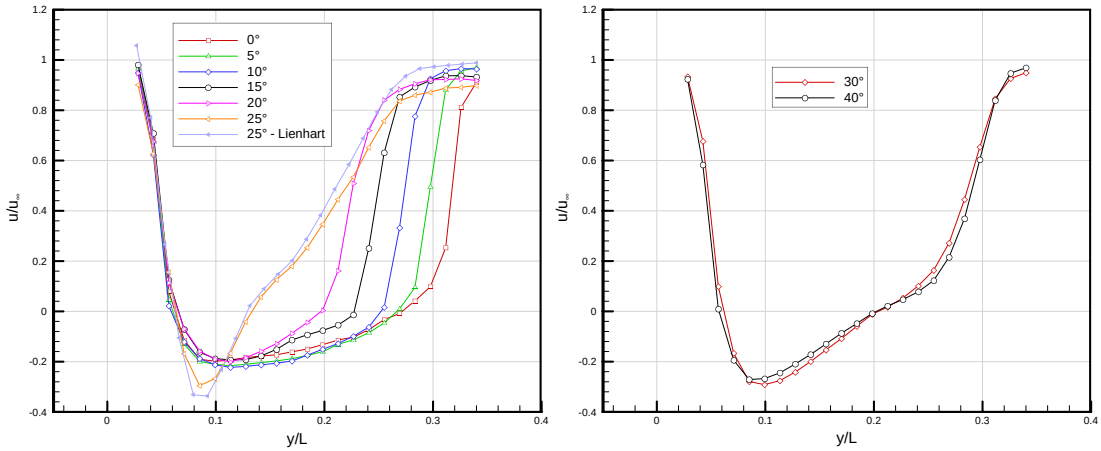

Figure 5.27 - Isolated Ahmed Model - vertical profiles of normalised u velocity at x/L = 0.077, z/L=0 - LDA data

to the shortening of the separation bubble. Once the flow has separated off the backlight (α>25°), the upper vortex centre returns to a height approximately the same as at 10°, but closer to the trailing edge. This is due to the separation now occurring further upstream at the front edge of the backlight. The variation in height of the upper vortex centres of approximately y/L=0.03 between the two separated cases measured in the current study (30° and 40°) and the one recorded by Lienhart (35°), is due to the differing flow structure over the backlight itself, as shown in Figure 5.10. The upper recirculatory region over the backlight will cause additional downwash at the trailing edge, tending to move the region of flow reversal in this region downward. This can be seen by comparing the regions of flow reversal in Figure 5.22. It is, as mentioned previously, possible that disturbances from the strut wake are responsible for this altered flow over the backlight and therefore these differences in wake structure.

Figure 5.24 shows both contour and LIC plots at z/L=0 and ±0.077 for the 25° backlight. Again both contours of u/u_∞=0 and vortex centres are shown in Figure 5.25 for easy comparison. Initial inspection of the contour plots shows the effect which the longitudinal vortices have even at only 0.077L from the model centreline. Effects can now be seen at only 0.06L downstream of the trailing edge. From a combination of the LIC and reversed flow comparison plots it can be seen that away from the model centreline the distance downstream to which the region of reversed flow extends shortens while increasing slightly in overall height. This is due to movement of the upper recirculatory region, as the lower region does not appear to alter its structure between the regions measured. The centre of the upper region moves upwards slightly and downstream by approximately 0.02L. The slight shortening of the downstream distance away from the model centreline is consistent with the flow structure recorded by Ahmed, shown by the shape of region A in Figure 2.2. There also appears to be very little variation between the z/L=±0.077 planes, signifying very good centreline symmetry of the data.

y-z planes

Shown in Figure 5.26 are contour plots of u velocity at 0.077L downstream of the model trailing edge with regions of negative streamwise velocity bounded by dashed lines. The geometry of the model and supporting strut are also included in the plots to aid comparison. As would be expected from previous analysis the height of the reversed flow region varies only slightly with increasing α between 0° and 10°, when the longitudinal vortices formed do not alter the flow significantly over the model centreline. The increase in the size of these as α tends towards 25°, in addition to the lowering of the height of the reversed flow region due to increased downwash over the backlight can also clearly be seen in these contour plots.

The flow at this position behind the 25° model can be seen to be significantly different in structure to that of the other backlight angles tested. It was shown in Figure 5.15 the extent to which the strength of the side vortices increases between 20° and 25°, and in Figure 5.12 the increase in boundary layer thickness at the model trailing edge caused by the adverse pressure gradient over the backlight. The effect of these is a region of lowered streamwise velocity (u/u_∞=0.7) at a position higher than the trailing edge, unique to the 25° case. The strong side vortices which prevented lateral widening of this region over the backlight now begin to dominate the flow. It was shown in Figure 5.20 that their effects can clearly be seen at z/L=0.077, x/L=0.06 downstream of the trailing edge, suggesting that in the plots shown in Figure 5.26 their effects would be obvious even further inboard. Indeed, the downward shift in position of the reversed flow region near the model centreline is evidence of the effects which the vortices have on the near wake of the 25° model.

Once the backlight flow is separated there is once again only slight variation with the height of the region of reversed flow. The effects of the flow tendency to turn around the top edge of the model can still be seen at this point, although, as stated previously, this has little effect on the flow over the remainder of the backlight.

To quantify the alteration of the wake with changing back angle lines of data have been extracted at the model centreline (z/L=0) for the contour plots in Figure 5.26, and are shown in Figure 5.27. For the sake of clarity the attached and separated cases are plotted separately, and Lienhart's 25° data have also been included for comparison.

It is noted that all backlight angles lower than 25° exhibit a minimum u velocity at approximately y/L=0.11. The value of this minimum also varies by only $0.03u_\infty$. This is explained by examining Figure 5.20, which shows that it is only when the separation bubble is significantly shortened at 25° that the region of higher magnitude reversed flow is forced into the region examined in Figure 5.26. The rapid increase in streamwise velocity evident for every backlight other than the 25° case (both attached and separated) occurs slightly below

the point where the flow separates. As would be expected due to the increased downwash generated, the distance below the backlight trailing edge at which this recovery occurs is lower as α increases to 20°. Once the flow has separated at the front edge of the backlight this recovery appears more gradual due to the extra distance upstream at which separation occurred.

The 25° case exhibits more gradual recovery to freestream velocity, though in this case it is a result of the increased boundary layer thickness and the 'squashing' of the higher magnitude reversed flow in the area examined. Comparing the current and Lienhart's 25° data it can be seen that, other than the $0.1u_{\infty}$ difference toward the top of the data recorded here (consistent with upstream analysis), the other point where the results differ significantly is in their relative measurement of the minimum u velocity. Again, inspection of Figure 5.20 shows that in Lienhart's data the region of maximum reversed flow magnitude is nearer to the trailing edge of the model, resulting in the lower velocity at the position recorded in Figure 5.27.

It is evident from the 30° and 40° line plots that once the flow has separated over the backlight there is only minor variation in the wake structure at this downstream position. This would be expected from inspection of Figure 5.26 which shows that these two angles exhibit almost identical flow structures in this region.

Far Wake

Figures 5.28 and 5.29 plot contours of u and v velocity respectively at x/L=0.5 and x/L=1 downstream of the model trailing edge for the 10°, 25° and 40° backlights. Again both the model geometry and the position of the supporting strut are included to aid analysis. The slightly irregular nature of the 10° plots is due to low data rates during the acquisition of those planes.

Inspection of these plots shows firstly that two counter rotating vortices are formed at each backlight angle tested (from Figure 5.29). This is evident from the positions of maximum and minimum vertical velocity in each case which suggest the formation of this wake structure. This was expected as Ahmed also found these two vortices in the wake for both the high and low drag 30° cases. Inspection of the streamwise velocities in Figure 5.26 however suggests the mechanisms which form these regions at each backlight angle are dissimilar.

In each of the plots in Figure 5.28 a small region of retarded flow due to the effect of the supporting strut can still be seen at x/L=0.5 downstream, and in each case this effect is no longer evident at x/L=1. Thus the strut wake, although previously shown to be relatively minor in its overall effect on the flow structure, extends to at least 0.5L downstream. As the three backlight angles presented here exhibit dissimilar flow structures over the model, it can be

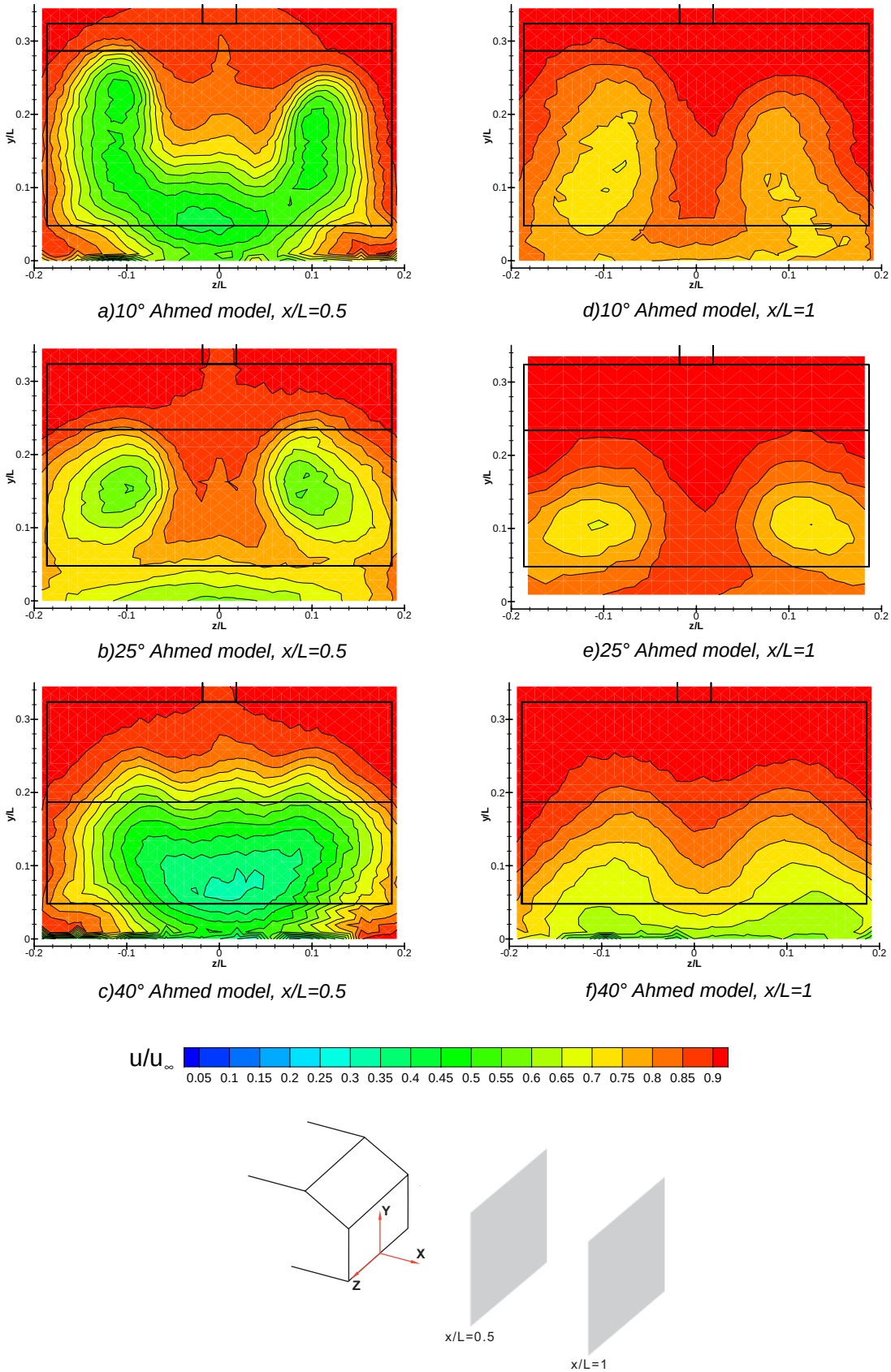

a)10° Ahmed model, x/L=0.5

d)10° Ahmed model, x/L=1

b)25° Ahmed model, x/L=0.5

e)25° Ahmed model, x/L=1

c)40° Ahmed model, x/L=0.5

f)40° Ahmed model, x/L=1

Figure 5.28 - Isolated Ahmed Model - contours of normalised streamwise velocity at two streamwise planes (x/L = 0.5, x/L=1) behind the model for 3 backlight angles (10°, 25°, 40°) - LDA data

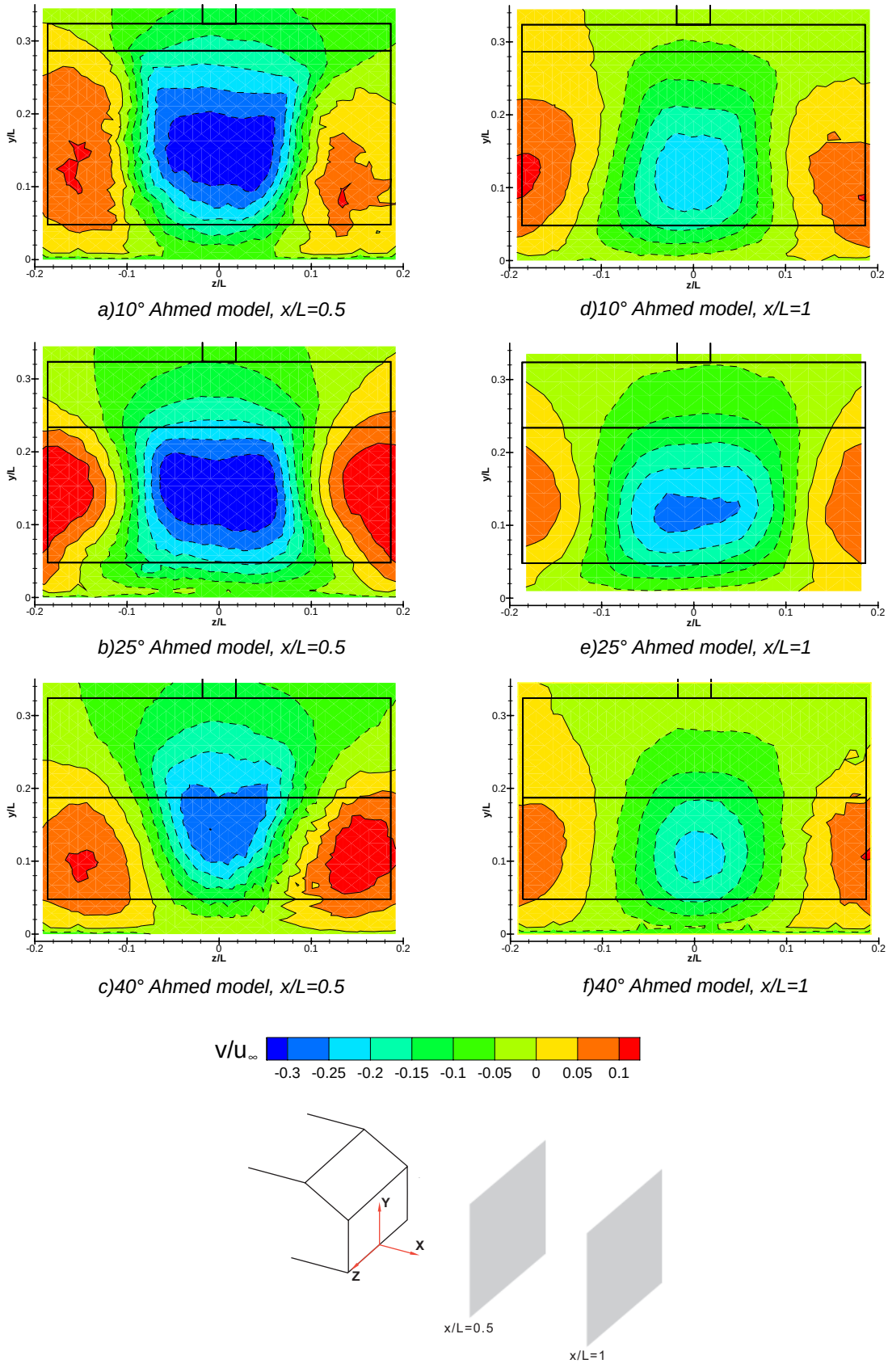

Figure 5.29 - Isolated Ahmed Model - contours of normalised vertical velocity at two streamwise planes (x/L = 0.5, x/L=1) behind the model for 3 backlight angles (10°, 25°, 40°) - LDA data

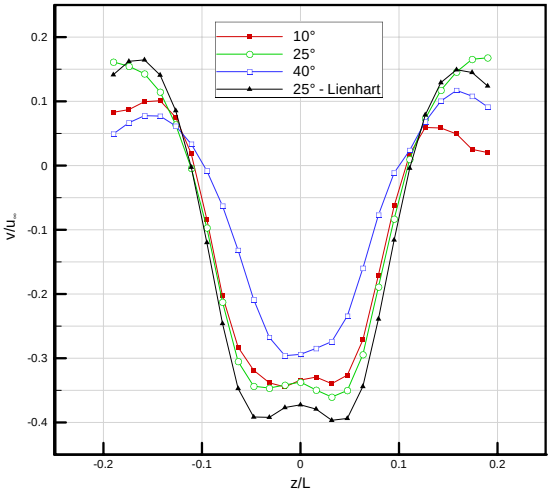

a) Horizontal profiles at y/L=0.15, x/L=0.5

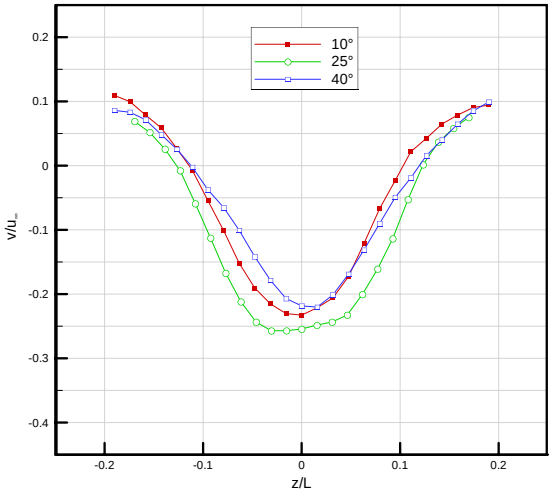

b) Horizontal profiles at y/L=0.1, x/L=1

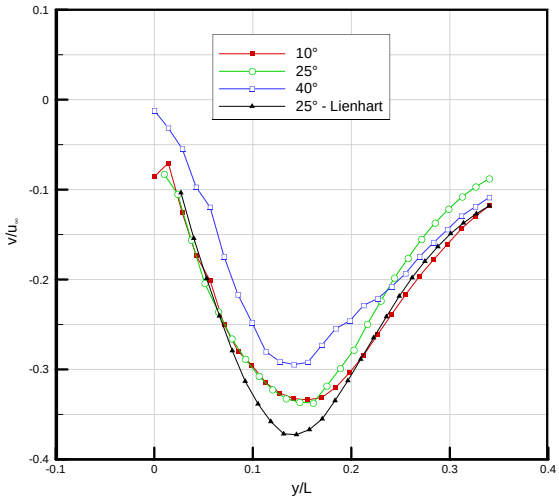

c) Vertical profiles at z/L=0, x/L=0.5

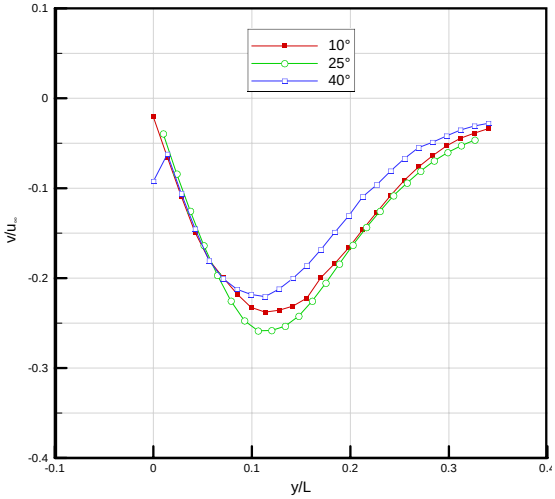

d) Vertical profiles at z/L=0, x/L=1

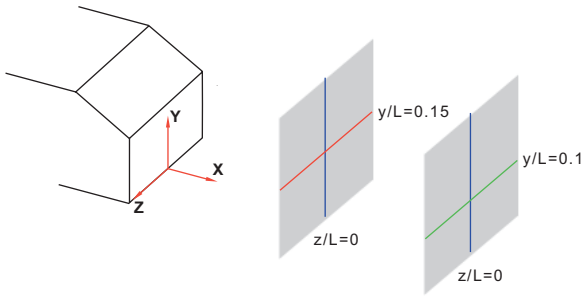

Figure 5.30 - Horizontal and vertical profiles of normalised vertical velocity at two streamwise planes (x/L = 0.5, x/L=1) behind the model for 3 backlight angles (10°, 25°, 40°) - LDA data

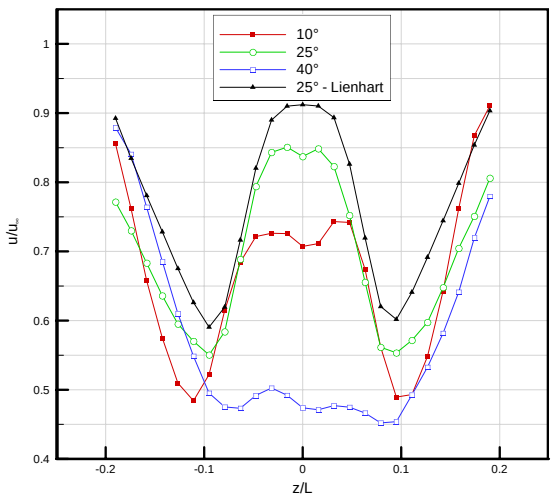

a) Horizontal profiles at y/L=0.15, x/L=0.5

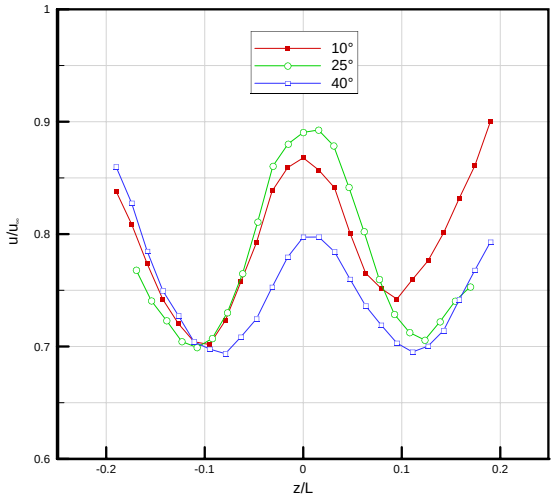

b) Horizontal profiles at y/L=0.1, x/L=1

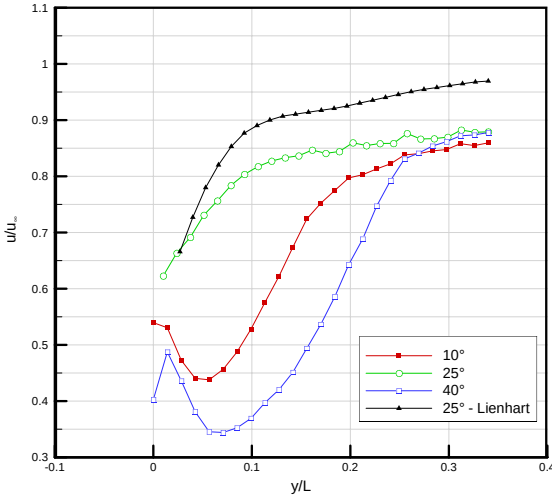

c) Vertical profiles at z/L=0, x/L=0.5

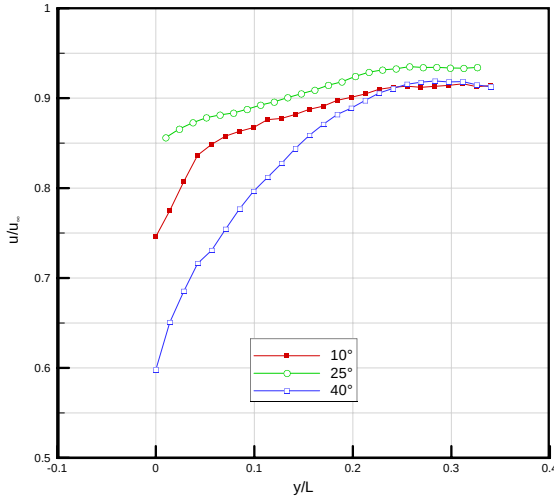

d) Vertical profiles at z/L=0, x/L=1

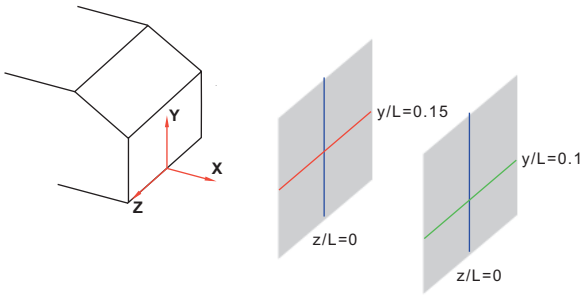

Figure 5.31 - Horizontal and vertical profiles of normalised streamwise velocity at two streamwise planes (x/L = 0.5, x/L=1) behind the model for 3 backlight angles (10°, 25°, 40°) - LDA data

assumed that this downstream distance is independent of backlight geometry.

In the 25° case the two longitudinal vortices formed over the backlight have now dominated the wake flow. The total pressure loss in the small vortex core can clearly be seen as retardation of the flow in the u velocity plot for x/L=0.5, and downstream at x/L=1. The retarded flow in the wake at 0.077L downstream (Figure 5.26) has been forced downward by these vortices, as can be seen by the region of lower u velocity below y/L=0.04 (Figure 5.28). By 1L downstream, however, there is no longer any obvious evidence of this region and the longitudinal vortices are now the only discernable feature of the wake.

The equivalent longitudinal vortices shed from the 10° backlight have also begun to have a significant effect on the wake flow by 0.5L downstream. Although data for these planes was hindered by low data rates the effect of these vortices forcing the remainder of the near wake flow toward the ground plane can clearly be seen. Due to the lower strength of these vortices they have not had as significant an effect on the flow as in the 25° case. The region of lower streamwise velocity evident in the 10° near wake plot (Figure 5.26) has again been forced downward by these vortices, but as expected this effect is not as pronounced as in the 25° case. Evidence of this region can also still be found at 1L downstream, which is not the case for the 25° backlight.

Due to the lack of formation of these longitudinal vortices in the 40° case no vortex core is visible in the model wake. The tendency of the flow to turn around the model top edge has had the effect of creating two noticeable 'dips' in the structure of the wake at z/L=±0.05, but otherwise the wake formation appears unaffected by them. Instead the downwash created by the downward tilt of the flow separating from the upper edge of the backlight has a similar effect as the longitudinal vortices in the 10° and 25° cases in forcing the wake of the model towards the ground plane. As this downwash is, as has been shown previously, far less than that created in the cases with strong side vortices, the wake still appears to be of comparable size to the model frontal area at 0.5L downstream. Once the small side sections of increased downwash have continued to move inward toward the model centreline, their effect in conjunction with the backlight downwash is to force this wake flow, in particular the region close to the model centreline, further towards the ground plane. This can clearly be seen in the x/L=1 40° plot of Figure 5.28.

The overall effect though of each of the three wake structures outlined is to set up two counter rotating vortices in the flow. This can be seen by the similarity in the v velocity plots in Figure 5.29. Initial inspection reveals a larger area of high positive v velocity flow in the 25° case not found in either of the other two, indicative of the stronger vortices formed in the wake. To aid further analysis of the wake flow, lines of data were extracted from various points on each

contour plot and are shown in Figures 5.30 and 5.31. Data from Lienhart is also included where possible, although it must be stressed that these data were taken slightly further upstream than the current data (x/L=0.48 in comparison to x/L=0.5).

From Figure 5.30 (a) the downwash created by all the backlights tested can clearly be seen. The slight drop in v velocity magnitude between approximately z/L=±0.02 for both the 25° and 10° cases is most likely due to the outboard positions of the vortex cores causing them to have less effect in this region. As the 40° case does not experience significant longitudinal vortex effects no evidence of this drop in v velocity magnitude is found. As the flow continues downstream and the vortex centres continue to move towards the model centreline (z/L=0), this drop no longer exists owing to the fact that the regions of higher magnitude v velocity close to the vortex cores are now affecting the region of flow near to the model centreline. This can be seen in Figure 5.30 (b).

As was mentioned previously the stronger vortices shed in the 25° case cause a higher maximum v velocity then in the 10° case at 0.5L downstream. This is confirmed by Figure 5.30 (a) which shows that at 10° the maximum v velocity measured was $0.1u_\infty$. This compares to a maximum v velocity reading of $0.17u_\infty$ in the 25° case. The downwash near the model centreline also follows expected trends, with a large decrease in minimum v velocity of approximately 15% between the 40° backlight (where the vortices have very little effect) and the 10° backlight. The greater strength of the 25° longitudinal vortices also cause a further 9% decrease in comparison to the 10° case. This variation in downwash between the 10°, 25° and 40° cases is continued at 1L downstream, although by this point the dissipation of the vortices ensures far less variation in minimum v velocities. This can again be seen in Figure 5.30 (b).

Evident from Figure 5.31 (a) are the drops in streamwise velocity due to the total pressure loss produced by the longitudinal vortices in the 25° cases. In addition, an increase in streamwise velocity close to z/L=0 for the 10° and 25° cases can be seen, this being due to the downwash forcing higher velocity flow from above the model downward and into the measured plane. This effect is, as expected, not noticeable for the 40° case due to the lower downwash and subsequent absence of introduction of higher velocity flow into this region. A dip in streamwise velocity between z/L=±0.02 at 0.5L downstream in the current data is not consistent with the results of Lienhart, and as such it must be assumed to be an effect of the strut wake.

In further comparing the current 25° case to that of Lienhart it can be seen that there is a stronger downwash produced by Lienhart's vortices, consistent with upstream comparisons. As a result the total pressure loss and subsequent drop in streamwise velocity produced by the vortex cores is greater in Lienhart's data, as can be seen in Figure 5.31 (a). Although the current data was taken slightly further downstream, these discrepancies cannot be accounted

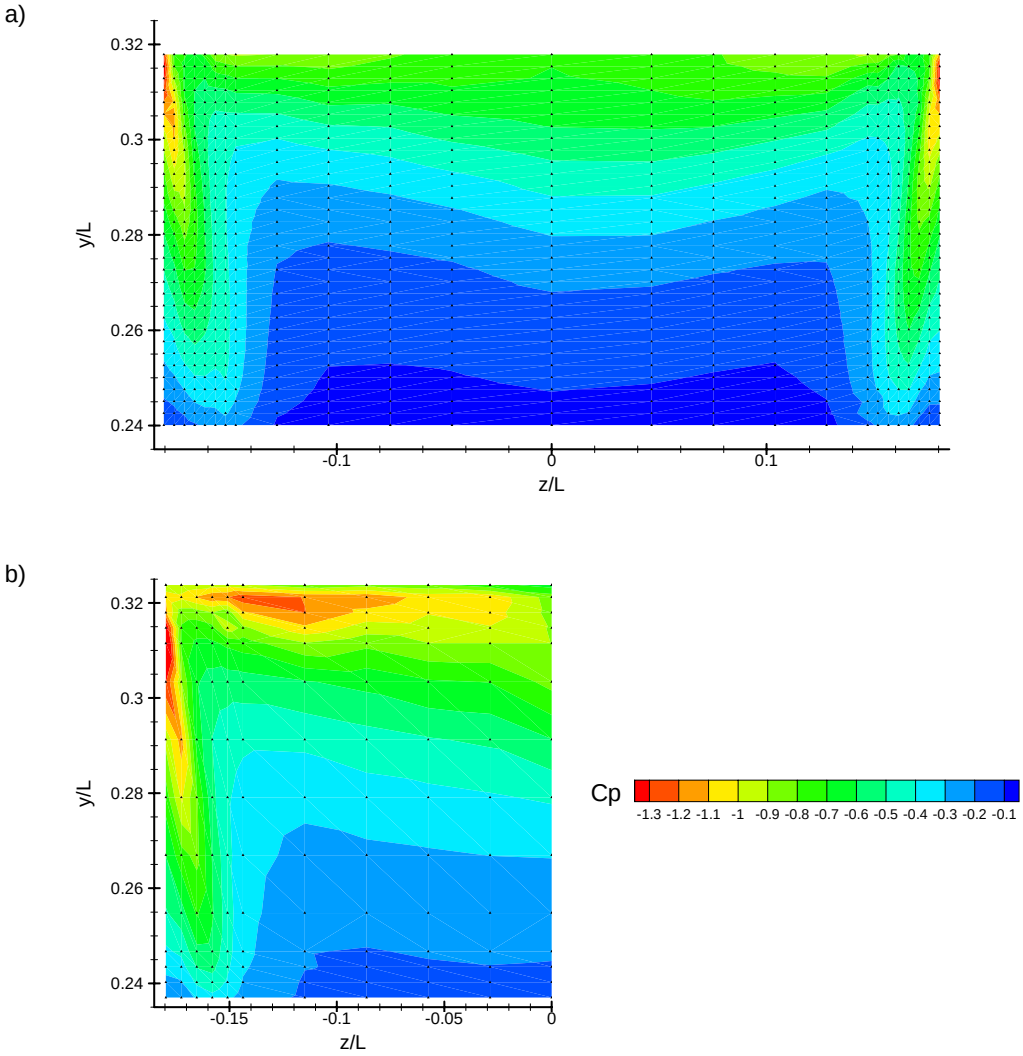

Figure 5.32 - Pressure distribution over 25° Ahmed model backlight - data from (a) current experiments (b) Lienhart and Becker [2000]. Black triangles mark positions of pressure tappings

for by this small variation in the measurement plane, and are in fact consistent with upstream comparisons of the vortex structure.

From Figures 5.30 c) and 5.31 c) it can be seen that there is a difference in streamwise velocity of approximately $0.1u_\infty$ above y/L=0.3 between Lienhart's data and all the current measured backlights. From the previous plot (Figure 5.30 (a)) it can be seen that the effect of the strut on the wake flow appears to be far less than this value, at most accounting for a drop of $0.025u_\infty$. Thus, this discrepancy is most likely due to the previously-analysed higher velocity flow over the top of the model in Lienhart's experiments. As would be expected from the downwash forcing higher energy flow into the measured plane, at 1L downstream the measured streamwise velocity at y/L=0.3 at the model centreline has risen from approximately $0.875u_\infty$ to approximately $0.95u_\infty$ for the current measured backlights.

It can also be seen from Figure 5.30 c) that, as expected, the region of lowered streamwise

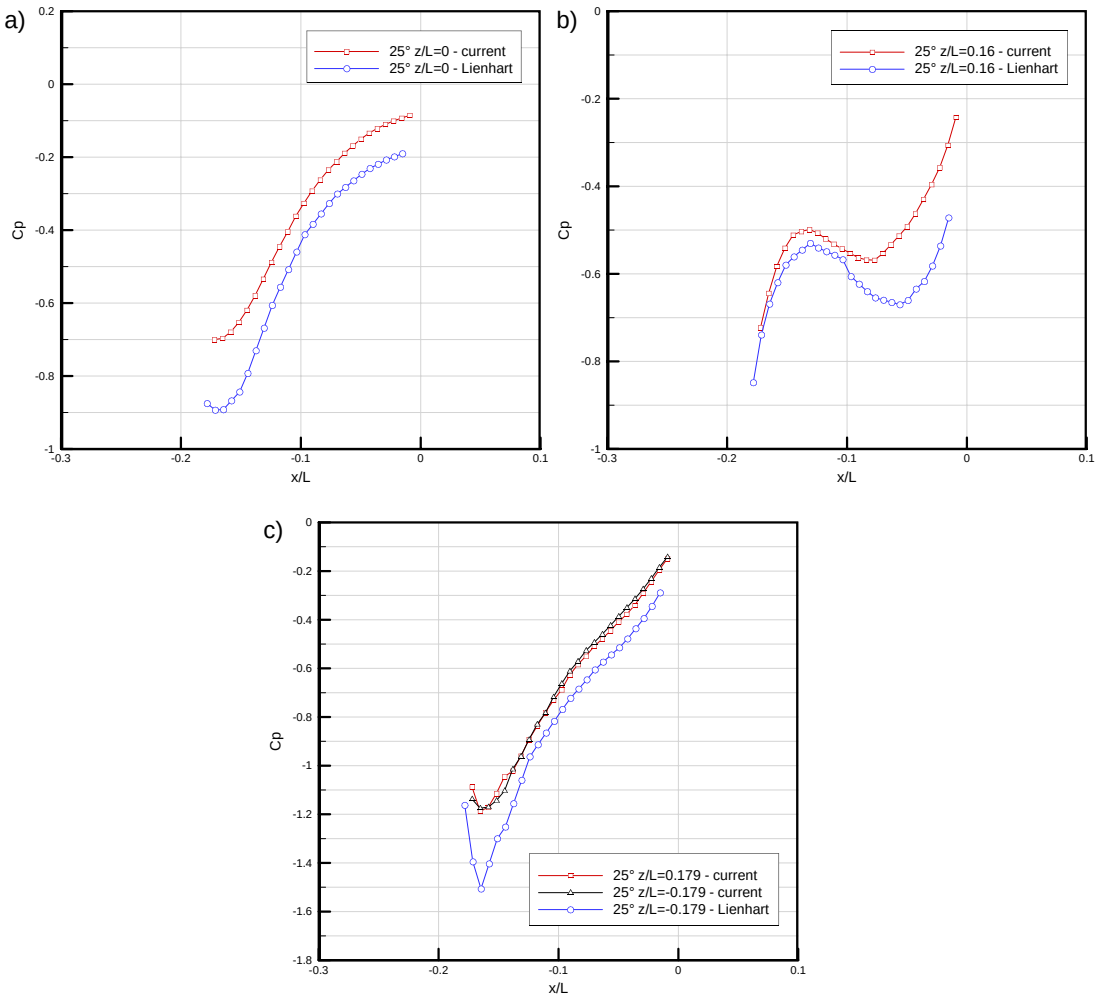

Figure 5.33 - Streamwise profiles of pressure distribution over 25° Ahmed model backlight - current and Lienhart data

velocity has been forced towards the ground by the presence of the strong vortices, evident from the relative positions above the ground plane at which the streamwise velocity begins to level off in each case. It should also be noted that due to reasons outlined previously the ground level points taken for the 10° and 40° cases should be ignored in these plots.

From Figures 5.30 d) and 5.31 d) the variations in downwash between the cases can again be seen. It appears from Figure 5.30 c) that there is no variation in downwash between the current 10° and 25° cases below y/L=0.15, however from the previous plots it was found that at z/L=0 and x/L=0.5 the longitudinal vortices have not yet moved far enough inward to create the same downward flow velocity which is found slightly away from the model centreline. Figure 5.30 d) shows that once these vortices have continued inward the expected higher magnitude downward flow is found in the 25° case.

5.1.3 Static Pressure Results

The static pressure readings taken for the 25° backlight in the current experiments are compared to the equivalent readings from Lienhart in Figure 5.32, with the distribution of pressure tappings for both experiments also shown. Only half of the model backlight was pressure tapped by Lienhart. In both experiments a finer density of tappings was employed in the region where the side vortices were expected to have a significant influence on the backlight flow, although more than 3 times as many tappings were employed in this side region in the current investigation (256 compared to Lienhart's 84). This number of points was considered necessary due to the expected alterations in vortex flow with the later inclusion of the side wall.

The regions of lower C_p outside -0.15<z/L<0.15 in both plots illustrate again the existence of the side vortices. The lower levels of C_p evident in this region of Lienhart's data are further evidence of the stronger vortices being formed in those experiments. This trend is continued over the remainder of the backlight, where the higher flow velocity analysed previously creates lower pressure over the entire region.

For quantitative evaluation lines of data have been extracted from Figures 5.32 (a) and (b), and are compared in Figure 5.33. The centreline (z/L=0) plot shows the suction peak over the front edge of the backlight, and subsequent drop in flow velocity (and subsequent rise in C_p) as the flow continues downstream. This is consistent with previous analysis of the 25° backlight flow. Also evident is the lower C_p measured in Lienhart's experiments. The difference in C_p between the experiments varies from a maximum of approximately 0.2 at the upper edge of the backlight to 0.1 at the trailing edge.

Two lines of data were extracted to investigate the vortex formation in both experiments - at z/L=0.16 and 0.179 (Figure 5.33 (b) and (c)). Very similar trends between the experimental results can be found in the z/L=0.16 plot. The C_p increases as the flow continues downstream until x/L=-0.13 where the side vortex has moved inward enough to affect the flow in this region, causing an increase in local flow velocity and a decrease in C_p. In the current data this decrease continues to -0.08L downstream, whilst in Lienhart's case this decrease is evident until -0.06L downstream. In addition the magnitude of this decrease in Lienhart's experiments is approximately double the current value - 0.14 compared to 0.07. This is expected owing to the stronger vortices in Lienhart's experiments.

The final line plot at z/L=0.179 (Figure 5.33 (c)) also includes current data at z/L=-0.179 to check flow symmetry. It can be seen that maximum variation between the two current lines of data is only approximately 5%, suggesting very good symmetry. The large difference of approximately 0.3 in max C_p between the current and Lienhart's data appears to be a result

simply of the slightly differing positions of the vortices in each case. This means that a single line plot does not intersect with the minimum C_p value for both. Interrogation of the data reveals that the values of minimum C_p recorded over the backlight differ by approximately 0.1, more consistent with previous pressure results analysis.

Analysis of the pressure readings from both experiments reveals a variation in average C_p between the current and Lienhart's data of approximately 0.11. This average was calculated on only the sections of the backlight which were measured in both cases. As explained previously the increased vortex strength and higher flow velocity over the backlight, due to the absence of upstream blockage effects in Lienhart's experiments, are responsible for this lower pressure.

5.2 Computational Validation

5.2.1 Flow Structure

Front End

Following a number of preliminary numerical studies, it was concluded that the model to be employed throughout the computational phase of the investigation would have no support system of any kind, owing to the limitations of the available computing power. Neither the overhead strut (used in the current experiments) nor the cylindrical support struts underneath the model (used in previous investigations) were modelled in the computational domain. It is necessary to consider this and the effects the support strut would have when analysing the current computational data. The computational model also employed a symmetry plane on the floor, rather than a moving ground as in the experiments, as it was found that at the modelled ride height this simplification had no effect on the flow over the model and reduced computational cost. A detailed description of the computational model can be found in Chapter 4, with the results of the preliminary numerical studies in the relevant appendix.

Figures 5.34 - 5.36 plot lines of data taken at the model centreline, and correspond to identical data points shown for the experimental cases in Figures 5.2 - 5.4. Although all backlight angles were tested computationally, only the 5°, 25° and 30° cases are shown here. Data from the other angles followed virtually identical trends in the areas investigated in these figures, and as such have been omitted for reasons of clarity.

The increased flow velocity underneath the model in comparison to the top can be seen again in the computational data, although disparities between the computational and the current experimental results are evident. The CFD over-predicts the maximum streamwise velocity over the model by approximately $0.06u_\infty$ (5%), a discrepancy which increases to

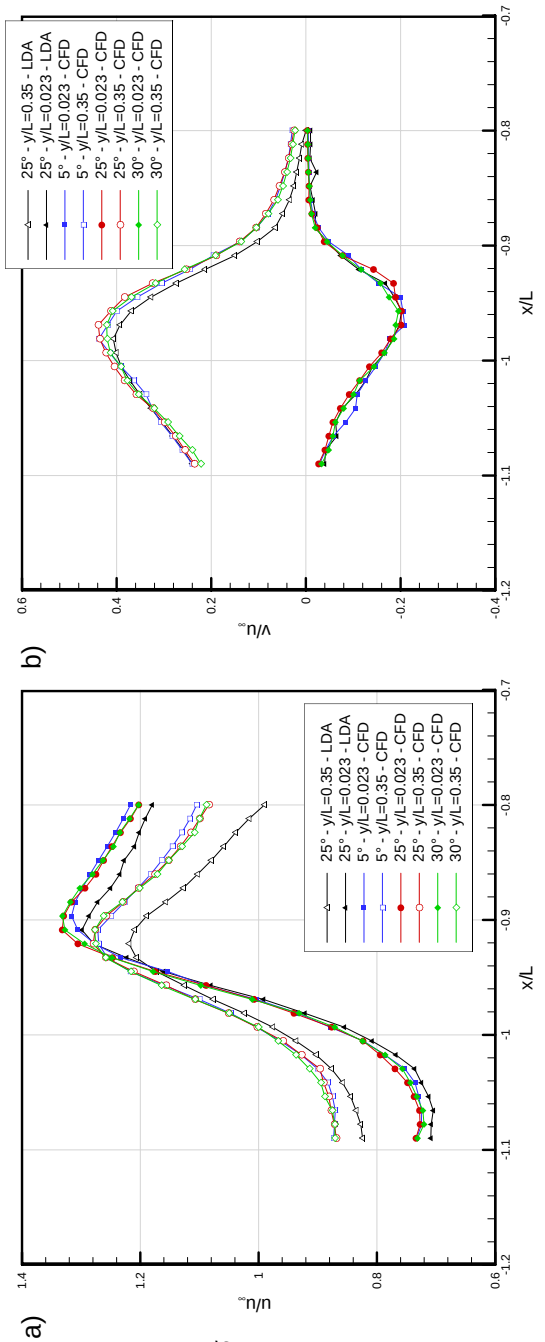

Figure 5.34 - Streamwise profiles of normalised u and v velocity at y/L=0.35 and 0.023 around Ahmed model front ends - experimental and computational data

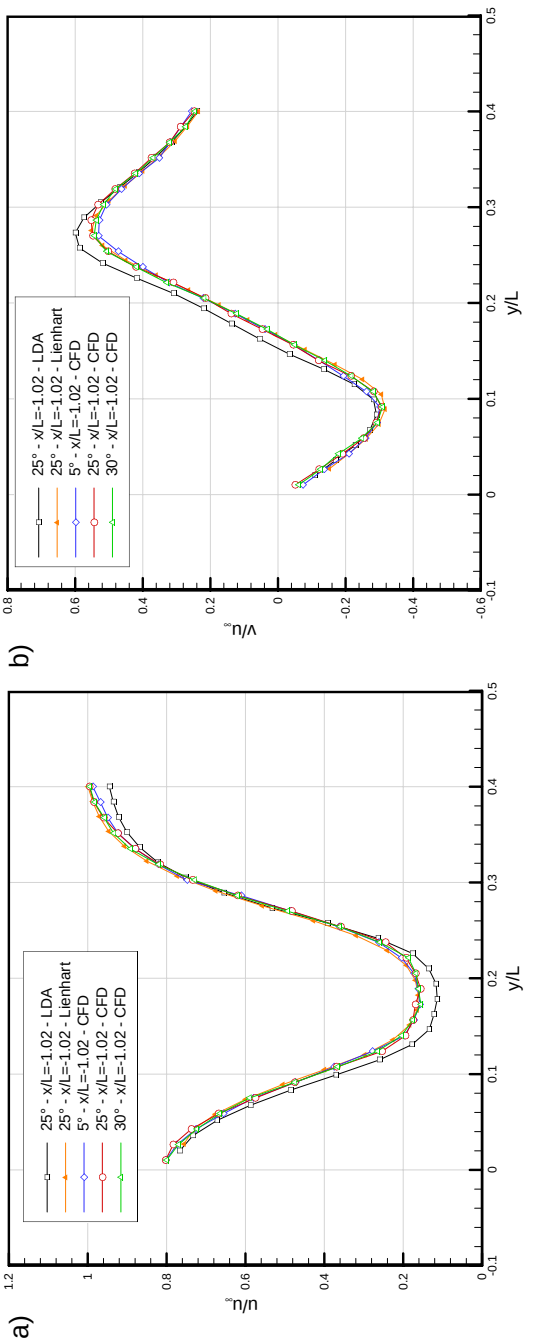

Figure 5.35 - Vertical profiles of normalised u and v velocity at x/L=-1.02 around Ahmed model front ends - experimental and computational data

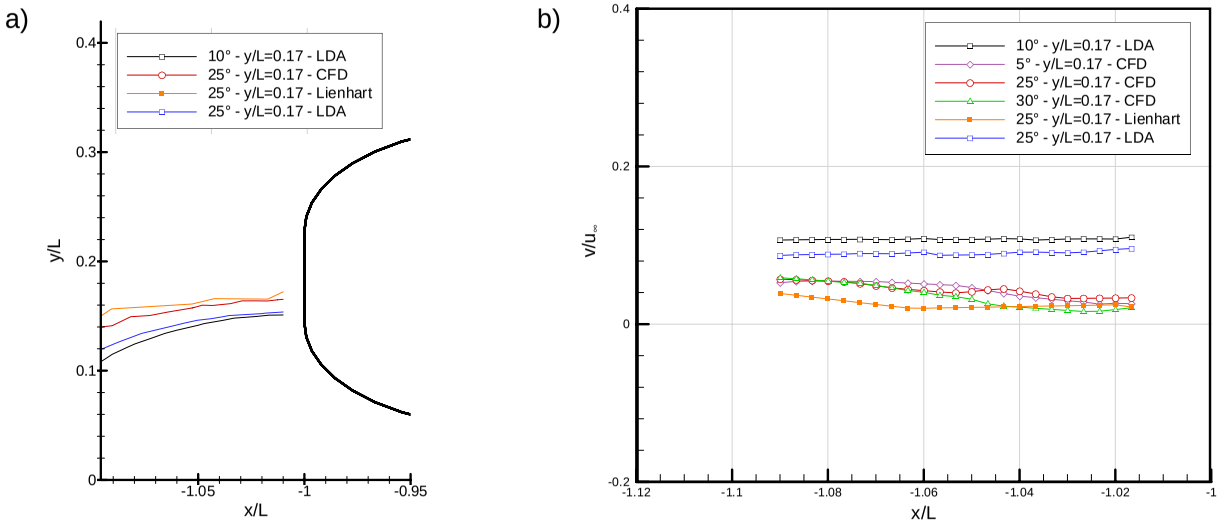

Figure 5.36 - (a) Contours of v=0 and (b) streamwise profiles of normalised v velocity at y/L=0.17 around Ahmed model front ends - experimental and computational data

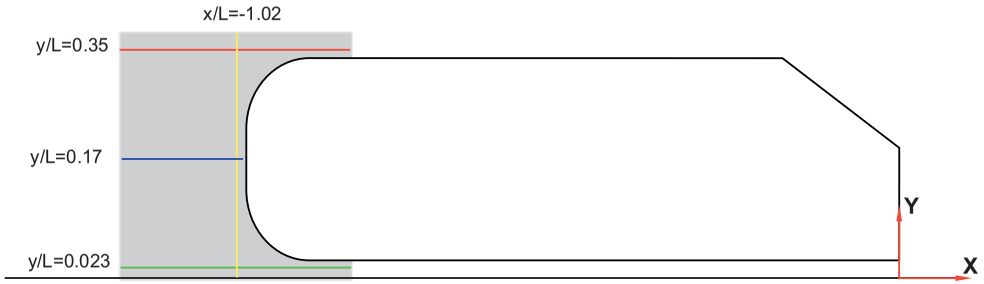

Figure 5.37 - Schematic diagram of model centreline plane investigated and positions of extracted data in Figures 5.34 - 5.36

approximately $0.1u_\infty$ by x/L=-0.8. This predicted increase in flow velocity in the CFD model over the top of the model would be expected, due to the absence of the overhead strut. With the lack of struts of any kind in the numerical model, greater similarity would be expected between the computation and the experimental results of Lienhart. As previously stated, the under-body supports used in Lienhart's experiments would not be expected to have significant effects on the flow over the model centreline where the data shown here were taken.

When compared to available data from Lienhart's experiments (omitted here due to insufficient resolution in the area of interest), the CFD in fact under-predicts the streamwise flow velocity by up to $0.02u_\infty$ upstream of x/L=-0.91. Beyond the suction peak however, the variation between the current computational and Lienhart's experimental results almost triples to an under-prediction of around $0.07u_\infty$. Due to the excellent agreement between these results upstream of the front end suction peak, it seems reasonable to assume that the differences downstream of this point may be due to a predicted weaker interaction between the front and rear end than was found in the experiments. It was shown previously that the suction peak over the backlight had an effect on the flow around the model front, and therefore the flow velocity over the top of the model. Weaker, or no predicted interaction of this type would account for these differences between the current computations and Lienhart's experimental data. This hypothesis is further strengthened by inspection of the variation in v velocity in Figure 5.34 (b). The variation in v velocity between the 10° and 25° cases measured in the current experiments remained constant at approximately $0.03u_\infty$ at points upstream of the model leading edge. This was a result of increased suction over the backlight relocating the stagnation point (Figures 5.2 and 5.5).

Comparatively, the CFD model predicts a variation in v velocity of $\pm 0.015u_\infty$ between all the backlight angles. Due to the small magnitude and inconsistent nature of this variation between the computational cases, it must again be inferred that the CFD under-predicts the effect of back angle on the front end flow.

From Figure 5.34 (b) it can also be seen that downstream of the leading edge the current experimental 25° case exhibits a lower v velocity of approximately $0.025u_\infty$ in comparison to the computational cases. This variation is consistent with Lienhart's data, again omitted from the diagram due to insufficient resolution. This is thought to be a result of the downwash induced by the strut affecting the flow in this region.

Figure 5.35 again shows excellent agreement between the computational results and those of Lienhart, with both velocity components being measured within experimental error. It was shown in Figure 5.3 that at x/L=-1.02 the streamwise velocity component appeared unaltered by the backlight angle, which is consistent with the CFD results here. Again the increased

streamwise velocity over the top of the model can be seen when comparing the current computational and experimental results.

Figure 5.35 (b) shows again the effect of the raised stagnation point caused by the increased top-edge suction in the CFD model. The maximum variation between the current experiments and the CFD was found to be $0.05u_\infty$. Again though, there was virtually no variation between the CFD cases, this despite it being shown previously that there was a maximum variation of $0.03u_\infty$ between the current 10° and 25° cases. This is again assumed to be a result of a weak predicted interaction between the front and rear end flow.

Figure 5.36 confirms the predicted relocation of the stagnation point with increased suction. As expected the stagnation point is predicted only slightly lower by the CFD in comparison to Lienhart's data, owing to the lowered suction over the top of the leading edge.

From this analysis it must be concluded that validation of the numerical model further downstream must be performed with reference to both the current experimental work, in addition to that of Lienhart. Although the CFD data shown in Figures 5.34 - 5.36 are generally within the error bands of Lienhart's experimental results, the discrepancy in the flow velocities above the model and downstream of the leading edge cannot be ignored. As it is the flow above the model which will have the greatest effect on the backlight, the lower streamwise velocity in the current experiments may prove to form more similar flow structures to the computation in this region.

Over Model

Figure 5.38 plots streamwise velocities over the top of the Ahmed model for both experimental and computational cases. Included are both a schematic diagram of the 25° model (heavy black line) to provide visualisation of the position of the flow along the model and the position at which each line of data was extracted (dashed line). Current experimental data are only included downstream of x/L=-0.21 because the strut wake caused too great a velocity deficit upstream of this position, so the measurements taken were not meaningful. Mention must also be made of the fact that the data resolution in Lienhart's experiments was low in the region examined here, which must be taken into account during analysis.

Initial inspection shows that for the 3 computational cases plotted, there is no evident consistent variation in streamwise velocities upstream of the model centre (x/L=-0.5). This confirms previous analysis which suggested there was little or no computationally-predicted interaction between the flow at the front and rear of the model. Downstream of x/L=-0.5L the CFD predicts increases in streamwise velocity relative to the predicted magnitude of the downstream suction peak. In agreement with experiments this downstream suction peak is

maximised at 25°, with lower suction found at 10° and lower still at 35° (when the flow has separated). It is noted that for the 30° model (data omitted from Figure 5.34 for clarity) the numerical model predicts separated flow, and the streamwise velocity follows an almost identical trend to that in the 35° case shown. As a result it will be possible to compare the experimental 30° case with the numerical model, as separated backlight flow occurred in both cases.

In contrast to the current CFD, the 25° and 35° Lienhart data exhibit a clear variation between the two measured backlights upstream of the model centre, with the lower suction case (35°) displaying lower streamwise velocity over the whole top section of the model. As would be expected this variation increases in magnitude as the flow progresses downstream towards the suction peak. This discrepancy between Lienhart's data and the current CFD model not only accounts for the variations noted around the front end of the model, but also the approximate $0.15u_{\infty}$ between the computation 25° backlight case and the respective Lienhart data upstream of x/L=-0.5. Due to the lower suction effects in the CFD, the plotted data are actually inside the boundary layer over a large section of the model, evidently not the case in Lienhart's experiments.

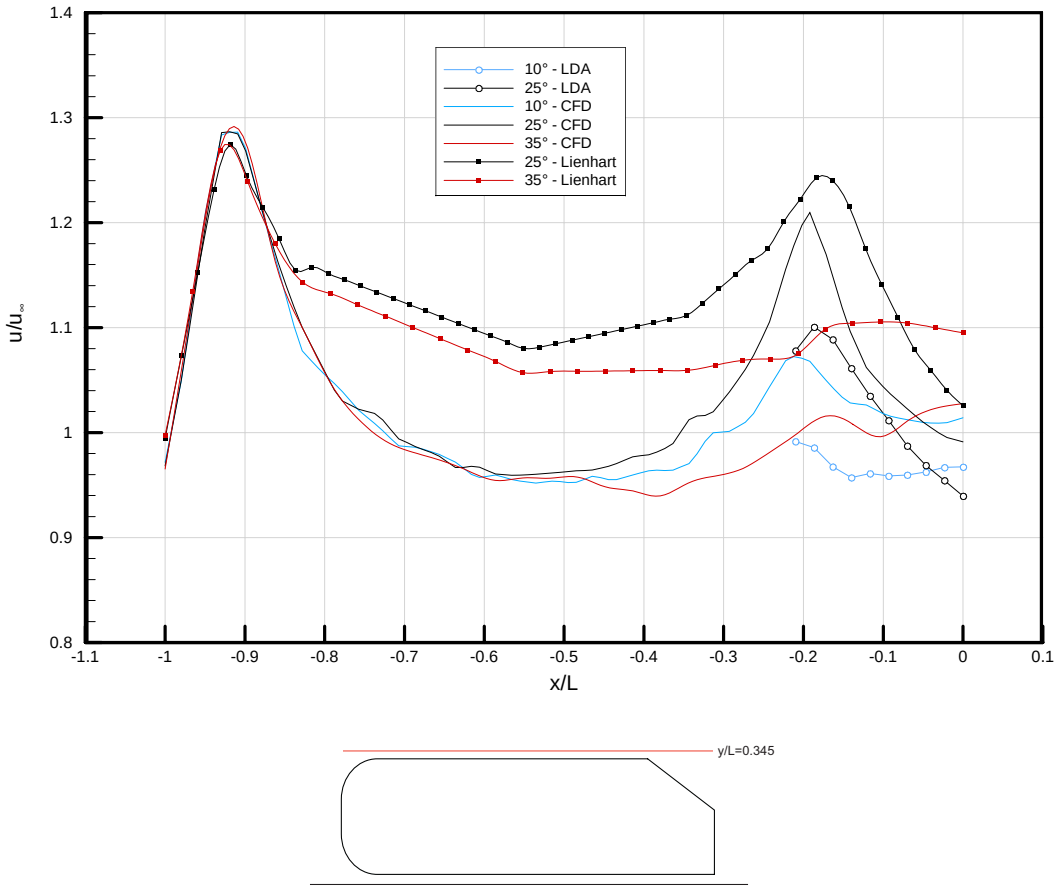

Figure 5.38 - Streamwise profiles of normalised u velocity at z/L=0, y/L=0.345 - experimental and computational data

It can also be seen that the variation in streamwise velocity at the suction peak in the 25° case between the CFD and Lienhart's experiments is far less than the corresponding variation upstream. The CFD predicts a peak velocity of $0.03u_\infty$ less than Lienhart's maximum value, and $0.1u_\infty$ greater than the maximum value recorded in the current experiments. Downstream of the suction peak however, this difference returns to a value similar to further upstream positions, averaging at approximately $0.7u_\infty$.

In comparing the 35° CFD and Lienhart cases, it is clear that the computation again predicts lower streamwise velocity over the entire model top. The difference is fairly constant at approximately $0.1u_\infty$ over the entire region investigated.

The differences between the current experimental and numerical results above the downstream end of the body tend to be of lower magnitude and opposite sign to the differences between the present computations and Lienhart's experiments. This is due to the outlined decrease in computational streamwise velocity in comparison to Lienhart's experiments and the further decrease streamwise velocity in the current experiments due to the blockage of the overhead strut. Indeed the difference between the two 10° cases shown was found to have a maximum at the suction peak of $0.08u_\infty$, (an over prediction of approximately 8%), dropping to $0.045u_\infty$ as the strut wake dissipates downstream. Similarity between these cases is slightly lower for the 25° backlight, where the CFD predicts higher streamwise velocity by approximately $0.11u_\infty$ (10%). Again though, further downstream this difference drops to around $0.05u_\infty$. It was shown previously that outside $-0.1<z/L<0.1$ the current experiments displayed an increase in streamwise velocity of between $0.3u_\infty$ and $0.1u_\infty$, varying with height above the model. It is therefore reasonable to assume that off the model centreline (where the strut wake causes the greatest velocity deficit), the smaller variations between the current numerical and experimental investigations, in comparison to the variations between the current numerical cases and experiments of Lienhart, would be further decreased. As such, CFD validation of the backlight flow, and subsequently the model wake flow, must be conducted again with reference to both available sets of experimental data.

As a final comment, it is important to note that, other than the outlined velocity variations, the numerical model and both sets of experimental results follow very similar trends in the region investigated. Thus it is reasonable to suggest that despite obvious quantitative shortcomings of the computational model, the predicted structure of the flow, at least in the regions analysed thus far, exhibits good correlation with experimental measurements.

Backlight Flow

Figure 5.39 plots flow over the model backlight for angles greater than 20°. Initial inspection

shows that for the 25° backlight the computational solution, like the current experimental results, does not exhibit a separation bubble over the angled model section. This will of course allow more direct comparison between these results both in this region and in the model wake. It is also evident that for both the 30° and 35° cases, the numerical model predicts a very similar flow structure to that found for the 30° case in the current experiments (see Figure 5.10). Both the upper and lower circulatory regions can clearly be seen, with the lower region becoming more dominant as backlight angle increases. The 40° plot though does not mirror experimental data, with the backlight seemingly unable to sustain these circulatory regions, and the reversed backlight flow becoming simply an upstream continuation of the upper circulatory region which dominates the near wake separation bubble. Subsequently, the lower of the two backlight flow regions shown in the 30° and 35° plots does not form, forcing the

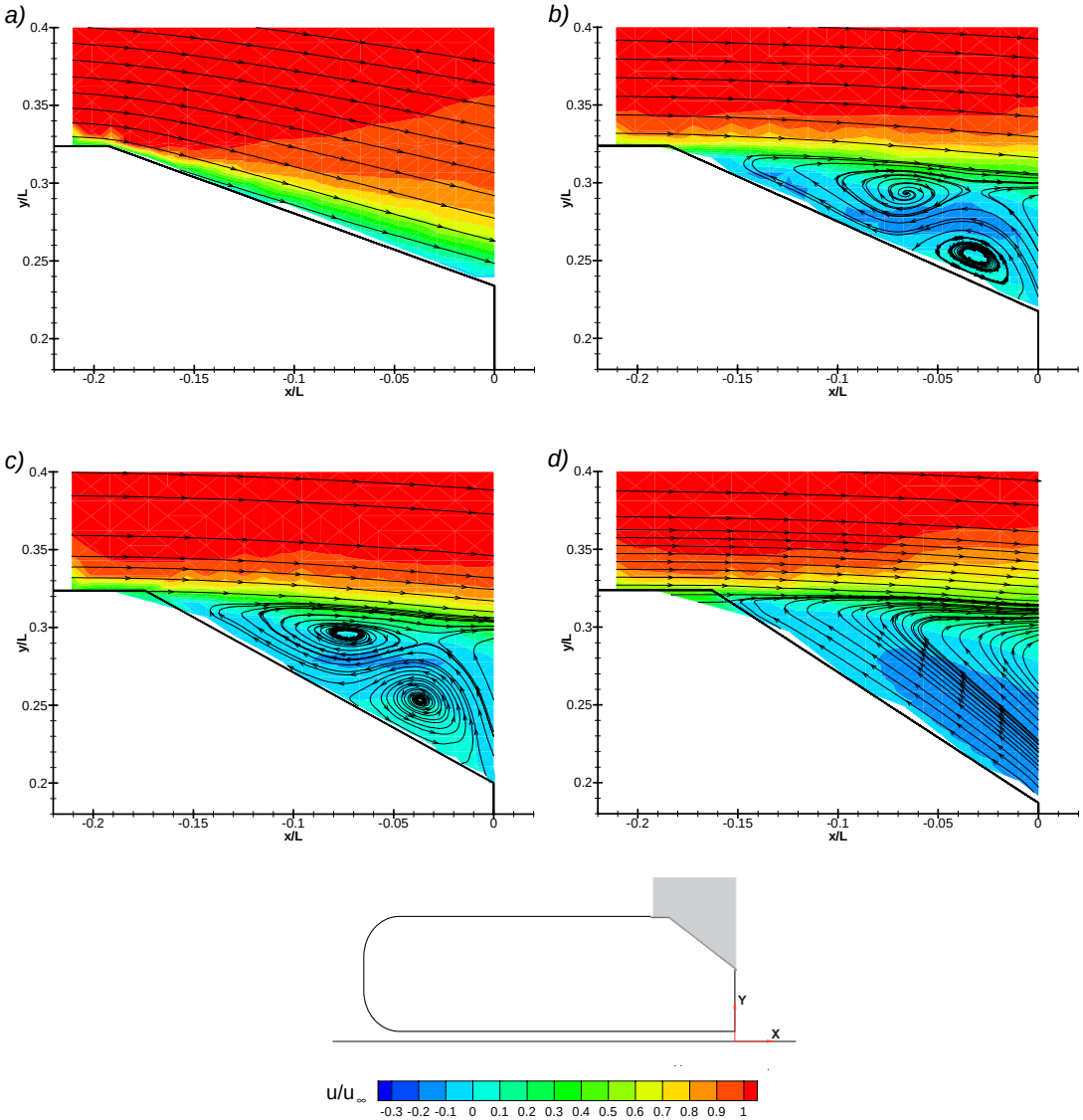

Figure 5.39 - Contours of normalised streamwise velocity and in-plane streamlines at z/L=0 for a)25° b)30° c)35° and d)40° back angles - CFD data

amalgamation of the upper region with the near wake separation bubble.

To further investigate the accuracy of the numerical prediction of the backlight flow, boundary layer profiles at three distinct positions over each model configuration are shown in Figure 5.40. As before all profiles are plotted as heights above the model (y_H), rather than in absolute values. Immediately apparent from the 0° plot (Figure 5.40 (a)) is that the streamwise velocity value to which the computational results converge in the region plotted is higher than its experimental counterpart. This is clearly due to the increased predicted velocity over the model (Figure 5.38) continuing downstream. This trend continues for all backlight angles, as would again be expected from previous analysis.

The 40° case (Figure 5.40 (h)) shows more variation between the two plotted boundary layers at the model trailing edge. The lower velocity of the numerical model is due to the absence of the additional circulatory regions formed over the backlight in the experiments.

The 25° boundary layer plot (Figure 5.40 (f)) shows the variations between the numerical results, current experimental results and those of Lienhart. Again the higher streamwise velocity can be seen in the numerical results, with Lienhart's data exhibiting higher velocities still. The magnitudes of these variations at the furthest upstream position plotted are clearly smaller between the numerical data and those of Lienhart, in comparison to the equivalent variations between the numerical data and the current experiments. The average variation between the numerical results and Lienhart's in this region is approximately $0.03u_\infty$, whereas the CFD differs from the current experiments by approximately $0.06u_\infty$. This trend is continued at the downstream positions, and again the numerical data converge to a higher streamwise velocity outside the boundary layer than the current experiments, owing to the increased flow velocity over the model. It must be assumed, therefore, that the numerical model more accurately represents the experiments without the overhead strut in this region. However, it has been shown in previous analysis that the formation and strength of the longitudinal vortices is the central factor in the model wake structure, particularly for backlight angles close to the 2nd critical angle (30°). To assess the accuracy of the numerical predictions of these vortices, plots of v velocity at the model trailing edge are shown in Figure 5.41. Experimental data have again been included for comparison.

From the 0° backlight it is immediately obvious that the numerical simulation does not predict the slight tendency of the flow to turn over the top of the model which was found in the current experiments. As the effects which cause this tendency in the angled backlight model configurations do not exist in the 0° case (due to the absence of backlight inclination), this discrepancy in the numerical prediction is not unexpected. In the cases where the flow is separated over the backlight, it can again be seen that the CFD does not predict any turning

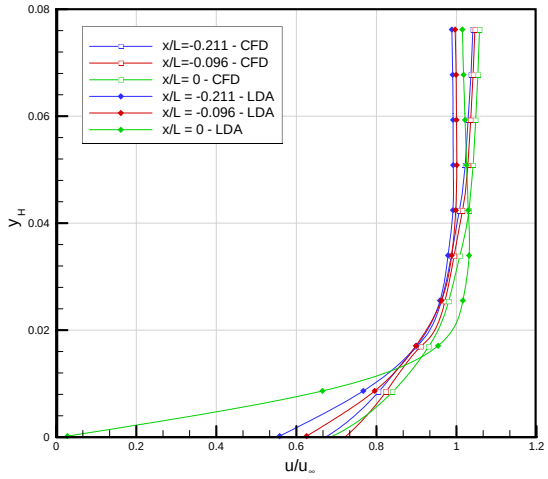

a) 0° backlight angle

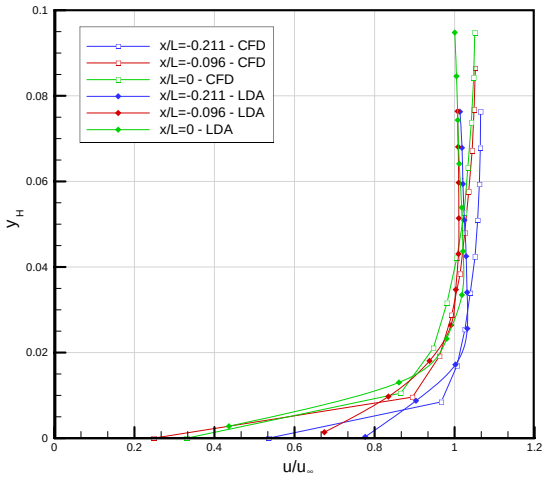

b) 5° backlight angle

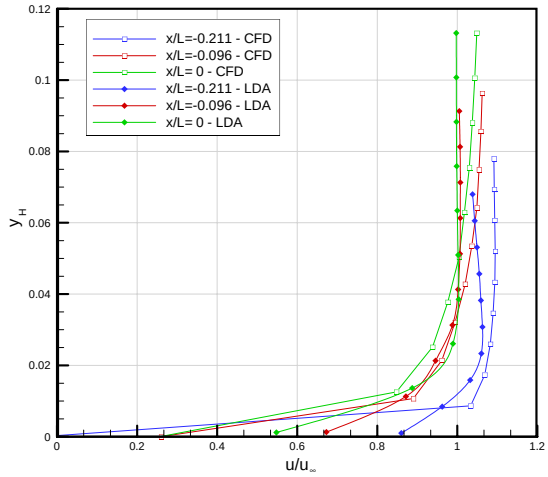

c) 10° backlight angle

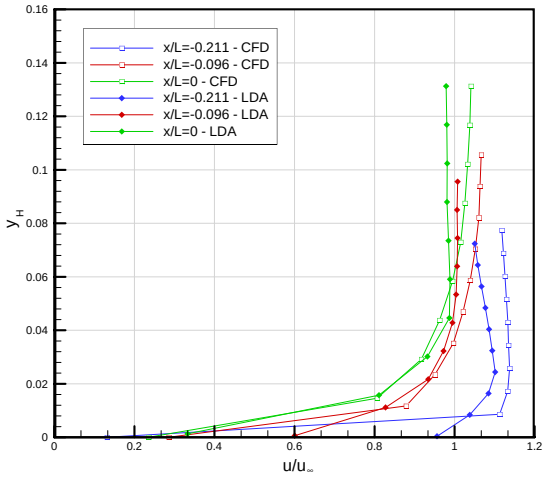

d) 15° backlight angle

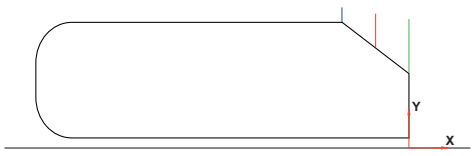

Figure 5.40 - Boundary layer profiles over Ahmed model backlights at z/L=-0.1 - experimental and computational data

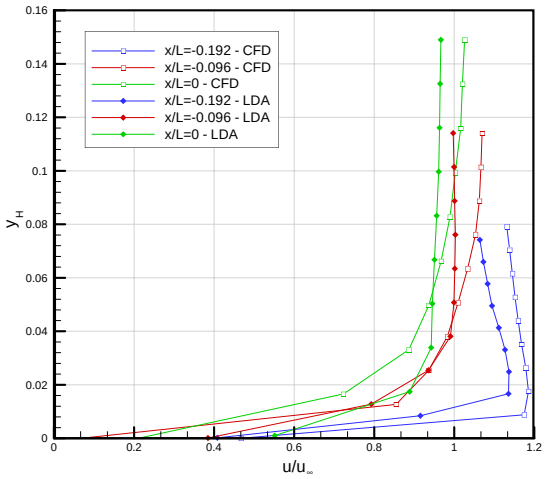

e) 20° backlight angle

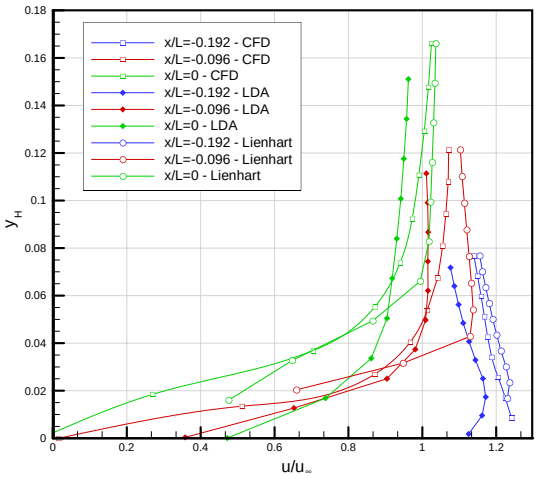

f) 25° backlight angle

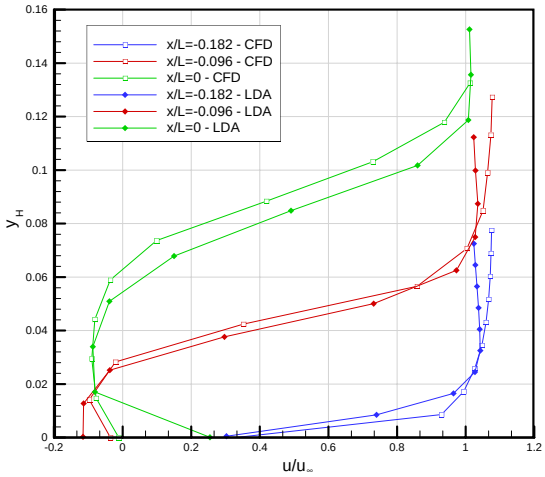

g) 30° backlight angle

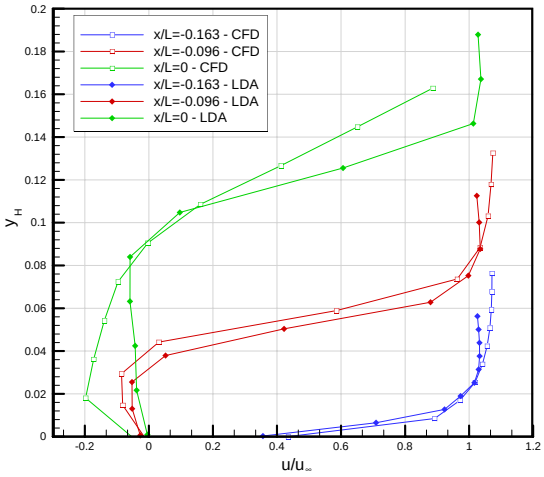

h) 35° backlight angle

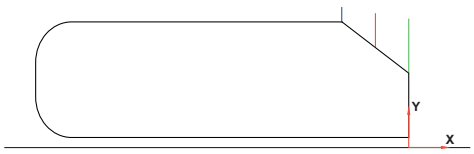

Figure 5.40 (cont) - Boundary layer profiles over Ahmed model backlights at z/L=-0.1 - experimental and computational data

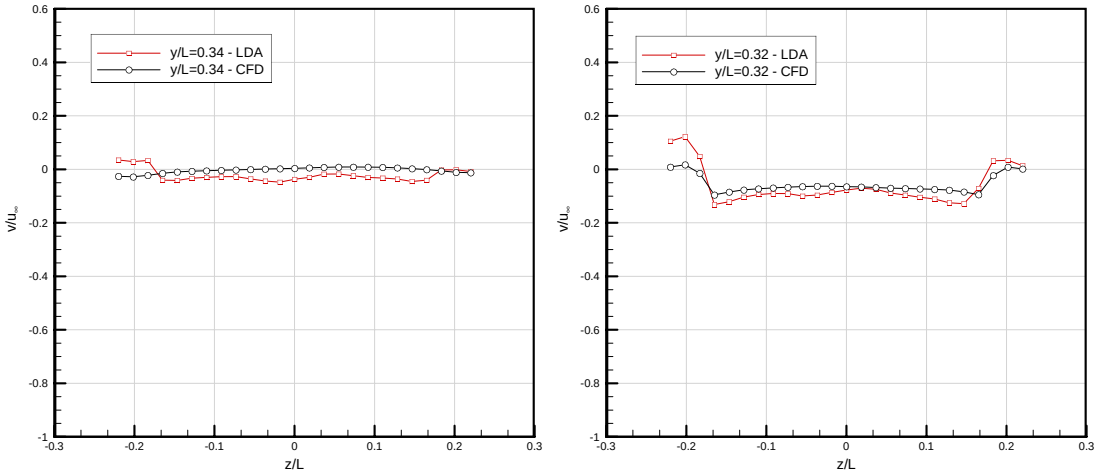

a) 0° backlight angle

b) 5° backlight angle

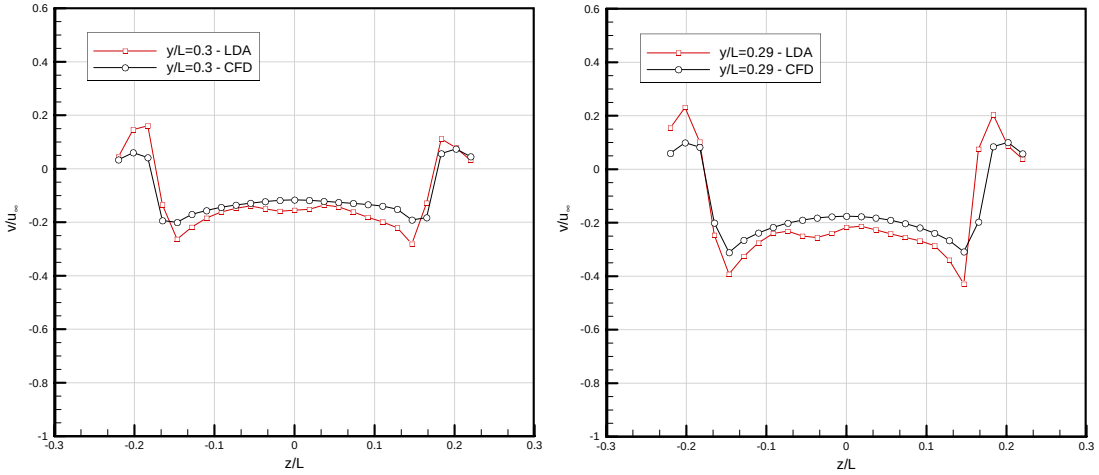

c) 10° backlight angle

d) 15° backlight angle

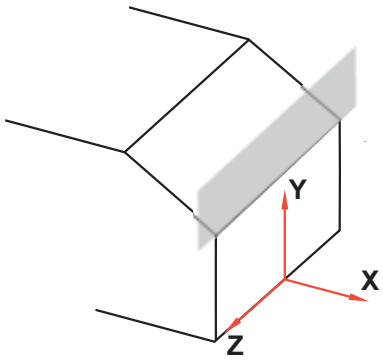

Figure 5.41 - Transverse profiles of normalised v velocity at model trailing edge for each backlight angle - experimental and computational data

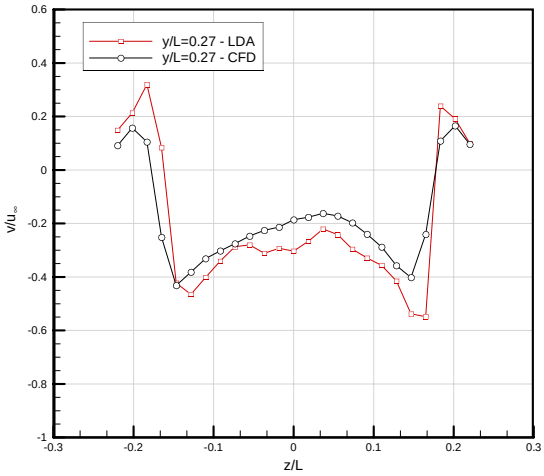

e) 20° backlight angle

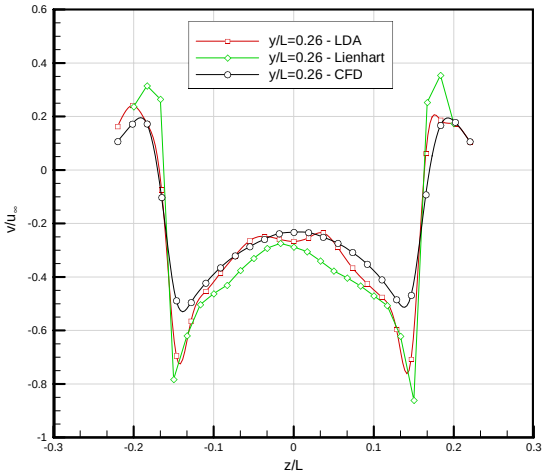

f) 25° backlight angle

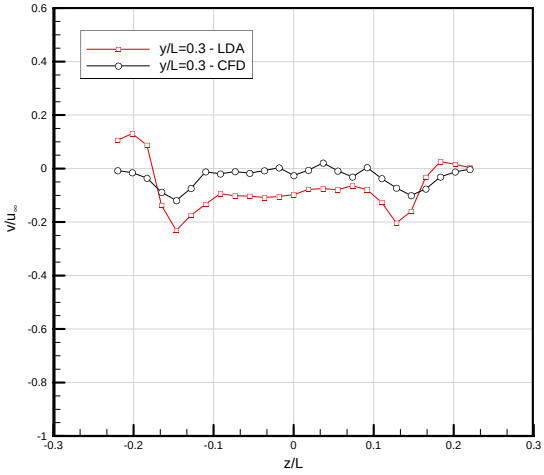

g) 30° backlight angle

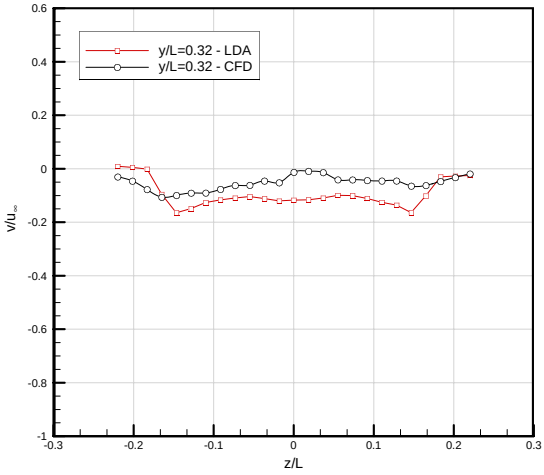

h) 40° backlight angle

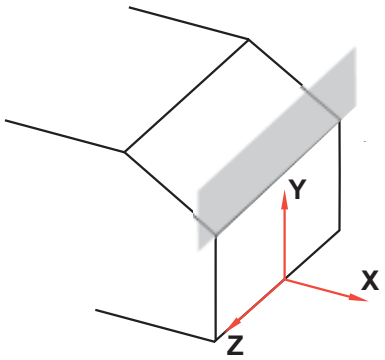

Figure 5.41 (cont) - Transverse profiles of normalised v velocity at model trailing edge for each backlight angle - experimental and computational data

of the flow over the top of the model, as no positive v velocities are evident in the region investigated.

For each other backlight, initial inspection shows that the CFD under-predicts the magnitude of both the maximum and minimum v velocities at the trailing edge, in comparison to the current experiments. The magnitude of the differences between both the maximum and minimum velocities is approximately equal for angles below 25°, rising from approximately $0.06U_{\infty}$ at 5° to approximately $0.11u_{\infty}$ at 20°. The 25° case, however, does not continue this trend. Instead it is found that the CFD under-predicts the maximum velocity by only around $0.02u_{\infty}$, but under-predicts the magnitude of minimum velocity by approximately $0.21u_{\infty}$. This appears to be a result of two factors. Firstly, the magnitude of maximum velocity measured in the current experiments actually drops between the 20° and 25° backlight angles, whereas

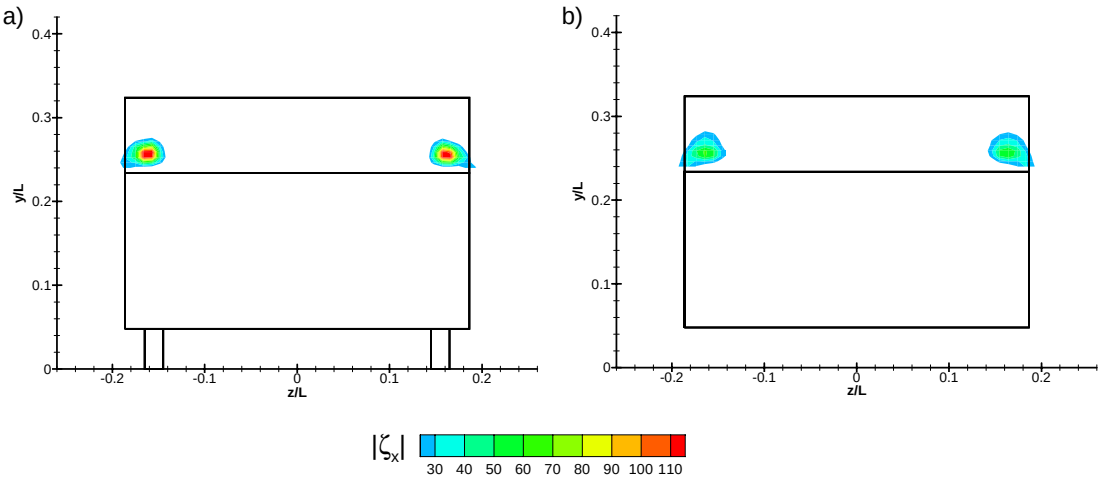

Figure 5.42 - Contours of vorticity magnitude about the streamwise axis at the 25° model trailing edge - (a) Lienhart and (b) current numerical data

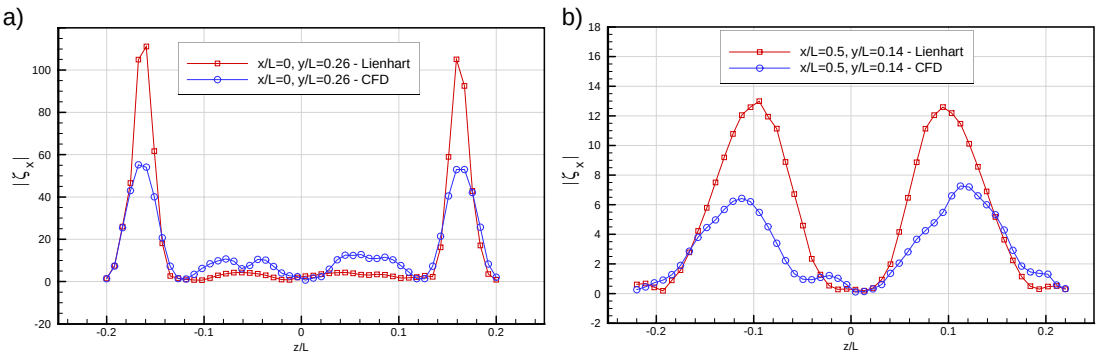

Figure 5.43 - Transverse profiles of vorticity magnitude about the streamwise axis at (a) x/L=0 (b) x/L=0.5 for the 25° backlight angle - comparison of current CFD with experiments of Lienhart

the CFD predicted a slight increase. As this computationally-predicted velocity was lower in the 20° CFD cases, at 25° the two values appear very similar. The drop in magnitude in the experiments is due to a large increase in vortex strength, which the CFD finds difficult to simulate. This suggests that the strength of the longitudinal vortices formed at this backlight angle is significantly under-predicted by the CFD. It is clear though from each of the plots that the prediction of the inboard position of the vortices at the model trailing edge is in good agreement with the experiments for all backlight angles.

It can also be seen from Figure 5.41 that for angles up to 25° the downwash predicted by the CFD follows experimentally-measured values to a similar accuracy to that found further outboard. It is evident, however, that the CFD does not predict the dip near the model centreline caused by the supporting strut. This agreement is continued in the 25° case, despite the variations in prediction of vortex structure.

In order to analyse further the extent to which the numerical model under-predicts the strength of the longitudinal vortices in the case of the 25° backlight, contours of vorticity about the streamwise axis are shown in Figure 5.42 for both the numerical model and Lienhart's experiments. For the sake of clarity contours beyond the given range are omitted. Initial inspection clearly shows the higher vorticity magnitude exhibited by Lienhart's data, an observation confirmed by the transverse profiles in Figure 5.43. It is clear from this that the vorticity measured by Lienhart in the vortex centre is in fact approximately double that of the numerical prediction. Vorticity data are also shown at 0.5L downstream of the trailing edge in Figure 5.43 (b). Again the approximate doubling of the maximum value between the numerical and experimental cases is evident.

Near Wake Flow

Figure 5.44 shows line integral convolution (LIC) plots produced from the model centreline in the near wake of each model configuration. Included also are the vortex centres and contours of 0 streamwise velocity for both the computational and current experimental cases to aid comparison. The corresponding LIC plots for the experimental cases were shown previously in Figure 5.21.

For backlight angles up to 20°, the numerical model predicts a shorter overall downstream length of the near wake separation bubble, evident from the boundaries of 0 streamwise velocities shown. It is also evident that in each of these three cases the upper vortex centres are predicted closer to the trailing edge than was measured experimentally, and that a lower vortex centre was evident in the numerical model for the 0° case. The latter was inconsistent with the experimental data, but low data rates caused difficulty with the 0° experimental plane (which is why no experimental upper vortex centre is marked).

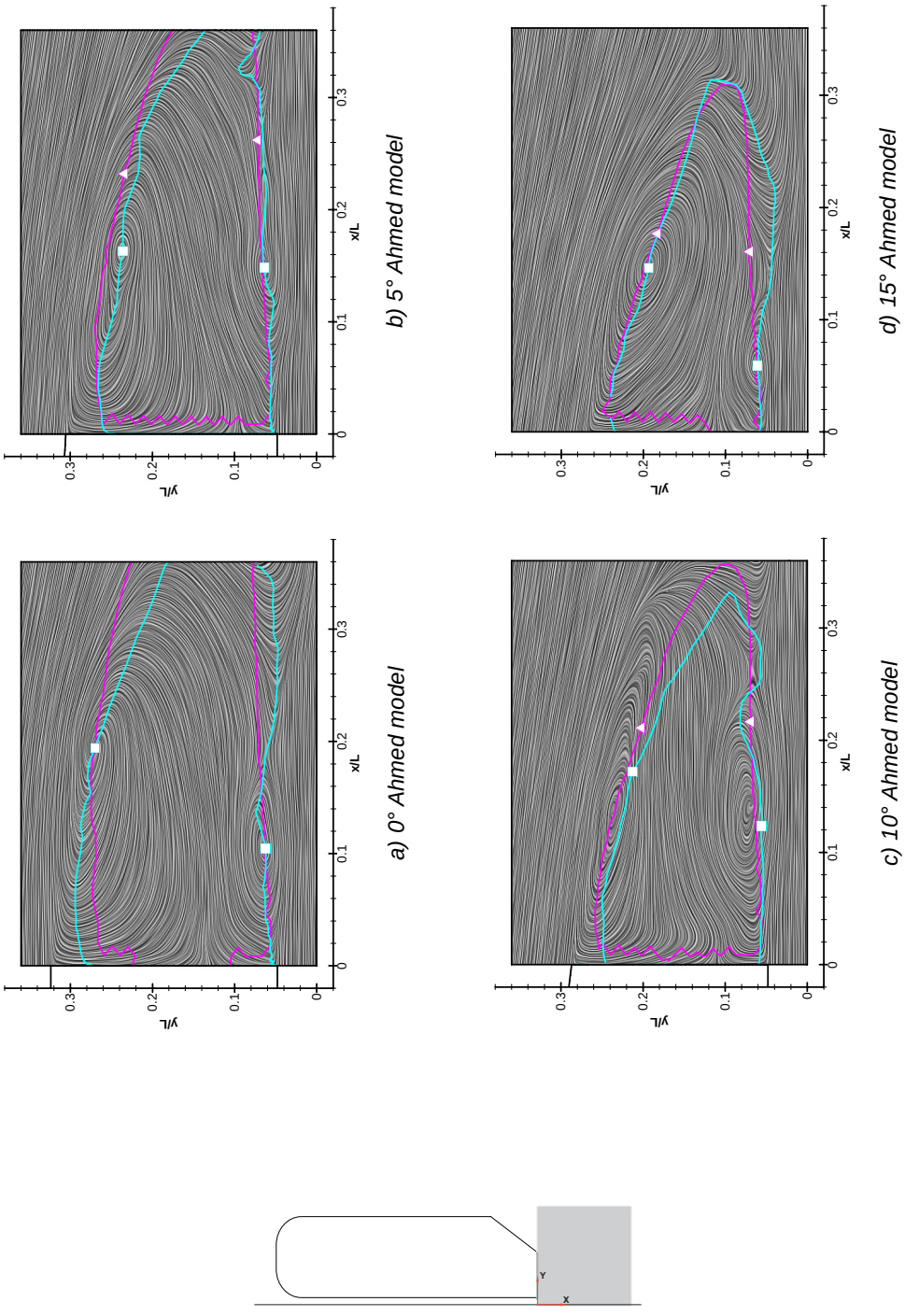

Figure 5.44 - Isolated Ahmed Model - Line Integral Convolution plots of CFD data on model centreline (z/L=0) behind model. Blue lines and squares mark CFD predicted contours of u=0 and vortex centres respectively; red lines and triangles mark experimentally-measured contours of u=0 and vortex centres respectively

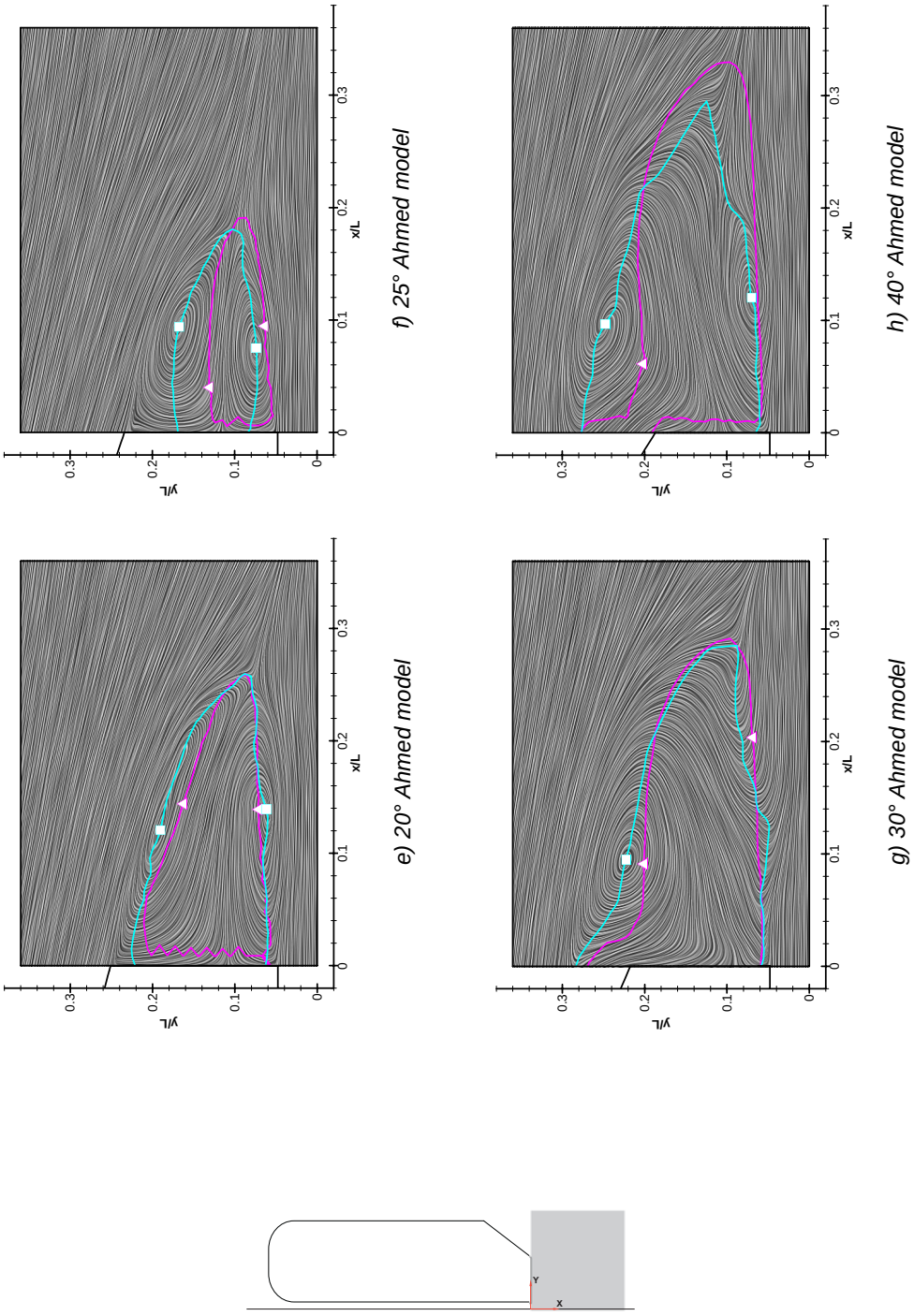

Figure 5.44 (cont) - Isolated Ahmed Model - Line Integral Convolution plots of CFD data on model centreline (z/L=0) behind model. Blue lines and squares mark CFD predicted contours of u=0 and vortex centres respectively; red lines and triangles mark experimentally-measured contours of u=0 and vortex centres respectively

The variation in structure of the upper vortex in the numerical model is very similar to that shown in the experimental data, up to α=20°. The increase downward deflection with increasing α of the flow shed from the top of the backlight forces this vortex to become smaller, and with its dominance over the separation bubble forcing the bubble's boundary to shift toward the trailing edge. The 20° case is particularly important in that, unlike the lower backlight angles, the upper vortex centre and 0 streamwise velocity line is actually predicted higher from the ground plane than was found experimentally. This appears to be an effect of the lower vortex strength in the numerical model creating less downwash over the centre section than in the experiments. This hypothesis is further strengthened by inspection of the 25° plot which shows that the separation bubble structure is significantly different from the experimental data. Again the lowered downward deflection of the flow causes the separation bubble to be predicted higher in the CFD model. This is again a result of the lowered vortex strength and subsequent downwash, with the larger discrepancies between the two cases for this backlight angle a result of the dominance of the longitudinal vortices on the overall wake structure at 25°.

From the plot for the 30° backlight it is clear that, aside from the absence of the lower vortex centre, the computational model again closely predicts the structure of the wake in the region investigated. It does appear that there is a lower numerically-predicted downward deflection of the flow at the model trailing edge, which accounts for the higher predicted position of the upper vortex centre. From comparison of Figures 5.10 and 5.39 it appears this reduced deflection is a result of a larger region of attached flow at the backlight leading edge in the experimental data. This suggests that where the flow is already separated at the trailing edge the numerical model can more accurately predict the wake formation than when the upper region is formed from the rolling up of the shear layer. As the lower vortex region in the near wake separation bubble is created by the rolled up shear layer for all backlight angles, this would account for the consistent computational prediction of the lower vortex centre closer to the trailing edge than was measured experimentally.

In the 40° case, despite the separated backlight flow, there are obvious discrepancies between the computational and numerical data. It was shown previously that the numerical model does not predict the two recirculatory regions over the backlight, causing the absence of a downward deflection of the flow evident in this plot, and the resulting relocation of the upper vortex centre.

Far Wake Flow

To investigate the numerically-predicted structure of the model wake at 0.5L and 1L downstream of the trailing edge, plots of u and v velocity data comparing the numerical and

experimental cases for the 10°, 25° and 40° backlight angles are shown in Figure 5.45. It was shown from previous analysis of experimental results that the longitudinal vortices generated have the greatest effect at 25°, with the corresponding vortices in the 10° case having a similar, but less dominant effect on the flow due to the lower vortex strength. As such, it would be expected that a result of the lower vortex strength predicted by the CFD at 25° backlight angle (in comparison to the corresponding experimental case) would be a wake structure more closely resembling that of the experimental 10° case. Furthering this hypothesis, the computational 10° case would be expected to predict a wake structure more closely resembling that of the experimental 40° case, where the tendency for the flow to turn over the backlight produces a smaller downwash than is found in the experimental 10° case. Finally, it was seen in Figure 5.41 that the 40° computational model predicts only a comparatively weak tendency of the flow to turn over the backlight in comparison to experimental data. Subsequently, the wake structure at 0.5L and 1L downstream would not be expected to exhibit a great deal of influence from it.

Examining Figure 5.45 it can be seen that the expected numerical flow structures have indeed been formed. For the 10° backlight the u velocity plot (Figure 5.45 (a)) shows a large variation at x/L=0.5 between CFD and experimental results, with a difference of approximately $0.2u_\infty$ near the model centreline. A result of the weaker longitudinal vortices formed upstream is that the downwash and subsequent forcing of freestream flow into the wake has fallen in comparison to the experimental data. Indeed, if the 10° y/L=0.15, x/L=0.5 CFD data is compared with the corresponding 40° experimental data (Figure 5.45 (e)), it can be seen that these two lines follow far more similar patterns, adding weight to the suggestion that these two cases would be expected to form similar wake structures. At 1L downstream the 10° experimental and numerical streamwise plots follow more similar structures, with a difference of around $0.1u_\infty$ now evident near the model centreline. The values of maximum and minimum streamwise velocities at this downstream distance for the numerical 10° case, however, are again closer to the corresponding experimental 40° data, being within $0.02u_\infty$ of each other.

Examination of the 10° v velocity plot in Figure 5.45 (b) again shows the lower downwash levels prevalent in the numerical model. As in the u velocity plot there is a large variation in velocity between the two 0.5L downstream cases of approximately $0.2u_\infty$ near the model centreline, which drops to approximately $0.1u_\infty$ at 1L downstream. In fact, comparison between the 10° numerical and 40° experimental cases here shows that the 40° case exhibits a minimum v velocity over double that of the 10° case. This despite the obvious larger downwash at the model trailing edge in the 10° case (Figure 5.41). Thus the numerical model both under predicts the strength of the longitudinal vortices in addition to the extent of their overall effect on the wake flow.

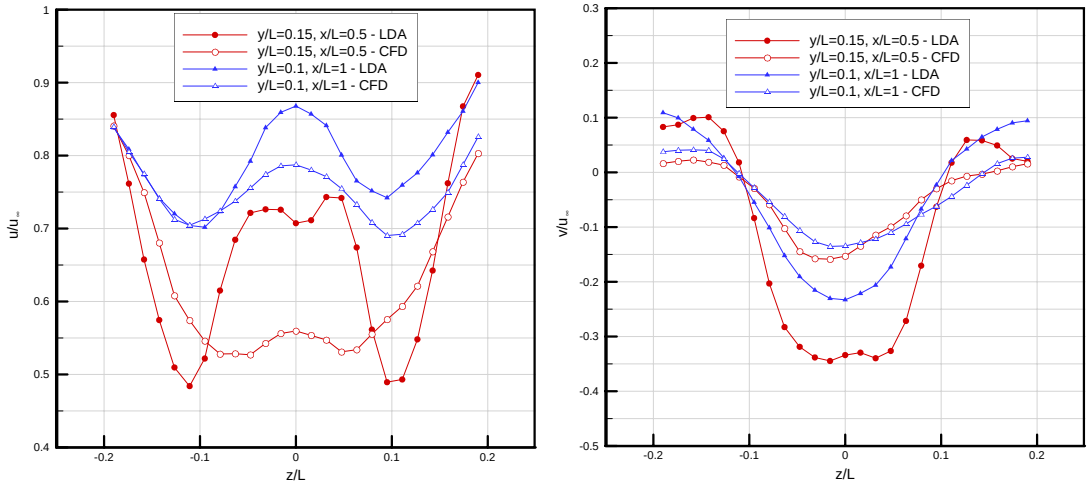

a) 10° backlight angle

b) 10° backlight angle

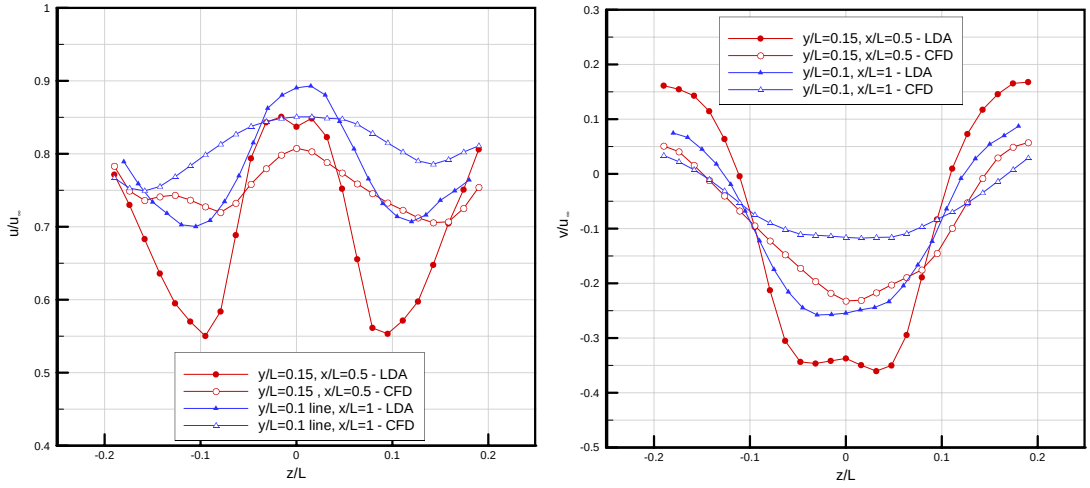

c) 25° backlight angle

d) 25° backlight angle

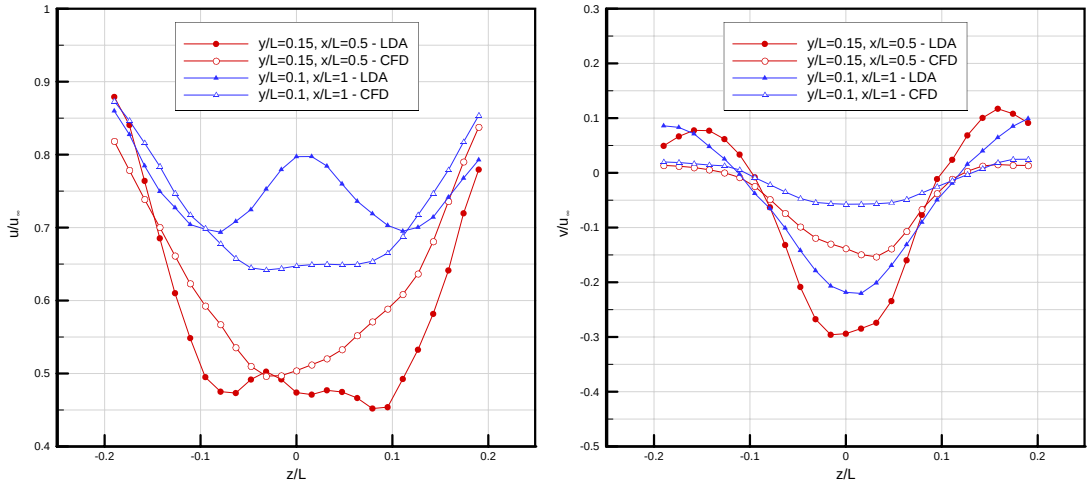

e) 40° backlight angle

f) 40° backlight angle

Figure 5.45 - Transverse profiles of normalised u and v velocity for two planes (x/L=0.5 and 1) behind the isolated Ahmed model for three backlight angles (10°, 25° and 40°) - comparison of current CFD and experimental data

The 25° u velocity plot (Figure 5.45 (c)) plot again shows a difference of approximately $0.15u_\infty$ between the numerical and experimental minimum velocities at 0.5L downstream. Noticeable too are the further outboard positions of the minimum velocities in the computational cases at both 0.5L and 1L downstream of the trailing edge, suggesting a reduced trend for the vortices to continue towards the model centreline. This is perhaps expected from the reduced tendency of the flow to turn from the model sides over the top of the model, causing a lowered velocity in the z direction. The 25° v velocity plot (Figure 5.45 (d)) continues the trend of lower numerically-predicted downwash, with maximum variations of $0.15u_\infty$ at both 0.5L and 1L downstream.

Inspection of the 40° u velocity plot (Figure 5.45 (e)) reveals a fairly uniform predicted velocity at 1L downstream between z=±0.05L. This is a result of the weaker predicted turning of the flow around the top of the model. Subsequently, there is no evidence of the increased downwash which can be seen in the experimental 40° data, and therefore a lower level of energised freestream flow being fed into the wake near the model centreline. There is in fact no numerically-predicted variation with z position in the tendency of freestream flow to enter the measured plane in either the 0.5L or 1L downstream positions. Therefore the increased downwash near the model edges, which can be seen in Figure 5.41, no longer has any effect on the wake by this position downstream.

It is clear, however, in all cases that despite the described variations between the numerical and computational results, all numerical cases do form the expected double vortex wake structure at these downstream positions. With the maximum and minimum v velocities in the 1L downstream 40° numerical case being separated by less than $0.1u_\infty$ though, it can be seen that these rotational structures are significantly weaker than their experimental counterparts.

5.2.2 Computational Force Results

Figure 5.46 plots the computational drag force results alongside previous and current experimental data. It is immediately apparent that the predicted drag value is significantly higher than all experimental values at most backlight angles, although the predicted variation of C_D with backlight angle does follow a similar trend to that measured both by Ahmed and in the current experiments. The difference between Ahmed's experiments and the computational C_D is approximately 0.15 between 0° and 10°, dropping slightly to 0.13 at 15°, and returns to a value of 0.15 until the prediction of separated backlight flow (at 30°). It was shown previously that the current experimental and numerical cases both exhibit separated flow over the 30° backlight, therefore recording only the low drag of the two 30° cases measured by Ahmed. Once the flow has separated the difference between Ahmed's data (using the low drag 30° case) case and the current numerical model is approximately 0.14 with the exception of the 40° case, where this variation drops again to its lowest recorded value of approximately 0.13.

From analysis of the relative contributions to the overall drag of the separate model sections it appears that the numerical simulation over-predicts the C_D on the front of the model by approximately 0.07 for each backlight angle, accounting for approximately half of the over prediction in overall C_D. This and further analysis of drag force predictions are taken from Ahmed's experiments, as individual model section contributions to the overall aerodynamic forces were not recorded during the current investigation.

The numerical model records only a small variation in front end drag with backlight angle, with the maximum variation between the cases being only around 5%. This is expected, due to the lack of interaction between the front and rear end flow patterns analysed previously. The over-prediction of the front end drag is a result of the turbulence model employed in the simulations. It has been shown previously that the k-ε turbulence model over-predicts the turbulent kinetic energy in the flow and subsequently turbulent viscosity near front stagnation points [Makowski and Kim, 2000]. This in turn creates an over-prediction of stagnation pressure, and as the Ahmed model has a comparatively large stagnation region the overall drag force prediction is significantly increased in comparison to experimental values as stated above.

A further increase in C_D between the current numerical and experimental data is found in the prediction of the overall model friction drag. This approximately accounts for a further 0.03 of the variation between the two cases. Thus, there remains a difference of between 0.03 and 0.05 (depending on backlight angle) between Ahmed's results and the numerical model due to the predicted pressure distribution over the backlight. Only limited experimental data are, however, available to ascertain the accuracy of the predictions of the backlight and model rear drag coefficients. From what data are available though, it appears that the remaining

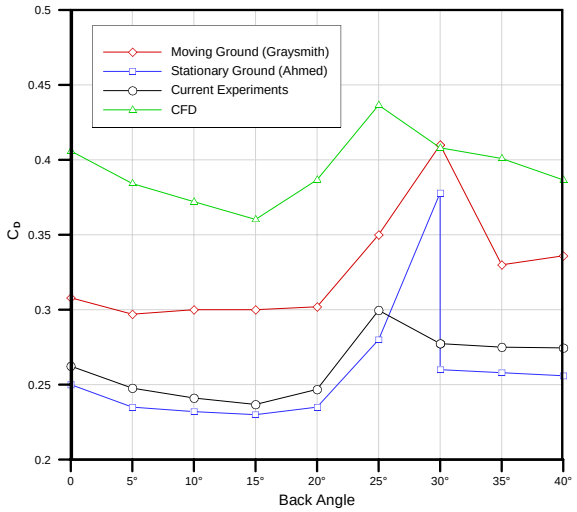

Figure 5.46 - Isolated Ahmed Model force results - CFD and experimental data

unaccounted-for variation in C_D is concentrated mainly on the prediction of pressure over the backlight itself.

It seems that the increase in vortex strength with increasing backlight angle occurs less rapidly in the numerical model, accounting for the smaller difference between the 15° numerical and Ahmed's experimental values in comparison to lower backlight angles. At this point the large increase in vortex strength and corresponding drop in pressure over the backlight is simulated by the CFD in accordance with the experiments.

For the 30° and 35° cases where the flow over the backlight has separated, the predicted backlight pressure is lower than was measured experimentally, causing the predicted increase in drag. The alteration to the backlight flow at 40°, which was discussed previously, causes a further drop in backlight pressure but increases the pressure on the model rear by more, causing the decrease in overall C_D shown in Figure 5.46. As this change in flow structure for the 40° backlight was not seen in either the current or previous experiments, the decrease in C_D is not consistent with them.

5.3 Summary of Isolated Model Results

The significant variations between the current and previous experimental results were found to be as follows.

i) There was found to be a weak interaction between the flow structure around the front and rear of the model, not obvious in previous experimental data.
ii) The overhead supporting strut has the expected effect of retarding the flow over the top of the model, and subsequently over the backlight.
iii) Weaker longitudinal vortices are subsequently formed over the 25° backlight in comparison to previous data.
iv) Two new circulatory regions are formed in the flow over the backlight at 30° and 40°, where the flow over the backlight is separated.

The current numerical model has been shown to provide accurate qualitative prediction of the flow structure in comparison to the current experiments, though the following quantitative variations were found.

i) The retardation of the flow over the model top and backlight was not reproduced owing to the absence of the overhead strut in the numerical model.
ii) No interaction was found between the front and rear end flows.
iii) Weaker vortices were formed over the backlight for each of the model geometries,

most noticeable for the 25° case.

iv) Subsequently the wake structure in each numerical case more closely resembled that of an experimental case where these vortices are less energetic, due to the significant effects they have on the wake flow.

v) The two new circulatory regions are evident in the 30° and 35° numerical cases, but not in the 40° case.

vi) The computational simulation over-predicts the overall drag coefficient on the Ahmed model for all configurations. A significant contribution to this is the over-prediction of the stagnation pressure on the model front caused by the k-ε turbulence model.

Owing to the predictable nature and consistency with varying model geometry of the differences between the numerical model and current experimental data, it is clear that so long as these discrepancies are accounted for the numerical model can be used to accurately assess the flow structure. It should, therefore, prove to be a useful tool during analysis of the wall proximity cases.

6. Near-Wall Model Experimental Results and Discussion

Near-wall investigations were conducted for three of the Ahmed model configurations, namely the 10°, 25° and 40° backlights. These were chosen owing to the fact that they cover the range of backlight flow structures outlined previously, namely two dimensional, three dimensional and separated flow cases. Computational near-wall analysis was also limited to these configurations, but encompassed a larger range of wall separations than were measured during the LDA experiments. Full experimental and computational test configuration data can be found in the Appendix A, and a schematic diagram outlining the four wall separations investigated experimentally is shown in Figure 6.1.

The following analysis is split into two distinct sections. In this chapter the experimental LDA and pressure measurements made around and downstream of the model will be analysed, comparing near-wall data to the corresponding isolated cases. From this the force changes experienced by the model when in wall proximity will be presented and discussed with reference to the analysed flow patterns.

Chapter 7 will then present and analyse the computational results. CFD data will be validated against experimental data, accounting for discrepancies outlined previously between the

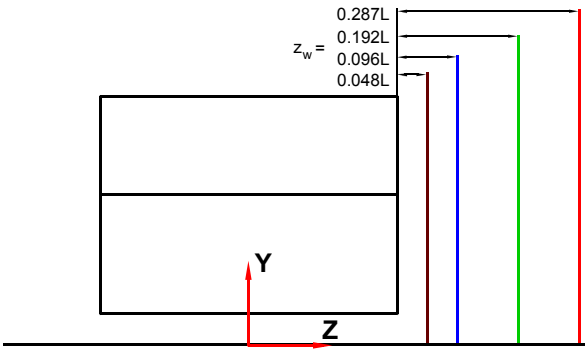

Figure 6.1 - Schematic diagram of Ahmed model outlining the four wall separations investigated experimentally

isolated model experiments and the CFD. Additional information will also be extracted from the computational model in order that additional flow features which could not be recorded by the experiments are analysed. This will include discussion of the prediction of pressure alterations with the inclusion of the side-wall on sections of the model which were not pressure tapped.

6.1 Time-Averaged Velocity Results

6.1.1 Front End

The analysis of the flow will, as before, begin upstream of the model leading edge and continue downstream. Figures 6.2 and 6.3 show vertical and streamwise profiles of u and v velocity at the model centreline (z/L=0) around the front end of the 25° Ahmed model at various wall separations. Although it has been shown during isolated model analysis that there exists a weak interaction between the front and rear ends of the Ahmed model, this effect was considered to be both of low magnitude and predictable in nature. It was therefore decided that, due to the limited testing schedule, the flow around the 10° and 40° model front ends would not be investigated experimentally.

It is apparent from both the u and v plot of Figure 6.2 that at this upstream distance there appears to be little alteration of the flow as a result of side wall inclusion. There does though exist a slight increase in the maximum recorded streamwise velocity measured as wall separation falls. The variation between the isolated and the z_w=0.048L cases is however only approximately 0.03u_∞, suggesting weak interaction between the wall separation and the flow at the plotted position, at least for the wall separations tested.

In Figure 6.3 the velocity profiles at y/L=0.025 above the model are shown. Measurements underneath the model are not included due to insufficient data rates in those positions during near-wall testing. Initial inspection of the u velocity plot reveals a large variation in maximum streamwise velocity with wall separation, in this case there being an increase of 0.1u_∞ between the isolated and z_w=0.048L cases. There is also an increase of 0.02u_∞ between wall separations of 0.287L and 0.192L, with a further increase of 0.05u_∞ between wall separations of 0.192L and 0.048L. Therefore the increase in suction over this section of the model appears to increase more rapidly as wall separation falls. This is confirmed by inspection of the v velocity plot of Figure 6.3 which also exhibits a comparatively large increase in maximum velocity between the isolated and nearest wall case (approximately 0.06u_∞, or 15%). It must also be noted that downstream of the suction peak an increase in streamwise velocity with decreasing wall separation is also evident, although the variation between the extreme cases has by the furthest downstream point measured fallen to approximately 0.05u_∞, around half

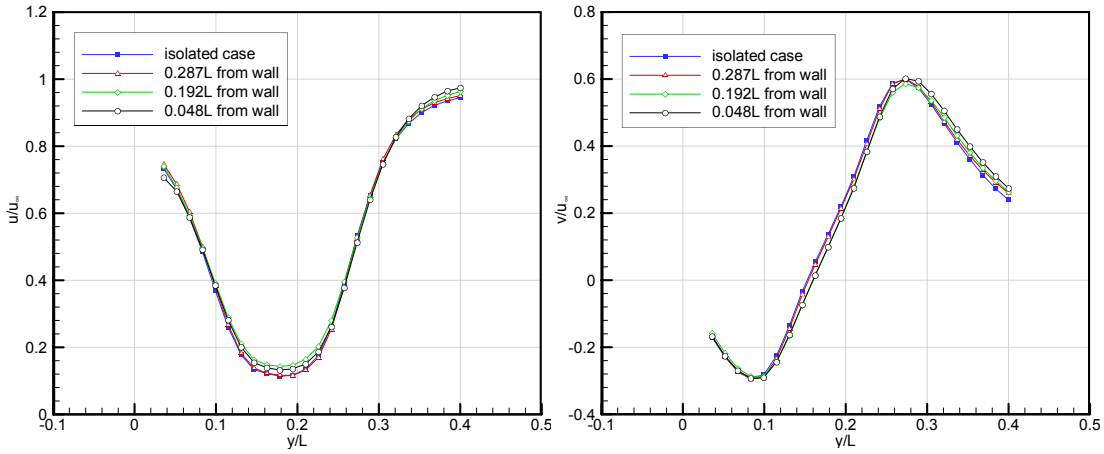

Figure 6.2 - Vertical profiles of normalised u and v velocity at x/L=-1.02 on the model centreline (z/L=0) around Ahmed model front end for 25° backlight angle at various wall separations

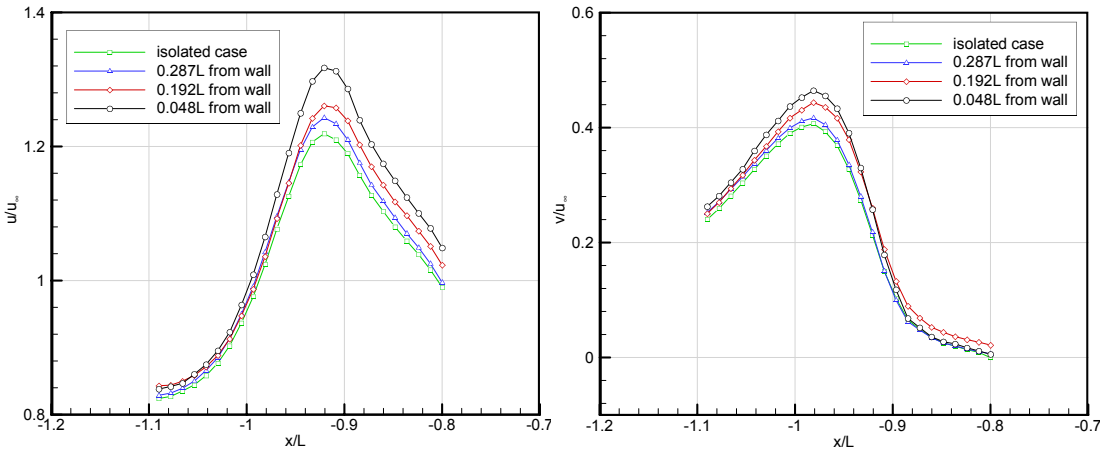

Figure 6.3 - Streamwise profiles of normalised u and v velocity at y/L=0.35 on the model centreline (z/L=0) around Ahmed model front end for 25° backlight angle at various wall separations

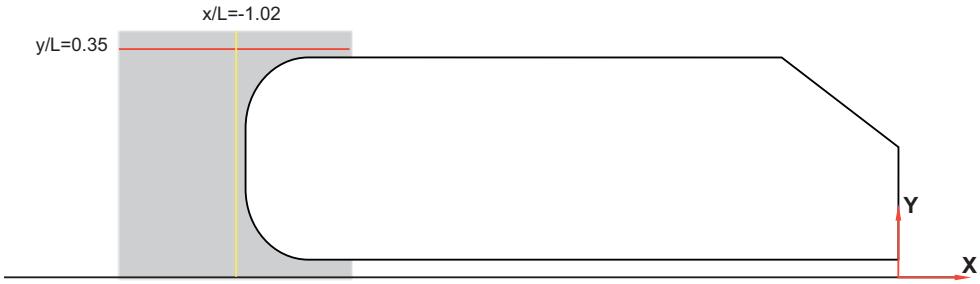

Figure 6.4 - Schematic diagram of model centreline plane investigated and positions of extracted data in Figures 5.2 - 5.4

the maximum value shown at the upstream suction peak.

Unlike the isolated cases presented previously, the inclusion of the side wall will produce asymmetric flow over the model. As such it would be expected that the evident increase in suction shown over the front end would be higher at positions closer to the wall, and vice versa. Data were not, however, taken away from the model centreline over the model front end and therefore this hypothesis cannot be confirmed by the available experimental data.

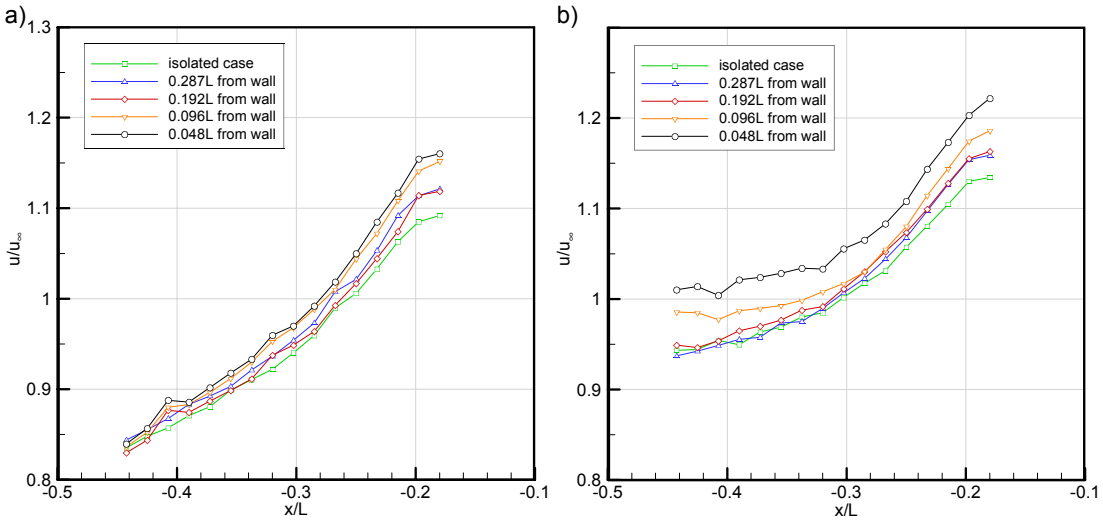

Figure 6.5 - Streamwise profiles of normalised u velocity at y/L=0.345, z/L= (a) 0 (b) -0.2 behind supporting strut on 25° backlight Ahmed model at various wall separations

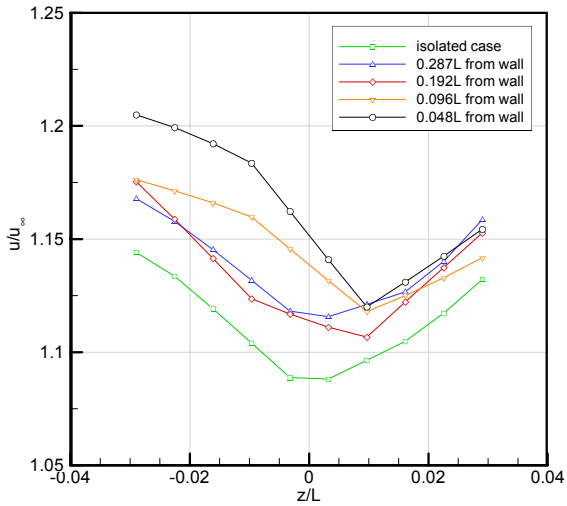

Figure 6.6 - Transverse profiles of normalised u velocity at y/L=0.345, x/L=-0.2 behind supporting strut on 25° backlight Ahmed model at various wall separations

6.1.2 Strut Wake

Shown in Figure 6.5 are streamwise profiles of u velocity close to the leading edge of the model backlight. As was the case for the model front end experiments, only the strut wake of the 25° backlight was tested experimentally. Figure 6.5 (a) plots the variation in streamwise velocity directly behind the centre of the strut (z/L=0). This shows that upstream of the backlight leading edge, there exists an increase in velocity with decreasing wall separation, with an increase of $0.07u_\infty$ (6.5%) between the isolated z_w=0.048L cases. Further inspection of the complete plane of data from which these line plots were extracted reveals that this increase appears not simply to be a result of the increased flow velocity over the top of the model with decreasing wall separation evident in Figure 6.3. At the furthest downstream position plotted in Figure 6.3 the variation in streamwise velocity between the extreme cases was found to be approximately $0.05u_\infty$, less than the variation shown in the model centreline (z/L=0) plot of Figure 6.5 (a). The additional recorded velocity appears to be a result of the lower pressure region formed between the wall and the model forcing the flow over the top of the model toward it, in addition to the lower pressure resulting from the expected higher velocity over the near-wall side top of the model. Subsequently, the largest retardation of the flow cause by the strut does not occur directly behind the strut in the z direction, but instead at an angle which is dependent on the wall separation (z_w). To investigate this effect further, Figure 6.5 (b) shows a streamwise velocity profile extracted at z/L=-0.02 (closer to the off-side). From the above reasoning it would be expected that a higher velocity would be found in the near-side cases, and indeed a variation of approximately $0.09u_\infty$ is found between the isolated z_w=0.048L cases just upstream of the backlight trailing edge. Due to the increased angle of the strut wake flow from the model centreline with decreasing wall separation, the wake has less effect on the off-side section of the model, resulting in this higher velocity. It is also shown that the variation between the isolated z_w=0.287L cases is approximately $0.025u_\infty$, with only a further $0.005u_\infty$ increase between the z_w=0.192L and 0.287L cases. There is then a $0.03u_\infty$ increase between the z_w=0.192L and 0.096L cases, with an additional $0.03u_\infty$ increase between the z_w=0.096L and 0.048L cases.

Figure 6.6 extends this analysis by plotting a transverse profile of streamwise velocity across the top of the model at x/L=-0.2, again upstream of the leading edge of the backlight. From this the alteration of the strut wake can clearly be seen by the relocation of the point of minimum streamwise velocity closer to the side wall. Despite the increasing suction the minimum u velocity position does not alter significantly between wall separations of 0.192L and 0.048L. The variations between the cases shown in Figure 6.6 close to the side wall are not unexpected as the effects of the relocation of the strut wake and the increased flow velocity over the top of the model will act in opposition, in contrast to the effects on the off-side. It will be recalled that the strut was previously shown to have a large effect on the formation of the longitudinal vortices formed over the backlight (particularly in the case of the

25° Ahmed model), and as such this alteration in its wake would be expected also to have significant effects on the backlight flow.

6.1.3 Backlight Flow

x-y planes

Shown in Figure 6.7 - 6.9 are contour plots of v velocity at various transverse positions over the 10°, 25° and 40° model near-wall cases. In-plane streamlines are also included in the 40° plots to illustrate better the alterations in flow structure from the isolated case. It is immediately apparent from the z/L=-0.14 25° model plots in Figure 6.7 (a)-(d) that there is an increase in magnitude of the minimum v velocity measured in this region as wall separation falls. There are two possible causes of this - either a movement of the off-side longitudinal vortex towards the centre of the model with falling wall separation, or an increase in the vortex strength. It has become clear from previous analysis that the pressure drop over sections of the model closest to the near-side forces flow towards this region, which it would be expected would force the off-side longitudinal vortex closer to the model centreline. It has also been shown that wall proximity raises the flow velocity over the model and therefore over the backlight, particularly in regions where the strut wake now has less effect. This would result in an increase in this vortex's strength. As these two factors would both produce the trend shown in Figure 6.7 (a)-(d), further investigation analysing the transverse planes taken over the backlight will be used to ascertain which has the greater bearing on the alteration of the flow.

In contrast to the large changes shown for z/L=-0.14 in Figures 6.7 (a)-(d) the corresponding plots for z/L=-0.077 (Figures 6.7 (e)-(h)) show less variation with wall separation. There is though again evidence of a slightly larger region of minimum v velocity, likely caused by increased downwash from the off-side longitudinal vortex in this region.

Continuing along the backlight towards the side wall, the z/L=0.077 plots of Figure 6.7 (i)-(l) exhibit the reverse effect from that seen in the z/L=-0.077 plots (Figures 6.7 (e)-(h)), with a decrease in size of the region of minimum v velocity as wall separation falls. This is likely to be a result of either a lower near-side longitudinal vortex strength, or a repositioning of the vortex to a position closer to the side wall and subsequently away from the plotted measurement plane.

From the z/L=0.14 plots of Figure 6.7 (m)-(p) it can be seen that these show the expected drop in v velocity magnitude between z_w=0.287L and 0.048L. This is a result of lower vortex strength predominantly caused by the tendency of the flow to continue towards the side wall, and therefore less tendency to turn over the backlight side edges. There is also the significant effect of the movement of the strut wake, causing additional retardation of the flow over the

near-side section of the backlight. This lowered velocity will again force less flow over the backlight edges, resulting in lower vortex strength. It is, however, also clear that this decrease in vortex strength is not nearly as well defined as the contrary trend in the z/L=-0.14 plots (Figures 6.7 (a)-(d)). As Figure 6.7 shows only streamwise slices along the backlight, and the vortex would be expected to shift position in the z direction as wall separation is changed, analysis of transverse planes across the backlight will be required to quantify the exact nature of the alterations in near-side longitudinal vortex structure. It is clear, however, that there exists an increase in the height of the minimum v velocity region as the model is moved closer to the wall. As before, this alteration in vortex structure will be analysed further with transverse planes of LDA data across the model backlight.

Figure 6.8 plots contours of v velocity at z/L=±0.14 for the 10° backlight. The 25° case was presented first as the vortices which affect the backlight flow are strongest in this case, and it is therefore anticipated that alterations in flow structure with varying wall separation at 25° would be similar to those at 10°, but would be of a higher magnitude and consequently more-readily detectable. It must be noted that the regions of positive v velocity shown at the model surface in some of the plots of Figure 6.8 are a result of reflection issues during acquisition of LDA data and not indicative of the actual flow velocity at those points.

Figure 6.8 mirrors the trends found in Figure 6.7, with an evident increase in the magnitude of the minimum v velocity with decreasing wall separation measured at the off-side position (z/L=-0.14), with the reverse effect at the near-side position (z/L=0.14). It is also again clear that there is an increase in the height of the minimum v velocity region at z/L=0.14 as the model is moved closer to the wall. It must be concluded therefore that despite the differences in flow structure between the 10° and 25° backlights analysed previously, the effects of wall proximity appear similar in the two cases. The data also suggest that alterations in backlight flow caused by wall proximity are primarily a result of alterations in the longitudinal vortices.

Figure 6.9 plots data taken for the near-wall 40° cases. Initial inspection reveals the two recirculatory regions found over the 40° backlight without the inclusion of a near side wall are still evident over the far-wall side of the model (z/L=-0.14), but not over the near-side (z/L=0.14). There is again an evident increase in the magnitude of the minimum v velocity on the off-side, a result of similar mechanisms as in the previous cases. The reverse is also again true for the near-side, with the result being an increase in v velocity near the trailing edge. This drop in downward velocity appears to result in the upper recirculatory region no longer forming over this section of the backlight. Indeed, with the increase in downward velocity as wall separation falls evident over the off-side of the model backlight, it is clear this region becomes more distinct from the upper circulatory region formed in the separation bubble downstream of the trailing edge. The centre of the upper vortex over the backlight moves upstream from

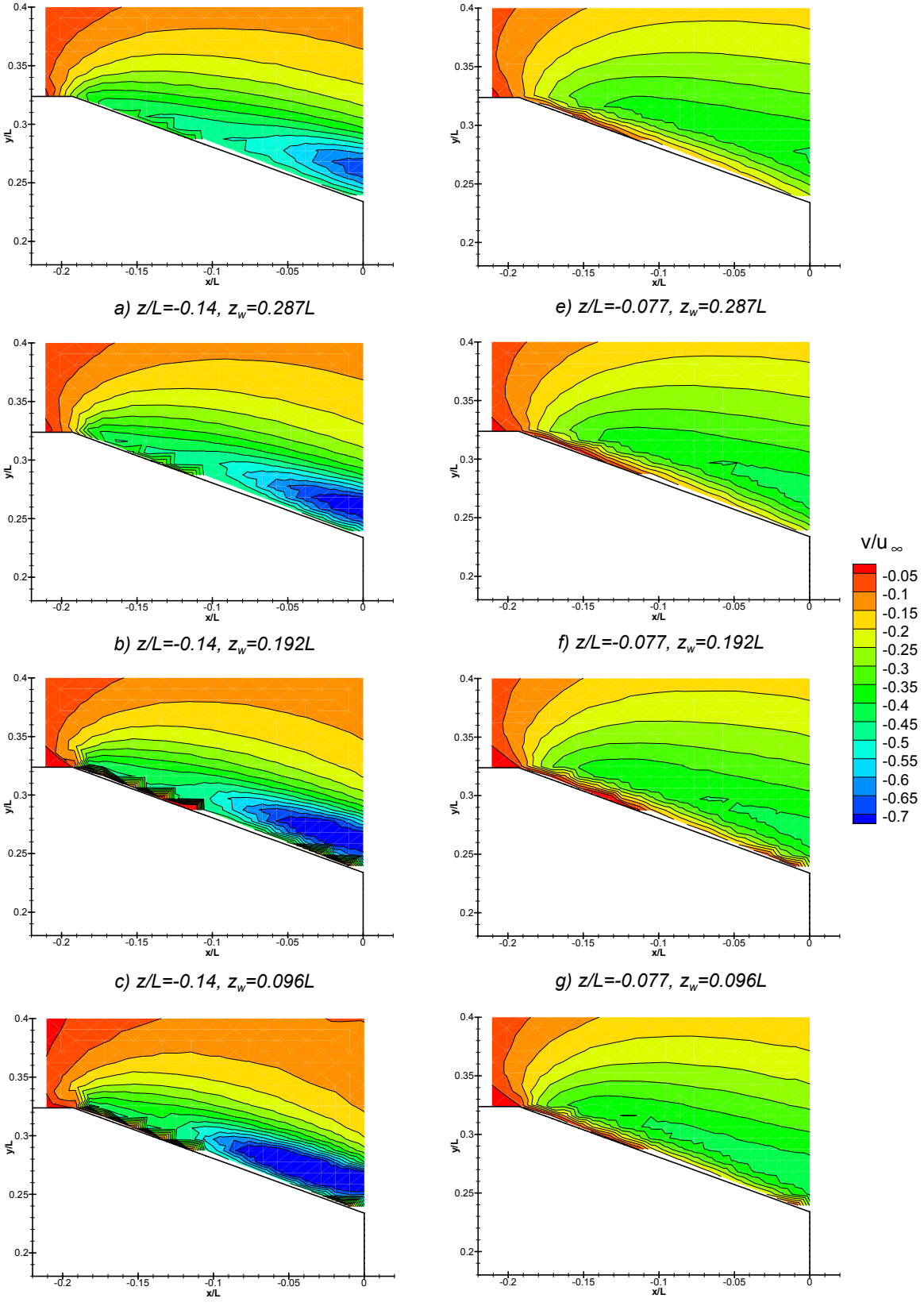

a) z/L=-0.14, z_w=0.287L

e) z/L=-0.077, z_w=0.287L

b) z/L=-0.14, z_w=0.192L

f) z/L=-0.077, z_w=0.192L

c) z/L=-0.14, z_w=0.096L

g) z/L=-0.077, z_w=0.096L

d) z/L=-0.14, z_w=0.048L

h) z/L=-0.077, z_w=0.048L

Figure 6.7 - Contour plots of normalised v velocity over backlight of 25° Ahmed model at various wall separations

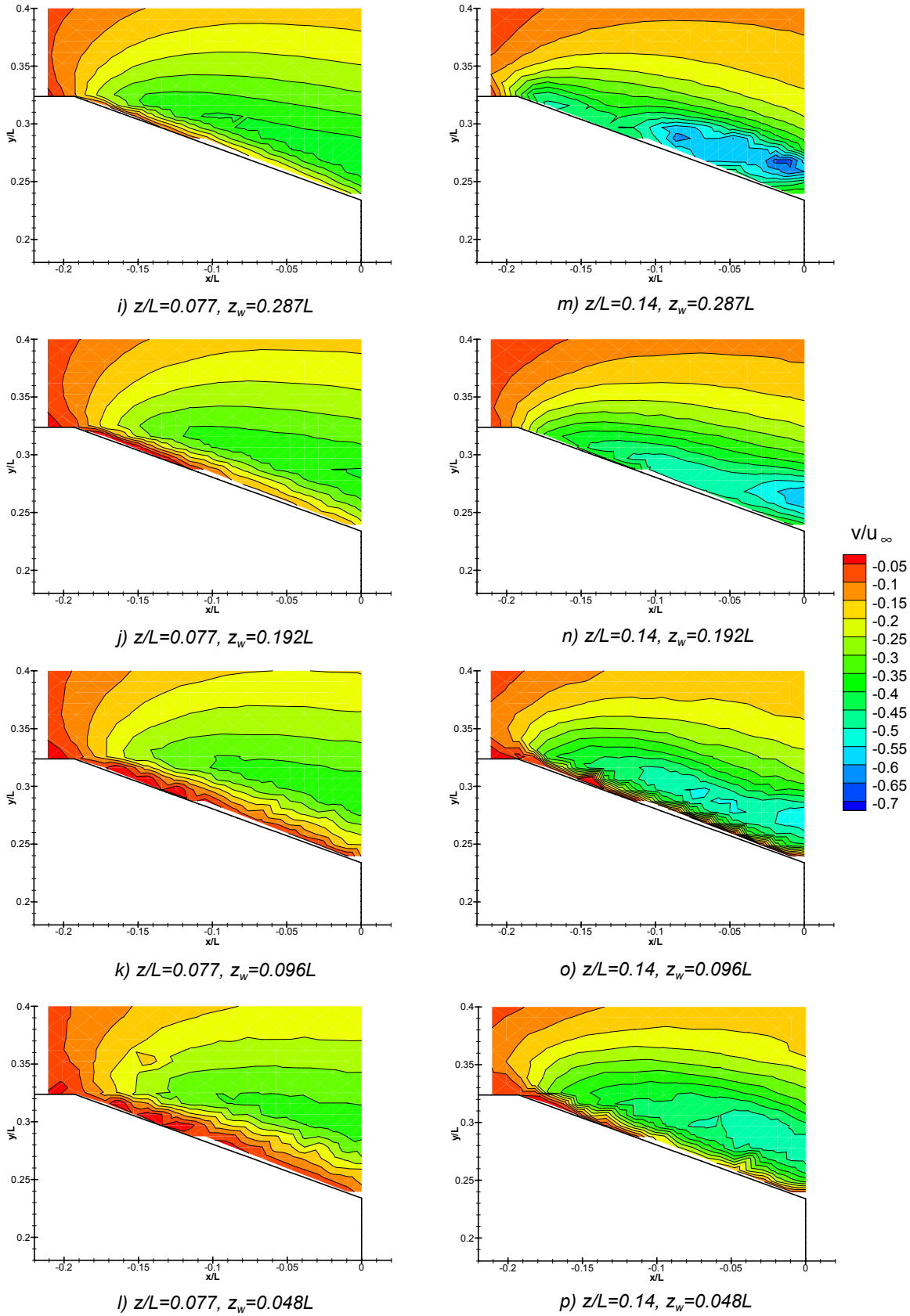

i) z/L=0.077, z_w=0.287L

m) z/L=0.14, z_w=0.287L

j) z/L=0.077, z_w=0.192L

n) z/L=0.14, z_w=0.192L

k) z/L=0.077, z_w=0.096L

o) z/L=0.14, z_w=0.096L

l) z/L=0.077, z_w=0.048L

p) z/L=0.14, z_w=0.048L

Figure 6.7 (cont) - Contour plots of normalised v velocity over backlight of 25° Ahmed model at various wall separations

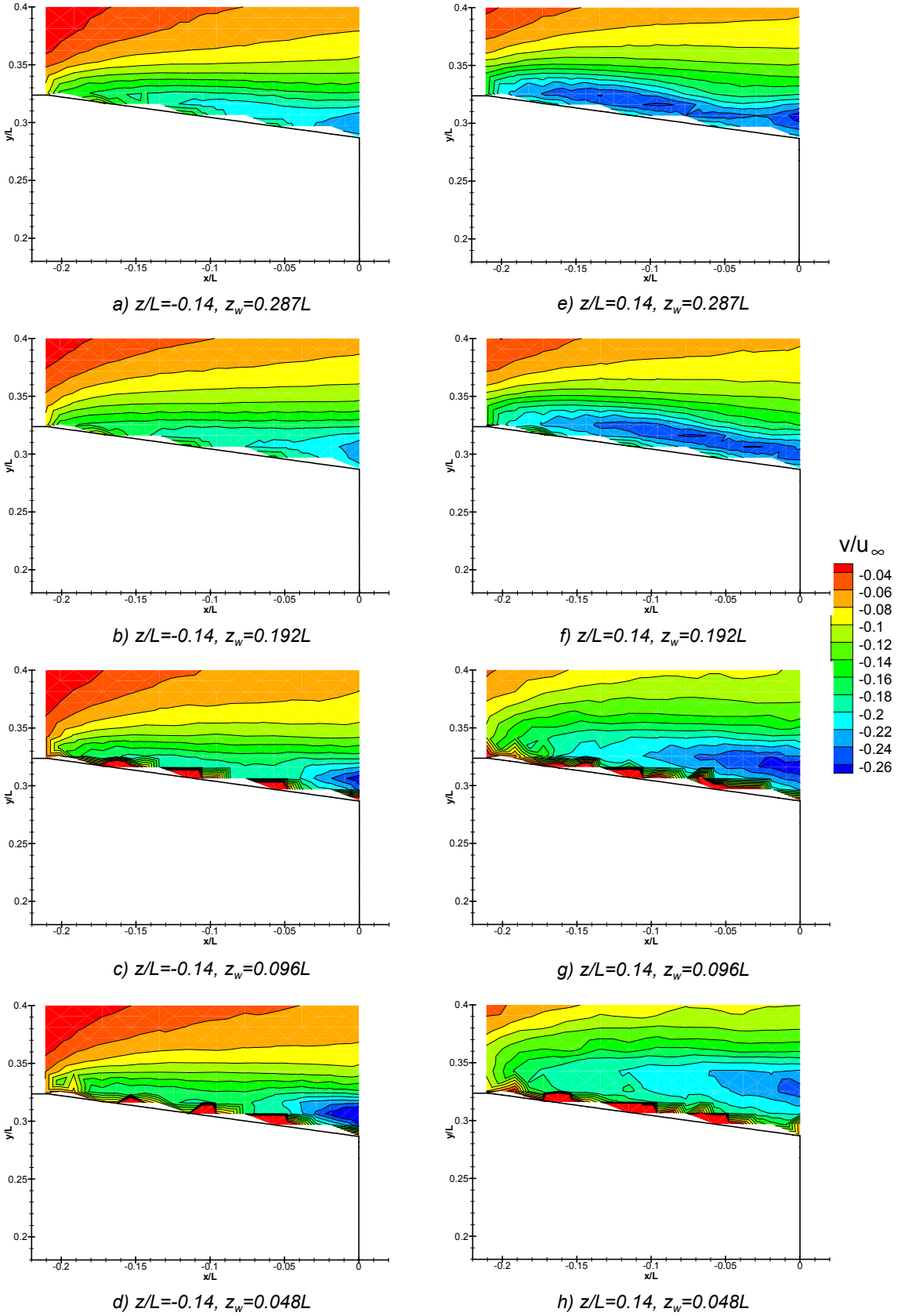

a) z/L=-0.14, z_w=0.287L

e) z/L=0.14, z_w=0.287L

b) z/L=-0.14, z_w=0.192L

f) z/L=0.14, z_w=0.192L

c) z/L=-0.14, z_w=0.096L

g) z/L=0.14, z_w=0.096L

d) z/L=-0.14, z_w=0.048L

h) z/L=0.14, z_w=0.048L

Figure 6.8 - Contour plots of normalised v velocity over backlight of 10° Ahmed model at various wall separations

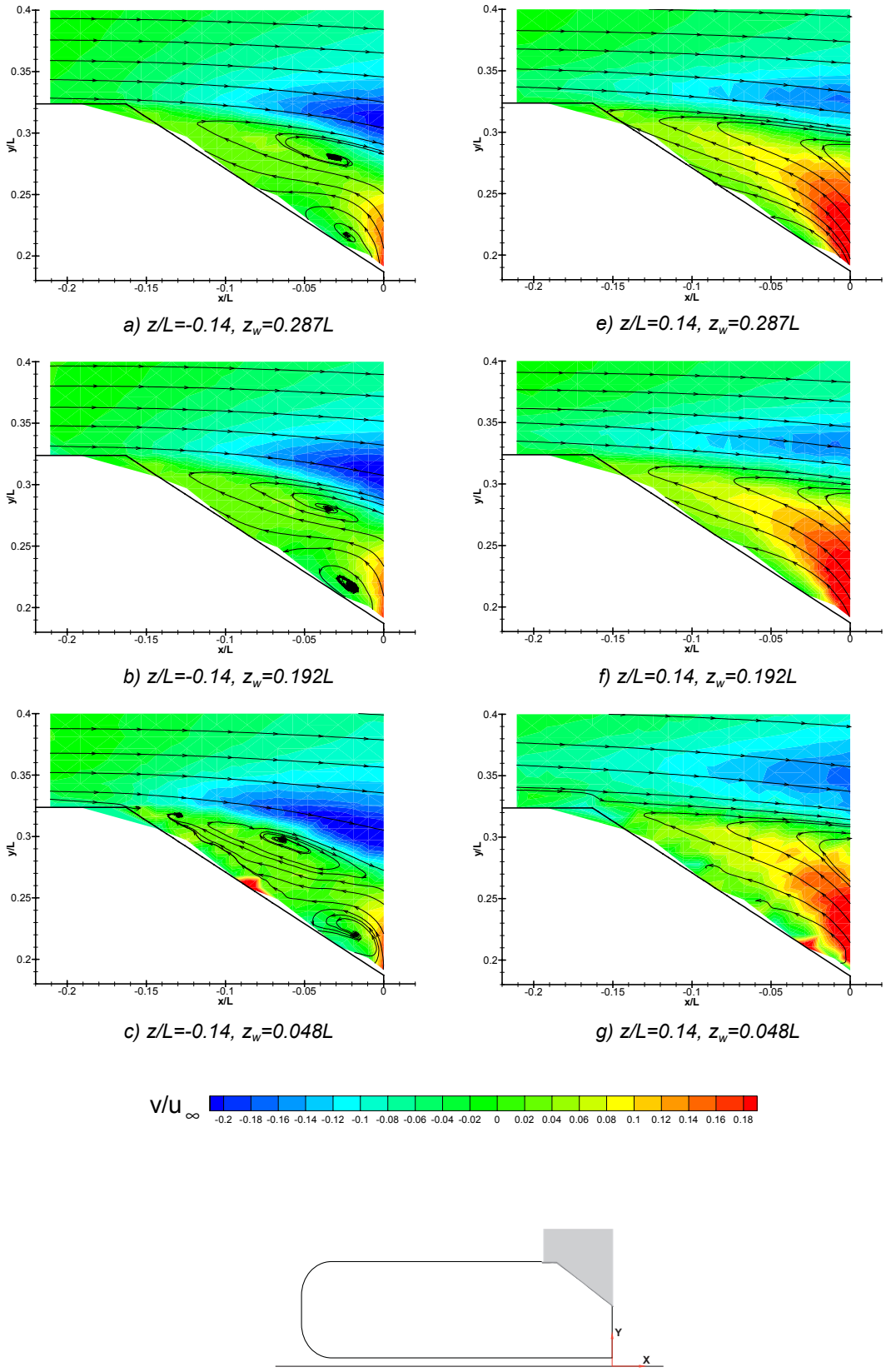

Figure 6.9 - Contour plots of normalised v velocity over backlight of 40° Ahmed model at various wall separations

x/L=-0.031 to x/L=-0.064 as wall separation falls from 0.287L to 0.048L. Over the near-wall section (z/L=0.14), this upper region has merged with the near-wake separation bubble, and therefore no evidence of either it or its lower counterpart is found.

From Figures 6.7 - 6.9 it can be seen that in both the 10° and 25° backlight cases there appears to be an increase in longitudinal vortex strength with decreasing wall separation on the off-side of the model, with the reverse effect on the near-side. There is also a corresponding increase and decrease of the tendency of the flow to turn around the respective side edges of the backlight in the 40° backlight case. From a point of view of the pressures on the model, the increased vortex strength on the off-side would be expected to reduce the pressure on the model in that area, with again the opposite effect on the near-side. Owing to the higher velocity over the model top which was shown previously, at the nearest measured wall separations this increased velocity would be expected to cause an overall pressure drop over the whole backlight, with the exception of the near-side vortex region. Investigation of the static pressure distribution over the backlight, necessary to ascertain which of these expected pressure changes is most dominant in terms of overall aerodynamic force contributions, will be presented in a subsequent section.

The greater downwash over the off-side of the backlight will also be expected to have a significant effect downstream of the trailing edge. It was shown during isolated model analysis that the longitudinal vortices determined to a large extent the formation of the wake flow. The above variations in vortex structure would therefore be expected to cause significant asymmetry in the wake flow. A larger region of high energy freestream flow would be forced into the wake on the off-side of the model in comparison to the isolated case, as a result of the higher vortex strength.

The effects of wall separation on the boundary layer slightly away from the model centreline (z/L=±0.077) for the 25° and 10° backlights are shown in Figures 6.10 -6.13. Again the 25° case will be analysed first as the effects on the boundary layer caused by variations in longitudinal vortex strength would be expected to be similar between the 10° and 25° cases, but should be more easily detectable in the 25° case.

Initial inspection of Figures 6.10 and 6.11 reveals an increase in maximum streamwise velocity with decreasing wall separation at the backlight leading edge at both off-side (z/L=-0.077, Figure 6.9) and near-side (z/L=+0.077, Figure 6.11) positions. It has been shown that the wake from the strut is moved toward the side wall, causing a larger velocity deficit in this area, but it was also stated that there is an increase in streamwise velocity over the near-side of the model top owing to its proximity to the side wall. It appears from the boundary layer profiles shown that the latter of these effects has the greater effect on the streamwise velocity

at the plotted positions. Indeed, the maximum streamwise velocity measured at the near-side position (z/L=0.077) increases from $1.18u_\infty$ in the isolated case to $1.25u_\infty$ at 0.048L from the wall. A similar variation (to within $0.005u_\infty$) is also found at the off-side (z/L=-0.077). It must be concluded, therefore, that the increased influence of the strut wake closer to the side wall is approximately equal and opposite to the effect of the increased flow velocity over the near-side of the model top, in comparison to the expected smaller velocity increase over the off-side at the plotted positions. It was, however, shown in Figure 6.5 that further from the model centreline (at z/L=-0.02) there is a larger variation of $0.9u_\infty$ between the isolated and z_w=0.048L cases just upstream of the backlight leading edge. At z/L=-0.077, as is shown in Figure 6.10, it seems that there are still significant strut wake effects even at this off-side position and at 0.048L wall separation. This would account for the lower velocity increase measured in comparison to the previous data taken further from the side-wall.

It can also be seen from Figure 6.11 that as wall separation falls the thickness of the boundary layer on the near-wall side experiences a significant increase. This is an expected result of the lowered longitudinal vortex strength on this side of the model, as the vortices inhibit the formation of the boundary layer close to the model side edges. The smaller (in comparison to the isolated case) near-side vortices have also been shown to be positioned higher from the model surface, and will therefore have still less effect on the boundary layer than in the case of the isolated model. As the effects of the vortices are greatest near to the trailing edge of the model, analysis of the boundary layer thickness will be restricted to the trailing-edge plots of Figures 6.9 and 6.10. Taking $u_{\infty 1}$ to be the streamwise velocity at the highest recorded point in the trailing edge plots, it is found that the height above the model at which the flow recovers to $0.9u_{\infty 1}$ on the near-wall side (z/L=0.077) increases from 0.024L in the isolated case to 0.051L at the nearest recorded wall position (0.048L). There is also a decrease in boundary layer thickness (following the same rationale) on the off-side section of 0.012L, less than half the variation found over the near-wall side. This suggests that the drop in near-wall vortex strength is greater in magnitude than the increase in the off-side longitudinal vortex strength at this distance from the side-wall.

Figures 6.12 and 6.13 mirror the findings of the 25° backlight. There exists an increase in maximum streamwise velocity over the backlight leading edge of approximately $0.065u_\infty$ between the isolated and nearest wall case at both near-side and off-side positions. This is slightly less then the corresponding increase measured in the 25° case, but it is again approximately equal (within 2.5%) at 0.077L either side of the model centreline.

There is, as in the 25° case, also an apparent increase in boundary layer thickness with decreasing wall separation at the near-wall position in the 10° backlight case (Figure 6.12). As would be expected this variation is of lower magnitude than that measured on the 25°

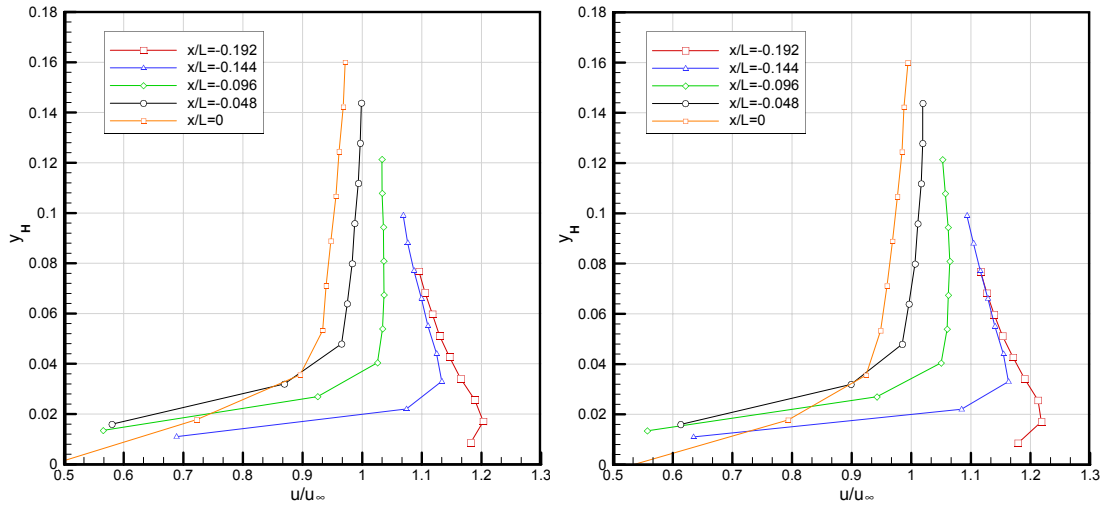

a) z_w=0.287L

b) z_w=0.192L

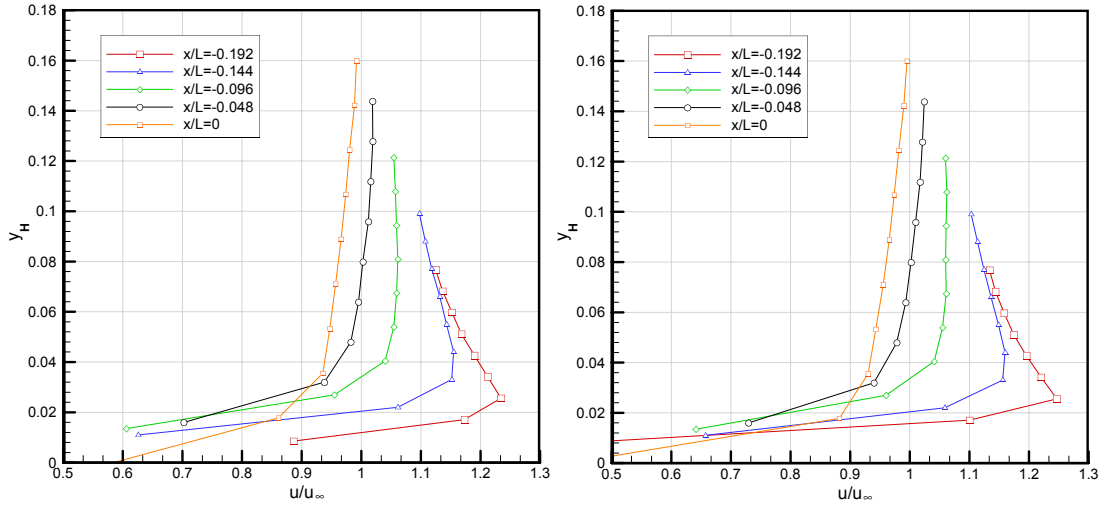

c) z_w=0.096L

d) z_w=0.048L

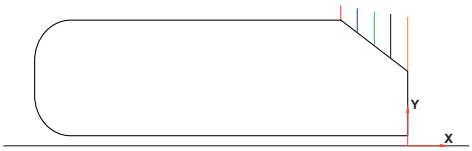

Figure 6.10 - Boundary layer profiles over 25° Ahmed model backlight at various wall separations for z/L=-0.077

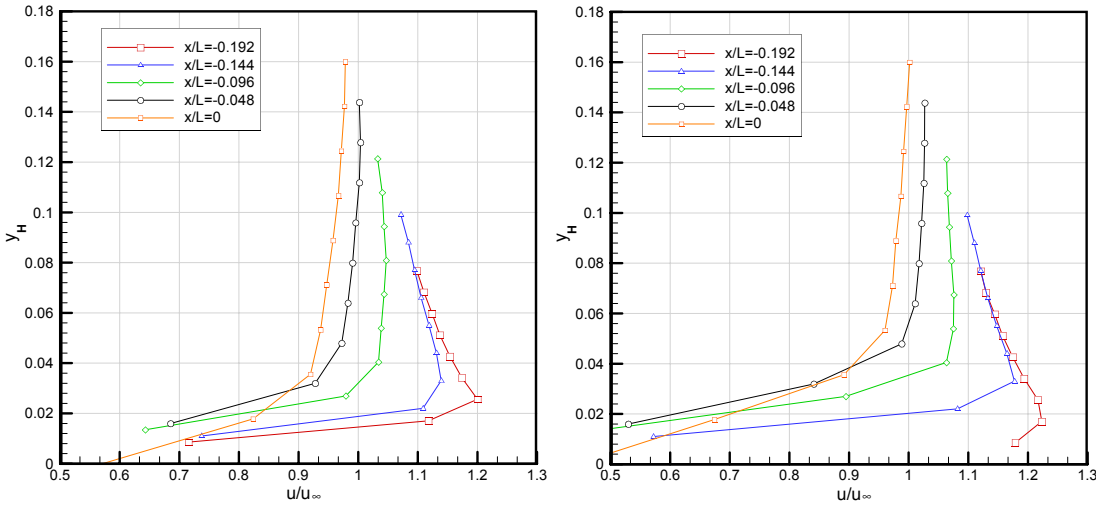

a) z_w=0.287L

b) z_w=0.192L

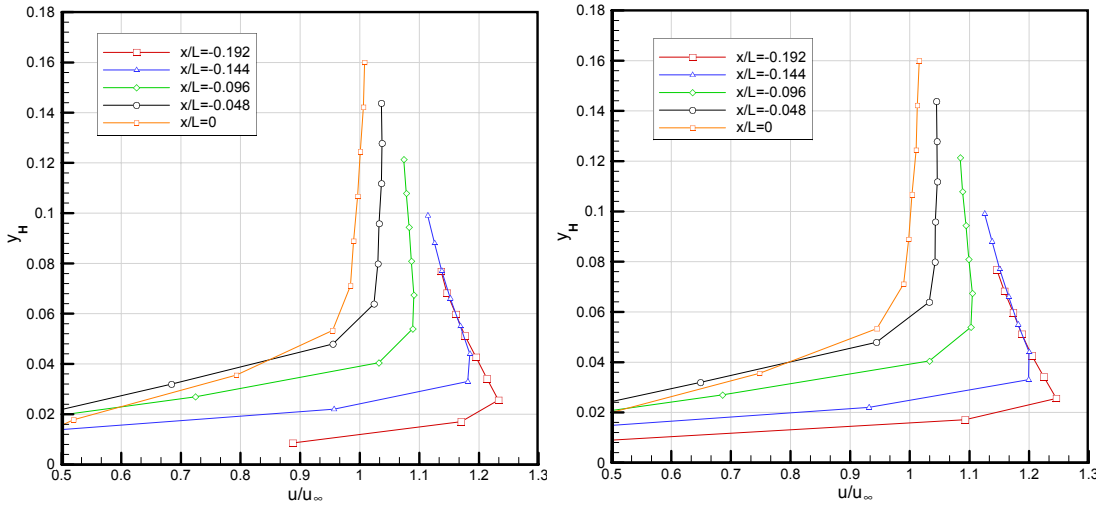

c) z_w=0.096L

d) z_w=0.048L

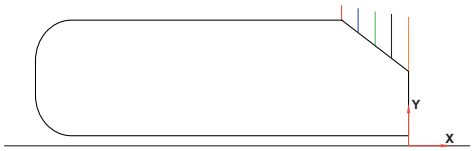

Figure 6.11 - Boundary layer profiles over 25° Ahmed model backlight at various wall separations for z/L=+0.077

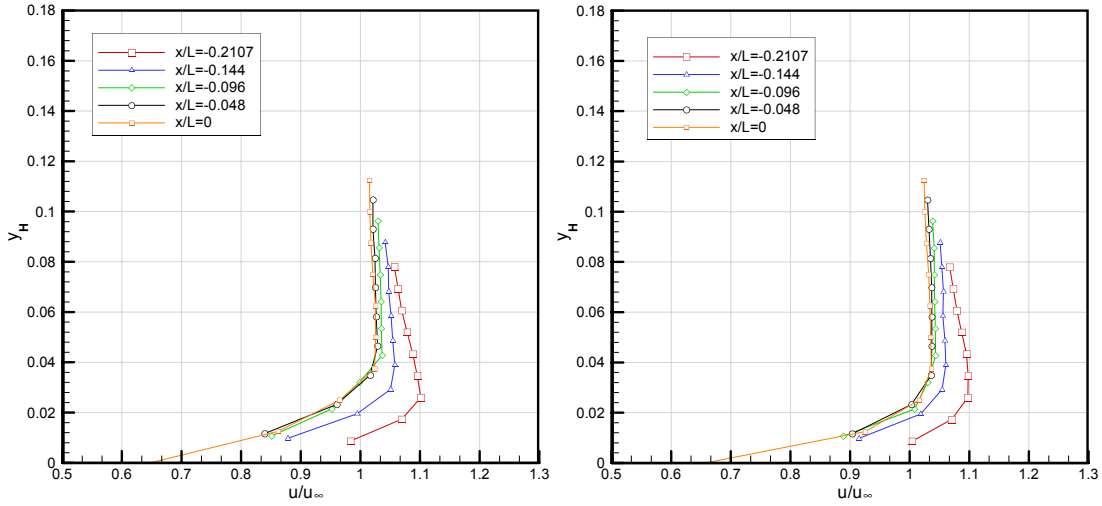

a) z_w=0.287L

b) z_w=0.192L

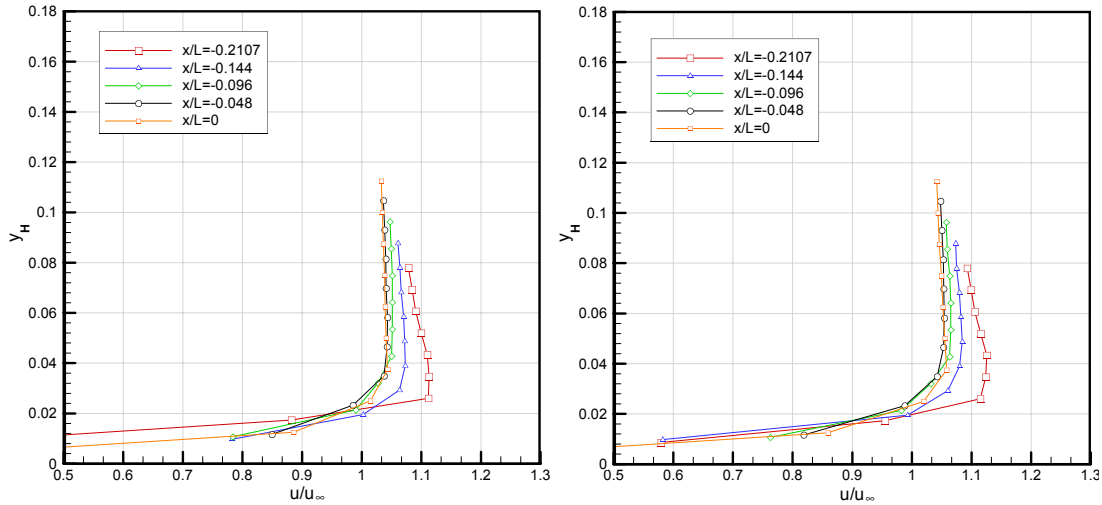

c) z_w=0.096L

d) z_w=0.048L

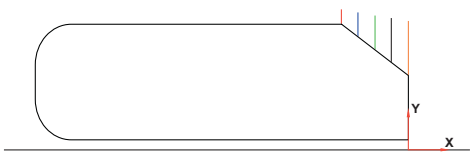

Figure 6.12 - Boundary layer profiles over 10° Ahmed model backlight at various wall separations for z/L=-0.077

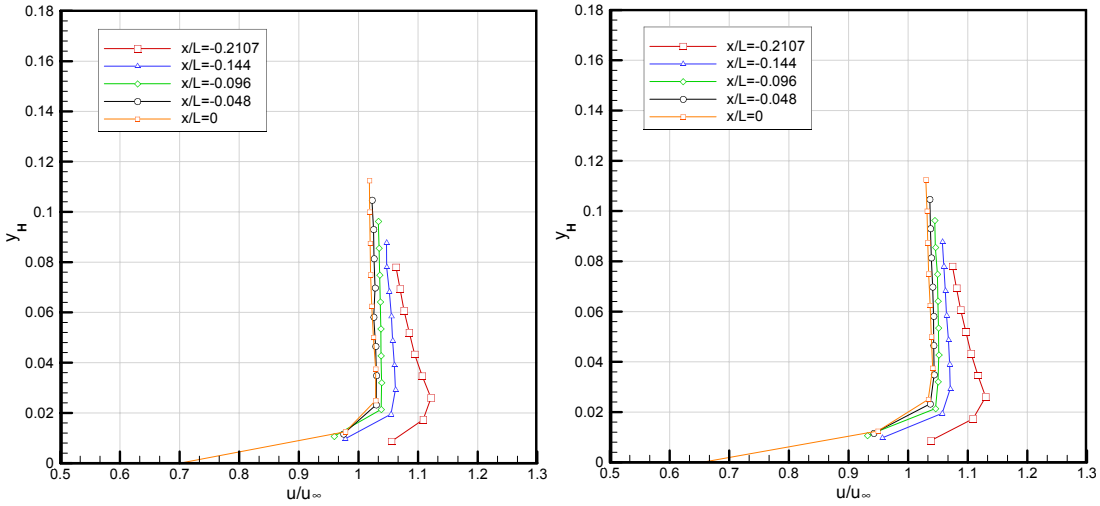

a) z_w=0.287L

b) z_w=0.192L

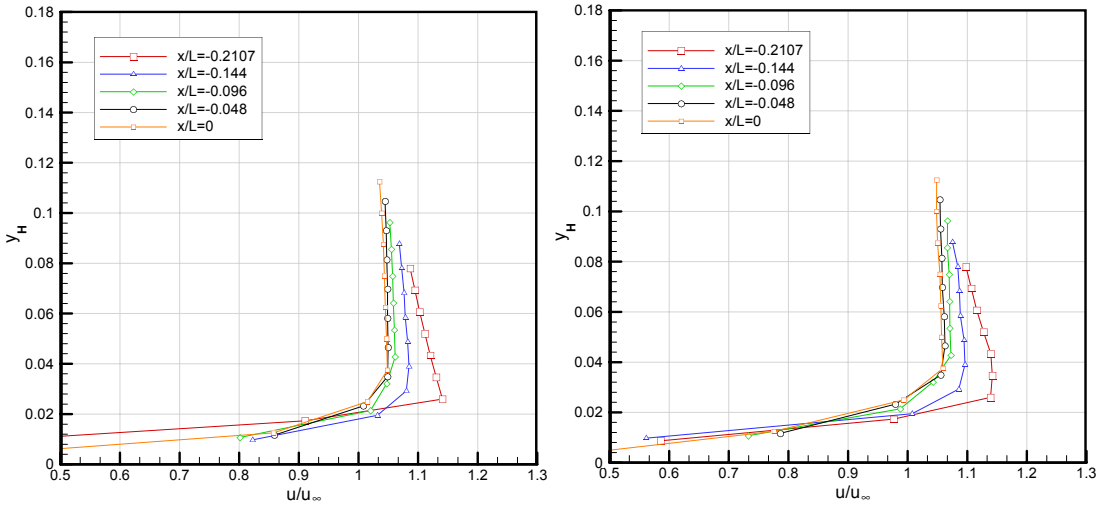

c) z_w=0.096L

d) z_w=0.048L

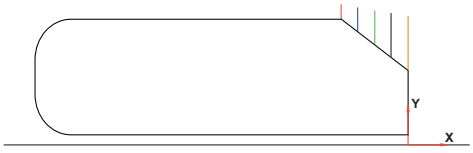

Figure 6.13 - Boundary layer profiles over 10° Ahmed model backlight at various wall separations for z/L=+0.077

model, owing to the formation of less-energetic longitudinal vortices. Employing the same measurement of boundary layer thickness as previously, there was found to be an increase of 0.014L between the isolated and nearest wall cases, around half of the increase measured over the 25° model backlight. Owing to the already comparatively small boundary layer thickness on the 10° backlight and some reflection issues near to the model surface, it proved impossible to measure accurately any variations in boundary layer height at the off-side position in Figure 6.12. It would be expected from the results presented, however, that this boundary layer height would decrease but by a smaller magnitude than the corresponding increase on the near-wall side.

y-z planes

Figure 6.14 shows contour plots of streamwise velocity above the trailing edge of the 10°, 25° and 40° backlights at 0.096L from the side wall. It is clear from Figure 6.14(a) that there is slight asymmetry in the boundary layer profile over the 10° model backlight. The increase in height on the near-wall side and corresponding decrease on the off-side can be seen as a general shift in the largest region of retarded flow toward the side wall. It is also evident that there is a significant variation in vortex structure between the near-side and off-sides of the model. There exists a larger region of retarded flow where the longitudinal vortex is formed on the near-wall side, with this region also being positioned higher than its off-side counterpart. This appears to confirm that the near-side vortex is positioned higher from the model surface in the near-wall cases.

Figure 6.14 (b) highlights again both the greater strength of the vortices found over the 25° backlight and their effect on the flow. The previously-analysed increase in boundary layer thickness on the near-wall section of the backlight in comparison to the off-side can clearly be seen. It can also be seen that there is a larger region of lower streamwise velocity in the region surrounding the off-side vortex in comparison to the near-wall vortex, again evidence of its greater strength when the model is in wall proximity.

Figure 6.14 (c) shows the 40° backlight angle at z_w=0.096L. From this it can be seen that there is a region of higher-magnitude reversed flow behind the backlight on the near-wall side. This is in agreement with previous analysis outlining the variation in flow structure in this region. As the upper and lower recirculatory regions are no longer formed in this area, owing to the lower strength and higher position of the flow turning over the model sides, a higher magnitude of reversed flow at the trailing edge would be expected.

In order to analyse both the positions and strengths of the longitudinal vortical structures formed over the model backlights at various wall separations, Figures 6.15 - 6.17 plot contours of v velocity at the model trailing edge for both the isolated cases and each experimentally-investigated wall separation. Initial inspection of Figure 6.15 shows that there

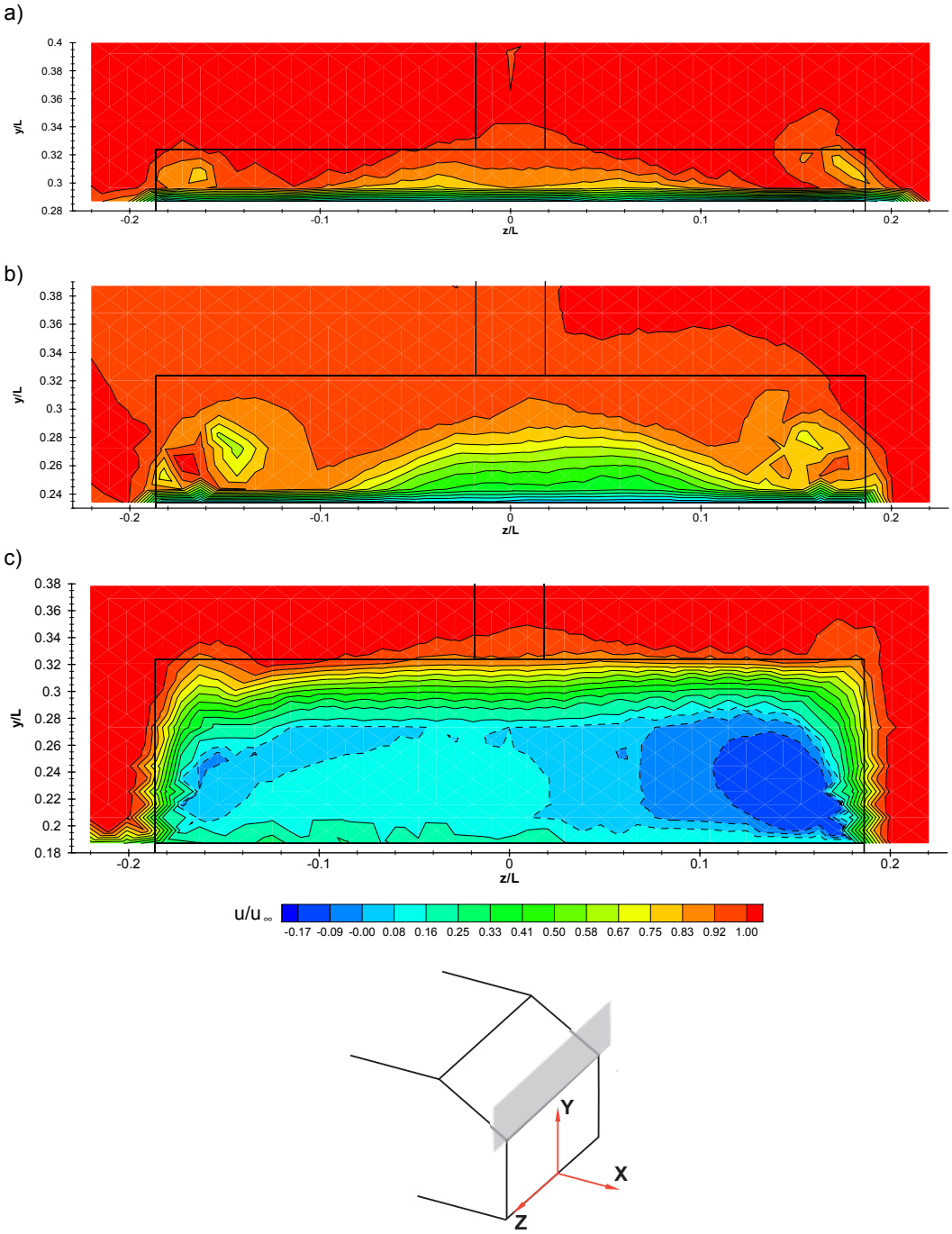

Figure 6.14 - Contours of normalised streamwise velocity above the Ahmed model trailing edge (x/L=0) at 0.096L from side wall for backlight angles of (a)10° (b)25° and (c)40°

is little variation in the position and magnitude of the maximum and minimum v velocities measured in the off-side longitudinal vortex. There is in fact an increase in minimum v velocity magnitude in this region of only approximately $0.02u_\infty$ between the isolated and z_w=0.048L cases, and an increase of again only approximately $0.02u_\infty$ in maximum v velocity magnitude. In comparison, there is a decrease in minimum v velocity magnitude of approximately $0.06u_\infty$ in the near-side vortex between the isolated and z_w=0.048L cases.

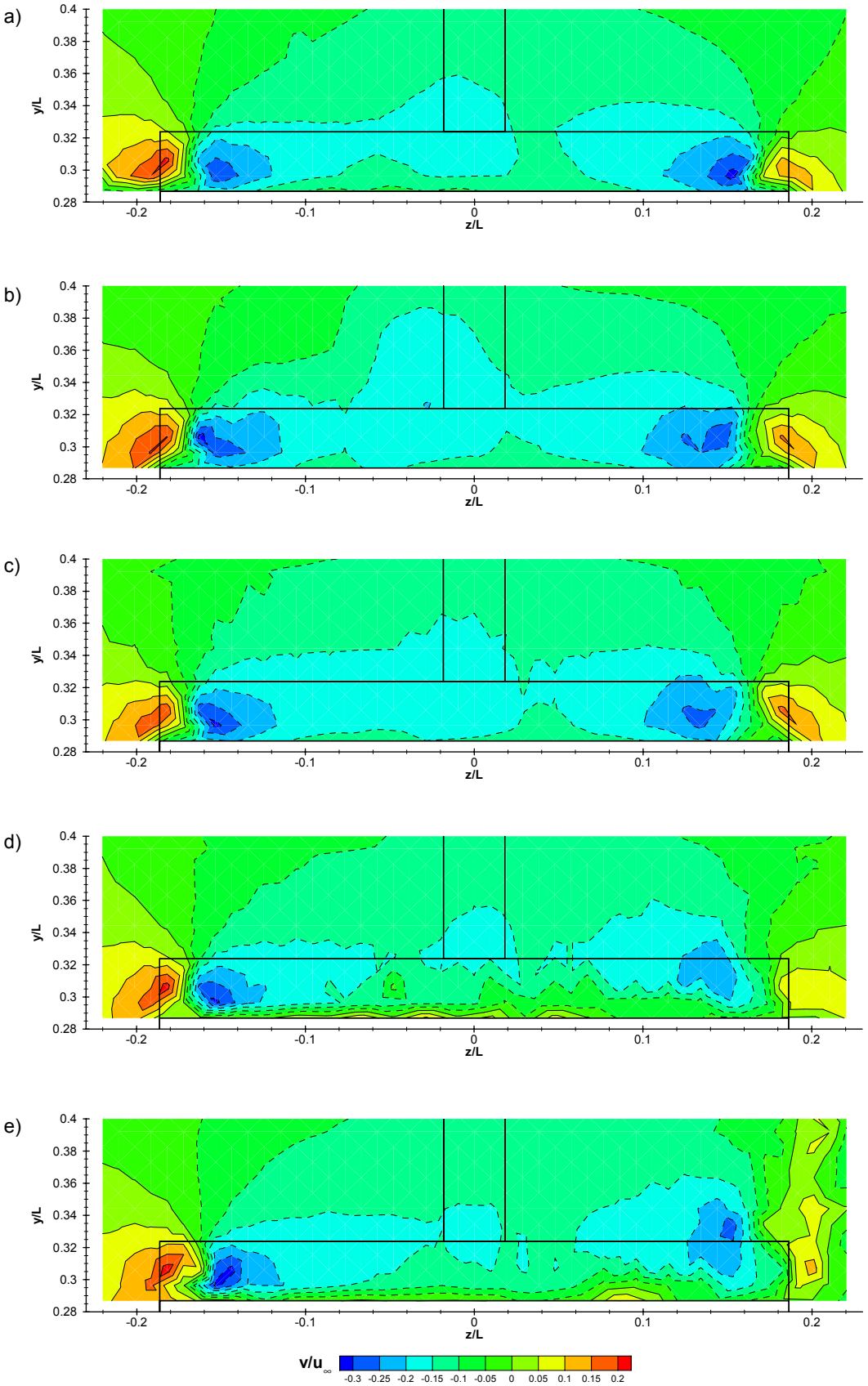

Figure 6.15 - Contours of normalised v velocity above the 10° Ahmed model trailing edge (x/L=0) - (a) isolated case and z_w= (b) 0.287L , (c) 0.192L (d) 0.096L (e) and 0.048

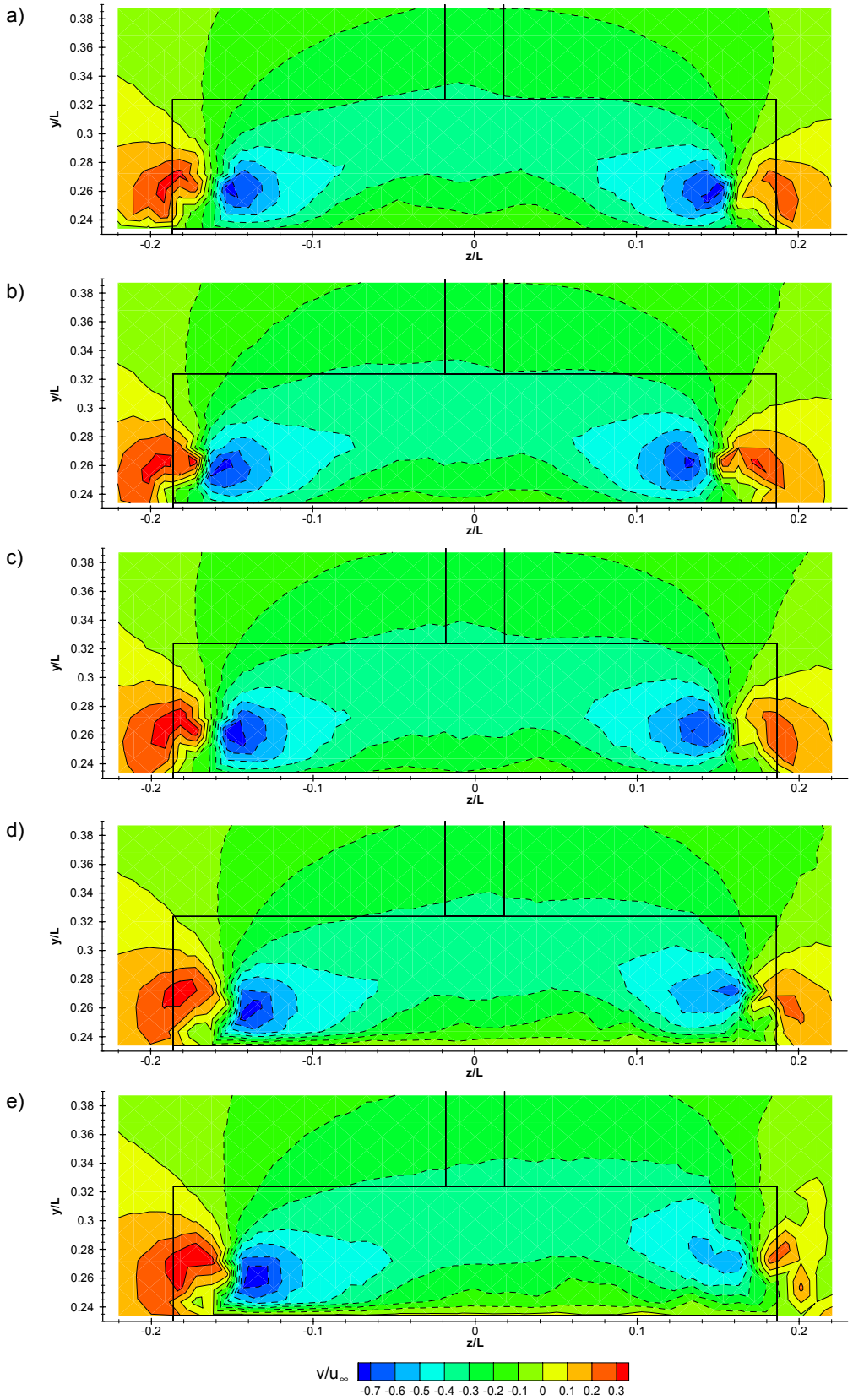

Figure 6.16 - Contours of normalised v velocity above the 25° Ahmed model trailing edge (x/L=0) - (a) isolated case and z_w= (b) 0.287L , (c) 0.192L (d) 0.096L (e) and 0.048

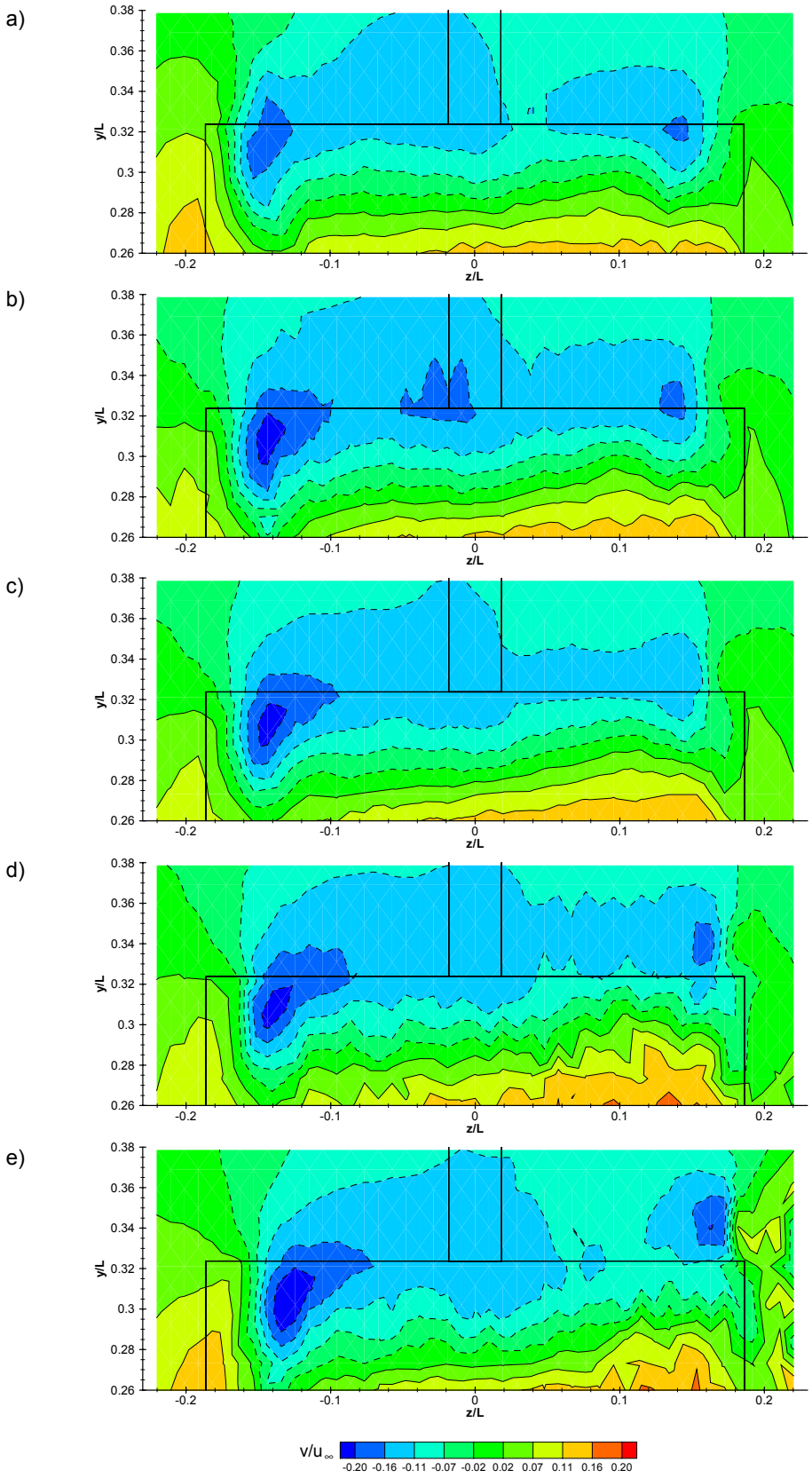

Figure 6.17 - Contours of normalised v velocity above the 40° Ahmed model trailing edge (x/L=0) - (a) isolated case and z_w= (b) 0.287L , (c) 0.192L (d) 0.096L (e) and 0.048

Owing to the fact that only the u and v velocity components were recorded experimentally, the exact position of the vortex centre cannot be found from the presented data. However, as the vortex centre must lie on a contour of v=0, the position on this contour which lies directly between the maximum and minimum v velocities in each vortex will be used for analysis of any positional movements of the longitudinal vortices. It is found, therefore, that between the isolated and z_w=0.048L cases there is little variation (0.002L towards the side wall) in this position in the off-side vortex. There is also no significant variation in the height of this position from the model surface with decreasing wall separation. In the case of the near-side vortex, however, there does exist a gradual movement in 'vortex centre' position as wall separation is altered. Again decreasing wall separation forces this 'vortex centre' toward the wall, by 0.002L between the isolated and z_w=0.287L cases, with a further movement of 0.002L between z_w=0.287L and 0.192L. There is then movement of approximately 0.008L to z_w=0.096L from the side wall, with again a further 0.01L movement to z_w=0.048L from the wall. There is also an evident increase in the height of the near-side longitudinal vortex above the model as wall separation decreases, as can be seen particularly in the z_w=0.096L and 0.048L plots (Figure 6.15 (d) and (e)). It is noted that at z_w=0.048L the point of minimum v velocity in the near-side vortex region is now positioned above the height of the model itself. It appears from the data that at both z_w=0.096L and 0.048L the wall has inhibited formation of the near-side vortex, causing earlier breakdown of the vortical structure. The weaker near-side vortex produces lower downwash, which in conjunction with the expected higher vertical velocity between the model and side wall due to wall proximity, results in the higher vortex positions evident at the 10° model trailing edge.

It appears, therefore, that for the 10° Ahmed model in proximity to a side-wall, the induced flow angle towards the wall has the effect of moving the near-side vortex closer but has little effect on the off-side vortex. It also appears that as wall separation falls the wall inhibits the formation of the near-side longitudinal vortex, resulting in lower downwash over the near-side section of the backlight.

In the 25° model cases shown in Figure 6.16, similar trends to those found in the 10° case are apparent. There is, however, a significant movement of 0.02L towards the model centreline in the off-side vortex centre (as defined previously) between the isolated and z_w=0.048L cases, approximately 10 times greater than the corresponding variation found in the 10° case. This suggests the near-side vortex has a greater effect on the position of the off-side vortex than the inclination of the flow towards the wall. It is expected that there would exist a greater tendency of the flow to move towards the side wall in the 25° case than the 10° case, as a result of higher levels of suction between the wall and model. This variation would not, however, be expected to be large enough to cause as significant a movement of the off-side

longitudinal vortex as was found.

There is again no definable variation in the height of the off-side longitudinal vortex centre with wall separation. There also exists a larger movement of the near-side longitudinal vortex centre toward the side wall, in this case amounting to approximately 0.04L between the isolated and z_w=0.048L cases. This is around double the movement found in the 10° case, which would account for the larger variation in position of the off-side vortex. There is, as was the case at the 10° backlight, a noticeable increase in the height of the near-side vortex centre with decreasing wall separation, although in the 25° case the total variation between the isolated and smallest wall separation cases was found to be approximately 0.01L, compared with the variation of 0.03L found in the 10° case. The majority of the vortex movement in both the y and z direction occurs between z_w=0.096L and 0.048L, similar to the 10° case. It seems therefore that between wall separations of 0.096L and 0.048L the wall begins to have a far greater effect on the longitudinal vortex formation, regardless of its initial strength.

From these observations it can be deduced that variations in flow over Ahmed model backlights below the 2nd critical angle in wall proximity are primarily a result of the wall interference on the formation of the near-side longitudinal vortex. The variations in boundary layer height shown previously are also a result of this interference, with the weaker near-side vortex causing an increase in boundary layer height over the near-side section of the backlight. The decreased strength of the near-side vortex also, in conjunction with the inclination of the flow toward the side wall, relocates the off-side vortex closer to the model centreline, causing a decrease in boundary layer thickness over the off-side region.

In the case of the 40° backlight shown in Figure 6.17, similar trends to those found in both the 10° and 25° cases can be seen, despite the absence of the strong longitudinal vortices. Low data rates were experienced during the acquisition of the data shown in Figures 6.17 (d) and (e), accounting for the jagged appearance of sections of the plots, in addition to wall reflection issues arising at z_w=0.048L as before.

It is apparent that there exists a larger region of higher v velocity flow near the side wall at the bottom edge of the near-side plots shown in Figure 6.17. This is consistent with the variation in the structure of the rear-end flow shown in Figure 6.9. Low data rates and reflection issues, however, make what is an apparent increase in the v velocity in this region with decreasing wall separation difficult to quantify. It was, however, shown in Figure 6.8 that although the flow is altered by the reduced downwash on the near-wall side, there is no extension of this effect to the opposite side, owing to the increased downwash in that region. Subsequently, there is little variation in the structure of the separated backlight flow between the near-wall cases investigated.

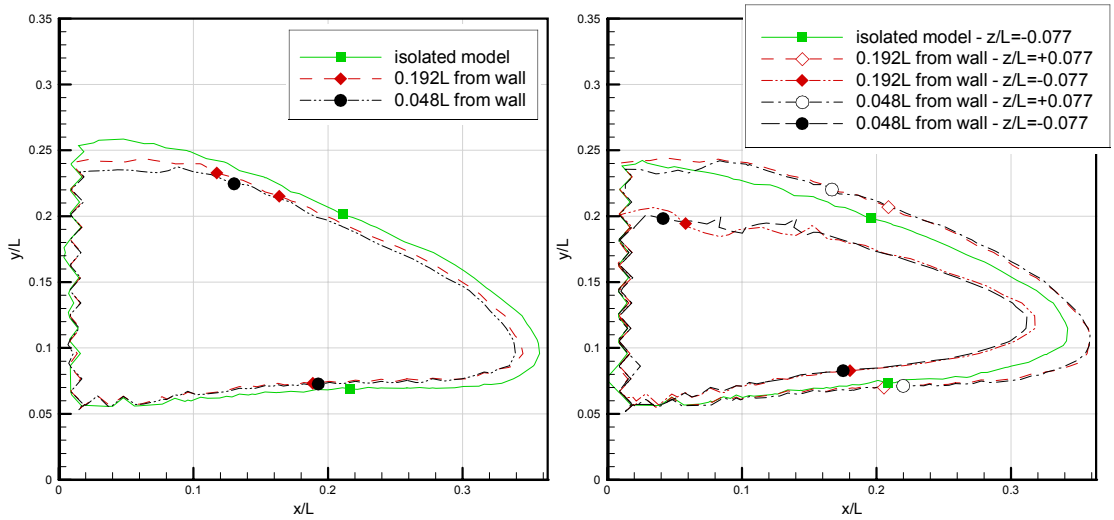

Figure 6.18 - Contours of u/u_∞ = 0 and vortex centres in near wake of 10° Ahmed Model at z/L = 0 (a) and z/L = +0.77 & -0.77 (b) behind model - isolated case & 0.192L and 0.048L from side wall

As a result of the flow angle over the model induced by the wall, there exists a larger tendency of the flow to turn around the off-side edge of the backlight. This results in a decrease in the minimum v velocity measured near the off-side of approximately $0.05u_\infty$. As the longitudinal vortices are not formed over the 40° backlight, and as the turning tendency over the side edges was shown previously to have minimal effect close to the model centreline during analysis of the isolated model, it must be concluded that this increase in downwash over the off-side edge is primarily a result of the induced flow angle. This is in contrast to the effects of the near-side vortex on its off-side counterpart evident in the 25° backlight case.

The position of minimum v velocity on the near-side is, as in the attached flow cases, higher as wall separation falls. The point of minimum v velocity in this region is moved higher from the model surface by 0.02L between the extreme cases measures (isolated model and z_w=0.048L), with an almost linear increase with decreasing wall separation. This linear increase contrasts with the previously-analysed backlights as there is no prevention of vortex formation and subsequent sharp alteration in flow structure.

6.1.4 Near Wake

To investigate the effects of the backlight flow on the separation bubble shown to be formed in the near wake of each Ahmed model configuration, Figure 6.18 plots contours of zero streamwise velocity and vortex centres for both the near-side and isolated 10° cases.

A decrease in length of the separation bubble with decreasing wall separation is evident in the centreline plot (Figure 6.18 (a)). This downstream distance falls from 0.357L in the isolated

case to 0.344 at z_w=0.192L and then to 0.34 at z_w=0.048L. This variation is consistent with the upper vortex centre variations also shown in Figure 6.18 (a). Although two upper vortex centres were plotted for the z_w=0.192L case, it is clear that this was due to ambiguity caused by low data rates. The actual, single, vortex centre would be between the two points marked, and therefore the movement of this vortex centre follows a similar trend to that of the overall separation bubble length. It was shown previously that the separation bubble's structure is predominantly determined by the upper vortex, and so this correlation would be expected.

At the off-side position (z/L=-0.077), the increased off-side longitudinal vortex strength and its movement toward the model centreline has, as might be expected, a significant effect on the position of the upper vortex centre. In comparison to the vortex centre movement found at the model centreline, there is a variation of 0.08L between the isolated and z_w=0.048L case upper vortex centres at z/L=0, and a corresponding variation of 0.155L at z/L=-0.077. There is also a larger variation in the length of the reversed flow region at the off-side position of 0.03L between the isolated and z_w=0.048L cases, in comparison to 0.017L at the model centreline, again a result of the influence of the off-side vortex at z/L=-0.077.

The upper boundary of the reversed flow region is moved downward when the model is in wall proximity at both the model centreline and at the off-side position. Again, as would be expected, this variation is larger at z/L=-0.077 as a result of the influence of the off-side longitudinal vortex in this region. Indeed, there is found to be a drop in height of the reversed flow region's highest point of 0.022L between the isolated and z_w=0.048L cases at the model centreline, with a larger drop of 0.04L at z/L=-0.077.

Variations at the near-side position (z/L=0.077) can be seen to be of lower magnitude than those at the off-side position (z/L=-0.077). It must be assumed that this is a result of the fact that at the transverse positions shown there is little effect of the longitudinal vortices evident when the 10° model was tested in isolation. Subsequently, the effects of wall interference (reduction of near-side vortex strength and repositioning the vortex centre nearer to the wall and higher from the model's surface) will be less apparent.

There exists an increase in the overall distance to which the separation bubble extends downstream at the near-side position plotted in Figure 6.18 (z/L=0.077), probably a result of the decreased downwash from the longitudinal vortex and subsequent upward relocation of the upper separation bubble vortex centre. As would be expected from previous reasoning, this increase is less than the decrease found at the off-side position, measuring 0.017L at z/L=0.077 compared to 0.03L at z/L=-0.077. The smaller variation in downwash in comparison to the off-side position also accounts for the slight increase in height of the reversed flow region, again smaller than the corresponding decrease on the opposite model side. Although

it was shown that the side wall had a greater influence on the near-side vortex, the fact that the flow over the 10° model is fundamentally two-dimensional at the transverse positions analysed here means the alterations to this near-side vortex have a minimal effect. This trend would not be expected to be found in the 25° case, as the stronger longitudinal vortices shed affect the flow over the entire model backlight, resulting in the three-dimensional flow analysed earlier. Subsequently, the breakdown of the near-side vortex would be expected to have an effect at all plotted transverse positions.

To investigate the effects of wall proximity on the near-wake separation bubble of the 25° Ahmed model, Figures 6.19 and 6.20 show the experimental data recorded in the near-wake at z/L=±0.077 and at the model centreline (z/L=0). From Figure 6.19 it is apparent that there exists an increase in the distance downstream to which the separation bubble extends with decreasing wall separation at z/L=-0.077. This is in contrast to the 10° model case where the opposite effect was observed. The upper vortex centre is moved further from the model trailing edge as wall separation falls, causing the increase in separation bubble length and again the opposite trend to that observed in the 10° model case.

It can also be seen in the z/L=-0.077 LIC plots that the influence of the off-side vortex has caused an increase in the vertical velocity of the flow toward the downstream end of the separation bubble. It would be expected that this effect would further extend the separation bubble in the streamwise direction in addition to increasing its height. This effect was not evident in the 10° off-side position plots, and therefore the resultant increase in separation bubble size was not observed. This increase in vertical velocity is explained by referring again to Ahmed's original experiments and the previously-presented description of the flow around the 25° model. It has been shown that the cores of the longitudinal vortices are fed from the near-wake separation bubble. The increased strength of the off-side vortex and its relocation toward the model centreline would be expected to increase this effect, subsequently imparting a greater vertical velocity in the separation bubble in the vicinity of this vortex. This results in both the extension of the downstream distance to which the separation bubble extends and the downstream relocation of the upper vortex centre.

Examining now the 25° model centreline LIC plots, there appears to be little variation in the overall size of the separation bubble between the two wall separations shown. There does, however, exist a significant shift of the upper recirculatory region centre downstream as wall separation falls from 0.192L to 0.048L. This is possibly a result of the significant near-side vortex breakdown between these wall separations.

As would be expected, no upward inclination of the flow from the off-side longitudinal vortex can be seen in the 25° z/L=0.077 LIC plots, as the reduced vortex strength would be expected

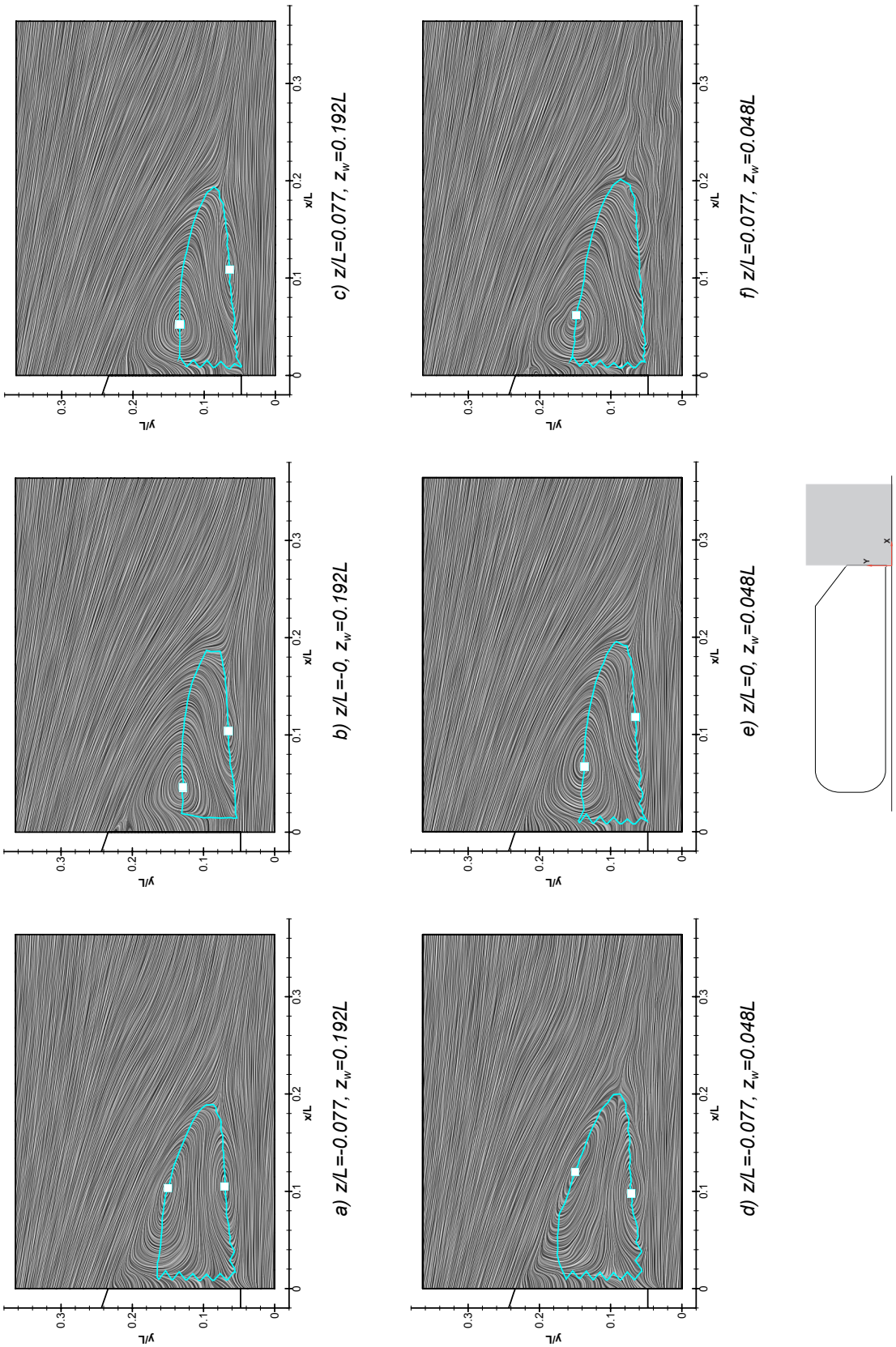

Figure 6.19 - Line Integral Convolution plots from LDA data at z/L=0, ±0.077 behind 25° Ahmed model, 0.192L & 0.048L from side wall. Blue lines and squares mark contours of u=0 and vortex centres

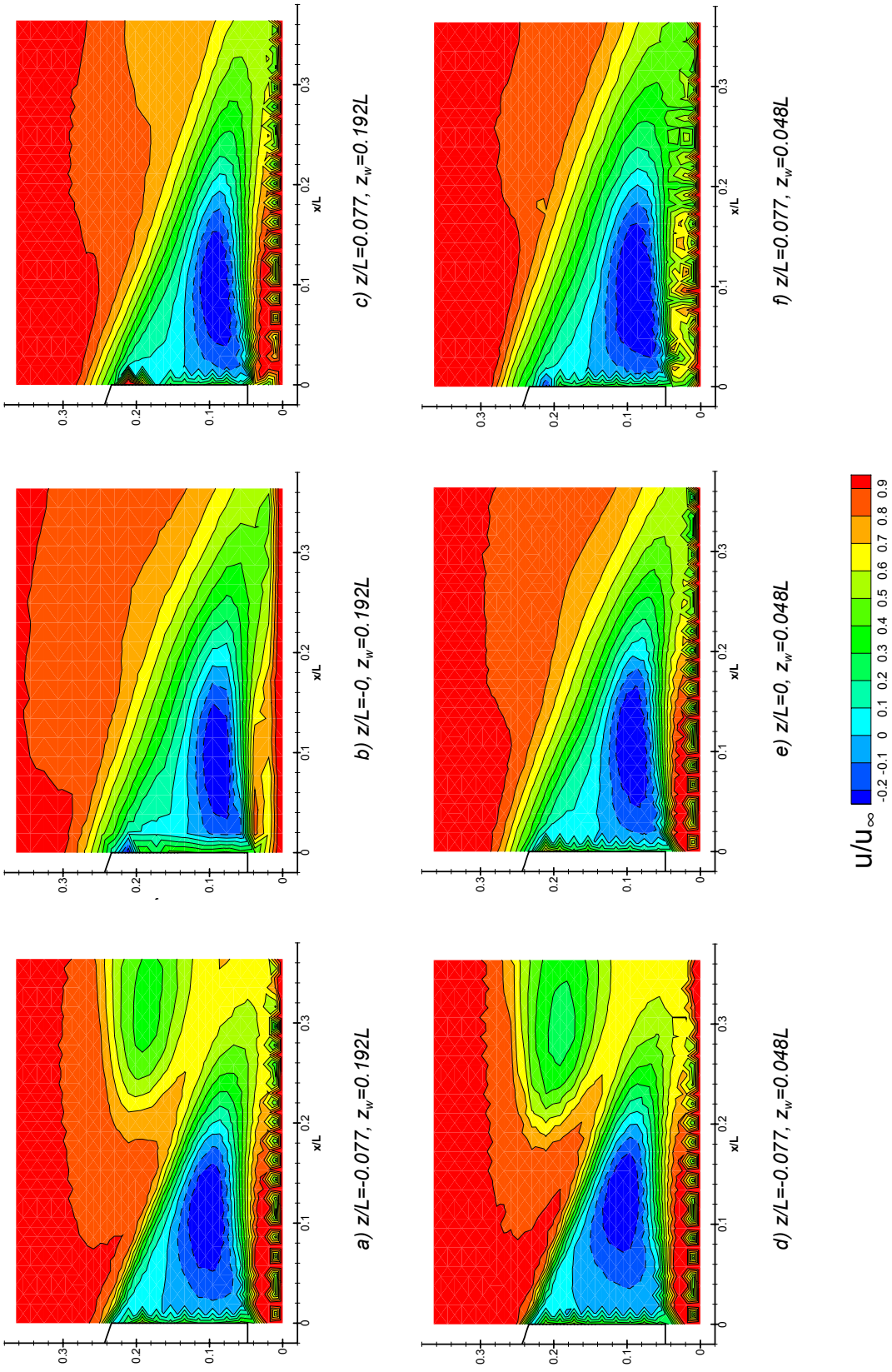

Figure 6.20 - 25° Ahmed model - contours of normalised streamwise velocity at z/L=0, ±0.077 behind model - 0.192L and 0.048L from side wall - LDA data

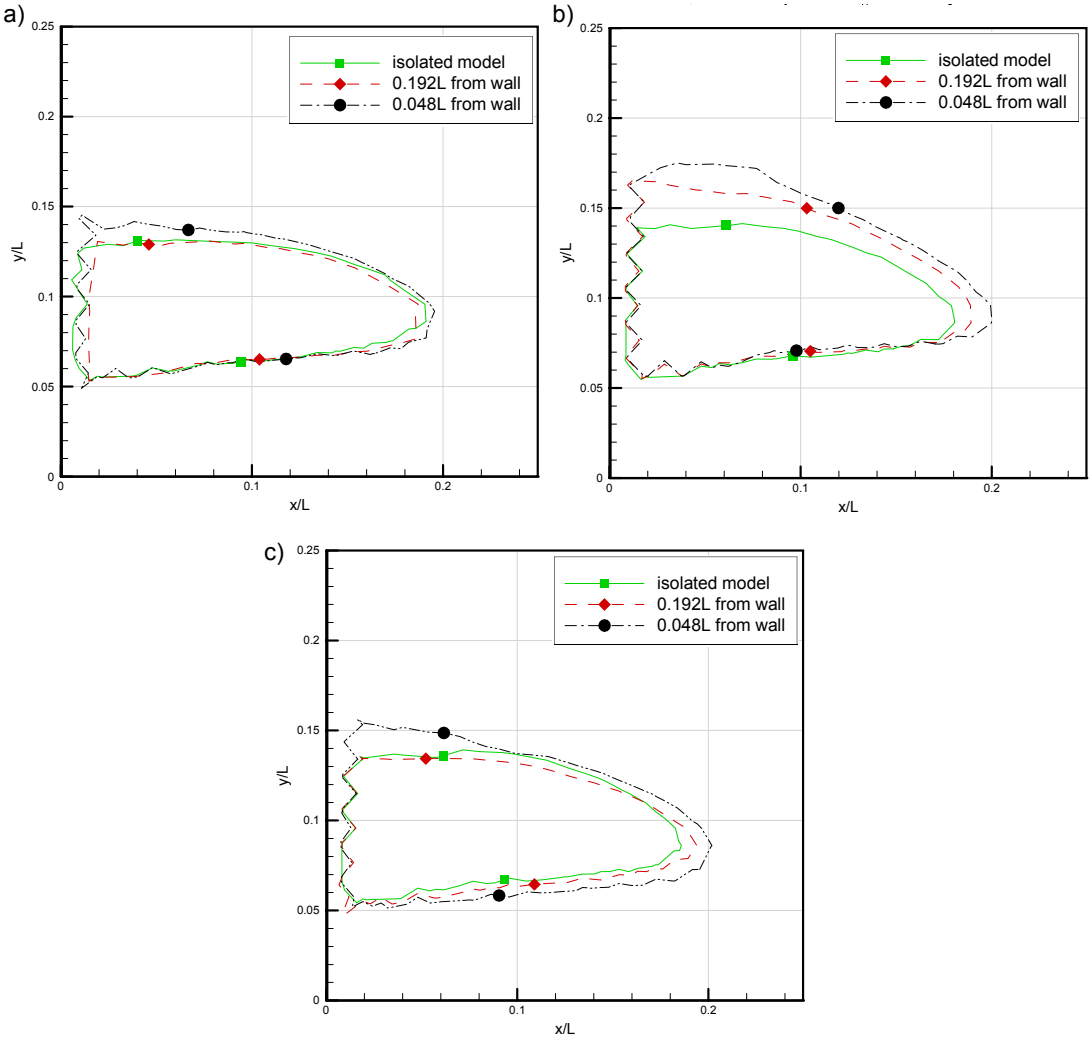

Figure 6.21 - Contours of u/u_∞ = 0 and vortex centres in near wake of 25° Ahmed Model at z/L = (a) 0 (b) -0.077 (c) +0.077 behind model - isolated case & 0.192L and 0.048L from side wall - LDA data.

to reduce the flow fed into the vortex core from the separation bubble. Although this would decrease the imparted vertical velocity it must also be noted that there is a greater decrease in vortex strength on the near-wall model side than corresponding vortex strength increase on the off-side. This effect would be expected to decrease the downwash in the investigated near-side region. The 25° model LIC plots at z/L=0.077 therefore exhibit a similar pattern to that found in the 10° case. There is again an extension of the separation bubble downstream, consistent with both the lower near-side longitudinal vortex strength and its higher position from the model surface. It must be noted that low data rates were experienced throughout the acquisition of the LDA data 0.048L wall separation z/L=0.077 plane, causing the slightly irregular pattern evident in the LIC plot. This also makes it more difficult to assess accurately the position of the upper vortex centre in particular. This fact must be taken into account during further analysis.

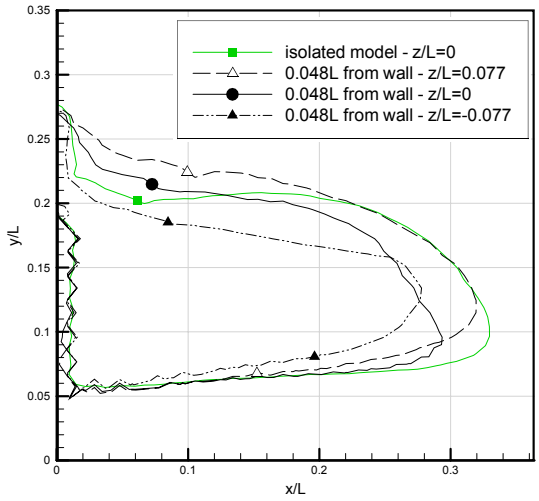

Figure 6.22 - Contours of u/u_∞ = 0 and vortex centres in near wake of 40° Ahmed Model at z/L = 0, 0.77 and -0.77 behind model - isolated case and 0.048L from side wall

To analyse further the structure of the separation bubble in the wake of the 25° model, contours of streamwise velocity are shown in Figure 6.20. The corresponding isolated model plots were presented in Figure 5.18. Initial inspection again reveals an increase in trailing edge streamwise velocity with decreasing wall separation for all three transverse positions, consistent with previous analysis. Also apparent is the greater increase in the effect of the off-side longitudinal vortex at z/L=-0.077 as wall separation falls. The reverse effect is, as expected, evident in the near-side plot (z/L=0.077). These variations are more obvious in the flow at 25° backlight angle than in the 10° case owing to the greater effect of the longitudinal vortices in the near-wake flow at this backlight angle.

In order to quantify the alterations in the separation bubble with wall proximity described above, Figure 6.21 plots contours of u=0 and vortex centres for both the near-side and isolated 25° model cases. Initial inspection shows that there is a larger variation in the size of the reversed flow region at z/L=-0.077 than at z/L=0.077. In particular there is an increase of 0.035L in the overall height of this region between the isolated and z_w=0.048L cases at z/L=-0.077, with a corresponding increase of 0.02L at z/L=0.077. There is also an increase in the overall length of this region between the same cases of 0.02L at z/L=-0.077 and 0.15L at z/L=0.077. At the model centreline (z/L=0) there is only a comparatively small increase in the length and height of the reversed flow region of 0.005L and 0.01L respectively.

There also exists a more gradual variation in the upper vortex centre with decreasing wall separation at z/L=-0.077 in comparison to the near-side position (z/L=+0.077). It is apparent that between wall separations of 0.192L and 0.048L there is a significant upward shift in this vortex centre at the near-side position, inconsistent with the variation between the isolated z_w=0.192L cases. This trend is repeated in the overall height of the reversed flow region at

z/L=0.077. Referring again to previous analysis of the backlight longitudinal vortices, it was shown that at a wall separation of 0.048L there was found to be a significant breakdown of the near-side vortex structure. This breakdown would be expected to cause a sharp drop in the overall downwash at the model trailing edge, accounting for both the increased height of the vortex centre and reversed flow region.

The variation in the upper vortex centre position at the model centreline also follows a similar pattern to that at z/L=0.077. It would appear, therefore, that the breakdown of the near-side vortex has a greater effect on the centreline flow than the variations in the off-side vortex. As before, this is a result of the three-dimensional nature of the 25° backlight flow and the larger effect of the longitudinal vortices at this back angle.

To analyse variations in the near-wake separation bubble behind the 40° Ahmed model trailing edge, Figure 6.22 plots vortex centres and contours of u=0 for both the isolated and z_w=0.048L cases. The variation in reversed flow region between the near-side and off-side positions reveals the decreased downwash over the near-side section, resulting in backlight flow structure alterations similar to those found in the 10° model cases. The overall length of the separation bubble at the three transverse positions shown therefore follows the expected pattern, with an increase in length with increasing proximity to the side wall. At the 0.048L wall separation shown there is an increase of 0.015L between z/L=-0.077 and z/L=0, with a further increase of 0.026L between z/L=0 and z/L=0.077. Owing to the lack of data away from the model centreline for the 40° isolated case it is impossible to quantify the variations in terms of wall proximity. It is noted, however, that at each of the positions shown the overall length of the separation bubble is shorter than at the model centreline in the isolated case.

6.2 Static Pressure Results

The static pressure measurements taken over the 25° backlight both in isolation and in wall proximity are plotted in Figure 6.23. Initial inspection reveals the large drop in C_p with decreasing wall separation evident at the off-side leading edge of the backlight, indicative of the increased longitudinal vortex strength. The previously-identified movement of the off-side vortex toward the model centreline with decreasing wall separation can also be seen in these plots. The decrease in near-side vortex strength with decreasing wall separation can also be seen by the increase in C_p close to the side wall. In addition, there appears to be a widening of the near-side vortex from the pressure distribution shown.

The increase in flow velocity over the majority of the backlight away from the immediate vicinity of the longitudinal vortices can also clearly be seen in Figure 6.23 by the drop in C_p in

this region. In particular there is a large drop in C_p evident over the backlight leading edge. There exists significant asymmetry between the pressure distribution on the near-side and off-sides of the model, with lower pressures evident closer to the side wall. This lower pressure is evident in all near-wall cases, but is particularly noticeable at z_w=0.048L. It is the case that a higher streamwise velocity and therefore lower pressure would be expected closer to the side wall as a result of the increased velocity in this region over the top of the model, despite the retardation of the flow expected from the encroachment of the supporting strut wake into this area. However, this asymmetry appears to become more pronounced nearer the trailing edge, suggesting that this is a result of the variations in longitudinal vortex structure. From the isolated case pressure plot of Figure 6.23 (a) it is shown that between z/L=0 and z/L=0.12 there is a decrease in flow velocity (and therefore increase in static pressure) with increasing z position caused by the strong vortices formed. At z_w=0.048L, when the near-side vortex strength has dropped significantly, this decrease is no longer as evident, particularly near the trailing edge where it was shown previously that the vortex had already begun to break down.

To quantify these observations Figures 6.24 - 6.26 plot various profiles of C_p data extracted from the contour plots. Figure 6.24 reveals that on the model centreline, and in particular close to the model trailing edge (x/L=0), the largest variation in C_p is found between the isolated and z_w=0.192L cases. Indeed there is found to be a drop in C_p of approximately 0.063 between the isolated and z_w=0.192L cases, with a further drop of only 0.014 between z_w=0.192L and z_w=0.048L. At the leading edge of the backlight, however, there is found to be a larger drop in C_p of 0.13 between the isolated and z_w=0.192L cases, with a further drop of 0.08 to z_w=0.096L and another of 0.025 at 0.048L from the wall. It is therefore clear that the large increase in suction with decreasing wall separation evident over the leading edge of the 25° backlight is not continued downstream. Also, as there is a large drop in C_p between the isolated and z_w=0.192L cases at the trailing edge, it seems reasonable to assume that this, is at least in part, a result of the relocation of the strut wake. As the main region of lowered flow velocity which this causes has already moved towards the side wall and away from the model centreline trailing edge at 0.192L wall separation, further movement of this region as wall separation falls further would not be expected to cause as dramatic an increase in flow velocity (and subsequent decrease in pressure). This is in accordance with the results shown in Figure 6.24. This shift of the strut wake does not cause an evident increase in C_p close to the side wall because the increase in velocity over the model top with decreasing wall separation was shown previously to have a greater effect on the flow.

Figure 6.25 plots pressure measurements taken at z/L=±0.166, close to the sides of the model backlight and within the direct effects of the near-side and off-side longitudinal vortices. The increased strength of the off-side vortex with decreasing wall separation can clearly be seen in the z/L=-0.166 plot. From the pressure plots in Figure 6.25 it can be seen that the peak in

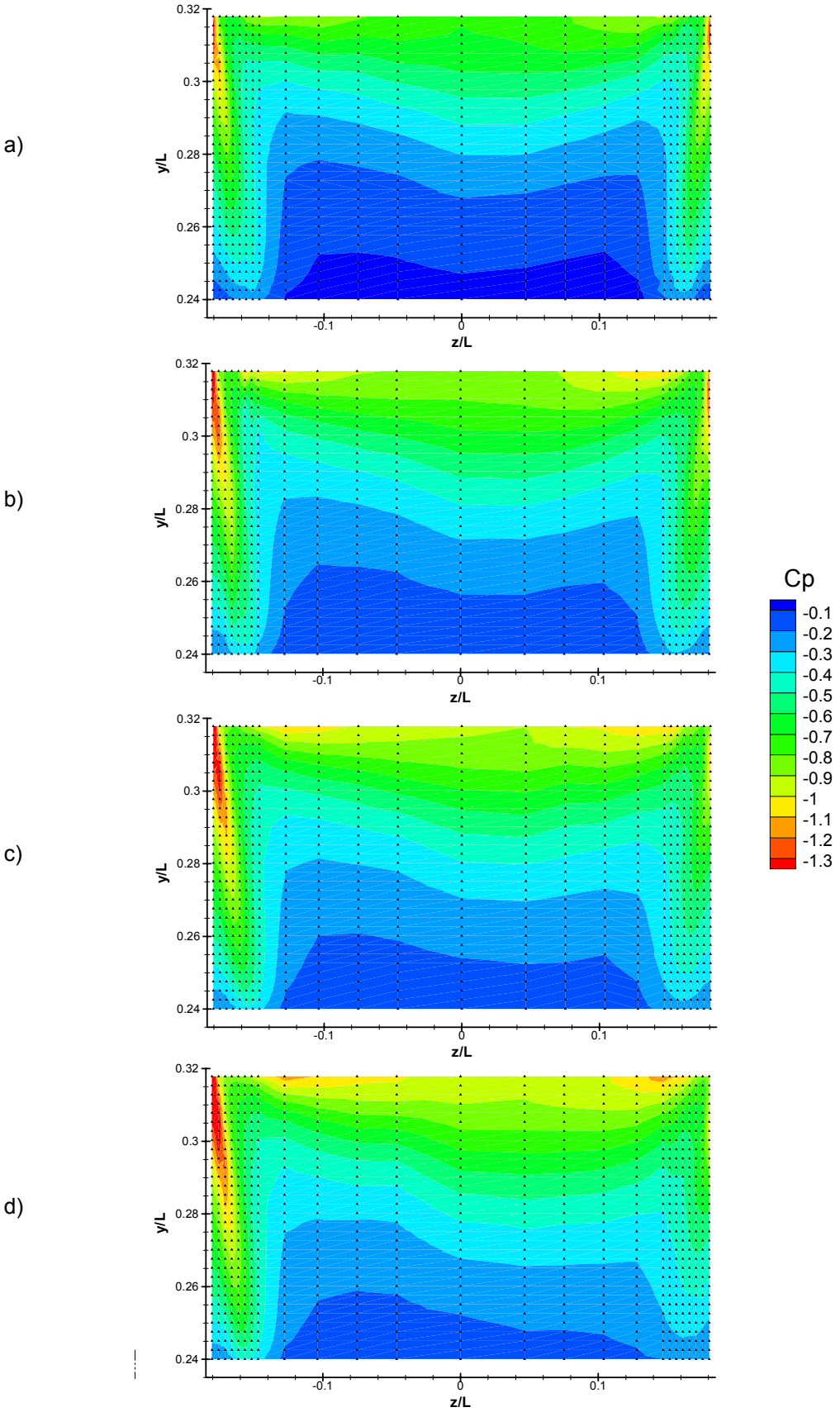

Figure 6.23 - 25° Ahmed Model backlight pressure distribution (a isolated model and (b)z_w=0.192L (c)z_w=0.096L (d)z_w=0.048L. Black triangles mark positions of pressure tappings

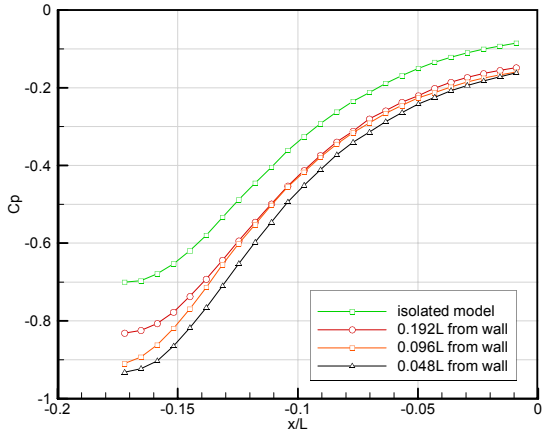

Figure 6.24 - 25° Ahmed Model - profiles of backlight pressure at model centreline (z/L=0) - various wall separations

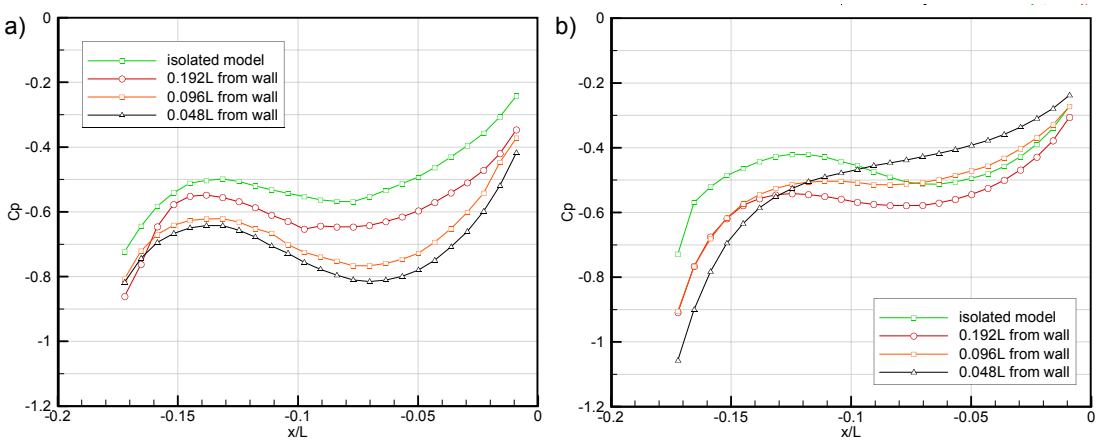

Figure 6.25 - 25° Ahmed Model - profiles of backlight pressure (a) z/L=-0.166 (b) z/L=+0.166 at various wall separations

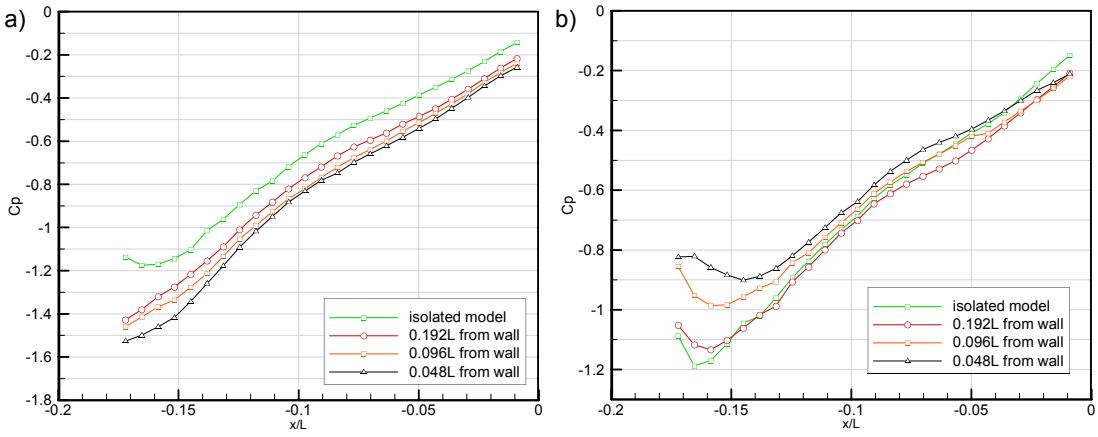

Figure 6.26 - 25° Ahmed Model - profiles of backlight pressure (a)z/L=-0.179 and (b)z/L+0.179 at various wall separations

C_p evident in each case closer to the model trailing edge is the most important feature, as it is here where the measurement plane crosses the longitudinal vortex. Therefore, measurement of this C_p peak will give the most accurate reading of off-side longitudinal vortex strength. There is found to be a drop in C_p of approximately 0.078 between the isolated and z_w=0.192L cases, with a further larger drop of 0.1193 between the z_w=0.192L and z_w=0.096L cases. Between wall separations of 0.096L and 0.048L there exists another drop in C_p of 0.05.

In comparison, the z/L=0.166 plot (Figure 6.25 (b)), does not exhibit a consistent trend in C_p with varying wall separation. It is clear that at the measured position the large variations in vortex structure and height from the model surface shift the vortex core enough to make analysis from this profile problematic. Therefore, data taken closer to the model sides, at z/L=±0.179, are shown in Figure 6.26. It can be seen in the z/L=0.179 plot (Figure 6.26 (b)), that there is both a rise in minimum C_p and a shift in position of this minimum towards the trailing edge with decreasing wall separation. The C_p in fact increases by 0.055 between the isolated and z_w=0.192L cases, with a further rise of 0.147 to z_w=0.096L and a further rise of 0.086 to z_w=0.048L. The position of this minimum shifts aft by 0.02L between the isolated and 0.048L from wall cases, with the majority of this shift occurring between wall separations of 0.096L and 0.048L.

The overall pressure over the backlight, and therefore the contribution of this region to the overall aerodynamic coefficients of the model are, as would be expected, significantly altered by the inclusion of the side wall. Inclusion of the side wall has been shown to result in an overall pressure increase close to the near-side due to the weaker vortex, with the opposite effect occurring over the off-side. In addition, there is an evident drop in pressure over the

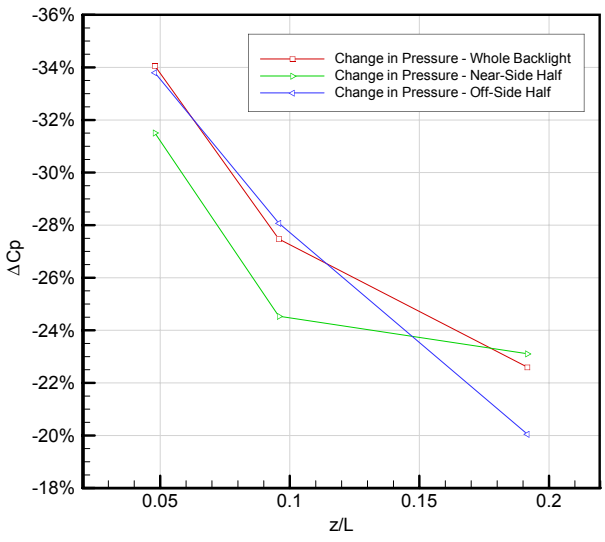

Figure 6.27 - Fractional change from isolated case in average C_p over 25° Ahmed Model backlight vs side wall proximity

remainder of the backlight as a result of the higher flow velocity measured over the top of the model. To quantify these alterations the decrease in average C_p from the isolated case is shown in Figure 6.27 for the whole backlight and for each half of the model.

Overall, the pressure over the backlight drops by 22.5% between the isolated and z_w=0.192L cases. It can be seen from Figure 6.27 that the largest drop in C_p between these two cases was found over the near-side half of the backlight. This would be expected from inspection of Figure 6.28 as although there is a rise in C_p where the near-side vortex is formed, the drop in C_p over the remainder of the near-side half of the backlight is more significant in terms of the overall backlight pressure. Between wall separations of 0.192L and 0.096L, however, this trend is reversed and it is the off-side half of the backlight which experiences the largest drop in C_p - a further 8% from the isolated value in comparison to the near-side half drop of only a further 1.5% from the isolated value. The formation of the near-side vortex has been shown previously to be significantly altered by the proximity of the side wall at 0.096L wall separation, causing a large increase in C_p over the backlight close to the wall. This effect is in opposition to the drop in C_p over most of the backlight as a result of the higher flow velocity over the top of the model, resulting in what is only a comparatively small decrease in C_p over the entire near-side half of the backlight.

At 0.048L wall separation it is again the case that the off-side half of the backlight experiences a larger drop in C_p (compared to the isolated case) than the near-side. There exists however a larger percentage drop in C_p over the near-side between wall separations of 0.096L and 0.048L - 6.9% in comparison to 5.7%. At this wall separation the higher position of the near-side longitudinal vortex has not only raised the C_p close to the near-side of the backlight, but the vortex now has little effect on the pressure distribution over the remainder of the backlight. Again inspecting Figure 6.22 it can be seen that close to the trailing edge the rise in C_p caused by the strong longitudinal vortices is absent. This has a greater effect than the increase in C_p close to the near-side of the backlight.

It should be remembered that the backlight pressure on the 25° Ahmed model accounts for almost 50% of the overall drag force (see Figure 2.4). Subsequently, the variations in overall C_p over the backlight (up to around 34%) will have a large effect on the overall aerodynamic coefficients, which must be considered throughout analysis of the force and moment results.

6.3 Force and Moment Results

Figures 6.28 and 6.29 plot the variation in C_L and C_M respectively with changing wall separation for the 10°, 25° and 40° Ahmed models. Values are plotted as variations from the

a)

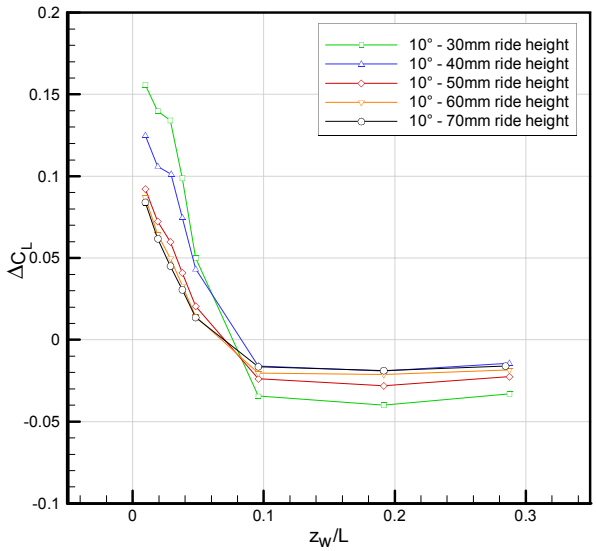

b)

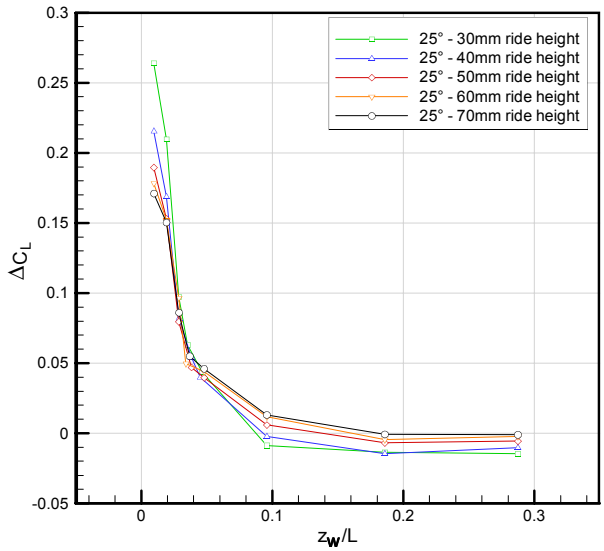

c)

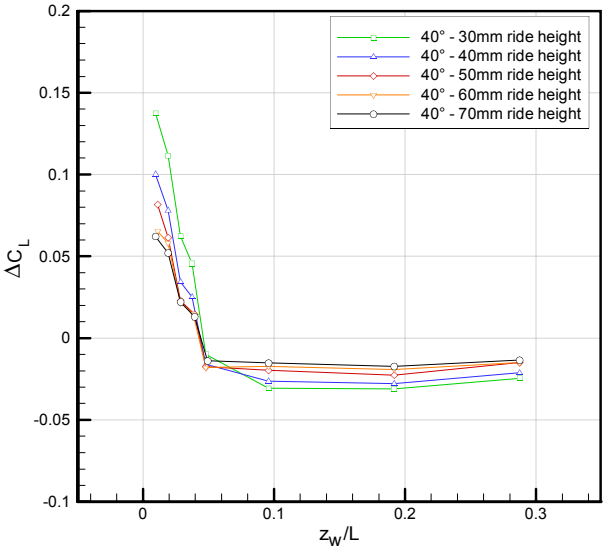

Figure 6.28 - Variation in lift coefficient (from force balance) with side wall proximity for various wall separations, ride heights and three Ahmed model configurations. (a)10° (b)25° (c)40° - Values plotted are variations from the equivalent isolated case

a)

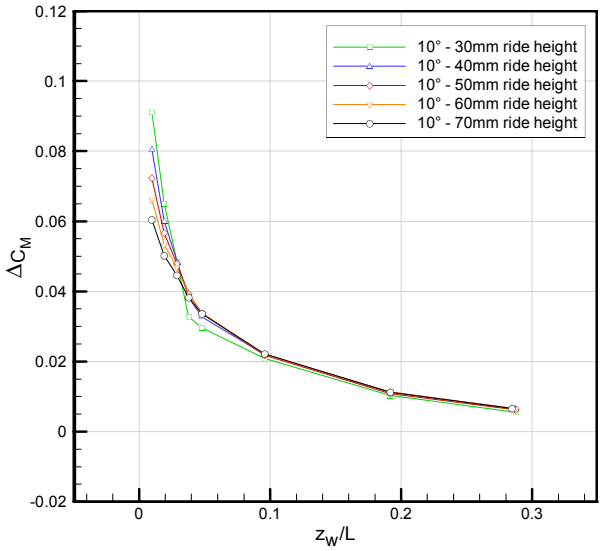

b)

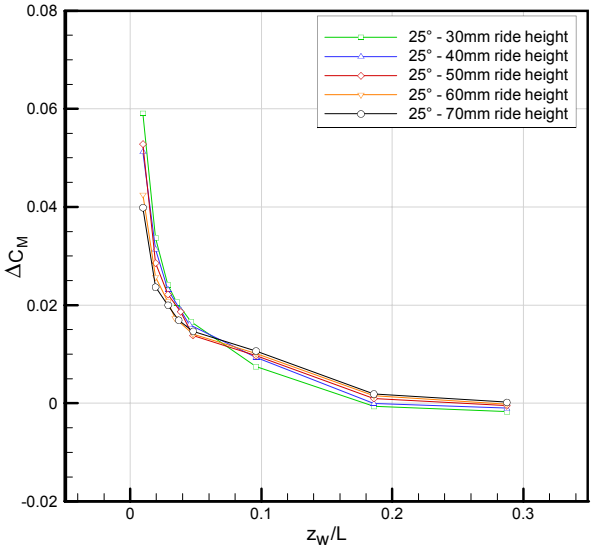

c)

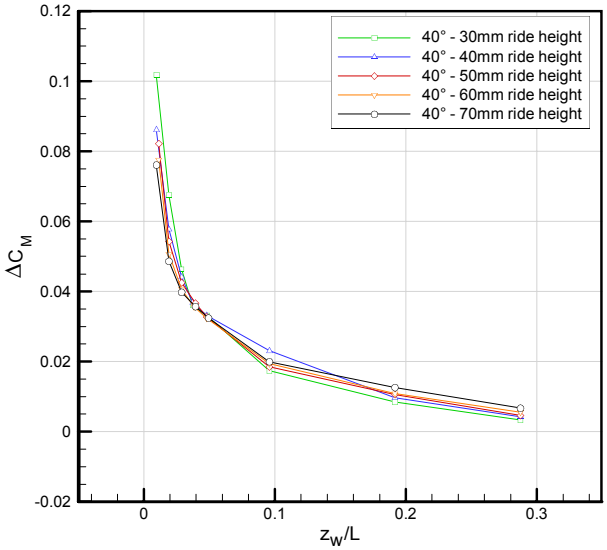

Figure 6.29 - Variation in pitching moment coefficient (from force balance) with side wall proximity for various wall separations, ride heights and three Ahmed model configurations. (a)10° (b)25° (c)40° - Values plotted are variations from the equivalent isolated case

corresponding isolated model cases. There is found to be a fall in lift coefficient between the isolated and z_w=0.287L cases for all model geometries and ride heights tested. It is also clear from Figure 6.27 that at a certain wall separation, which varies with model geometry, C_L increases rapidly and continues to do so as wall separation decreases further. It is clear, therefore, that up to a point wall proximity causes a larger drop in C_p under the model than on the top with the corresponding overall decrease in C_L. The wall separations at which the lift has reached a level above that measured on the corresponding isolated model are found to be 0.048L for the 10° case, 0.038L for the 40° case, and 0.192L/0.096L for the 25° backlight angle. Two wall separations are given for the 25° case as the results suggest this value is dependent on ride height. It appears, therefore, that wall separation has the greatest effect on the 25° model. This is confirmed by analysing the overall increase in C_L between the isolated and smallest wall separation cases for each backlight angle and for the extremes of the recorded ride heights. The 10° model experiences a rise in C_L of approximately 0.156 between these two wall separations at 30mm ride height, and just over half this increase (0.084) at 70mm ride height. The 25° model experiences a greater increase in C_L of approximately 0.264 at 30mm ride height, with around a 35% drop to an increase of 0.17 at 70mm ride height. Finally, the 40° model experiences the smallest increase in C_L between the isolated and nearest wall cases of 0.144 at 30mm ride height and 0.064 at 70mm ride height. It is therefore clear that the decrease in wall separation lowers the pressure in the region of the 25° model rear end suction peak and backlight by a greater amount than either the 10° or 40° backlights. Previous analysis showed the extent to which the lower backlight pressure prevalent in the 25° case increased flow velocity significantly upstream of the backlight leading edge. As such, the decrease in pressure with decreasing wall separation (also analysed previously) would be expected to have a similar effect over the top of the model. This would cause a larger increase in C_L than would be found by inspecting the effects of only the backlight and model front end. It is also seen from these results that there exists a more rapid increase in C_L with decreasing ride height, and that this is the case for all backlight angles tested. Owing to the separated flow over the 40° model, it must therefore be concluded that this effect is a result of the pressure drop over the front end and top of the model, rather than over the backlight.

It appears that as wall separation falls the previously-discussed (§6.2) pressure drop over the 25° model backlight is greater than the corresponding drop over either the 10° or 40° backlights, resulting in the larger overall increase in C_L between the isolated and nearest wall cases shown. Although previous analysis showed a relationship between the flow over the front and rear ends of the model, this was found to have only a minor effect. As such, the decrease in C_p over the front end suction peak with decreasing wall separation would be expected to be almost equal between the three tested model configurations. As there is a larger decrease in C_p over the 25° rear end though, there would be expected to be a smaller overall increase in C_M between the isolated and nearest wall cases at this backlight angle than

at the 10° backlight angle. Following the same reasoning, there would be expected to be a smaller increase in C_M over the 10° model than over the 40° model, owing to the expected lower pressure drop over the 40° back end as a result of the separated backlight flow. To analyse this we consider the plots of C_M against wall separation shown in Figure 6.29. There is found to be an overall increase in C_M between the isolated and nearest wall cases of the 10° model at 30mm ride height of 0.091, with corresponding increases of 0.059 and 0.101 over the 25° and 40° models respectively. This is in agreement with the expected results. At a ride height of 70mm this trend is continued with a rise in C_M of 0.06 over the 10° model, 0.041 over the 25° model, and 0.075 over the 40° model.

Figure 6.30 plots variations in C_D against changes in wall separation at a range of model ride heights. It is apparent there is little variation in C_D with ride height for all three backlight angles. The maximum variation was in fact found to be 0.015 over the 25° model at z_w=0.01L, with the maximum variation in the 10° and 40° cases found to be 0.01 and 0.005 respectively. The larger variation over the 25° case was expected from analysis of the variation in C_L with ride height, due to its larger backlight projected frontal area in comparison to the 10° case and the subsequent increased effect of what appear to be similar backlight pressure changes. Also, the lowest variation in C_D with ride height experienced by the 40° model was also expected as a result of the lack of significant backlight pressure changes as a result of the separated flow in this region.

Inspection of Figure 6.30 also reveals an evident increase in C_D with decreasing wall separation for the three model geometries. Between the isolated and nearest wall cases there is an increase in C_D of 0.142 on the 10° model, 0.111 on the 25° model, and 0.134 on the 40° model, with each measurement taken at 30mm ride height. The larger pressure drop over and upstream of the 25° model backlight which caused the highest increase in C_L of the three configurations, would also be expected to cause a large increase in C_D. In fact at the three wall separations for which pressure readings were taken, the drop in C_p over the 25° backlight was found to increase the contribution to the overall C_D of the backlight by 0.033 at z_w=0.192L, 0.04 at z_w=0.096L, and 0.05 at z_w=0.048L. This corresponds to 82.5%, 80% and 76% of the overall drag increase experienced by the 25° model at 0.192L, 0.096L and 0.048L from the wall respectively. In each case these values were calculated from the average C_p over the pressure tapped backlight. It is therefore clear that at these wall distances the backlight pressure changes have the greatest effect on the C_D of the 25° model. It also appears that although pressure changes and subsequent influence on C_D would be expected over the model front end, these are secondary to alterations over the model rear. As the 10° and 40° models experience larger increases in C_D than the 25° model, it must be assumed that variations in C_p over the vertical rear of the model are significant. However, as pressure readings were not taken in this region, nor over the 10° and 40° backlights, further

a)

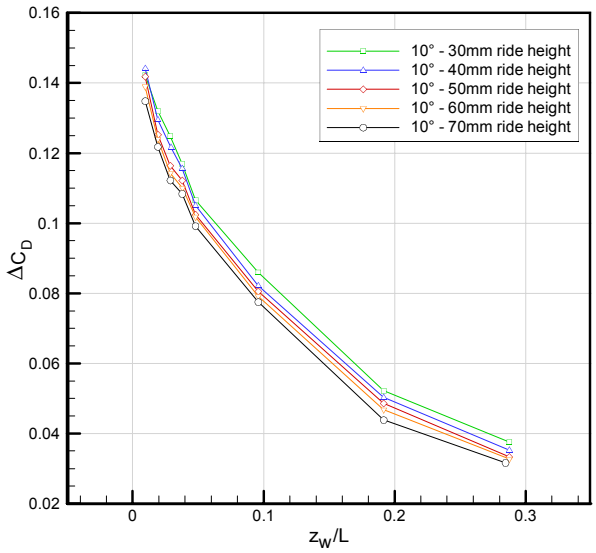

b)

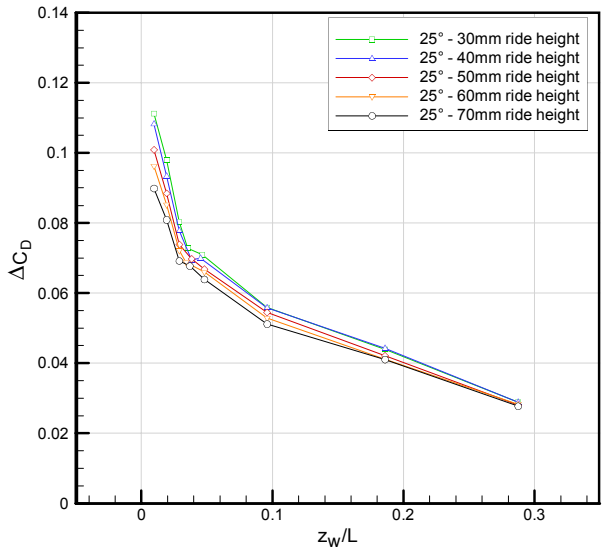

c)

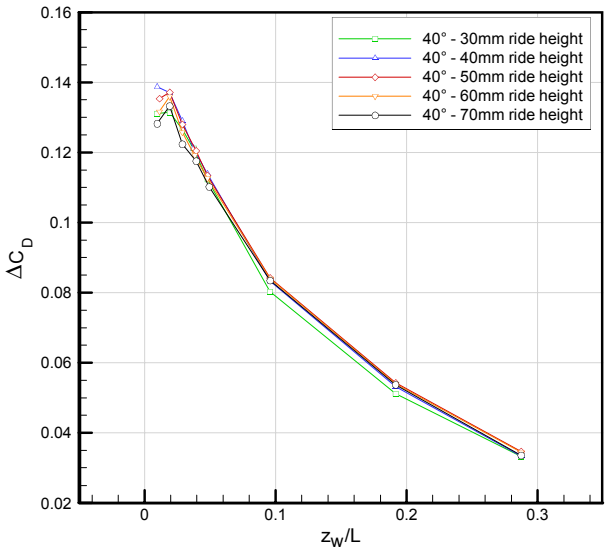

Figure 6.30 - Variation in drag coefficient (from force balance) with side wall proximity for various wall separations, ride heights and three Ahmed model configurations. (a)10° (b)25° (c)40° - Values plotted are variations from the equivalent isolated case

a)

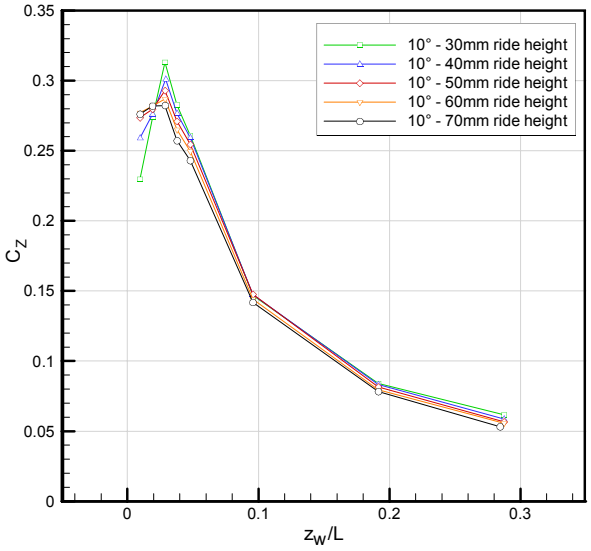

b)

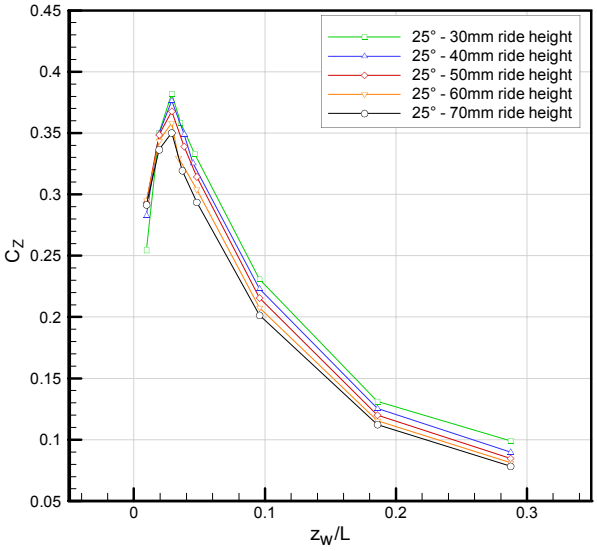

c)

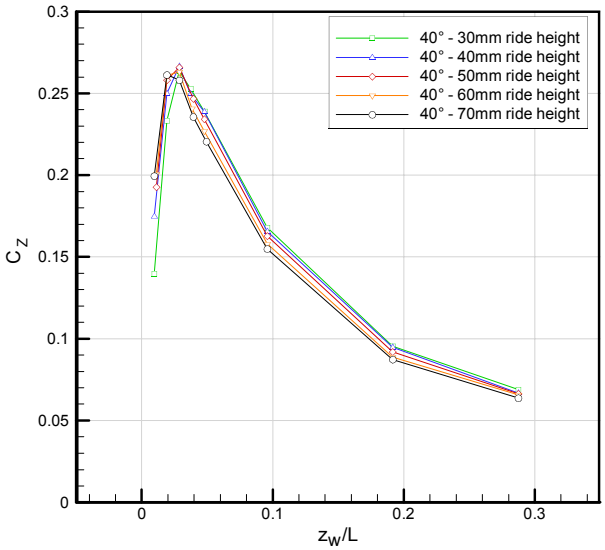

Figure 6.31 - Variation in side force coefficient (from force balance) with side wall proximity for various wall separations, ride heights and three Ahmed model configurations. (a)10° (b)25° (c)40°

investigation of the variations in C_D cannot be conducted from the available experimental data.

Figure 6.31 plots variations in side force coefficient over the three model configurations with wall separation, with positive values of C_Z corresponding to a force towards the side wall. It is clear that for all model configurations, ride heights and wall separations tested, there remains a positive value of C_Z. It is equally apparent from Figure 6.31 that for each of the three backlight angles, and at almost all of the recorded ride heights, there exists a maximum measured C_Z at z_w=0.029L, after which there is a decrease which becomes more rapid with further decreasing wall separation. It would be expected that this positive side force is a result of the pressure drop between the side of the model and the wall with decreasing separation, similar to the effect observed in the C_L variation with decreasing ride height. The sudden drop in side force is also expected to be the effect of the wall and model boundary layers and resultant pressure distribution restricting the flow. This decrease was not found when examining the variation of C_L with ride height in Figure 6.28 (where this effect would naturally have produced an increase in C_L) as the lowest tested ride height was 30mm (0.029L), the same wall distance at which the highest values of C_Z were measured. In addition, the inclusion of ground simulation in the form of a rolling road would reduce the ride height at which viscous effects would become significant in comparison to the side wall, on which boundary layer control was not employed. The sharp decrease in C_Z close to the wall has not been shown to cause a negative side force at any of the wall distances measured, however, if the extreme case (model touching wall) is considered it becomes clear that there must come a point where the side force will act away from the wall.

Attention must also be paid to the geometry of the model front end. The increased suction between the wall and the near-side of the model would be expected to relocated the stagnation point on the model front closer to the wall. Owing to the shape of the model this increase in pressure would cause a negative (away from wall) side force. It would be expected that this increase would be greater than the resulting pressure drop over the off-side of the front end, resulting in an overall negative C_Z contribution from this section of the model. From the plots it is clear that this effect is less significant than the afore-mentioned pressure drop over the near-side of the model, but nonetheless must be considered during analysis. The maximum value of C_Z was found to be 0.31 in the 10° case, 0.38 in the 25° case, and 0.27 in the 40° case. The higher value of C_Z in the 25° case is most likely a result of the lower pressure at the rear end suction peak causing a larger pressure gradient over the near-side of the model.

In both the 10° and 40° cases the plots of C_N against wall separation (Figure 6.32) exhibit a gradual increase with decreasing wall separation before a drop in yawing moment as the model is brought closer to the side wall, with the exact point at which this shift occurs being

located closer to the wall with decreasing ride height. There also exists a large increase in C_N between z_w=0.019L and z_w=0.001L for the 10° and 40° cases, which is not consistent with the 25° case. Closer inspection though reveals that despite the large variations in C_N between the three model geometries at z_w=0.019L (up to approximately 0.02, or 50% of the overall values), variations at z_w=0.001L are found to be only around 0.004, now around 6% of the overall values. Clearly, at wall separations less than 0.019L, the effects of the backlight angle become largely insignificant in terms of the yawing moment of the model. Instead, the forces which dominate at the front end determine this value.

The variation in rolling moment coefficient (C_R) with wall separation (z_w) for all the model configurations tested is plotted in Figure 6.33. There are three areas on the model which would be expected to have significant effects on C_R. Firstly, the increased pressure over the near-side section of the model front end would be expected to be skewed toward the ground plane as a result of the lowered pressure over the model top, subsequently imparting a negative (clockwise if looking from behind the model) rolling moment. Secondly, the lowered pressure over the model top is skewed towards the near-side, resulting in a positive rolling moment. Thirdly, the pressure drop over the near-side of the model would be expected to be skewed toward the top of the model as a result of the lower pressure in that region. This would contribute a negative rolling moment to the model. Pressure analysis over the 25° backlight also showed significant variations in pressure with wall separation very close to the model sides as a result of changes in longitudinal vortex strength. As the near-side vortex was found to decrease in strength, with the subsequent increase in pressure over the model, with the opposite effect on the off-side vortex, the net result would be a positive rolling moment on the model. As the strength of these vortices at 25° has been shown to be far greater than their counterparts on the 10° model, and as they are not formed over the 40° model, any discernable effect they may have on C_R would only be expected in the 25° model results. However, even in the case of the 25° model, these effects would not be expected to contribute a large rolling moment in terms of the overall model C_R.

It can be seen from Figure 6.33 that for all bar one of the recorded cases there was found to be a negative rolling moment on the model. This suggests that, in general, the increased pressure over the front end and pressure drop over the near-side have a greater effect on the rolling moment than the pressure drop over the top of the model. It is also clear, though, that at z_w=0.029L wall separation there exists in every tested configuration a minimum C_R, and as wall separation falls further there is a significant increase in rolling moment. Referring back to the plots of C_Z against wall separation (Figure 6.31) it was shown that at 0.029L wall separation there was evidence of the boundary layers on the model and wall restricting the flow between them. This would lead firstly to the previously-discussed drop in suction between the wall and the model, and secondly to the drop in pressure over the near-side section of the

a)

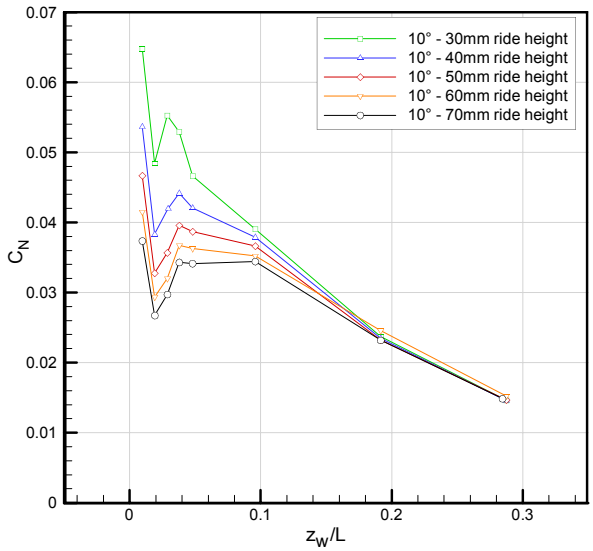

b)

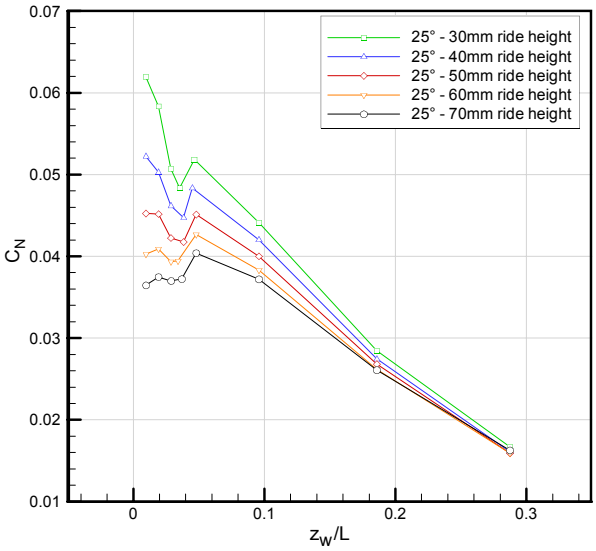

c)

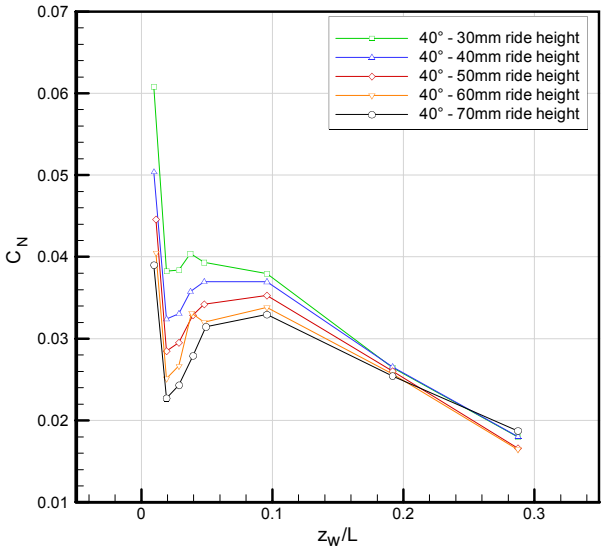

Figure 6.32 - Variation in yawing moment coefficient (from force balance) with side wall proximity for various wall separations, ride heights and three Ahmed model configurations. (a)10° (b)25° (c)40°

a)

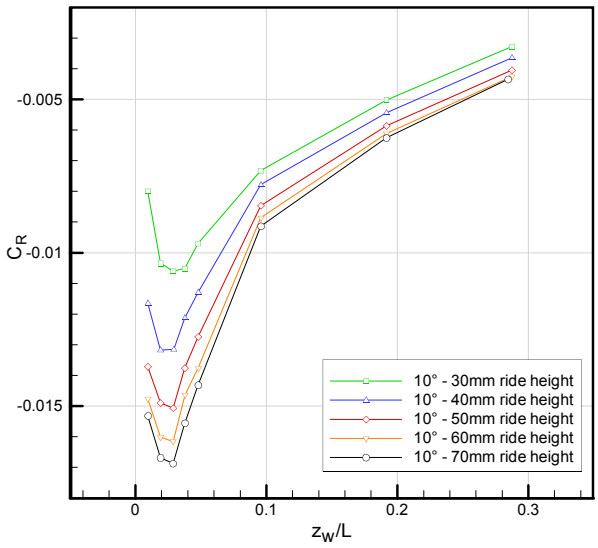

b)

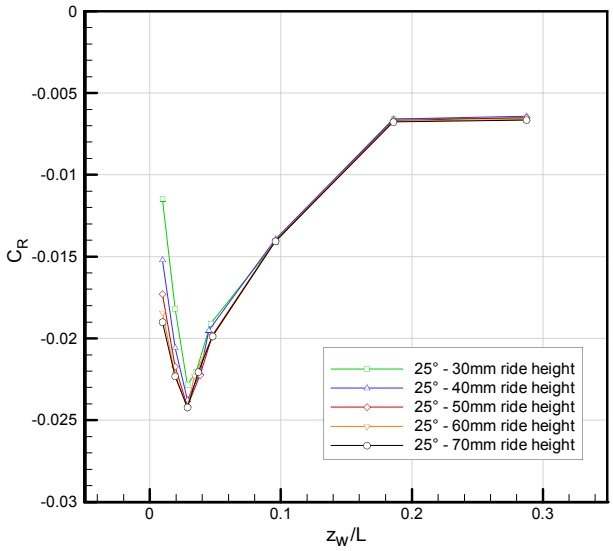

c)

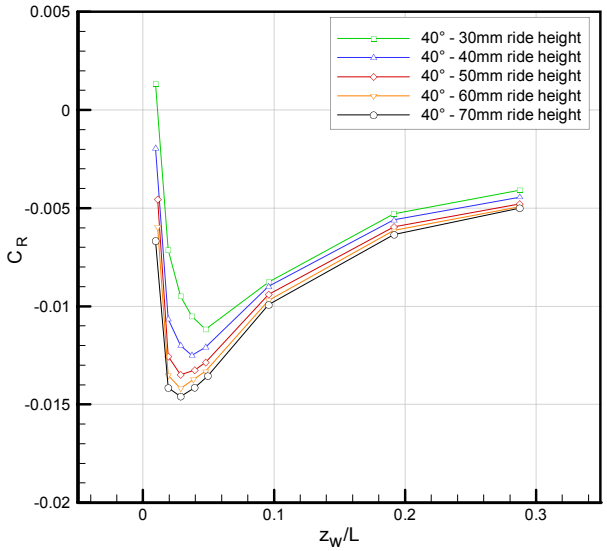

Figure 6.33 - Variation in rolling moment coefficient (from force balance) with side wall proximity for various wall separations, ride heights and three Ahmed model configurations. (a)10° (b)25° (c)40°

model front end. As a result, there is at this point a significant shift not only in side force but also in rolling moment, as it is these model sections which have the greatest effect on both model C_R and C_Z.

It is apparent from Figure 6.33 that the minimum values of C_R are also significantly influenced by the backlight angle of the model. Indeed, these are found to be -0.017 for the 10° model, -0.024 for the 25° model, and -0.0145 for the 40° model, in each case the results being taken for the 70mm ride height cases, where these minima are lowest. Referring again to the C_Z against wall separation graph of Figure 6.31 these variations between the backlight angles can be readily explained. It was found that there was very similar variation in the maximum levels of side force between the three model configurations, corresponding to the greater suction between the wall and the 25° model than either the 10° or 40° models, with the subsequent effect on the overall rolling moment. As such the minimum rolling moment on the 25° case is lower than the 10° case, which is again lower than the 40° case.

From Figure 6.33 it can also be seen that there is a significant variation in C_R with ride height for the 10° and 40° model configurations, but that this is not evident in the 25° model results. There is a variation of 0.0063 between the minimum recorded values of C_R at the 30mm and 70mm ride heights of the 10° model, a corresponding variation of 0.0052 for the 40° model, but a variation of only 0.0015 for the same configurations of the 25° model. In each of the model configurations though there is a decrease in C_R with increasing ride height. This is the expected result of the lower pressure which would be evident over the near-side of the model front end and reduced suction between the model and side wall.

6.3.1 Summary of Force and Moment Results

The following main points provide an overview of the variation of aerodynamic forces and moments experienced by the Ahmed model with decreasing wall separation.

- C_L drops slightly as the model approaches the wall, as a result of increased suction under the model. At smaller wall separations however, the increased suction over the top of the model front end becomes dominant in the variation of lift, causing a rapid increase in C_L when the wall is in close proximity.

- C_D increases with decreasing wall separation for all tested configurations. In the 25° model case it is found that this is predominately a result of the large pressure drop over the backlight.

- C_Z acts towards the side wall for all tested configurations. However, the increase in side force with decreasing wall separation reaches a maximum point before experiencing a rapid

decrease. This is thought to be a result of the boundary layer restricting the flow between the wall and the model at small separations.

• C_M increases with falling wall separation for all tested cases, owing to the concentration of the pressure drop over the top of the model near the leading edge. At the closest wall separations measured, where the drop in pressure over the top of the model is greater than that on the underside (causing the increase in C_L), C_M experiences a more rapid increase.

• C_N is found to be positive (nose away from wall) in all the tests conducted. This is a result of the increase in C_p on the lower near-side section of the model front end being the dominant factor in the overall value of C_N for all wall separations tested.

• C_R decreases with falling wall separation up to a point. At smaller wall separations, where the boundary layer growth on the body near-side and on the side wall has restricted the flow between the model and wall and both the high pressure over the near-side of the front end and the pressure drop over the near-side fall, C_R begins to increase rapidly.

7. Near-Wall Model Computational Results and Discussion

The CFD for the Ahmed model in wall proximity will be analysed in this chapter. CFD data will first be validated against experimental data, accounting for differences outlined previously between the isolated-model experiments and the CFD, before additional data are extracted from the computational model in order that additional flow features, which could not be recorded by the experiments, can be analysed.

7.1 CFD Validation

7.1.1 Front End

Figure 7.1 plots profiles of streamwise velocity at the model centreline (z/L=0) over the top front end of the 25° Ahmed model. Both computational and experimental results are shown for comparison. As was found during analysis of the experimental data, there is for each wall

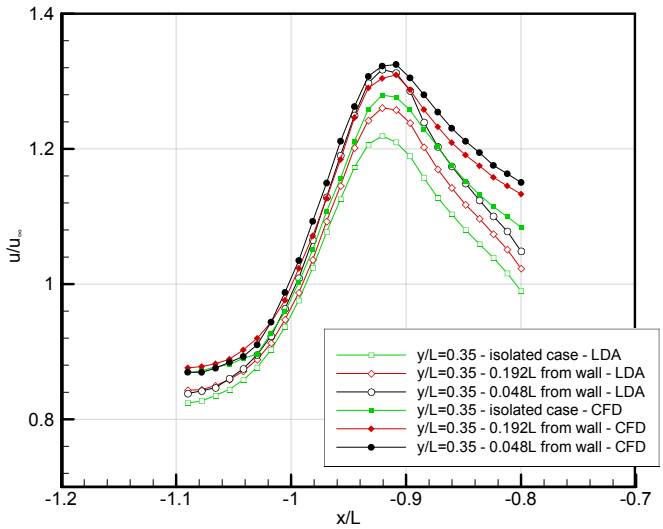

Figure 7.1 - Streamwise profiles of normalised u velocity at model centreline (z/L=0) over front end of 25° Ahmed model at various wall separations - CFD and experimental data

separation measured a higher predicted streamwise velocity in comparison to the isolated case in the region shown. It is clear though that the overall difference in streamwise velocity at the upstream suction peak between the isolated and nearest wall (z_w=0.048L) cases is lower in the computational case than was recorded experimentally. The experimentally measured increase between these cases was found to be approximately $0.1u_\infty$, whereas the CFD predicted an increase of only around $0.04u_\infty$. In addition, the majority of this increase (≈58%) was found to occur between wall separations of 0.096L and 0.048L in the experiments, whereas most of the computationally-predicted increase (≈62%) occurred between the isolated case and a wall separation of 0.192L. It appears, therefore, that as wall separation falls the CFD predicts a drop in the rate of increase in suction over the model top (at the model centreline), whereas the opposite is true in the experimental case. If this trend is continued over the near-side of the model top, where the largest changes in suction occur, it would be expected that the rapid increases in C_L and C_M as wall separation falls would not be well predicted by the computational model. It would also be expected that at wall separations less than the 0.048L case shown here the computational model would in fact under-predict the maximum streamwise velocity, in contrast to isolated model results.

At the furthest downstream point plotted in Figure 7.1 (x/L=-0.8), the higher computationally-predicted streamwise velocity in comparison to the experimental data found in the isolated case is continued for all measured near-side positions. The variation between the CFD and experiments at this position remains virtually constant at $0.1u_\infty$.

7.1.2 Backlight Flow

To investigate both the computationally-predicted streamwise velocity away from the model centreline and the flow over each of the three model backlights, Figures 7.2 - 7.4 plot boundary layer profiles at z/L=±0.077 near the backlight leading edge and at the model trailing edge. The trailing-edge profiles for the 40° case are omitted because of the separated backlight flow. As before all profiles are plotted against height above the model surface, rather than in absolute values of y/L.

Initial inspection of each of the plots shown in Figures 7.2 - 7.4 highlights again the higher streamwise velocity at the highest plotted point from the model surface which is predicted by the CFD in comparison to the experiments, consistent with the isolated model analysis. It is found though that the overall increase in this velocity with decreasing wall separation is, for each of the investigated backlight angles, predicted significantly lower than experimental results by the CFD. At the near-side position (z/L=0.077), the CFD predicts a 35% smaller increase in this streamwise velocity in the 10° case between the isolated and nearest wall (z_w=0.048L) sets of results, with variations of 25% and 60% for the 25° and 40° model cases

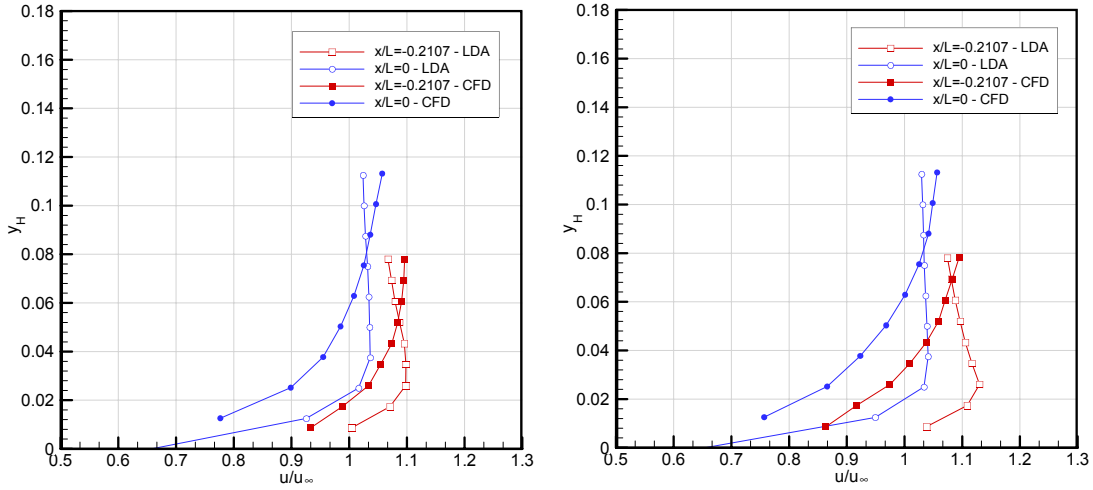

a) z_w=0.192L, z/L=-0.077 b) z_w=0.192L, z/L=+0.077

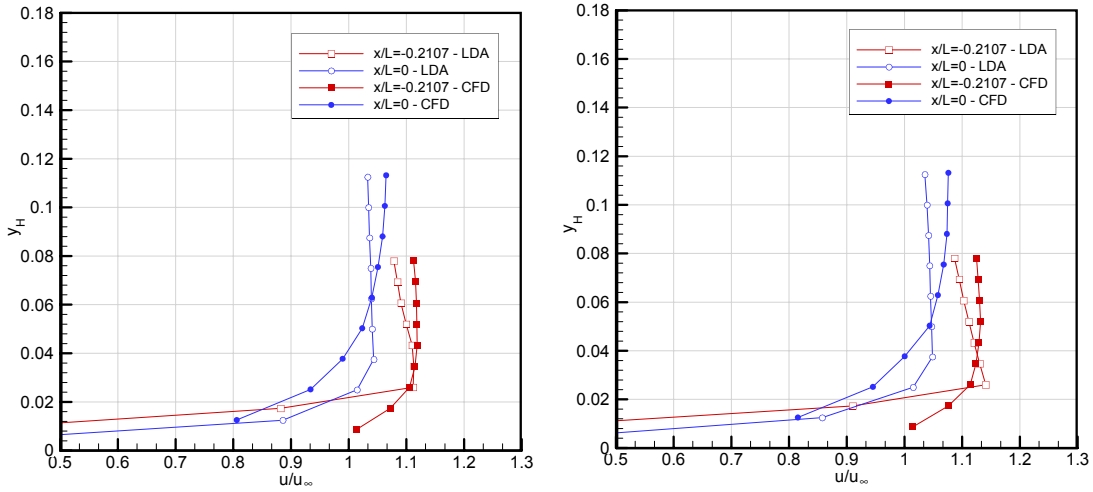

c) z_w=0.096L, z/L=-0.077 d) z_w=0.096L, z/L=+0.077

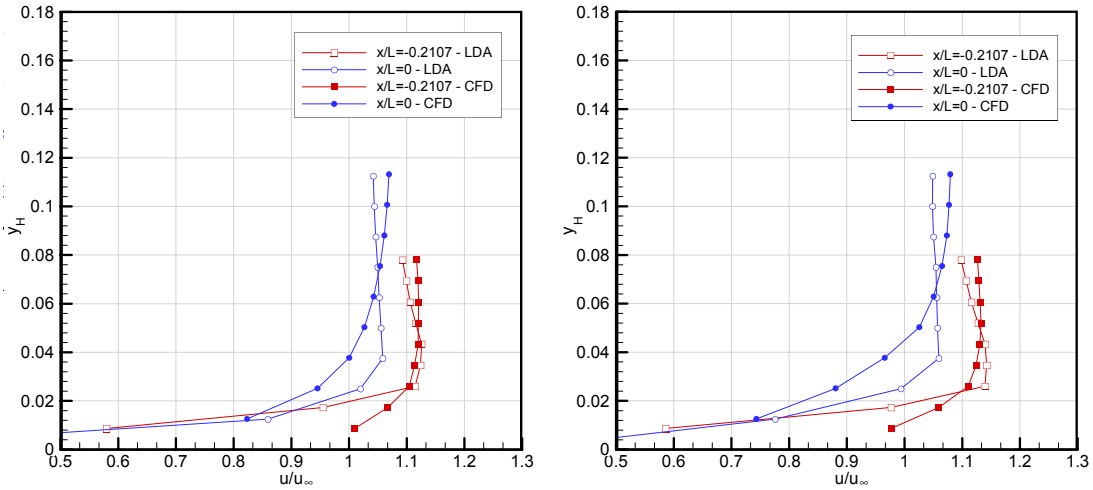

e) z_w=0.048L, z/L=-0.077 f) z_w=0.048L, z/L=+0.077

Figure 7.2 - Boundary layer profiles at z/L=±0.077 over 10° Ahmed model at various wall separations - CFD and experimental data

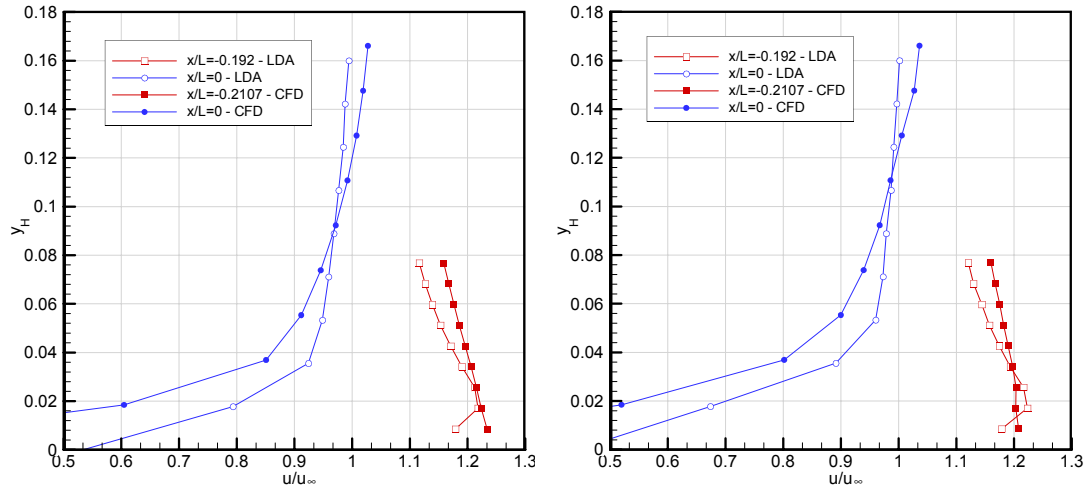

a) z_w=0.192L, z/L=-0.077 b) z_w=0.192L, z/L=+0.077

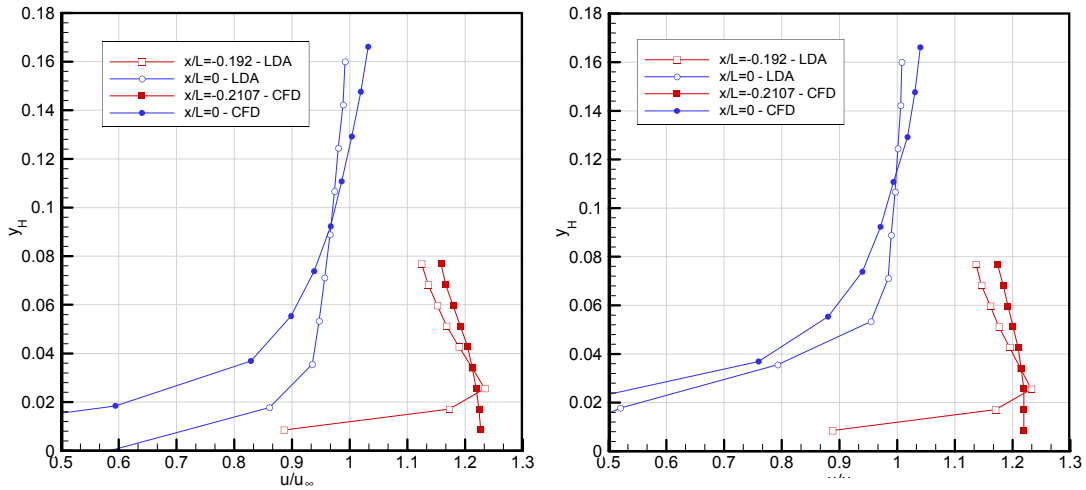

c) z_w=0.096L, z/L=-0.077 d) z_w=0.096L, z/L=+0.077

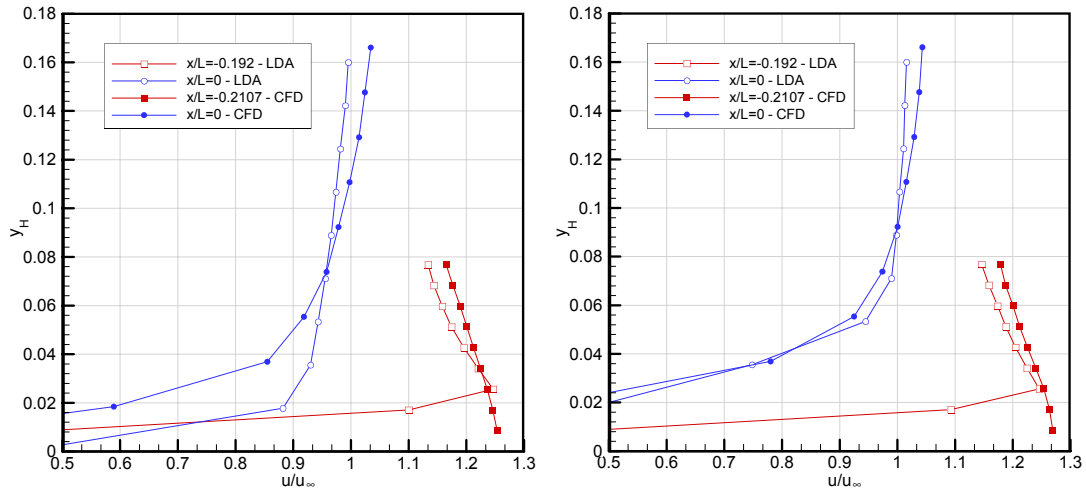

e) z_w=0.048L, z/L=-0.077 f) z_w=0.048L, z/L=+0.077

Figure 7.3 - Boundary layer profiles at z/L=±0.077 over 25° Ahmed model at various wall separations - CFD and experimental data

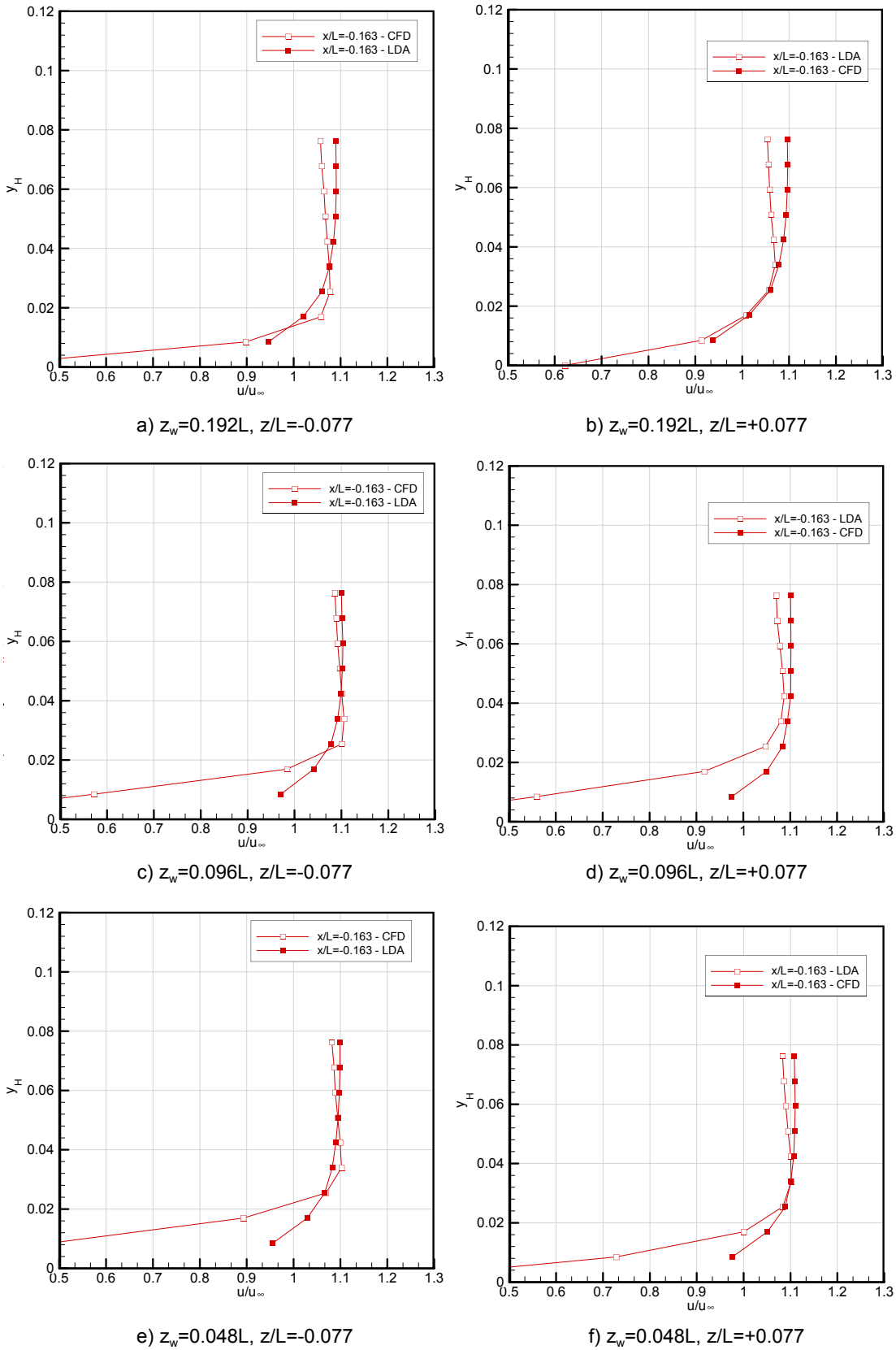

Figure 7.4 - Boundary layer profiles at z/L=±0.077 over 40° Ahmed model at various wall separations - CFD and experimental data

respectively. On the off-side (z/L=-0.077) there exists a similar trend, with the CFD predicting lower streamwise velocity increases between the isolated and nearest wall cases of approximately 62%, 66% and 64% for the 10°, 25° and 40° model cases respectively. It is clear though that these variations are more consistent than those found at the near-side position.

These results are readily understood when the effect of the supporting strut, not included in the computational model, is considered. It was shown previously the extent to which the retarded flow in the wake of the strut was inclined towards the near side of the model as wall separation fell, causing lower streamwise velocity to be measured at the near-side position shown than would be the case were the strut to be removed. This lowered velocity will cause the under-predicting computational model to report values closer to that of the experimental case than at the off-side position where the relocation of the strut wake has less effect. It was also shown previously that the higher suction level near the side wall in the 25° case in comparison to the 10° and 40° cases resulted in a larger inclination of the strut wake toward the wall. Subsequently, there would be expected to be a greater effect of the strut wake in lowering the streamwise velocity at the near-side position shown in the 25° case than at either the 10° or 40° cases, confirmed by the smaller under-prediction of the streamwise velocity reported above. This is continued in the smaller under-prediction in the 10° case in comparison to the 40° case, as a result of the same effect, albeit less than that on the 25° model.

It appears, therefore, that the smaller computationally-predicted increase in velocity over the model front end is continued downstream. It would be expected that overall C_L variations with changing wall separation would be lower in the CFD than were measured experimentally, owing to the predicted lower suction over the model top. It should be noted that the CFD does predict both the variation in velocity between the near and off-side positions shown and the increase in streamwise velocity between the 40°, 10° and 25° model configurations respectively. The differences in the magnitudes of these variations from experimental results though must be taken into account when analysing the computed forces.

Considering now the boundary layer profiles taken at z/L=±0.077 at the trailing edges of the 10° and 25° models (Figures 7.2 and 7.3) a number of observations can be made. It must be remembered that, particularly in the case of the 25° model, the experimental results showed that the boundary layer at this point is greatly dependent on the formation of the longitudinal vortices, and that it was found during isolated model analysis that the CFD model under-predicts the strength of these vortices. It was also found during analysis of the pressure distribution over the isolated model 25° backlight in the CFD that, unlike in the experiments, the longitudinal vortices had little influence away from the sides of the backlight. The flow,

instead, closely resembled the two-dimensional case found below the first critical angle (12.5°). As a result, the inclusion of the side wall and subsequent longitudinal vortex variations were not found to alter the trailing-edge boundary layer in the computational model in the same way as was observed experimentally.

Instead of the increase in boundary layer thickness at z/L=0.077 found at the trailing edges of both the 10° and 25° near-side experimental cases, with the opposite effect at z/L=-0.077, there was, between the isolated and z_w=0.048L cases, a decrease in boundary layer thickness predicted at both these transverse positions by the CFD. This is further evidence of the inability of the computational model to accurately model the backlight flow, and in particular the effects of the longitudinal vortices. Using the same measure of boundary layer thickness as outlined previously, the CFD predicts a decrease in thickness of approximately 0.01L at z/L=0.077 on the trailing edge of the 25° model, in comparison to an experimentally-measured increase of around 0.027L. This is continued for the 10° model where, at the near-side position (z/L=0.077), the CFD predicts a decrease in boundary layer thickness of approximately 0.004L in comparison to the experimentally-measured increase of approximately 0.014L. Despite this, the CFD does predict the expected variation in boundary layer thickness between the near and off-side positions when the model is in wall proximity. There is found to be a decrease in boundary layer thickness of approximately 0.004L between the near-side and off-side positions on the 25° model trailing edge, in comparison to a decrease of 0.027L between the same positions measured experimentally. Owing to experimental difficulties outlined earlier the same boundary layer variation over the 10° model could not be accurately assessed, but the CFD predicts an increase in height of approximately 0.002L between the near and off-side positions at the trailing edge. This is significantly less than that predicted by the CFD over the 25° case, in line with expectations.

Contours of vertical velocity and in-plane streamlines above the trailing edge of the 10° model at various distances from the side wall are plotted in Figure 7.5. Initial inspection reveals the expected significant variation in the structure of the near-side longitudinal vortex. It is also clear that the off-side vortex is not altered by the same degree, in line with experimental observations. Additionally, it can be seen from the streamlines plotted that the expected tendency of the flow over the model to travel toward the low pressure region on the near-side is evident, particularly in the z_w=0.096L and z_w=0.048L cases. The increased vertical velocity between the model and the side wall caused by the low pressure region over the near-side model top, and thought to be partially responsible for the observed increase in near-side longitudinal vortex centre height, is also evident in the z_w=0.048L case (Figure 7.5 (c)).

To quantify alterations in the strengths of the longitudinal vortices and compare with experimental analysis, we will consider again the maximum and minimum recorded v

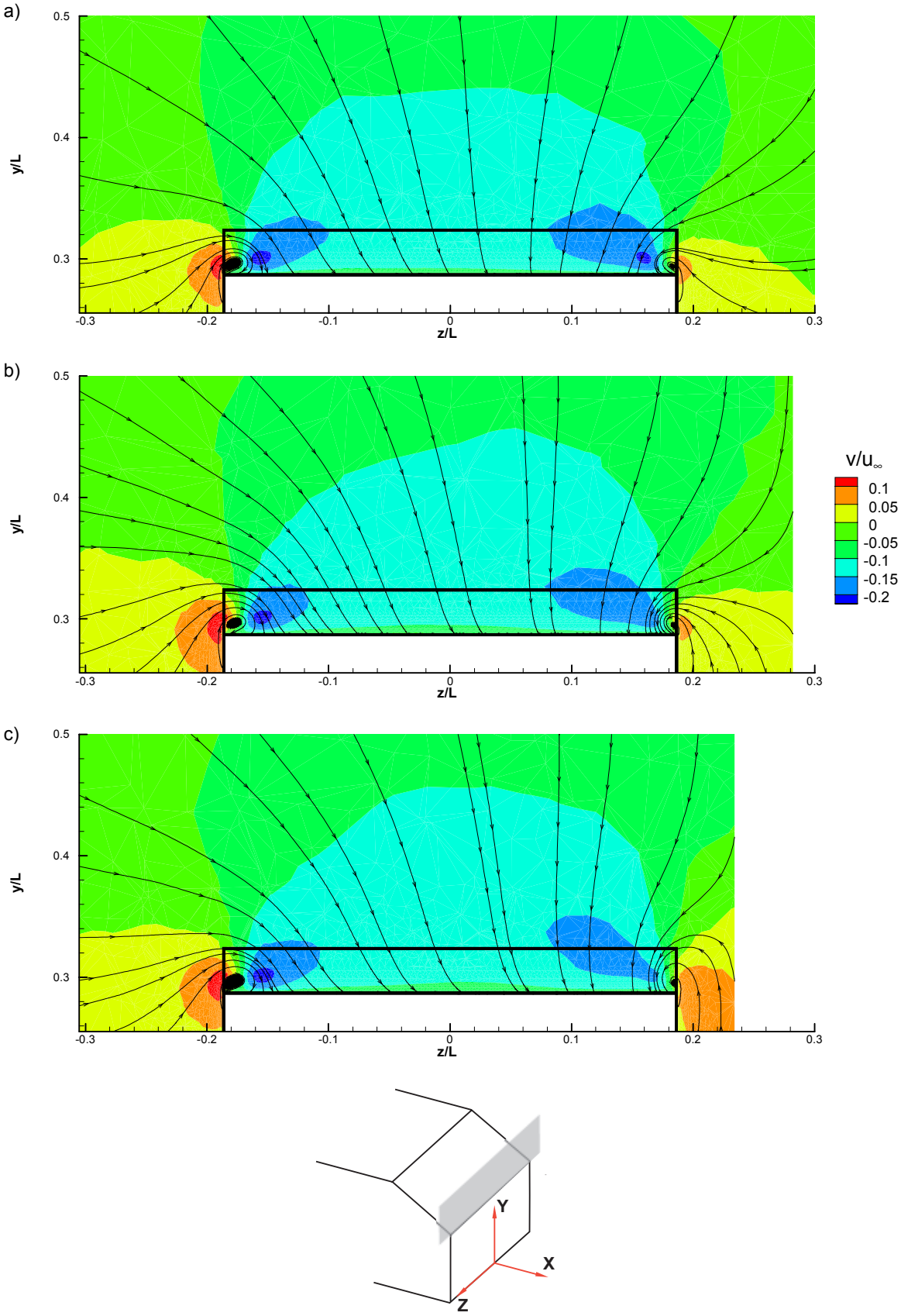

Figure 7.5 - Contours of normalised v velocity and in-plane streamlines above the trailing edge of the 10° Ahmed model - CFD data a)z_w=0.192L b)z_w=0.096L and c)z_w=0.048L from side wall

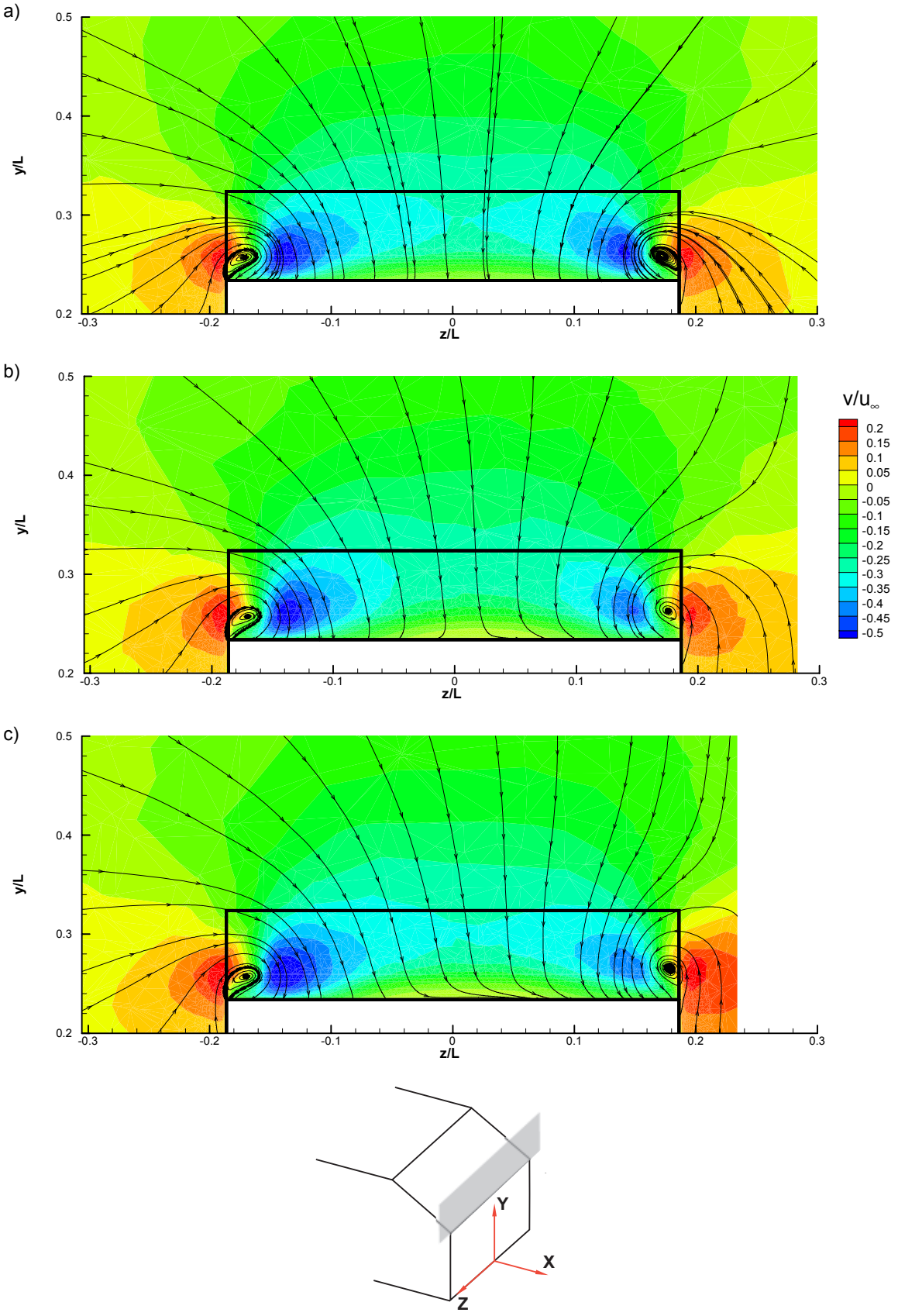

Figure 7.6 - Contours of normalised v velocity and in-plane streamlines above the trailing edge of the 25° Ahmed model - CFD data a)z_w=0.192L b)z_w=0.096L and c)z_w=0.048L from side wall

velocities near the model sides. It was found experimentally that between the isolated and z_w=0.048L 10° model cases there exists an increase in maximum v velocity of $0.02u_\infty$ in the region of the off-side vortex with an almost identical drop in minimum v velocity. In the computation, however, there was a predicted increase in maximum v velocity of only $0.01u_\infty$, approximately half of the experimental value. There was also found to be no predicted variation in the minimum v velocity. In the case of the near-side longitudinal vortex, the experiments recorded a larger increase in the minimum v velocity of approximately $0.06u_\infty$ between the isolated and nearest wall (z_w=0.048L) cases. In comparison the CFD predicted an increase of around $0.055u_\infty$. It appears that the alteration in vortex strength is predicted more closely by the CFD for the near-side vortex than for the off-side one.

The movement of the longitudinal vortex centres at the 10° model trailing edge toward the near-side as z_w decreased was also analysed from the experimental results, albeit without the third velocity component, allowing only an estimate of this variation to be made. It was shown that the off-side vortex centre was moved approximately 0.002L towards the side wall with a similar movement of approximately 0.022L of the near-side longitudinal vortex centre between the isolated and z_w=0.048L cases. The CFD, however, predicts a relocation of the off-side vortex centre of approximately 0.001L towards the side wall with the near-side vortex centre moving by 0.0065L between these cases. It seems that the computational model again under predicts the effects of wall proximity on the near-side of the model, with a greater under-prediction on the off-side, in line with analysis of the longitudinal vortex strength.

It is also clear from Figure 7.5 that the CFD under-predicts the upward shift of the near-side longitudinal vortex centre in comparison to the experiments. It was shown that the position of minimum v velocity was found to be above the height of the model at the trailing edge of the 10° backlight when z_w=0.048L, clearly not the case in the computation. It is thought that this large discrepancy is a result of the breakdown of this vortex in the experiments, an occurrence not consistent with the CFD.

Examining the corresponding 25° model plots in Figure 7.6, the variations in longitudinal vortex structure with decreasing side wall separation can again be seen. In particular the stronger vortex strength and the subsequent effects on the in-plane streamlines in comparison to the 10° cases are evident. There was found during the experiments to be an increase in magnitude of the maximum and minimum v velocities close to the off-side of the 25° model trailing edge between the isolated and nearest wall cases of approximately $0.02u_\infty$ and $0.055u_\infty$ respectively. This compares to the computationally-predicted variation of $0.01u_\infty$ in the maximum v velocity with no variation in minimum v velocity between the isolated and z_w=0.048L cases. This is in line with comparisons made between CFD and experiments for the 10° model case. The experiments also recorded a decrease in magnitude of minimum v

velocity close to the near-side of the 25° model trailing edge of approximately $0.15u_\infty$, again between the isolated and z_w=0.048L configurations. As before, the CFD under-predicts this wall effect, reporting a corresponding drop of only approximately $0.085u_\infty$.

The variations in the vortex centre positions toward the side wall between the isolated and z_w=0.048L cases were estimated from the experimental data to be 0.02L and 0.04L for the off-side and near-side vortices respectively. As discussed previously these variations are significantly greater than those over the 10° Ahmed model. The CFD, however, predicted a shift of only around 0.002L and 0.007L for the off-side and near-side vortices respectively. Although these computationally predicted vortex centre movements are greater than those predicted for the 10° model, the differences between the two cases are far less than those measured experimentally. It is also clear in Figure 7.6, as it was in Figure 7.5, that unlike the experiments, significant breakdown of the near-side longitudinal vortex has not taken place at the 25° model trailing edge when at 0.048L wall separation.

It is therefore clear that the general trends in both longitudinal vortex strength and position with decreasing wall separation predicted by the CFD correlate well with those observed experimentally. However, the magnitudes of these variations and the effects on the 25° backlight flow in particular are not accurately modelled by the computations.

7.1.3 Static Pressure Results

The pressure distributions over the 25° backlight are plotted in Figure 7.7 for the same wall separations as in the experiments. Figure 7.7 is also plotted on the same scale as that which was used on the corresponding experimental plots (Figure 6.23) to aid comparison between the two. Initial inspection reveals again that the CFD under-predicts the strength of the longitudinal vortices on both sides of the 25° model backlight. This can be seen both from the higher static pressure (hence lower velocity) at both sides of the backlight leading edge and the shorter distance downstream to which the lowest pressure region (C_p<-1) extends in comparison to the experiments. It is also evident that at each of the wall distances plotted in Figure 7.7 there still appears to be little or no effect of the longitudinal vortices on the pressure distribution over the central section of the backlight, which was not the case in the experimental results.

It can also be seen, however, that the CFD predicts an increase in the strength of the off-side longitudinal vortex with decreasing wall separation, shown in the reduction in static pressure near the off-side leading edge, with the reverse effect occurring at the near-side of the backlight. This is in line with experimental data and would be expected from previous analysis of numerical predictions of the vertical velocities at the 25° model trailing edge. To quantify the

a)

b)

c)

d)

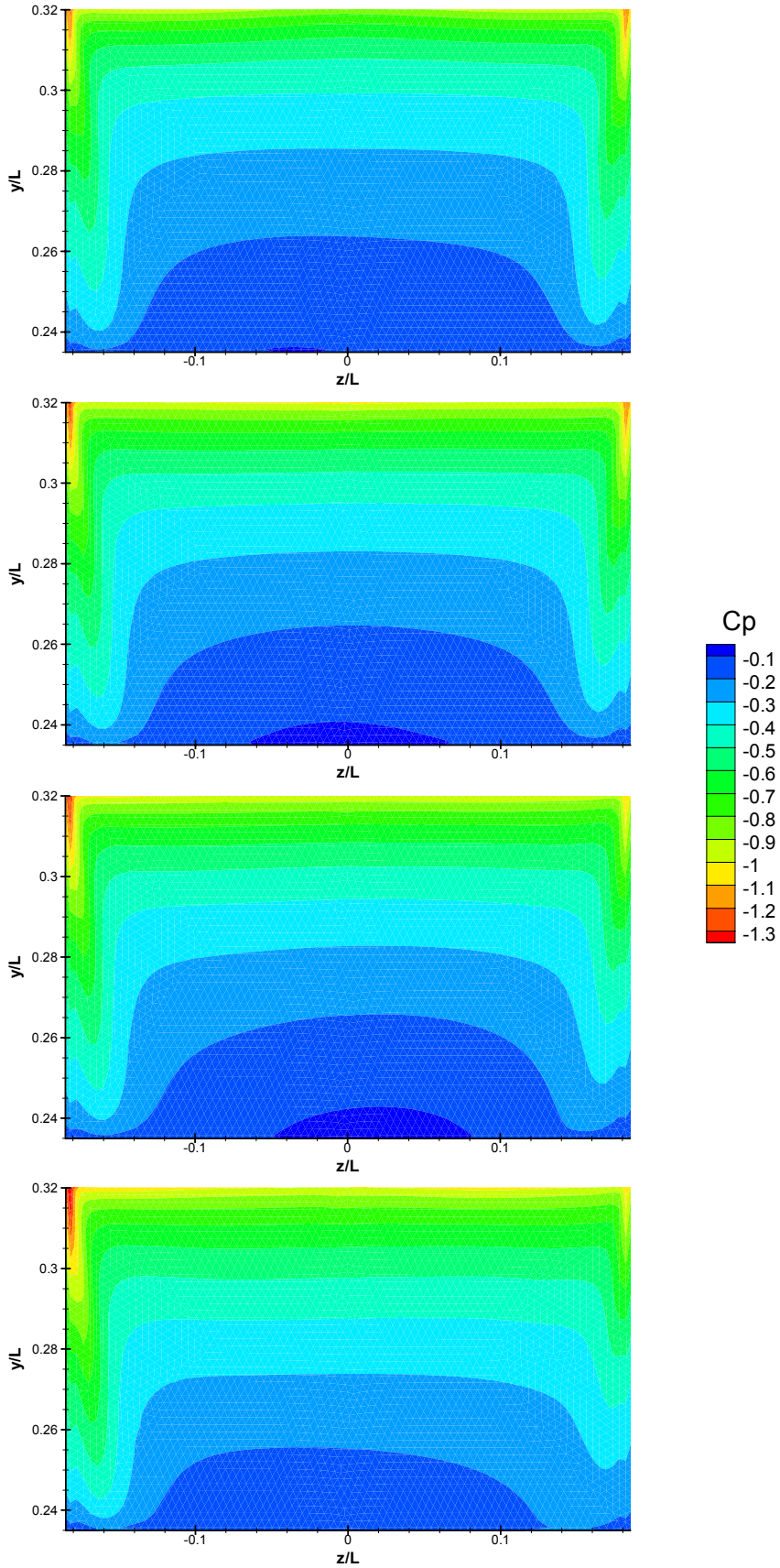

Figure 7.7 - 25° Ahmed Model backlight pressure distribution - a)isolated model b)z_w=0.192L c)z_w=0.096L d)z_w=0.048L

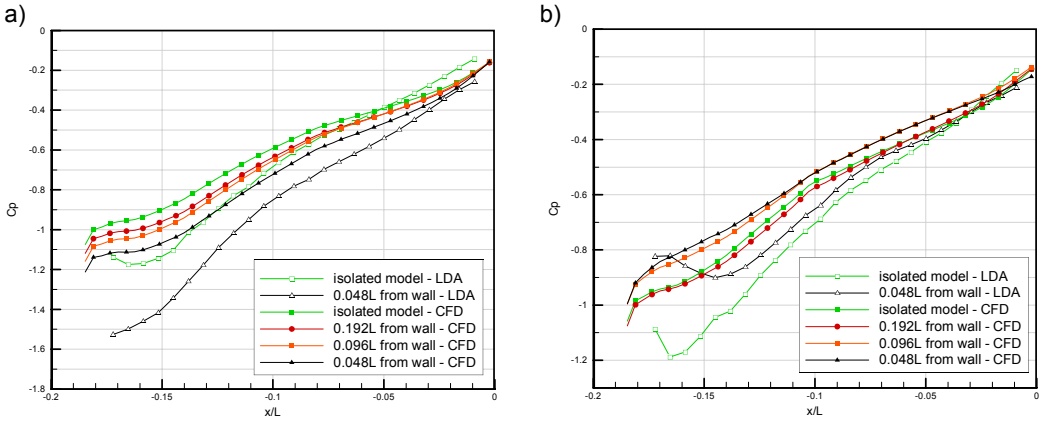

Figure 7.8 - 25° Ahmed Model - profiles of backlight pressure (a) z/L=-0.179 (a) z/L=+0.179 - all wall separations - CFD and experimental data

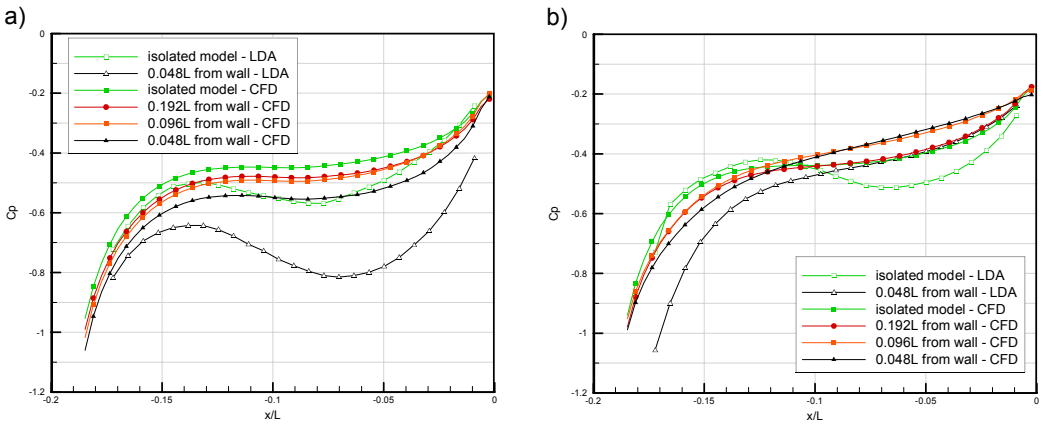

Figure 7.9 - 25° Ahmed Model - profiles of backlight pressure (a) z/L=-0.16 (b) z/L=+0.16 - all wall separations - CFD and experimental data

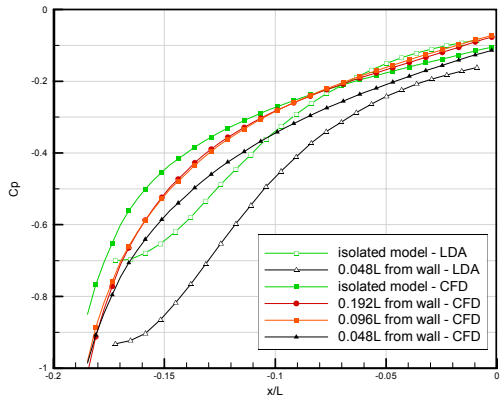

Figure 7.10 - 25° Ahmed Model - profiles of backlight pressure at model centreline (z/L=0) - all wall separations - CFD and experimental data

variations in pressure with wall separation predicted by the CFD and compare them to those measured experimentally, Figures 7.8 - 7.10 plot profiles of pressure data at the four wall distances shown in Figure 7.7 for the computational cases and both isolated and z_w=0.048L experimental cases.

From Figure 7.8 (a) it is found that, unlike the experimental results, the CFD does not exhibit an obvious peak in suction near the backlight leading edge when the 25° model is tested in isolation. This is a result of the weaker vortex strength in the computational model which makes it more difficult to identify the regions where they have greatest effect. In the experimental results this suction peak became gradually less obvious as wall separation fell, as can be seen in Figure 7.8 (a) by the difference in pressure distribution between the isolated and z_w=0.048L experimental data. As this peak cannot be identified in the isolated CFD results no movement of it as wall separation falls can be found. It in fact appears that other than a slight overall drop in C_p as wall separation falls, there is virtually no change to the pressure distribution in this region, at least over the forward half of the backlight. This is a result of the previously-analysed computational under-prediction of the off-side longitudinal vortex's tendency to move toward the side wall as separation from the wall falls. It is this effect which is responsible for the movement of the suction peak in the experimental results, which explains the absence of this effect in the CFD. It is also clear from Figure 7.8 (a) that the overall pressure drop over this section of the backlight is also under-predicted by the CFD. If the measurements at x/L=-0.15 are examined, for example, it is found that between the isolated and z_w=0.048L cases the experimental results show a drop in C_p of approximately 0.26, whereas the CFD model reports a corresponding drop of approximately 0.17.

Inspecting now Figure 7.8 (b) it is again found that the peaks in suction, evident in the experimental results at all measured wall distances, are not evident in the computation. It was shown experimentally that this peak was lowered in magnitude and moved toward the model trailing edge as wall separation fell, as a result of both the movement of the near-side longitudinal vortex toward the side wall and its reduced strength. The fact that these phenomena have both been shown to be under-predicted by the CFD also results in a smaller increase in C_p with falling wall separation near the backlight leading edge in the computational model. It is further shown in Figure 7.8 (b) that there is an inconsistent variation in C_p with falling wall separation in the CFD, with a predicted slight drop between the isolated and 0.192L from wall cases, before rising with further decreasing wall separation, as would be expected from the experimental results. It would therefore appear that the computational model has particular difficulty in accurately modelling the variations in near-side vortex structure with changing wall proximity.

Figure 7.9 (a) again highlights the weaker vortices predicted by the CFD. The 25° isolated

model experimental results displayed a drop in C_p toward the backlight trailing edge at this position, a result of the off-side longitudinal vortex affecting the pressure distribution in this region. It was also found that as wall separation fell, the movement of this vortex toward the side wall and its increase in strength caused this pressure drop to increase in magnitude. This can be seen by the variation in the isolated and z_w=0.048L from wall experimental cases shown in Figure 7.9 (a). The weaker numerically-predicted vortices are not strong enough to cause such a pressure drop in the case of the 25° isolated model, as can also be seen in Figure 7.9 (a). As wall separation falls, however, the increased numerically predicted vortex strength causes a slight drop in C_p to register when the model is 0.048L from the side wall. This drop is evidently lower than the experimentally-measured value, with the CFD predicting a drop of 0.012 from the highest recorded value upstream of the suction increase in comparison to the corresponding experimentally-measured drop of 0.172. Also, as this suction increase is barely discernable in the CFD even at 0.048L, any movement of the off-side longitudinal vortex and subsequent rearward relocation of this suction peak cannot be determined from this plot. Figure 7.9 (a) again serves to highlight the lack of suction increase near the trailing edge in the 25° isolated CFD case. The experimental model exhibited a reduction in the magnitude of this suction increase as wall separation fell, to the extent that at 0.048L wall separation it was no longer evident at z/L=-0.16. The CFD, however, exhibits only a steeper rise in C_p toward the trailing edge as wall separation falls, with the pressure distribution at 0.048L separation closely resembling that found at the model centreline (z/L=0), shown in Figure 7.10. This is a result both of the decreasing vortex strength and its movement toward the side wall, which moves it out of the plotted transverse position and results in virtually no longitudinal vortex effects.

Inspection of Figure 7.10 reveals again that the overall pressure drop caused by wall proximity is under-predicted by the computational model. If the point at x/L=-0.1 is considered, there is found to be a drop in C_p of 0.13 between the isolated and z_w=0.048L experimental cases, with a corresponding drop of 0.07 predicted by the CFD. However, at the trailing edge of the model at 0.048L wall separation the CFD predicts a higher pressure than that measured experimentally, in contrast to the isolated case where the CFD predicted a lower trailing-edge pressure. There is also, at every wall separation measured, a significantly lower C_p at the leading edge of the backlight, continuing the trend found in the isolated case. It will be recalled that it was this over-prediction of the suction peak which caused a corresponding over-prediction of the contribution of the backlight to the overall value of C_D in the isolated case. With the influence of the side wall, however, the lower value of backlight C_p predicted by the CFD model in comparison to the experimental results in the isolated case is no longer evident. As the CFD model is unable to account for the large drop in C_p which was shown to occur over the 25° backlight as wall separation falls, the experimental value of backlight C_p is found to be lower than its computational counterpart for all recorded near-side cases. There was

shown previously to be an overall drop in 25° model backlight C_p of approximately 34% between the isolated and z_w=0.048L cases, in contrast to the CFD which predicts a corresponding drop of approximately 16%. The under-prediction of the increase in off-side longitudinal vortex strength (and subsequent pressure drop) and under-prediction of the decrease in near-side longitudinal vortex strength highlighted previously are of less importance to the overall backlight C_p than the influence that these changes have over the central section of the backlight. As the CFD model does not exhibit any significant influence of the longitudinal vortices over this region, the overall backlight C_p drop cannot be accurately predicted.

7.1.4 CFD Force and Moment Results

The computationally-predicted force and moment data are presented in Figure 7.11 as variations from the corresponding isolated cases. Data are presented for the three backlight angles (10°, 25° and 40°) against wall separation (z_w). In addition to the overall force and moment changes, the influence of separate model sections on the overall values will be used to aid analysis of the CFD results. Inspection of the ΔC_D plot of Figure 7.11 reveals that for each of the three backlights there exists an increase in C_D with falling wall separation, the rate of which also increases as wall separation decreases. This corresponds well with the trend in the experimental results shown previously. The experimental results also recorded the largest increase in C_D on the 40° model which is also the case in the CFD results. The actual values of the drag increases between the the isolated and z_w=0.048L cases differ significantly between the experimental and computational data. The experiments measured an overall C_D increase of approximately 0.09 for the 10° model between these two cases, with a corresponding increase of 0.056 and 0.1 for the 25° and 40° models respectively. In comparison, the CFD predicts increases of 0.033, 0.04 and 0.062 for the 10°, 25° and 40° models respectively. These are significant under-predictions, with the largest occurring for the 40° case where the CFD under-predicts the increase in C_D between the isolated and z_w=0.048L cases by over 38%. Despite this, it is clear from both the CFD and experimental results that the greatest increase in drag is experienced by the 40° model.

Breaking down the computational results into contributions of separate model sections a number of observations can be made. Firstly, the front end drag was shown during isolated analysis to vary by less than 5% between the whole range of backlight angles, owing to a weak fore-aft model aerodynamic interaction. As such, it would be expected that the influence of the side wall would have an almost identical effect on the pressure distribution over the front end for each of the three model configurations. This is indeed found to be the case, with a computationally-predicted variation in C_D contribution of again less than 5% between the three model front ends when at 0.048L from the side wall. The absolute value of front-end drag also does not vary significantly with wall separation in the computational model, with only around

a 3% variation between the isolated and nearest wall cases measured for each model configuration. As stated previously, it would be expected that there would be an increase in pressure over the near-side of the model front end, with a pressure drop over the remaining three sides. It has also been shown that the pressure drop over the top of the model front end is greater than that over the rear, resulting in the large increase in C_M shown in the experimental results. It seems that the computational model predicts that these pressure variations cancel one another out, resulting in virtually no change in overall C_D contribution from the front end. However, without experimental measurements of the front end static pressure distribution it is impossible to definitively assess the accuracy of this computationally-predicted front end C_D variation. It was, however, shown previously (§6.2 and §6.3) that for each of the experimentally-tested wall distances the variation in backlight pressure accounted for 82.5%, 80% and 76% of the overall C_D variation with wall separation on the 25° model at 0.192L, 0.096L and 0.048L from the wall respectively. It was also shown during analysis of the isolated model that Ahmed found the model front end to contribute approximately 6% of the overall drag force over the 25° model. It must therefore be considered that any variation in front-end pressure with side wall proximity would be small in the context of overall model C_D.

Considering now the variations in pressure over the three model backlights with wall proximity, further evaluations of the computational prediction of C_D can be made. It was previously shown that between the isolated and z_w=0.048L cases the CFD under-predicted the 25° backlight pressure drop by approximately 50%. This corresponds to an under-prediction of the increased backlight contribution to the model C_D between the isolated and z_w=0.048L cases of 23.5%. If this discrepancy is taken into account, and the additional backlight drag added to that predicted by the CFD, the computation appears significantly more accurate. Instead of a 29% under-prediction of the 25° model C_D increase between the isolated and 0.048L from wall cases, there would now be an 8% over-prediction.

Considering the 10° and 40° backlights, the CFD predicts backlight C_p drops of 0.056 and 0.062 respectively, in comparison to the 0.06 C_p drop predicted over the 25° backlight, between the isolated and z_w=0.048L cases. This corresponds to an increase in model C_D from the backlight of approximately 0.0075 and 0.0357 for the 10° and 40° models respectively, or 23% and 57% of the total C_D increase as the model is moved from isolation to 0.048L from the side wall. The predicted pressure drops over each of the backlights are of similar magnitudes, and therefore it is the geometry of the models which produces the greatest contribution to overall C_D increase from the 40° backlight, a result of its greater projected frontal area.

Finally, computationally predicted drag contributions from the vertical base of each of the

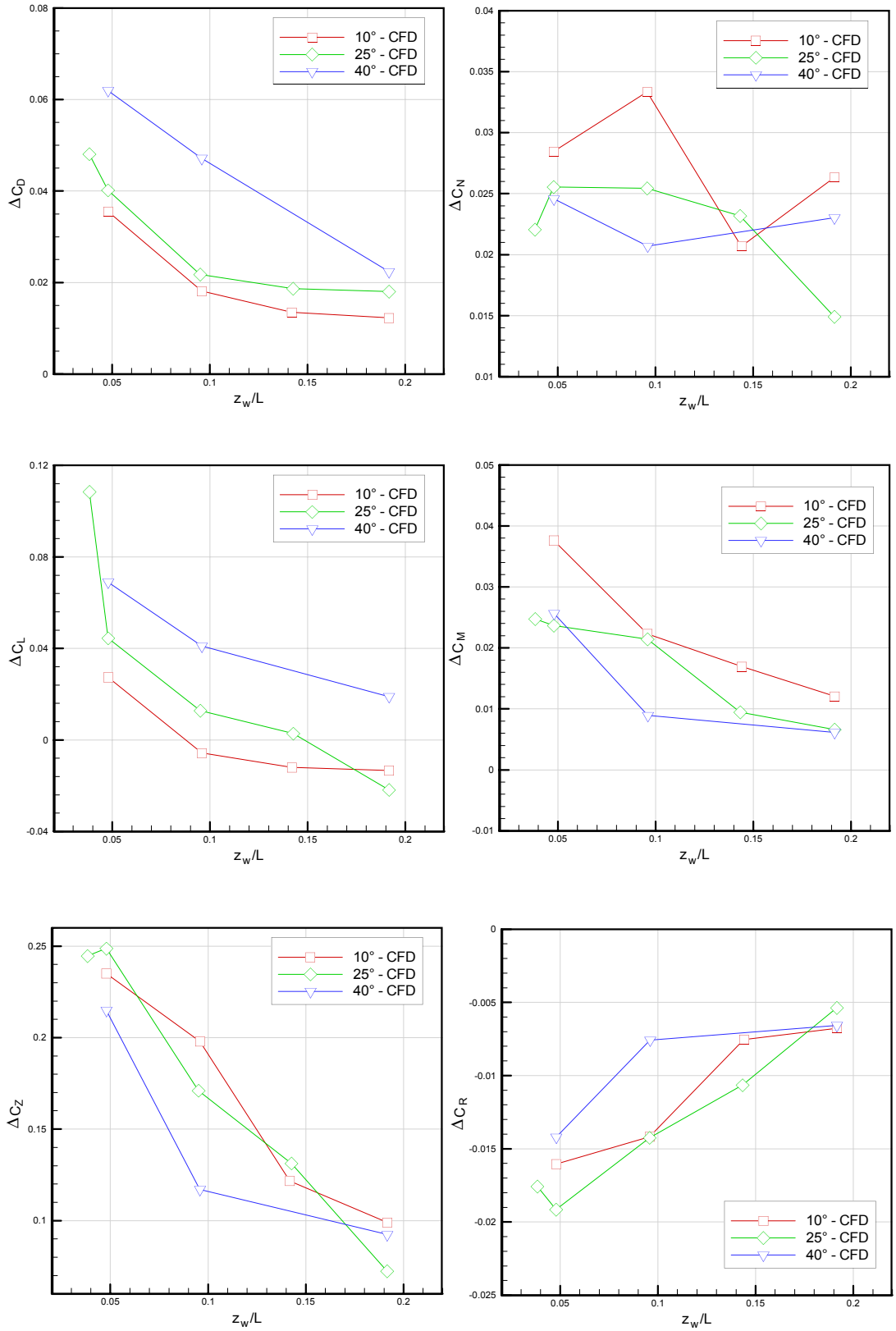

Figure 7.11 - Computational force and moment data vs wall proximity for the 10°,25° and 40° Ahmed models. Values plotted are variations from the equivalent isolated case

models must be considered. Again the largest pressure drop over this region was found on the 40° model, and despite the small area of the vertical base it still accounted for 25% of the overall C_D increase between the isolated and z_w=0.048L cases. Similar pressure drops were observed between the 10° and 25° models and the result of their respective geometries was that the 10° vertical base accounted for 70% of the overall model C_D increase, with the 25° vertical base accounting for 38%.

It appears, therefore, that the 10° and 25° models are predicted by the CFD to have very similar pressure drops over both the backlight and vertical base as the models are moved towards a side wall. This results in a similar C_D increase on both models, with the contributions from either back end section (backlight and vertical section) being determined by the respective projected frontal areas. The 40° model, however, experiences a greater C_p drop on both the backlight and vertical base end, resulting in the greater C_D increase shown in Figure 7.11. It appears though that for each of the backlight angles the value of the pressure drop with decreasing wall separation is under-predicted by the CFD, causing a smaller increase in C_D than was measured experimentally.

The general trends in C_L displayed in Figure 7.11 are also in agreement with experimental results. It was shown that the model experiences a drop in overall C_L as wall separation falls to approximately 0.048L in the 10° model case, 0.038L for the 40° case, and 0.096L for the 25° backlight angle, using experimental results which correspond to the same ride height as was used throughout the computational investigation (50mm). The CFD predicts an overall increase in C_L in comparison to the isolated case occurring before 0.048L wall separation in the 10° model case, by 0.144L wall separation in the 25° case, and for all tested 40° model wall separations. It appears that there exists a consistent over-prediction of the lift coefficient on the 40° model as at all wall separations values of ΔC_L are found to be greater than the corresponding 10° and 25° values, in contrast to experimental data.

Analysis of the experimental force and moment results revealed a large increase in front end lift as wall separation fell. It is also expected that this increase in suction around the top of the front end would be larger in the case of the 10° model in comparison to the 40° model, and larger still in the 25° model owing to the pressure variations with decreasing wall separation at the rear end suction peak. However, it was shown previously that the backlight angle had little effect on the pressure distribution over the front end in the CFD, which would be expected to result in an equal prediction of lift from this section of the model for all three backlight angles. This is confirmed by the data which show a large increase in the front-end contribution to the overall lift between the isolated and z_w=0.048L cases of approximately 0.07 for each backlight angle. The variation in this value between the model configurations is less than 5%, as was the case with the front end drag coefficient.

The greatest computationally-predicted contribution to the overall lift coefficient comes from the top of the model, as would be expected. It would also be expected there would be significant variation in the increase in model top C_L between the backlight angles, owing to the previously analysed suction increases evident near the backlight leading edge. It is found that the CFD does predict a large increase in C_L over the top of the model for each of the backlight angles, and that variation of this increase with backlight angle does follow the expected trend. There is a predicted 0.2 increase in top of model C_L for the 40° model between isolated and z_w=0.048L cases, with corresponding increases of 0.225 and 0.238 over the tops of the 10° and 25° models respectively. It is clear from previous analysis that these values will be significant under-predictions, as a result of both the lower predicted velocity over the forward section of the model tops (due to a computationally predicted weak interaction between the rear suction peak and this region of flow), and an under-prediction of the rear suction peak itself. It is, however, also clear that the rear suction peaks over the 10° and 25° models have the expected effect of causing an increase in lift over the rear of the model top, ensuring that the top of the model experiences the expected variation of lift with backlight angle as wall separation falls.

Despite this, for the three tested model configurations at 0.048L wall separation, the CFD actually over-predicts the increase in model C_L from the isolated case. It must therefore be concluded that the pressure drop underneath the model experiences a greater under-prediction than that over the top. It would, however, be expected that were nearer wall cases computed the under-prediction of the suction over the model, found during analysis of the experimental force results to increase rapidly at the smallest tested wall separations, would become the most significant shortcoming of the CFD with respect to the prediction of model C_L values. At closer wall separations therefore it would be expected that the CFD would under-predict the lift increase.

The prediction of pressure changes over the model backlight with decreasing wall separation also have a significant influence on the prediction of C_L. The under-prediction of this pressure drop over the 25° model backlight results in a computationally predicted increase in C_L contribution from the backlight of 0.0445 in comparison to the experimental value of 0.087 between the isolated and z_w=0.048L cases. Although the contribution from the backlight to the C_L increase with falling wall separation is relatively small in comparison to that from the top of the model, and becomes less significant as wall separation drops below 0.048L and front end lift increases begin to dominate, it must still be considered when analysing the computational results.

The side force plot of Figure 7.11 again exhibits similar trends to those measured

experimentally, albeit with an overall under-prediction in the increase in C_Z with falling wall separation. The experiments also recorded a drop in C_Z once the model had moved to within 0.029L of the side wall for each backlight angle, whereas the CFD model recorded a drop in C_Z on the 25° model between the 0.048L and 0.038L wall separations. There was also found experimentally to be a larger increase in C_Z with falling wall separation on the 25° model in comparison to the 10° model, which in turn experienced a larger C_Z increase than the 40° model. As it is thought that these variations with backlight angle are a result of the higher suction peak causing a lower pressure on the near-side of the model, it would be expected that these variations would be consistent with the CFD case, but would be of lower magnitude, owing to the computational under-prediction of the rear end suction peak increase with falling wall separation. The results in fact show that at 0.048L wall separation the CFD predicts a C_Z of 0.235 on the 10° model, 0.247 on the 25° model and 0.215 on the 40° model, following the expected trend. These, however, correspond to under-predictions of overall C_Z of approximately 8%, 21% and 8% respectively. It would be expected that the greatest under-prediction would occur for the 25° model, owing to the previously-analysed experimentally-measured large increase in suction near the backlight leading edge as wall separation falls. This increase was found to be less evident in the 10° case and absent from the 40° case as a result of the separated backlight flow, and was also found to be consistently under-predicted by the CFD.

As in the cases of C_L and C_D it is found that the prediction of side force contribution from the model front end does not vary significantly between the backlight angles. At 0.048L wall separation there is found to be less than a 2.5% variation in the side force caused by the expected pressure increase over this section of the model between the three backlight angles. The contribution of C_Z by the front end of approximately -0.1 in each case acts in opposition to the pressure drops on the near-side model side, found to be 0.88, 0.91 and 0.83 for the 10°, 25° and 40° models respectively. It appears, therefore, that the relative pressure drops on either side of the model are the main contributors to the overall change in model C_Z as wall separation falls. It would again be expected that the relatively-accurate prediction of C_Z at 0.048L wall separation for the 10° and 40° backlight angles would be a result of an under-prediction of both of these model side pressure drops.

Inspection of the pitching moment graph of Figure 7.11 it can be seen that, unlike the experimental results, the largest increases in C_M with falling wall separation are measured on the 10° model. It was shown during experimental results analysis that the greatest increase in C_M as wall separation falls was found over the 40° model, owing to the lower drop in C_p over and near the leading edge of the backlight in comparison to the 10° and 25° models. There was found to be an overall increase in C_M in comparison to the isolated case at all near-wall separations measured for every investigated backlight angle. It is, therefore, clear that the

prediction of the lift increase over the model front end and leading edge of the model top is most important with respect to prediction of the model C_M. It has also already been shown that there is little computationally-predicted variation in pressure over the front end of the three tested model configurations at a given wall separation. It would, therefore, be expected that the predictions of the pressure drops over the backlight of each of the three models would be the determining factor in the relative computational predictions of the change in C_M with wall separation on each model.

The results show that at 0.048L wall separation the CFD predicts an increase in C_M (nose up) from the isolated case of approximately 0.0376, 0.0237 and 0.0256 over the 10°, 25° and 40° models respectively. This corresponds to a computational over-prediction of the 10° value of 14%, a 72% over prediction of the 25° model C_M increase, and an under-prediction of the 40° model increase of 21%. This follows the expected pattern as the largest under-prediction of pressure drop over the backlight has been shown to occur on the 25° model, with a lower under-prediction over the 10° model and an over-prediction of the overall backlight pressure drop on the 40° model. This over-prediction of the 10° model increase in C_M also accounts for the highest overall increases being measured on this model configuration. The importance of the lift produced by the model front end is emphasised by analysis of its contribution to the overall C_M increase as wall separation falls to 0.048L in the computational model. It is found that the computationally predicted front end lift accounts for 67%, 114% and 100% of the overall C_M change (with negative contributions resulting from the both the bottom of the model and the backlight) on the 10°, 25° and 40° models respectively, despite the previously analysed under prediction of the lift in this region.

It is clear from the yawing moment plot in Figure 7.11 that there is little discernable pattern to the computationally-predicted variation in C_N with wall separation for the three backlight angles tested. The experimental results displayed a significant positive yawing moment (nose away from wall) at the wall separations measured by the CFD. It would be expected that the near side wall pressure drop with falling wall separation, responsible for the large toward wall side force reported by both the experimental and computational results, would be skewed toward the front end, resulting in a negative contribution to the overall yawing moment. It has also been shown that the off-side pressure drop, although it would also be expected to be skewed toward the model leading edge and therefore contributing an overall positive contribution to the model C_N, is significantly less than that experienced on the near-side. It is therefore concluded that the determining factors in the change in overall model C_N as wall separation falls are the pressure changes on the front end of the model. It is the case that both the pressure increase over the near-side of the model front end and the subsequent pressure drop over its off-side will both result in a positive yawing moment on the model. As the pressure changes over the front end with falling wall separation have previously been shown

to be significantly under-predicted by the CFD this will result in an under-prediction of this yawing moment contribution. This under-prediction will be more significant than that of the case of the pitching moment, as the pressure changes on the top and bottom of the model front end act in opposition, and subsequently the under-prediction of them both served, to a certain extent, to cancel one another out. This is not true in the case of the yawing moment, where the under-prediction of the near-sides and off-sides increase and decrease in pressure respectively serve only to compound the computational error.

This under-prediction of front end C_N is coupled with an inconsistent prediction of the change in near-side C_N with falling wall separation on each of the models tested. Although the overall magnitude of the pressure drop over this region follows the expected trend, with an increase in C_Z as wall separation falls, C_N does not follow any discernable pattern. To highlight this, Figure 7.12 plots the variation in the model near-side C_N contribution with decreasing wall separation for the 25° model. It is clear that the computational over-prediction of the near side's relative importance on overall model C_N coupled with this inconsistent variation in near-side C_N, results in the variations shown for each of the models in the C_N plot of Figure 7.11. It must therefore be concluded that, owing mainly to the under-prediction of the model front end yawing moment contribution, no useful trends can be observed from the computational prediction of the change in model C_N with decreasing wall separation.

The final plot to be considered in Figure 7.11 is that of the rolling moment (C_R). Analysis of the experimental results showed that for each backlight angle, up to the minimum wall separations measured by the CFD, there existed a negative (model top toward the side wall) rolling moment. It is further expected that this is predominantly a result of the large pressure drop over the near-side of each model configuration being skewed toward the top of the

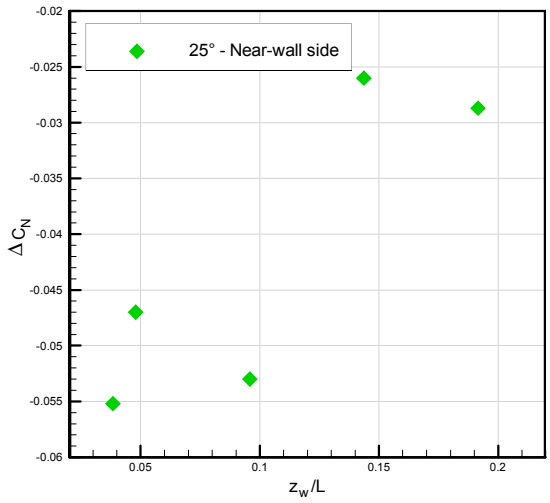

Figure 7.12 - Contribution to ΔC_N from near-wall side of 25° Ahmed model in wall proximity- CFD data

model. The drop in pressure over the off-side would also be expected to be skewed toward the model top, counteracting the negative C_R over the near-side. It has previously been shown through analysis of the variation in C_Z as wall separation falls that the near-side pressure drop is significantly greater than that over the off-side, resulting in a net negative rolling moment from these regions, which increases with decreasing wall separation until the point where the boundary layers on the wall and model restrict the flow between them, with the subsequent drop in C_Z and C_R. This trend is consistent with the computational results, which also report a drop both in C_R as wall separation falls for each of the backlight angles, until the boundary layers restrict the flow between the wall and model. This has only been shown to occur at 0.038L wall separation in the 25° case, resulting in the drop in C_Z and increase in C_L between the z_w=0.048L and z_w=0.038L cases analysed previously. It can be seen from the C_R plot that the expected increase in C_R also occurs between these two wall separations.

It was also found during analysis of the experimental results that the overall drop in C_R with falling wall separation was found to be larger in the 10° model case than in the 40° case, and larger still in the case of the 25° model, with an overall increase in the magnitude of the C_R drop at 0.048L wall separation of 53% between the 25° and 40° cases. It is thought that this is a result of the increased suction over the near-side in the 25° case, caused by the increased suction near the backlight leading edge, which also resulted in the increased side force on the 25° case in comparison to the 10° and 40° cases. This variation in C_R with backlight angle again strengthens the hypothesis that it is the pressure drop over the near-side which is dominant in the overall model C_R. This experimental variation in C_Z with backlight angle was also found in the CFD results and therefore it would be expected that the variation in C_R with backlight angle would also follow a similar trend to that measured experimentally. The overall drops in C_R between the isolated case (when C_R is naturally 0 owing to model symmetry) and z_w=0.048L predicted by the CFD are found to be -0.016, -0.019 and -0.014 over the 10°, 25° and 40° cases respectively, following the experimental variation in C_R with backlight angle. The predicted contributions to these overall model coefficients from the near-side of the model were found to be -0.0573, -0.0638 and -0.0547 for the 10°, 25° and 40° models respectively, highlighting both the importance of the near-wall contribution to the overall model C_R and its variation with backlight angle, which as expected follows an identical trend to that of the overall model C_R.

The predicted contribution of the model front end to the model C_R must also be considered. There is, as before, little variation (<5%) between the computationally-predicted contribution of the front end to model C_R between the three tested backlight angles at 0.048L wall separation, with an almost constant predicted positive rolling moment of 0.09. It would be expected that both the pressure increase on the near-side and pressure drop on the off-side of the front end would be skewed toward the bottom of the model, producing a negative and

positive rolling moment respectively, with the near-side pressure increase being shown previously to be greater than the off-side pressure drop (the front end providing a negative contribution to model side force). The large pressure drop over the near-side of the top of the front end would also produce a positive rolling moment on the model, and it appears therefore that it is this pressure drop which determines the front end C_R.

Although the overall rolling moment contribution of the backlight is predicted by the CFD to be small in comparison to those from the sides of the model, the variation in C_R contribution with backlight angle at 0.048L wall separation must be considered. The CFD predicts a positive contribution to the model C_R of approximately 8% of the total model value for the 10° and 40° models, but a negative contribution to overall C_R of approximately 10% at 0.048L wall separation for the 25° model. It appears that in the case of the 10° and 40°, models where the longitudinal vortices shed from the back end are weak or absent (respectively), the CFD model predicts the largest pressure drop over the near-side of the backlight, resulting in the positive contribution to overall C_R stated above. In the 25° model case, however, the increase in pressure on the near-side of the backlight as a result of the weaker near-side longitudinal vortex, coupled with the pressure drop over the off-side section caused by the increased off-side longitudinal vortex strength, produces a negative contribution to model C_R.

7.2 Additional CFD Analysis

7.2.1 Model Pressure Distribution

In order to assess the variation in pressure over the model with decreasing wall separation, a number of pressure plots will be presented for each of the sections of the Ahmed model. These will highlight the computational prediction of the C_p changes over each model as wall separation falls. In each plot, the pressures on the model will be plotted as ΔC_p - the variation in pressure from the corresponding isolated model case. The accuracy of the predictions will be discussed with reference to the previously-presented CFD validation.

The variation in pressure over the front end of the 25° model is plotted in Figure 7.13, with the side wall in each case located at the left hand side (positive z) of the diagram. Only the 25° model front end is plotted owing to the lack of variation in front end pressures with backlight angle discussed previously. Despite the analysed under-prediction of all front-end pressure variations with decreasing wall separation, it has been shown that the trends in force and moment contributions from this region of the model follow that which would be expected from the experimental results. It would, therefore, be expected that the trends in pressure variation shown would be an accurate representation of those which occurred in the experiments, notwithstanding the discrepancies in magnitude. Immediately apparent from Figure 7.13 is both the increased pressure over the near-side of the front end, shown to be predominantly responsible for the negative side force contribution of this region of the model, and the increased suction over the top and off-side. The higher suction increase over the near-side of the top of the model front end, shown previously to be responsible for the large increase in C_M and the positive contribution of the front end to model C_R, is also evident. The large increase in the rate of C_p variation as wall separation falls can be seen by comparing the z_w=0.048L and z_w=0.038L plots. A large increase in both the high pressure on the near-side of the front end and decrease in C_p over the model top can both clearly be identified, both of which appear to be significant variations despite a movement of the model of only 0.01L toward the wall. To quantify these pressure variations Figure 7.14 plots profiles of pressure across the model width at mid-height up the model front end (y/L=0.185, Figure 7.14 (a)) and at the position of greatest suction on this section of the model (z/L=0.16, Figure 7.14 (b)).

Initial inspection of Figure 7.14 (a) reveals the rate of increase in pressure over the near-side of the 25° front end with decreasing wall separation. There is found to be an increase in maximum measured C_P at the position shown of 0.123 between the isolated and z_w=0.192L cases, with a further increase of 0.071 to z_w=0.144L, 0.112 to z_w=0.096L, 0.247 to z_w=0.048L and a final increase of 0.141 between z_w=0.048L and z_w=0.038L. The fact that approximately 56% of the total increase measured occurs between wall separations of 0.096L and 0.038L is again evidence of the increased rate of change in C_p with falling wall separation. It is also

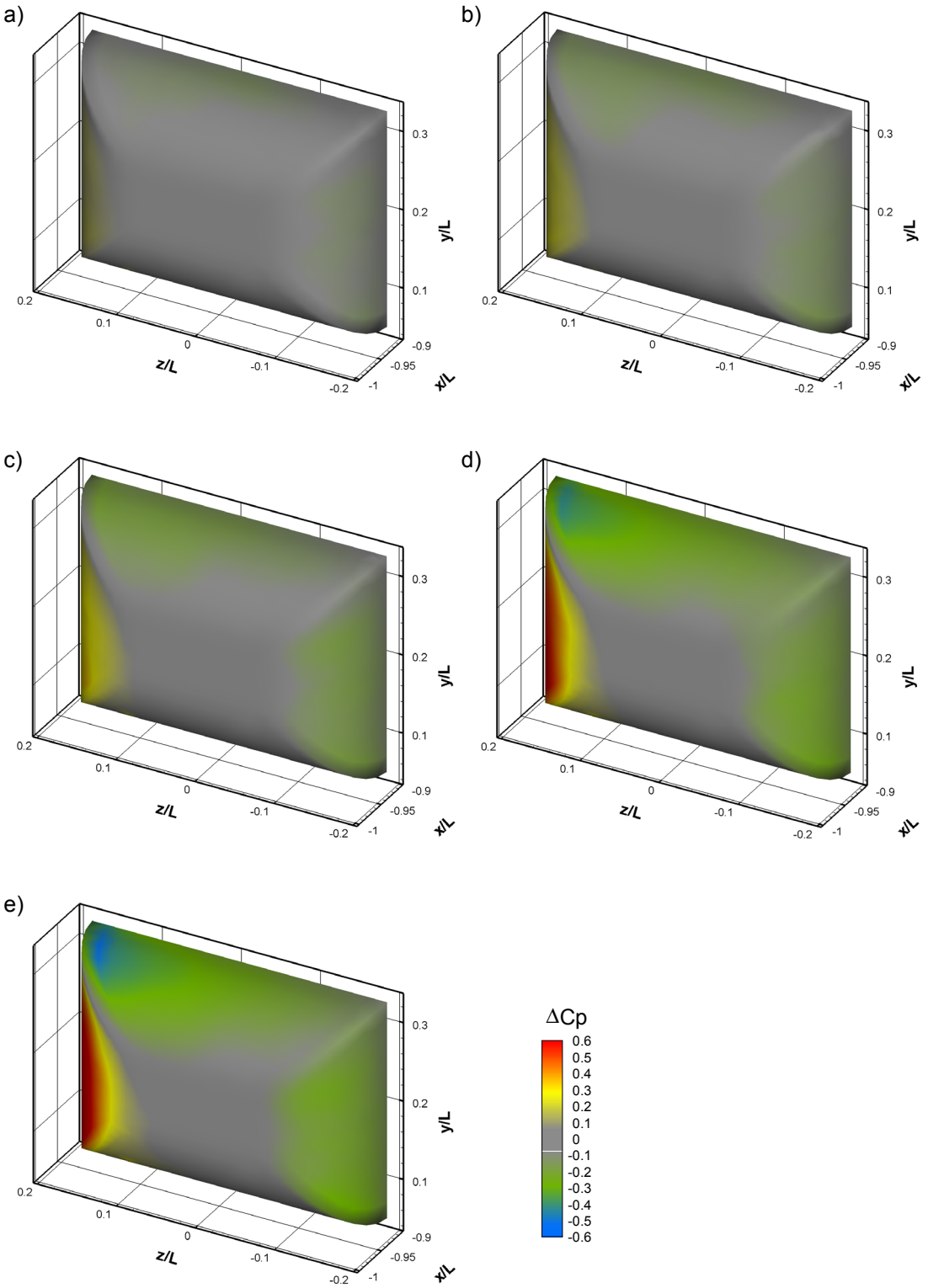

Figure 7.13 - CFD-predicted pressure variation from isolated case over 25° model front end at a)z_w=0.192L b)z_w=0.144L c)z_w=0.096L d)z_w=0.048L and e)z_w=0.038L

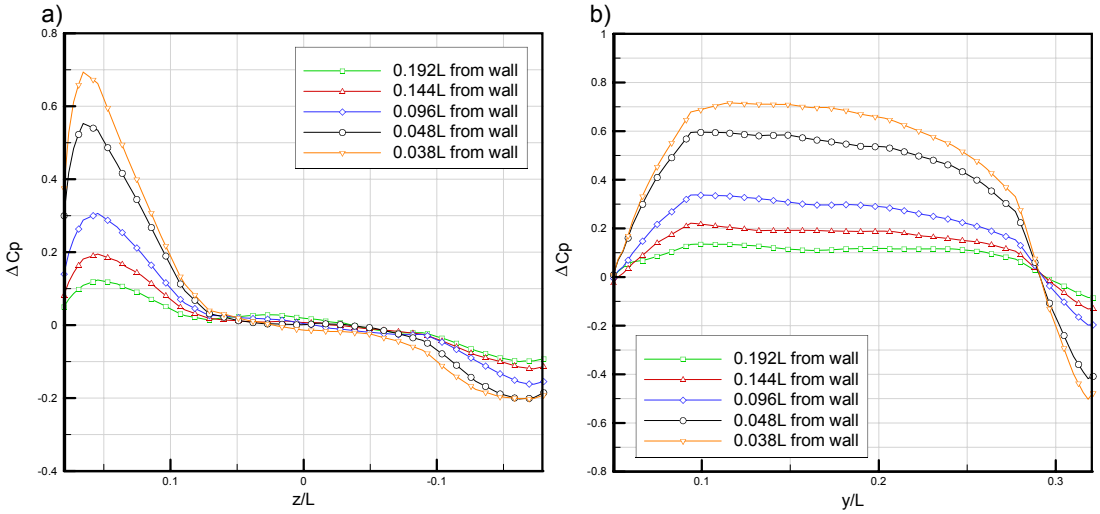

Figure 7.14 - Computed profiles of pressure variation from isolated case on 25° Ahmed model front end for various wall separations (a) at y/L=0.185 and (b) at z/L=0.16

found from Figure 7.14 (b) that the position of maximum C_p is moved closer to the side wall with decreasing wall separation. There is a movement of approximately 0.012L of maximum C_p position between the z_w=0.192L and z_w=0.038L cases, which would be expected from the increased suction between the model and the wall. Also evident is the comparatively small drop in C_p over the off-side section of the front end. Between the isolated and z_w=0.038L cases, where there was found to be an increase in C_p at this position of approximately 0.694 on the near-side, there is a predicted drop of only -0.099 on the off-side. This large variation in ΔC_p between the two sides results in the negative contribution of C_Z from the model front end. The lack of significant variation in C_p over the centre section of the model front end, which can be seen for all measured wall distances in both Figures 7.13 and 7.14, is a result of the fact that this region experiences stagnated flow in the both the near-wall and isolated model cases.

From Figure 7.14 (b) it is seen that the maximum predicted pressure drop over the top of the model front end follows a similar pattern to that of the C_p increase on the near-side. There is found to be a drop in C_p of approximately 0.502 between the isolated and z_w=0.038L cases, with again over half of this increase (≈61%) occurring between wall separations of 0.096L and 0.038L. It is also clear the pressure increase (in comparison to the isolated case) over the near-side of the model front end at this transverse position, is of greater magnitude than the pressure drop on the top. The positive contribution to C_R from the front end is a result of the fact that the pressure drop on the top is localised very close to the side of the model, whereas the pressure increase on the near-side, although as expected is skewed slightly toward the bottom of the model, exists both above and below the position about which moment readings were taken. This will result in only a relatively small negative contribution to the front of model C_R.

Variations in C_p from the isolated case on the near-side of the 25° model are plotted in Figure 7.15. Initial inspection reveals the large drop in C_p with decreasing wall separation, responsible for the positive side force which the model experiences at the plotted wall distances. Equally evident are the regions of highest C_p drop, close to the leading edge of this model section and close to the leading edge of the backlight, the latter of these regions being most evident in the z_w=0.038L plot. The pressure drop near the backlight leading edge is thought to be largely responsible for the overall skewing of the C_p drop over the near-side of the model toward the model top, resulting in the negative contribution to model C_R discussed previously.

Figures 7.16 and 7.17 plot the pressure variation from the isolated case over the near-side of the 10° and 40° models respectively. Again evident is the increased suction with decreasing wall separation, with the largest C_p drop also being located near the leading edge of this region. It has been shown though that the 25° model experiences a larger pressure drop over the near-side than either the 10° or 40° models at a given wall separation. The 25° near-side is in fact found to experience a 0.023 larger C_p drop than its 40° counterpart at 0.096L wall separation, and 0.028 at 0.048L wall separation. This results in the larger C_Z contribution from the 25° near-side, despite the smaller side area than on the 40° model.

To investigate the effects of both side-wall proximity and backlight angle on the pressure drop near the leading edge of the near-side, Figure 7.18 plots ΔC_p half way up the side of the model for both the 25° backlight at various wall separations, and for all three tested backlights at 0.048L from the side wall. It is apparent from Figure 7.18 (a) that, similar to the pressure increase on the near-side of the model front end, there exists a more-rapid drop in the minimum ΔC_p as wall separation falls. As in the cases of the maximum and minimum ΔC_p increases and decreases respectively over the front end, over 50% of the total drop in minimum ΔC_p between the isolated and z_w=0.038L cases occurs between wall separations of 0.096L and 0.038L. It is further found from Figure 7.18 that the position of minimum ΔC_p is moved toward the model leading edge as wall separation falls, with a movement in this point of 0.068L toward the model leading edge between the z_w=0.096L and z_w=0.038L cases. To quantify the variation in ΔC_p at this position between the backlight angles, Figure 7.18 (b) must be considered. As would be expected from previous analysis of the variation in C_Z with backlight angle, there is found to be a greater increase in suction from the isolated case over the majority of the 25° model at 0.048L wall separation. The minimum ΔC_p between the three backlight angles at this wall position is in fact found to be -0.298, -0.313 and -0.283 for the 10°, 25° and 40° models respectively.

Figures 7.19 - 7.21 plot the variation in C_p from the isolated cases over the backlights of the

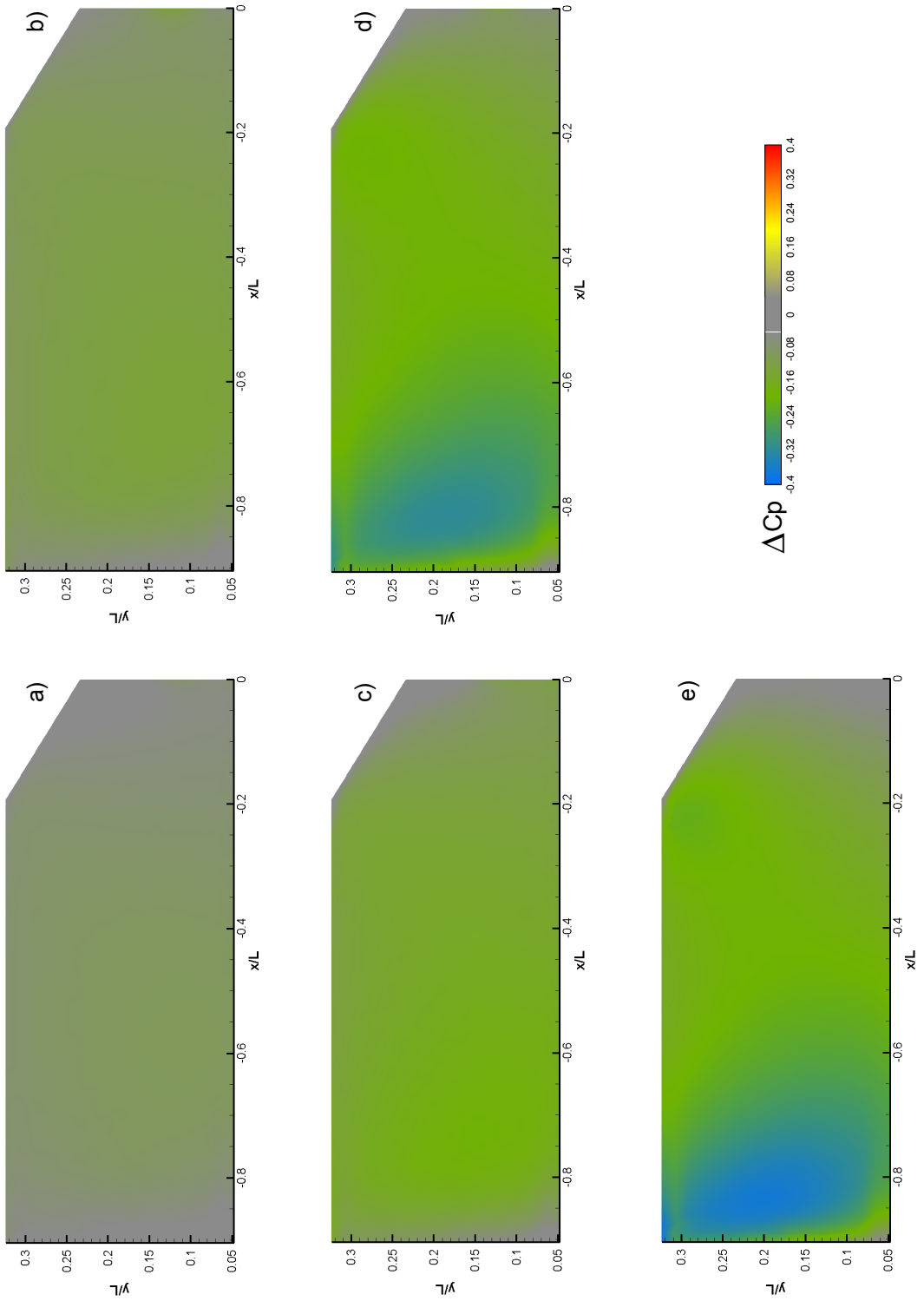

Figure 7.15 - Computed pressure variation from isolated case over the near-side of the 25° model a)z_w=0.192L b)z_w=0.144L c)z_w=0.096L d)z_w=0.048L e)z_w=0.038L

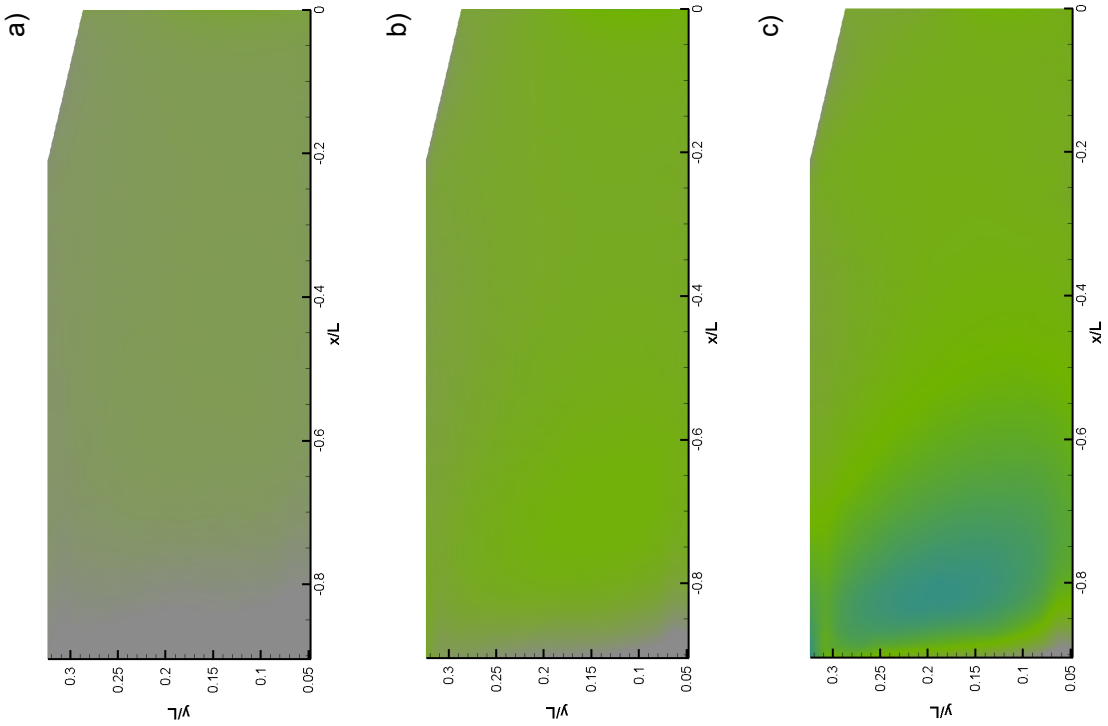

Figure 7.16 - Computed pressure variation from isolated case over the near-side of the 10° model a)z_w=0.192L b)z_w=0.096L c)z_w=0.048L

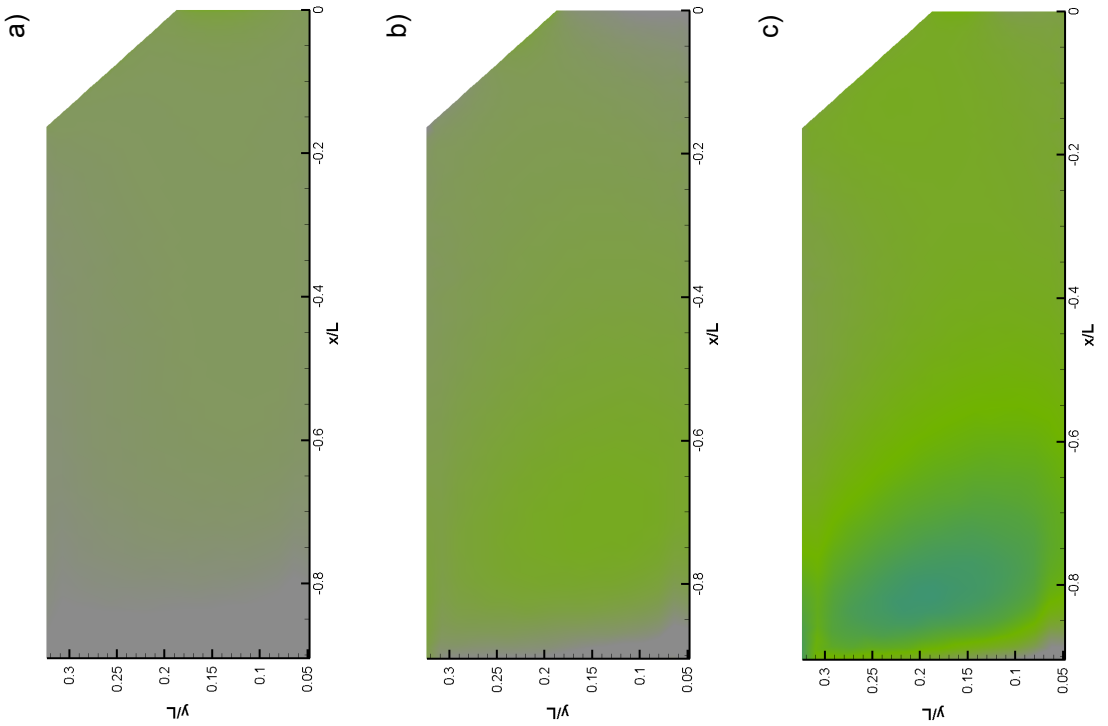

Figure 7.17 - Computed pressure variation from isolated case over the near-side of the 40° model a)z_w=0.192L b)z_w=0.096L and c)z_w=0.048L

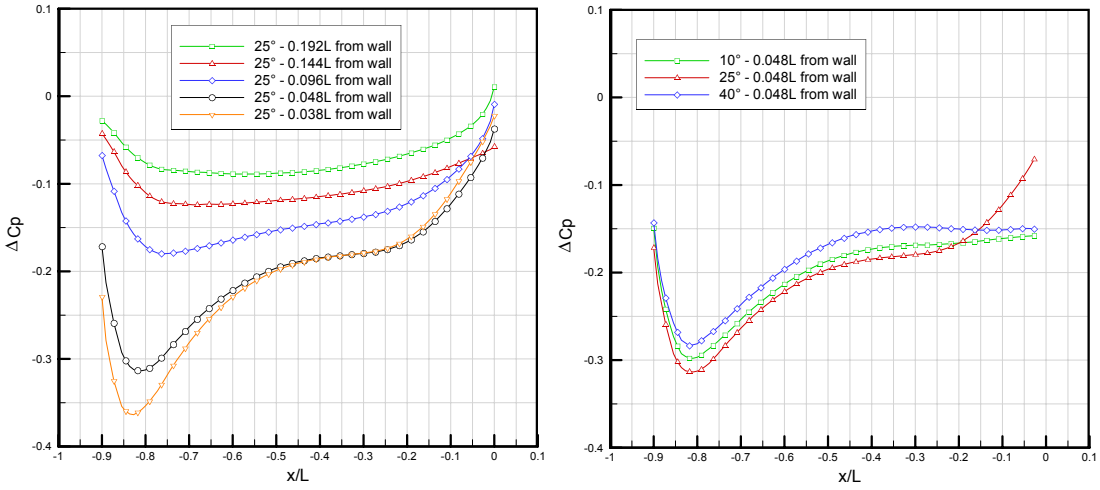

Figure 7.18 - Streamwise profiles of pressure variation from isolated case over 10°, 25° and 40° near-side of Ahmed model at y/L=0.185 - various wall distances - CFD data

three tested model geometries. The previously analysed larger pressure drop over the 40° backlight in comparison to the 10° and 25° cases can clearly be identified. At 0.048L wall separation, there is found to exist a 29% and 13% larger drop in ΔC_p over the 40°model than the 10° and 25° models respectively. It was shown previously that it is this larger C_p drop, coupled with the larger projected frontal area of the 40° backlight, which was responsible for the higher increases in C_D with falling wall separation experienced by this model geometry. It can also be seen that there is significant variation between the backlight angles in the predicted distribution of ΔC_p with decreasing wall separation. On both the 10° and 40° backlights the majority of the pressure drop occurs over the near-side. In the case of the 25° backlight, however, the pressure drop remains almost symmetrical about the model centreline (z/L=0) as wall separation falls. The previously-analysed pressure increases and decreases over the near and off-side sections of the backlight, caused by variations in the longitudinal vortices, can also be distinguished from Figure 7.19. The result of this is the positive rolling moment contribution from the 10° and 40° model backlights in wall proximity, and the negative rolling moment contribution from the 25° model backlight. The effects of the variation in structure of the 10° near-side longitudinal vortex can be identified in Figure 7.20 where there is found to be no drop in C_p, despite the significant drop found closer to the model centreline. The variation in C_p is lower than that found in the case of the 25° model owing to the previously-analysed weaker vortices over the 10° model. A slight drop in C_p can also be distinguished on the off-side section of this plot, though again this variation is significantly smaller than its 25° counterpart.

It was shown previously that, in comparison to the experimental results, the CFD under-predicted the variation in C_p over the 25° backlight, in particular the section away from the immediate vicinity of the model sides. It appears from Figures 7.19 - 7.21 that, as was the

case in analysis of the isolated results, the CFD is particularly unable to model accurately the flow over the 25° backlight.

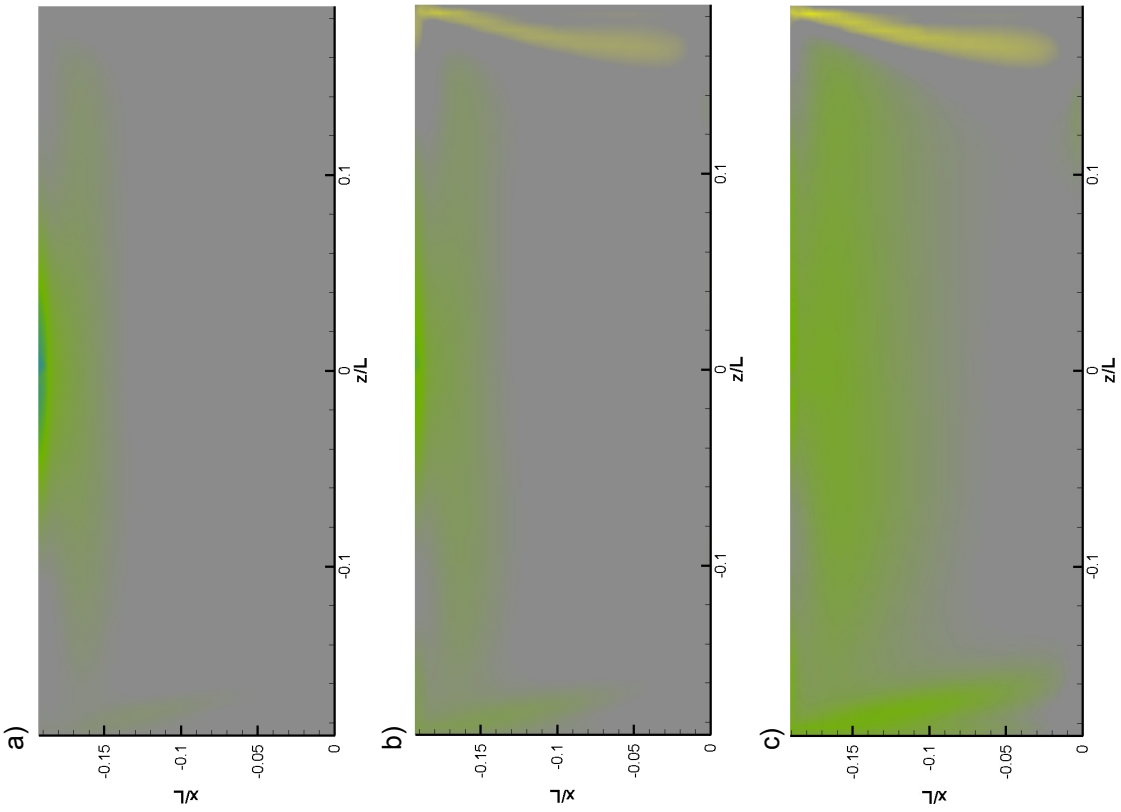

Figure 7.19 - Computer pressure variation from isolated case over the backlight of the 25° model a)z_w=0.192L b)z_w=0.096L c)z_w=0.048L

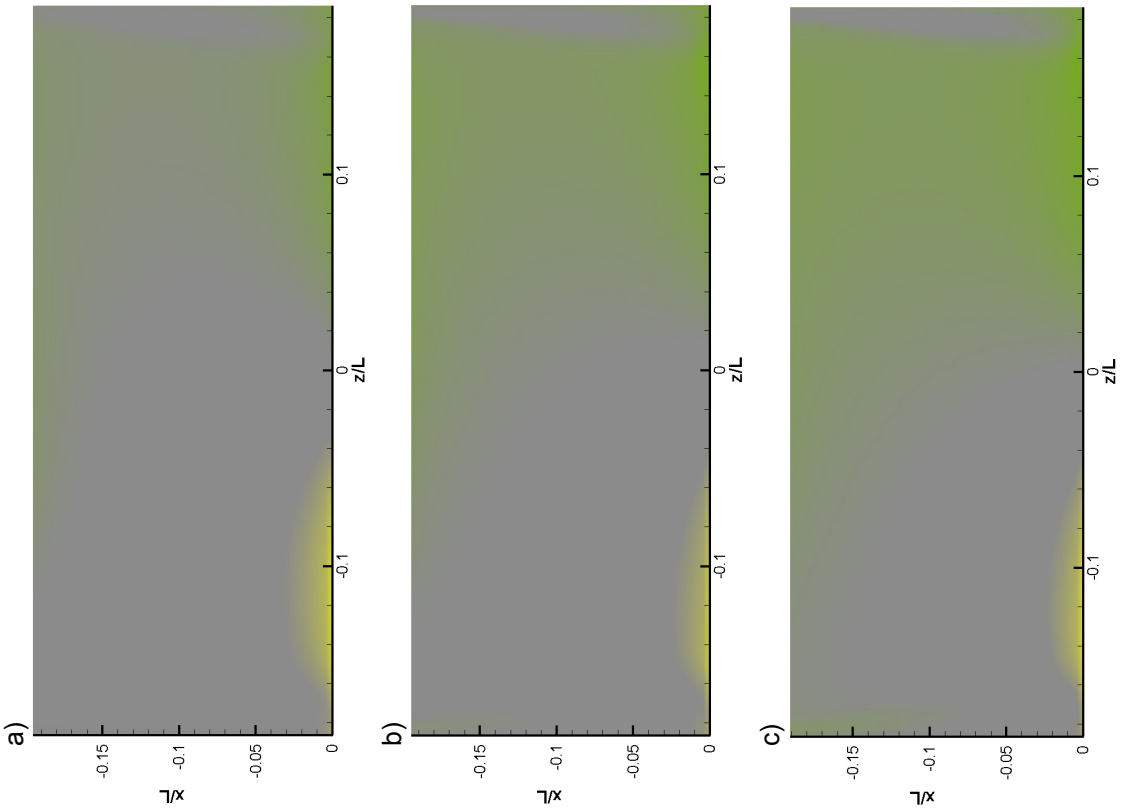

Figure 7.20 - Computed pressure variation from isolated case over the backlight of the 10° model a)z_w=0.192L b)z_w=0.096L c)z_w=0.048L

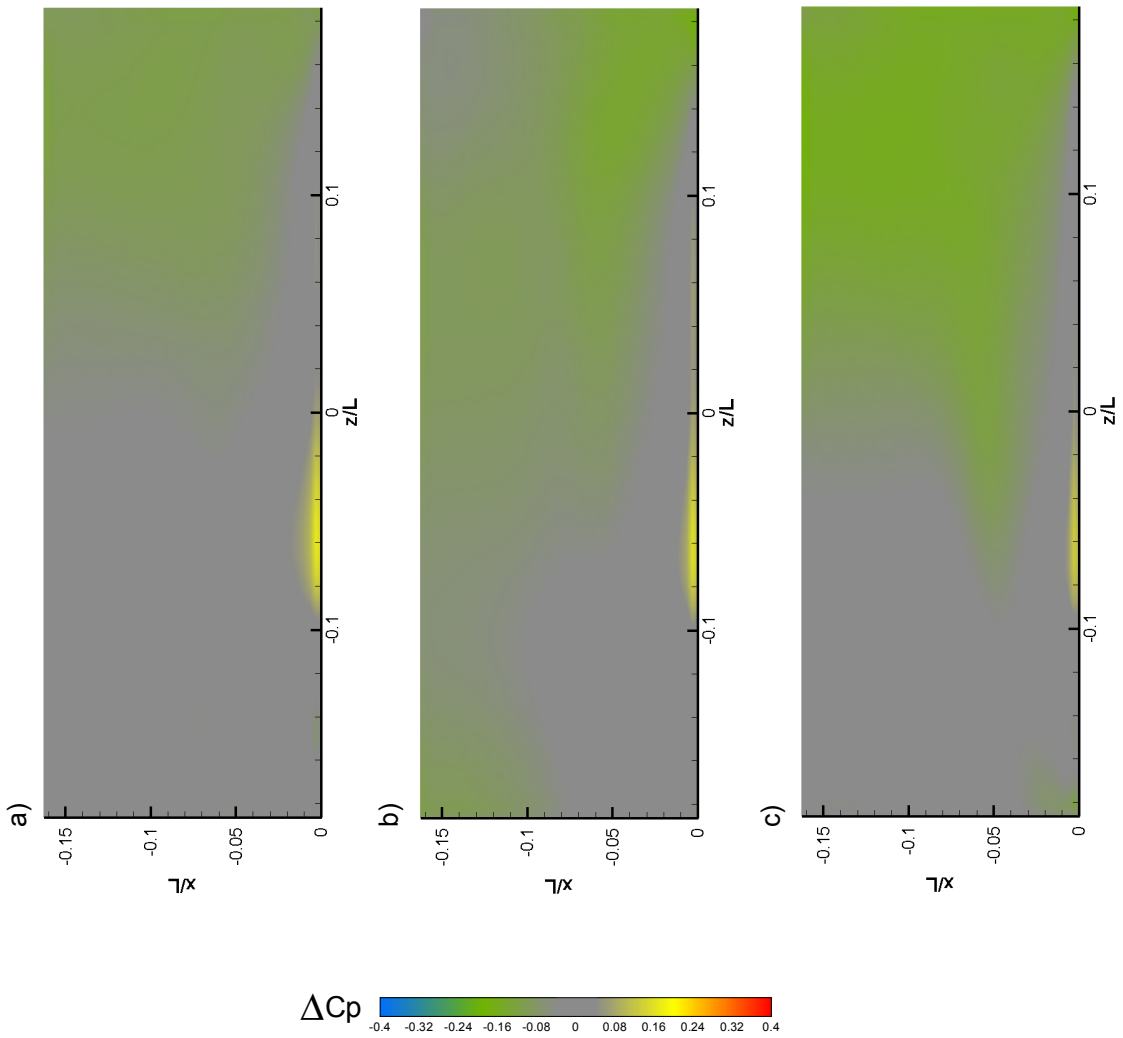

Figure 7.21 - Computed pressure variation from isolated case over the backlight of the 40° model a)z_w=0.192L b)z_w=0.096L c)z_w=0.048L

7.3 Summary of Computational Force and Moment Results

• C_L drops slightly as the model approaches the wall, before increasing rapidly as wall separation falls further. This is in agreement with the trends shown in the experimental data. The CFD was found to over-predict values of ΔC_L for the cases tested, owing to a smaller under-prediction of the pressure drop on the top of the model than under-prediction of the pressure drop underneath. It is expected that were nearer wall cases computed the under-prediction of the C_L contribution from the model top would become most significant and the CFD would then under-predict the overall model ΔC_L.

• C_D increases with decreasing wall separation for all tested configurations, as was the case in the experimental data. The magnitudes of the C_D increases over each of the model geometries are though found to be under-predicted by the CFD by up to 38% of the experimental value at 0.048L wall separation, largely as a result of an under-prediction in C_p drop over the backlight.

• C_Z acts towards the side wall for all tested configurations, as was the case in the experiments. There is again an under-prediction of this force by the CFD, in this case a result of the under-predicted suction increase with decreasing wall separation between the model and near side wall. There was in fact found to be a maximum computational under-prediction of model C_Z of 21% of the experimental value at 0.048L wall separation.

• C_M increases with decreasing wall separation for all tested cases, again following experimental trends. The inability of the CFD to model variations in pressure near the model front end with changing back angle results in the pressure drop over the model backlights becoming the determining factor in overall C_M. The under-predicted C_P drop over the 10° and 25° backlights therefore results in an over-prediction of model C_M of up to 72% of the experimental value at 0.048L wall separation, with the over-predicted C_p drop over the 40° backlight resulting in an under-prediction of overall C_M of 21% of the experimental value at 0.048L wall separation.

• C_N is not found to follow any discernable pattern as wall separation decreases in the computational model. This is a result of the under-predicted pressure increase and decrease on the near and off-sides respectively of the mode front end, resulting in a large under-prediction of C_N contribution from this section of the model. As it is the model front end which was shown through analysis of the experimental results to be largely responsible for the overall positive value of C_N, the CFD is unable to follow experimental trends.

• C_R decreases with falling wall separation, as was the case in the experimental results up to the wall separations tested by the CFD. Under-predictions of the contribution to model C_R from both model sides, front end and model top appear to balance one another in this instance, resulting in computationally predicted C_R values which are close to those measured experimentally.

7.4 Summary of Computational Results

The presented CFD has added significant insight into the effects of side-wall proximity. In particular, the pressure distributions on sections of the Ahmed model which were not pressure tapped during the experiments have allowed conclusions to be drawn concerning the relative contributions to the forces and moments from these sections when in side-wall proximity. The z-velocity component, not available from the experimental data, has also been important as it has allowed analysis of the longitudinal vortex centres. It is also clear that flow visualisation can be made from the CFD at positions in the flow where LDA data were not taken, again adding usefulness to the computations.

8. Comparisons with Previous Work

To assess the generality of the Ahmed model near-wall results, the presented data will be compared directly with those of Brown [2005]. It will be recalled that this purely experimental study involved the use of a Type C race car model above a moving ground plane and a model side-wall without boundary layer control. Force and moment measurements only were recorded throughout the investigation. A more detailed overview of both the type C race car model used and of the results presented in Brown's investigation was given in Chapter 2. A general description of the flow around the Type C car will be presented here, followed by direct comparison between the available results from both the type C and the Ahmed models. Where necessary, computational predictions of the flow around the Type C model both in isolation and at 50mm wall separation (z_w=0.045L) will be presented, in order to aid understanding of the effects of side wall proximity. The computational model used was very similar to that employed for the Ahmed model CFD results analysed previously and as such similar shortcomings would be expected and taken into account. It will be recalled that results from another experimental near-wall investigation, on a NASCAR model, was also presented in Chapter 2 [Wallis & Quinlan, 1988]. Owing to the highly complex geometry involved in that study, it is considered impossible to understand fully the effects that side wall proximity would have on the flow from the data available. As such, comparison between this study and either the current or Brown's experimental studies will not be presented.

8.1 Type C Model

The flow around the Type C model differs significantly from that around the Ahmed model. Firstly, the model has a sharp leading-edge and front splitter (Figure 8.1), causing the formation of leading edge vortices. Evidence of one of these can be seen in Figure 8.2 by the region of low pressure behind the leading edge on the model side. There is also a 10° diffuser on the Type C model, which adds significant rear-end downforce. This can be considered similar to the backlight on the Ahmed model, but acting in the opposite direction. However, the longitudinal vortices formed on the 10° diffuser will be stronger than those formed over the 10°

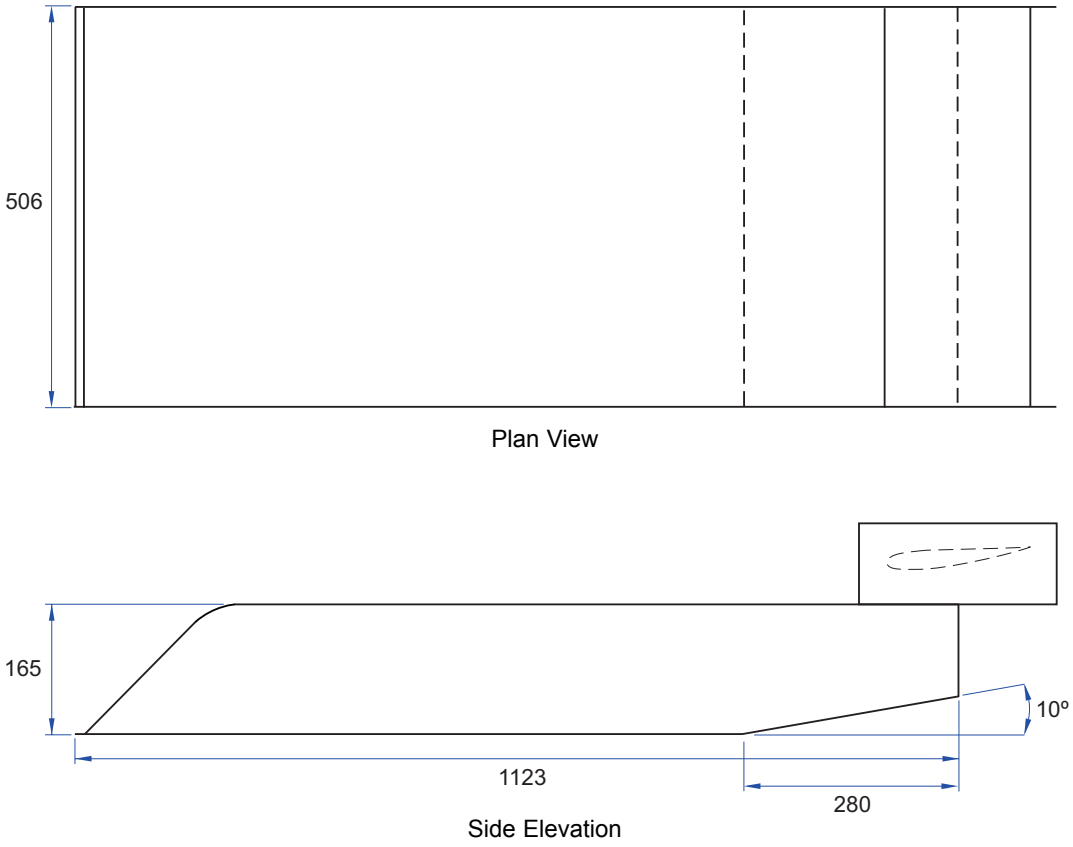

Figure 8.1 - Schematic diagram of Type C Model - After Brown [2005]

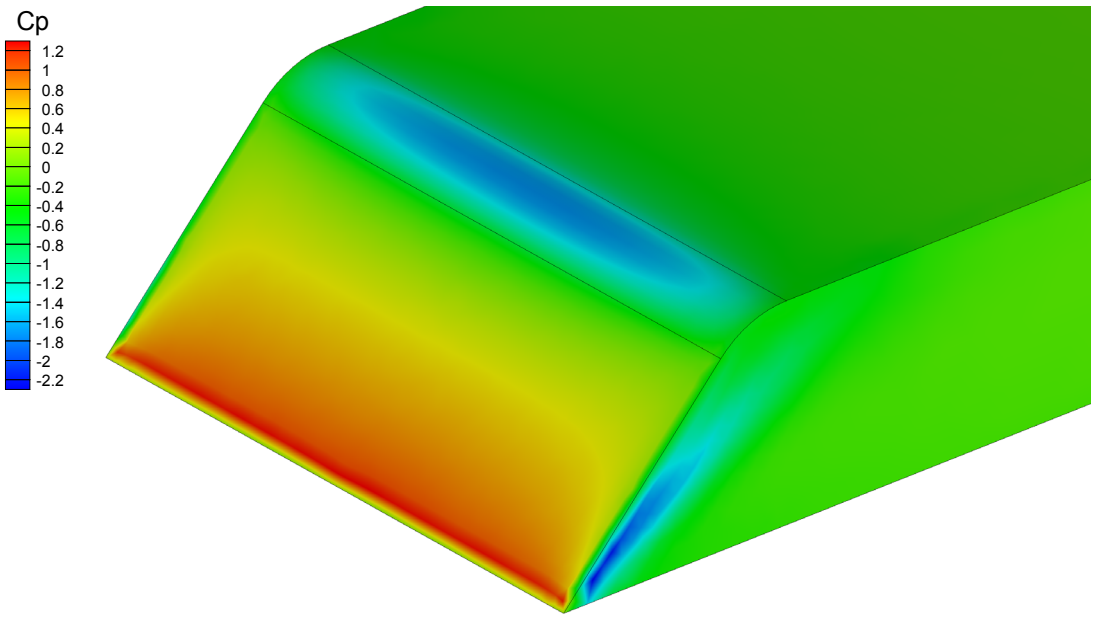

Figure 8.2 - Pressure distribution over front end of Type C race car model in isolation - CFD data

Ahmed model backlight, and as such it would be expected that the flow over this section will more closely resemble that found over the 25° Ahmed model backlight. The addition of the rear wing will also add rear-end downforce which was not experienced by the Ahmed body.

The Type C model is significantly wider than the Ahmed model (506mm in comparison to 389mm), whilst also being of similar overall length (1123mm in comparison to the Ahmed model's 1044mm). It would, therefore, be expected that wall proximity would cause a greater pressure drop over the top and bottom of the model in comparison to the off-side than was found to be the case for the Ahmed model in wall proximity.

As a result of both the greater detail available concerning the flow over the 25° Ahmed model, and the expectation that the flow over the rear diffuser on the Type C model will more closely resemble that over the 25° backlight rather than any of the other model configurations investigated, the 25° results will be primarily compared with the work of Brown [2005], with discussion of the influence of backlight angle included only where considered appropriate.

8.1.1 Lift Comparison

Owing to the comparative complexity of the Type C model, front-end and rear-end contributions to lift will be considered separately. Figure 8.3 plots the variation from the respective isolated cases on both Type C and Ahmed models at various ride heights. As was the case in Brown's investigation, the Ahmed model front and rear lift have been assumed to act at the leading edge and trailing edge of the model respectively. It is initially apparent that variation in ride height has opposite effects on the two tested models, with a drop in ride height producing an increase in front end lift on the Type C model, and a decrease in front end lift on

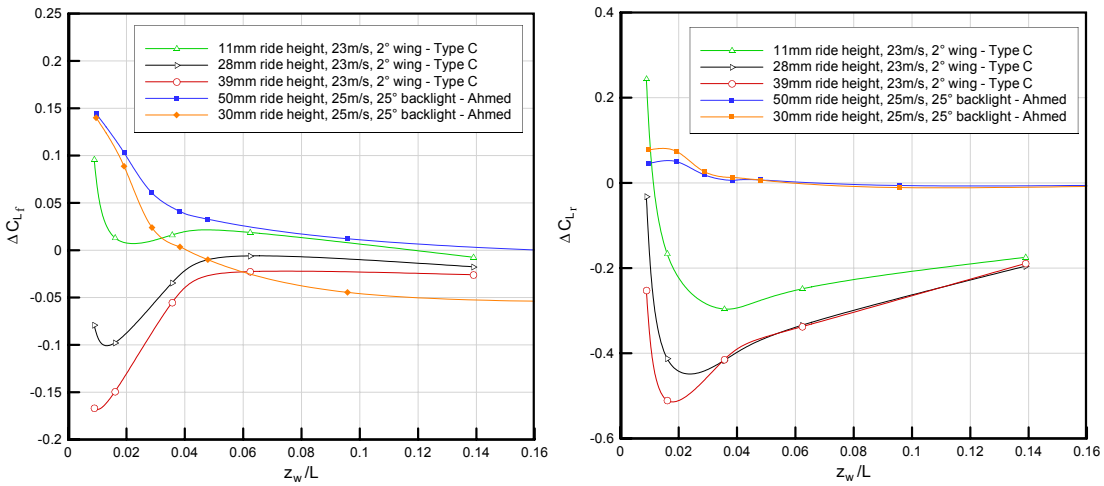

Figure 8.3 - Front and rear lift variation with wall proximity and ride height - Ahmed and Type C car models - experimental data

the Ahmed model. This is a result of the ride heights tested by Brown. If the isolated model cases are considered, Brown's results at 23ms^{-1} and with 2° of rear wing exhibited a decrease in front-end lift of approximately 1% between the 39mm and 33mm ride height cases, but with a subsequent increase in C_{Lf} as ride height was further reduced. Between the 39mm and 11mm ride height cases, there was found to be a total drop in C_{Lf} of approximately 13%. It is therefore clear that, unlike the ride heights tested tested during Ahmed model analysis (30mm - 70mm), there is evidence of viscous forces raising the pressure (and subsequently reducing the downforce), at those ride heights tested by Brown. As wall separation falls, therefore, the pressure drop under the front end of the Type C model and subsequent decrease in front-end lift, is found to be greater for the higher ride-height cases tested by Brown.

There is also the front-end splitter and overall shape of the front end on the Type C model to consider. It is clear from Figure 8.3 that for all Brown's cases, aside from the lowest ride height tested (11mm), there exists a drop in front end lift as wall separation falls. Owing to the 45° nature of the Type C front end, the additional pressure on both the near-wall side and bottom of the front end, the expected results of wall proximity, will result in both an increase in model drag (as was the case in the Ahmed model), and a decrease in lift. To highlight this effect, Figure 8.4 plots the variation in front-end C_p between the isolated model and a near-wall (50mm, z/L=0.045) case at 39mm ride height. It has been shown previously that despite a consistent under-prediction of the influence of side wall proximity, the trends in C_p are modelled sufficiently accurately for useful conclusions to be drawn. The largest increase in pressure appears to be a result of the expected breakdown of the near-wall leading-edge vortex at 50mm wall proximity. The region of stagnation pressure on the front end of the Ahmed model was perpendicular to the freestream, and subsequently no effect on lift was

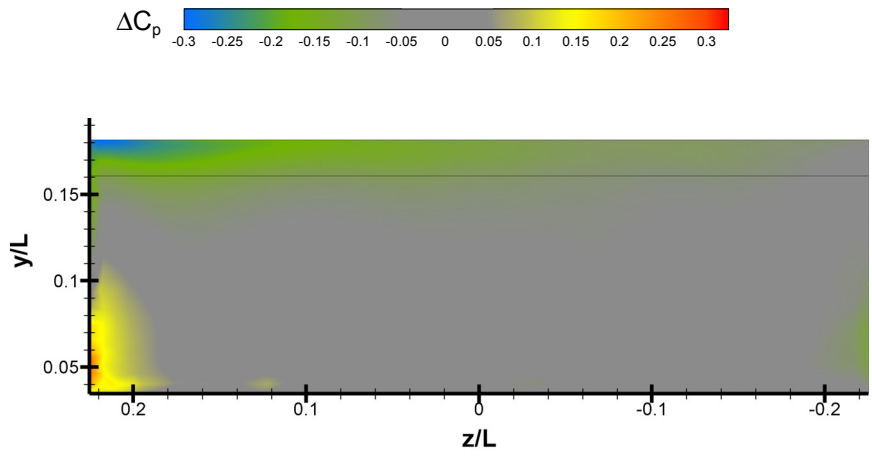

Figure 8.4 - Variation of C_p from isolated case over front-end of Type C race car model at 39mm ride height and 50mm (z_w/L=0.045) from side wall - CFD data

produced. Instead, the drop in C_p over the top of the front end of the Ahmed model, which can also be seen over the Type C model front end in Figure 8.4, determined the value of ΔC_{Lf}, resulting in the positive values shown in Figure 8.3.

As wall separation reached its smallest measured values, the Ahmed model was found to experience a rapid increase in both model C_L and C_M, a result of the increase in C_{Lf} which can be seen in Figure 8.3 below wall separations of approximately $z_w/L=0.05$. It is clear that the Type C model also experiences a similar increase in C_{Lf}, but at positions which are closer to the wall and are found to vary with ride height. It should be noted that no C_{Lf} increase was found to occur on the 39mm ride height Type C model at the smallest tested wall separations, but the trend shown by the other ride height cases suggests that this is due to insufficiently-small wall separations being investigated for this increase to be observed. The reason for the evident dip in front-end lift for each of the cases run by Brown as the wall is brought closer, and resulting in the nearer wall position at which the model experienced the rapid C_{Lf} increase found in the Ahmed model results, is again the geometry of the front end. The increased pressure over the front end and increased pressure over and suction under the front splitter as the model is brought very close to the wall simply exaggerates the effect outlined previously. Only at very small wall separations, therefore, when the further reduction in wall separation causes both a greater drop in suction over the front end than underneath it, and when this is also enough to offset the increased pressure over the bottom of the front end, does the Type C model experience an increase in C_{Lf}. The decreasing wall separation with increasing ride height at which this C_{Lf} rise begins to occur is the expected result of the fact that at most of the ride heights tested by Brown the model boundary layer and resultant pressure distribution is restricting the flow under the model.

If we now consider the rear-end lift plot of Figure 8.3, significant differences between the two models can again be seen. It is apparent that, unlike the Ahmed model, the rear end is the dominant section of the Type C model, as far as the overall variation in C_L with wall separation is concerned. The maximum change in lift recorded at the front end of the Type C model shown in Figure 8.3 was found to be approximately -0.17, whereas the maximum variation of C_{Lr} is found to be -0.51, three times greater. This is in contrast to the Ahmed model, where the maximum variation in C_{Lf} plotted in Figure 8.3 is 0.14, but the maximum plotted variation in C_{Lr} is 0.08. The flow around the downforce-producing sections of the Type C model rear end (diffuser and rear wing), responsible for the large downforce on the model when tested in isolation, would be expected to be significantly altered by the presence of the side wall, and as such the larger variation in C_{Lr} in comparison to C_{Lf} on the Type C model would also be expected.

The 2° angle of attack of the rear wing would not be expected to provide the main contribution

to rear-end downforce on the Type C model. As such, variation in C_{Lr} with wall separation would be expected to be predominantly a result of flow under the model and through the diffuser. This is confirmed by inspection of Figure 2.12, which showed that reducing the wing angle of attack to 0° raised the minimum measured ΔC_{Lr} by less than 0.05 at each ride height tested. To analyse the variation in pressure under the Type C model, Figure 8.5 plots the computationally-predicted variation in model underside C_p between the isolated and 50mm (z_w/L=0.045) from wall cases at 39mm ride height. Initial inspection of Figure 8.5 reveals the similarity of the variation in C_P over the rear diffuser on the Type C model and the 25° Ahmed model backlight. The strong longitudinal vortices responsible for creating the low pressure over the diffuser (and the subsequent downforce), experience the same increase and decrease in strength on the off-sides and near-sides respectively, as were found on the 25° Ahmed model backlight. This is again the result of the inclination of the flow towards the side wall, as before increasing the tendency of the flow to turn around the off-side of the model (and causing the longitudinal vortex strength increase), and reducing the tendency of the flow to turn around the near-side of the model (with the opposite effect). The increase in suction at the leading edge of the diffuser with decreasing z_w, also evident in Figure 8.5, will also have the opposite effect on the flow between the wall and model as was the case on the Ahmed model, this time causing a lower pressure near the bottom of the near-side, and subsequently producing a lower vertical velocity. This in turn would be expected to move the near-side longitudinal vortex down towards the ground plane and away from the surface of the model, similar to the relocation of the near-side longitudinal vortex upward and away from the model surface in the case of the 25° Ahmed model. The under-prediction of the pressure drop over the Ahmed model backlight would be expected to be mirrored by an under-prediction of the

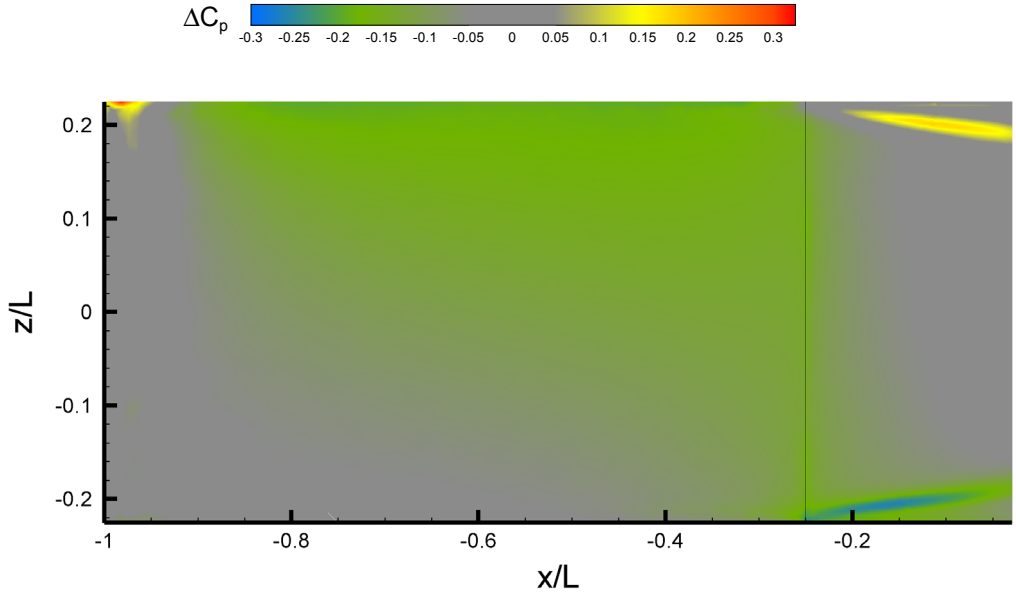

Figure 8.5 - Variation of C_p from isolated case over underside of Type C race car model at 39mm ride height and 50mm (z_w/L=0.045) from side wall - CFD data

pressure drop on the Type C model diffuser, with the subsequent under-prediction of the pressure drop over the remainder of the model underside. It is clear though that the variation in ΔC_p over the Type C model underside between the front and rear end follows the pattern expected from analysis of the force results. There exists a significantly larger drop in C_p at the rear than at the front, in line with the experimentally-measured larger drop from isolated case values in C_{Lr} and C_{Lf} of -0.374 and -0.03 respectively, at the wall distance and ride height used in the computation. In the case of the Ahmed model, it was the pressure drop over the 25° backlight which caused a significantly larger increase in C_L with decreasing wall separation than over either the 10° or 40° models (over twice the increase in C_L than was measured over either the 10° or 40° cases at 70mm ride height at the smallest wall separation measured). This backlight pressure drop is also responsible for the increase in C_{Lr} with decreasing wall separation experienced by the Ahmed model at small wall separations and which can be seen in Figure 8.3. This is further evidence that the large drop in C_{Lr} with decreasing wall separation experienced by the Type C model is primarily a result of a pressure drop on the diffuser. The pressure drop would also be expected to be greater on the 10° diffuser than on the 25° backlight, as a result of ground proximity.

As was the case for the variation in C_{Lf} shown in Figure 8.3, it is found that the Type C model experiences a greater drop in C_{Lr} with decreasing z_w as ride height is increased. This results in a minimum measured ΔC_{Lr} of -0.296, -0.449 and -0.514 for the 11mm, 28mm and 39mm ride height cases respectively. As would be expected, the variation in minimum C_{Lr} between the extreme ride height cases of 0.218 on the Type C model is significantly greater than the corresponding variation in minimum C_{Lf}, found to be -0.174 between the extreme ride height cases.

It is also clear from Figure 8.3 that at the smallest wall separations investigated experimentally the Type C model experiences a rapid increase in C_{Lr} for each ride height tested. Again this would be expected to be primarily a result of variation in the contribution to C_{Lr} from the diffuser, and it must therefore be assumed that at very small wall separations the near-side longitudinal vortex breakdown, combined with the model boundary layer and resultant pressure distribution restricting the flow underneath the model, cause the flow to separate from the diffuser, resulting in a large increase in C_p. As was the case in C_{Lf}, the wall separation at which there is a rapid increase in C_{Lr} becomes smaller with increasing ride height. As a result, the variation between the minimum and maximum C_{Lr} measured at each of the ride heights plotted in Figure 8.3 are found to be 0.245, 0.395 and 0.518 for the 39mm, 28mm and 11mm ride heights respectively.

8.1.2 Drag Comparison

Figure 8.6 plots the variation in C_D with wall separation for both the 25° Ahmed model and Type C model at various ride heights. It has been shown previously that the backlight is the main contributor to the the overall increase in C_D with wall proximity on the 25° Ahmed model, and as such the ΔC_D variation follows a similar trend to that shown for C_{Lr} in this case. It has also been shown that the diffuser is the main contributor to the overall model lift variation with wall proximity, and it would therefore be expected that this section of the Type C model would also be primarily responsible for the variation in C_D with wall proximity.

It must be noted that despite the fact that the Type C model diffuser has an angle of only 10°, the comparatively small overall height of the Type C model (165mm to the Ahmed model's 288mm), and the fact that the diffuser covers the rear quarter of the model, results in its projected frontal area being approximately 30% of the total frontal area of the model. In comparison, the 25° Ahmed model backlight has a projected frontal area of 33% of the overall model frontal area. As such, it would be expected that the found to be larger pressure drop caused by the diffuser with decreasing wall separation than that experienced on the 25° Ahmed model backlight, would result in a larger increase in model C_D with decreasing wall separation on the Type C model. Inspection of Figure 8.6, however, shows that this is not the case for all ride heights plotted. It is instead found that for the 11mm ride height Type C model case, where the values of ΔC_L were previously shown to be lowest of the tested ride heights, there is a smaller increase in C_D with decreasing wall separation for each of the tested wall separations than on the plotted Ahmed model configurations. Inspection again of the CFD data in Figure 8.5 explains this to an extent. It can be seen that the influence of the side wall creates the majority of the pressure drop under the model close to, but upstream of the diffuser leading edge. Pressure drops in this region will, of course, have no effect on ΔC_D. It

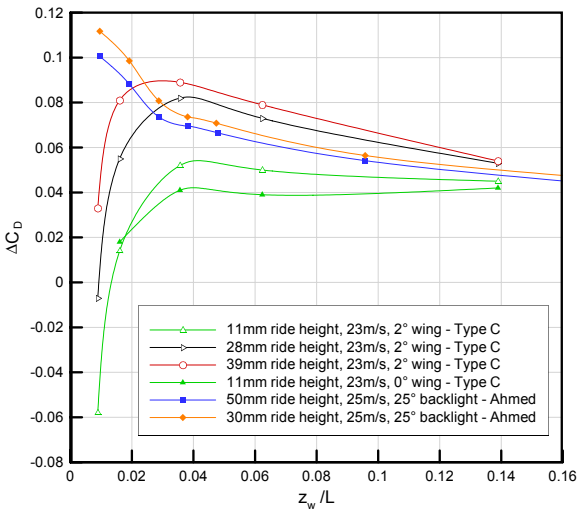

Figure 8.6 - Drag variation with wall proximity and ride height - Ahmed and Type C car models - experimental data

is only at the higher ride heights of 28mm and 39mm that there exist larger values of ΔC_D on the Type C model than on the Ahmed model, in line with the predicted larger increase in C_{Lr} at these ride heights. As would be expected, there exists a rapid drop in ΔC_D on the Type C model at the smallest experimentally-measured wall separations for each of the tested ride heights. This occurs closer to the wall with increasing ride height, following the trend in ΔC_{Lr} shown in Figure 8.3, and again emphasising the dominance of the diffuser on the change in C_D with wall separation. As the Ahmed model experiences an increase in drag with decreasing wall separation for all cases tested, owing largely to the pressure drop over the backlight, at the points where the Type C model diffuser is no longer producing significant downforce, and subsequently less drag, the Ahmed model exhibits larger values of ΔC_D. At the smallest wall separation and ride height tested by Brown, there was found to be a significant drop in model drag from the isolated case (-0.06, or 9% of the isolated value). This illustrates both the sensitivity to wall proximity of the diffuser flow at small ride heights, and also the significant drag contribution this section of the model produces when in isolation.

The influence of the rear wing on the Type C model is also shown in Figure 8.6. Only the 11mm ride height case with a 0° angle of attack is shown for reasons of clarity, as for the other ride height cases a very similar trend is observed. As would be expected, the 0° rear wing case exhibits a smaller increase in ΔC_D than its 2° counterpart. This is a result of the lack of downforce increase experienced by the model from the 0° wing in wall proximity as a result of increased flow velocity over the model, which would occur in the 2° wing cases with the corresponding increase in ΔC_D. The diffuser is, in comparison to the rear wing, efficient in its production of downforce, as can be seen by the relative decreases in C_{Lr} and increases in C_D with increased wing angle of attack. It was stated previously that for each of the cases tested by Brown that there was a maximum recorded drop in ΔC_{Lr} by including a 2° wing rather than a 0° wing of approximately 0.05, corresponding to drop of 17% of the overall 2° wing minimum value of ΔC_{Lr} at 11mm ride height. In comparison, there is found to be an increase in maximum measured ΔC_D by the additional 2° angle of attack of around 21% at 11mm ride height.

8.1.3 Side Force Comparison

Figure 8.7 plots the variation in C_Z with wall separation for both the 25° Ahmed model and Type C model at various ride heights. Initial inspection shows both models experience an increase in side force (toward the wall) as wall separation falls, before reaching a maximum point after which there exists a significant drop in C_Z. It was shown previously that in the case of the Ahmed model, the pressure drop over the backlight as wall separation fell had a significant effect on the side force. Where this backlight pressure drop was greatest, for the 25° model, the largest drop in C_p over the near-side, and subsequently the largest maximum value of C_Z was recorded. It has also been shown that the pressure drop on the Type C model

underside, primarily near the diffuser leading edge, is significantly greater than the pressure drop over the 25° Ahmed model backlight, resulting in the much larger variations in C_{Lr} with wall separation found on the Type C model. It would, therefore, be expected that the pressure drop on the near-side of the Type C model would be greater than that found over the near-side of the 25° Ahmed model, resulting in a larger measured C_Z. It can be seen from Figure 8.7 that for wall separations greater than z_w=0.04L, the Ahmed model actually experiences a larger side force than the Type C model, but that the Type C maximum measured values of C_Z are significantly greater than those on the Ahmed model. This can be explained by considering both the relative shape of the model sides, and the computationally-predicted pressure variation on the near-side (excluding the wing end plates) of the Type C model between the isolated and 50mm from wall cases, shown in Figure 8.8.

The pressure variation shown in Figure 8.8 follows that which would be expected from near-wall Ahmed model analysis. The largest pressure drops are evident close to the model leading edge, and close to the diffuser leading edge, similar to that found near the 25° Ahmed model backlight. The significant difference though is the apparent increase in C_p at the leading edge of the near-side of the Type C model. This is a result of the breakdown of the front end vortices shed from the sharp leading edge, the formation of which is hindered by the proximity of the side wall. This causes a decrease in vortex strength, and hence local velocity, resulting in the increase in C_p from the isolated case seen in Figure 8.8. The opposite effect would be expected on the off-side leading edge vortex as a result of increase flow velocity, but the subsequent decrease in C_p would be expected to be less than the increase shown over the near-side.

The Type C model also has a significantly smaller overall side area in comparison to the Ahmed model. It is found that if side areas are considered as a percentage of corresponding

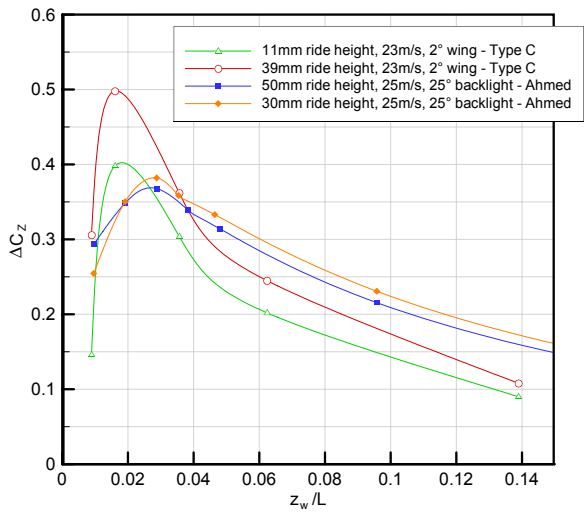

Figure 8.7 - Side force variation with wall proximity and ride height - Ahmed and Type C car models - experimental data

frontal area, then the Type C model side is 38% of the frontal area smaller than the Ahmed model side. This would account to some extent the lower side force experienced by the Type C model at most measured wall separations. It must also be considered that a significant proportion of the side area on the Type C model is made up of the wing end plates (≈14%). These thin end plates have little frontal blockage to force air between them and the wall and cause a similar drop in C_p with decreasing wall separation found on the rest of the near-wall model side. This would be expected to result in a smaller increase in C_Z with decreasing wall separation on the Type C model than if the side plate area was part of the main body of the model. It is therefore only when there exists the greatest drop in C_p near the diffuser leading edge that the side force becomes greater than that measured on the Ahmed model at the same wall proximity.

The maximum side force measured on the Type C model also varies significantly with ride height, as would be expected from the previous analysis outlining both the dependence of C_Z on the suction increase near the diffuser and the variation in C_{Lr} with ride height. There is found to be an increase in maximum C_Z of 0.1 between the extreme ride height cases measured (39mm and 11mm), similar to the larger decrease in C_{Lr} in the higher ride height case. The maximum measured C_Z in the 39mm ride height Type C model case is also 0.13 greater than that measured on the 50mm ride height Ahmed model.

8.1.4 Pitching Moment Comparison

Figure 8.9 plots the variation in C_M with wall separation for both the 25° Ahmed model and Type C model at various ride heights. It was found during analysis of the near-wall Ahmed model results that as the model was brought very close to the wall, there was a large nose-up pitching moment, a result of the pressure drop over the front end. This can also be seen Figure 8.3, which show that when the Ahmed model is tested at the smallest wall separation shown, the front-end lift begins to dominate, causing the nose-up pitching moment seen at the smallest wall proximities in Figure 8.9. It will also be recalled that the 25° Ahmed model experiences a smaller increase in C_M with decreasing wall separation as a result of the greater

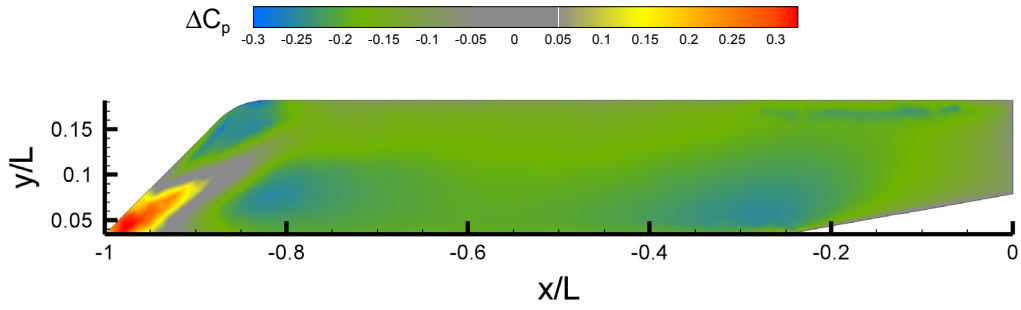

Figure 8.8 - Variation of C_p from isolated case over near-wall side of Type C race car model at 39mm ride height and 50mm (z_w/L=0.045) from side wall - CFD data

pressure drop over the backlight in comparison to the 10° and 40° Ahmed model configurations. This acted against the increase in C_{Lf} with decreasing wall separation, producing the small ΔC_M in comparison to the Type C model values evident in Figure 8.9. It was found in Figure 8.3 that, unlike the Ahmed model, it is the rear lift on the Type C model which provides the greatest contribution to ΔC_L, and subsequently to ΔC_M. Inspection of Figure 8.9 also reveals this to be the case, with a large positive (nose-up) ΔC_M evident for each ride height tested at all but the smallest wall separation. This follows an almost identical trend to that found for Type C model ΔC_{Lr}, as would be expected.

It is also the case that at the smallest tested wall separations there exists a rapid decrease in ΔC_M for all Type C model configurations. At this point there was found to be a rapid decease in rear-end downforce which proves again to be the dominant section of the model, as the increase in ΔC_{Lf}, which would impart a corresponding increase in ΔC_M, is not sufficient to offset the diffuser downforce loss.

8.1.5 Yawing Moment Comparison

The variation in yawing moment with wall separation for both the 25° Ahmed model and Type C model at various ride heights can be seen in Figure 8.10. There was found to be a positive (nose away from wall) C_N for each Ahmed model configuration at every tested ride height. Analysis suggested this was primarily a result of the increased pressure on the near-side of the model front end, in addition to the increase in suction near the trailing-edge suction peak, particularly in the case of the 25° backlight. It was further found that C_N was virtually independent of backlight angle at the smallest tested wall separation (10mm), with the near-side of the front end again providing a positive yawing moment. The Type C model does not

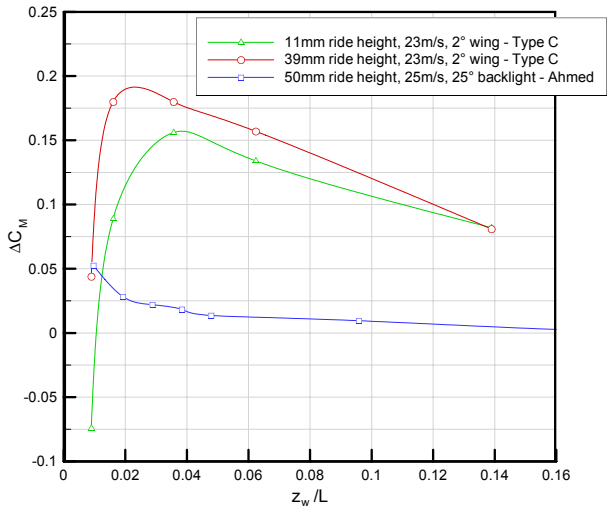

Figure 8.9 - Pitching moment variation with wall proximity and ride height - Ahmed and Type C car models - experimental data

have a front end which curves around the side, and as such any pressure increases over this section of the model will not provide a positive yawing moment. Inspecting again Figure 8.8, however, shows that the breakdown in the near-side leading edge vortex also provides an increase in C_p, resulting in a positive contribution to yawing moment.

It is also clear from Figure 8.8 that the pressure drop near the diffuser would also be expected to have a large effect on yawing moment. The pressure drop would be greater than that near the 25° Ahmed model backlight, subsequently contributing a greater positive yawing moment to the model. This can be seen in Figure 8.10 as a greater increase in C_N with decreasing wall separation on the Type C model than on the Ahmed model. The maximum values of C_N were in fact found to be 0.045 and 0.21 for the 25°, 50mm ride height Ahmed model and the 2° wing, 11mm ride height Type C model respectively. As the pressure in the diffuser is found to increase rapidly as the wall is moved to within the smallest tested separations, this would be expected to cause a sharp increase in C_p on this section of the near-side. As such the yawing moment would be expected to experience a severe drop at wall separations where there was found to be a decrease in diffuser downforce, as is the case in Figure 8.10.

8.1.6 Rolling Moment Comparison

The rolling moment was found, in the case of the Ahmed model, to be most significantly influenced by the pressure drop near the top of the near-side of the model as wall separation fell, the larger pressure drop on the top of this side being largely a result of the suction near the leading edge of the backlight. Owing to the previously-analysed greater pressure drop with decreasing wall separation on the bottom of the near-side of the type C model, a result of the underbody diffuser, it would be expected that this model section would provide a positive rolling moment. This is in contrast to the negative (top of model towards the side wall)

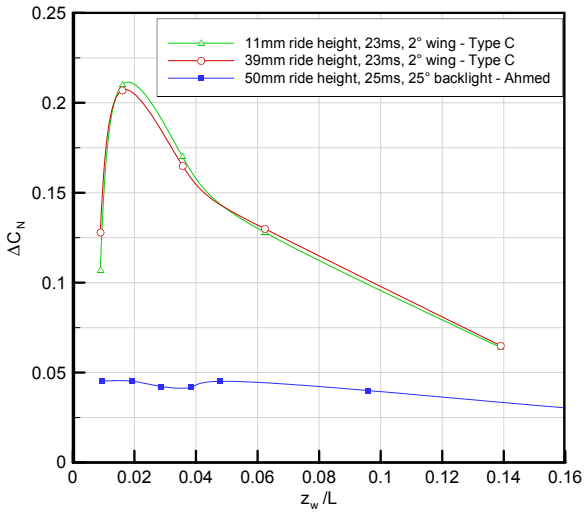

Figure 8.10 - Yawing moment variation with wall proximity and ride height - Ahmed and Type C car models - experimental data

contribution from the near-side of the Ahmed model. It would further be expected from previous analysis of the variation in C_N with wall separation, which highlighted the greater suction near the rear diffuser than near the Ahmed model backlight, that the skewing of the near side wall pressure drop toward the model underside in the Type C model would be greater than it was toward the top of the Ahmed model, resulting in a greater contribution to C_R (albeit in opposite directions). The expected opposite tendencies in C_R and greater magnitude of ΔC_R in the Type C model case can both clearly be identified in Figure 8.11.

As would also have been expected from previous analysis, there is a greater rolling moment evident at higher ride heights on the Type C model, with maximum values of 0.057 and 0.142 being recorded for the 11mm and 39mm ride height cases respectively. These, as expected, are also greater in magnitude than the maximum variation of -0.024 found on the Ahmed model. As the rolling moment is primarily a result of the increased suction on the bottom section of the near-side of the Type C model, the plot of C_R follows a similar pattern to that found in Figure 8.3 for C_{Lr}. Where the diffuser has begun to stop producing downforce, the suction increase on the near-side is no longer evident, with the subsequent sharp drop in C_R.

8.1.7 Computational Models Comparison

Figures 8.12 and 8.13 plot variation in C_L, C_D and C_Z from the respective isolated cases on sections of both the Type C and Ahmed models in wall proximity. From Figure 8.12 the larger pressure drop underneath the Type C model in comparison to the Ahmed model can be seen, with the respective variations in C_D at the plotted wall separations under the models being approximately -0.5 and -0.3 respectively. As discussed previously, this is a result of the underbody diffuser, in addition to the greater underbody area on the Type C model. It can also be seen from Figure 8.12 that there is a greater magnitude contribution to ΔC_L from the 10°

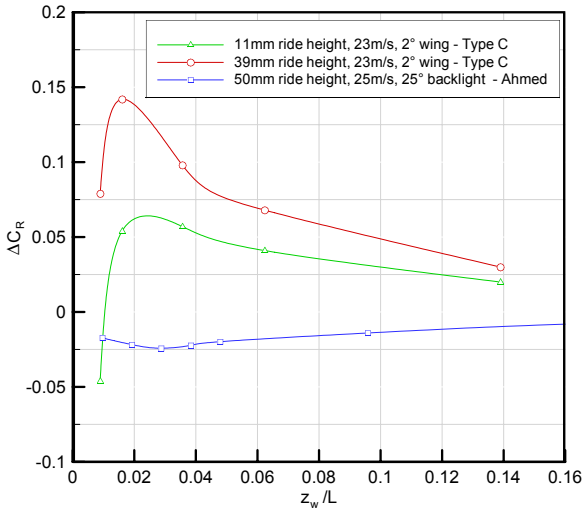

Figure 8.11 - Rolling moment variation with wall proximity and ride height - Ahmed and Type C car models - experimental data

diffuser than from the 25° backlight, amounting to approximately double the magnitude at the plotted wall separations. This highlights the effect that ground proximity has on the pressure distribution in this region. The variation in lift from the top of the model in each case is, however, found to be very similar in each case, approximately 0.23 and 0.24 on the Type C and Ahmed models respectively. The pressure drop on this section of the Ahmed model, caused by the angled backlight (an effect absent from the Type C model), would be expected to be offset to some extent by the greater area of the model top on the Type C model. This, combined with the previously-discussed under-prediction of the variation in model-top C_p caused by the backlight when in wall proximity, results in the very similar values of ΔC_L shown.

Figure 8.13 (a) again highlights the greater variation in C_Z predicted on the near-side of the Ahmed model in comparison to the Type C model, as was analysed previously. Comparing the side force contributions from the off-side of each model, which naturally produce a negative contribution to C_Z, it is found that the off-side of the Ahmed model produces a 40% greater contribution to total C_Z in comparison to the Type C model. The near-side of the Ahmed model, however, produces only a 24% greater contribution to C_Z than its Type C model counterpart. This is believed to be largely a result of the greater width of the Type C model, resulting in a lower magnitude of near-side-wall influence at the off-side sections of the model.

Figure 8.13 (b) provides an illustration of the greater increase in C_D over the Type C model front end in comparison to the Ahmed model. This is a result of the respective model front end geometries, as was previously discussed. The greater contribution to C_D from the 25° Ahmed model backlight in comparison to the Type C model 10°diffuser can also be seen from Figure 8.13 (b). There is found to be an increase in C_D from the isolated cases of 0.017 and 0.02 on the Ahmed model backlight and Type C model diffuser respectively, again highlighting the greater pressure drop experienced by this section of the model in ground proximity.

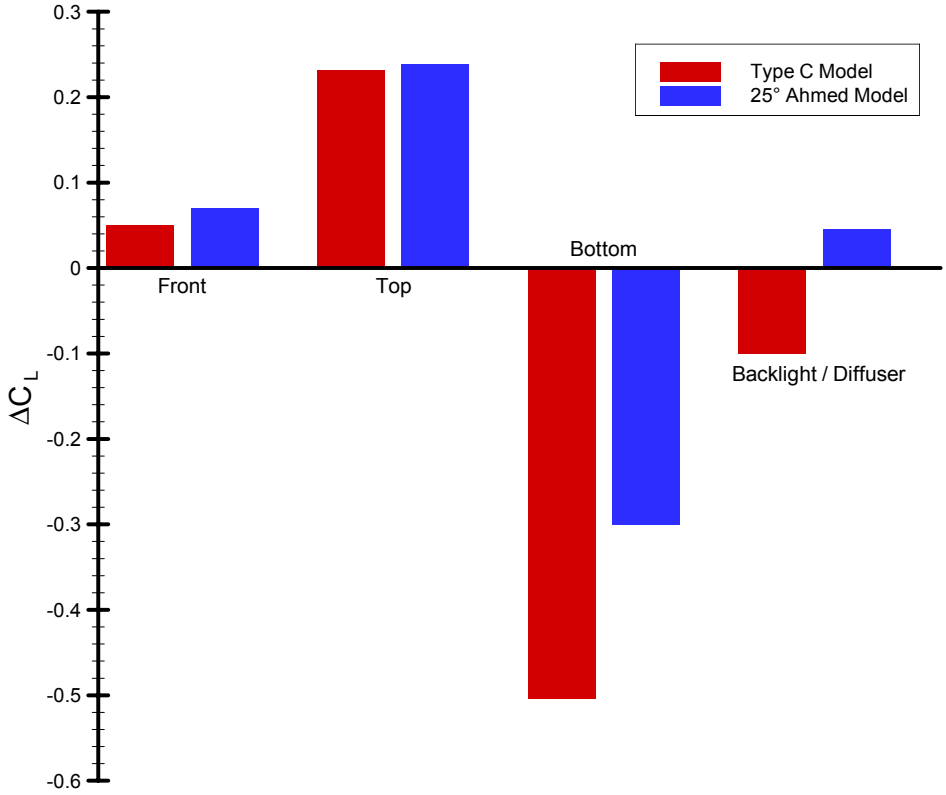

Figure 8.12 - Variation in Lift from isolated case on sections of the 25° Ahmed and Type C models at wall separations of z_w=0.048L (Ahmed) and z_w=0.045L (Type C) - CFD data

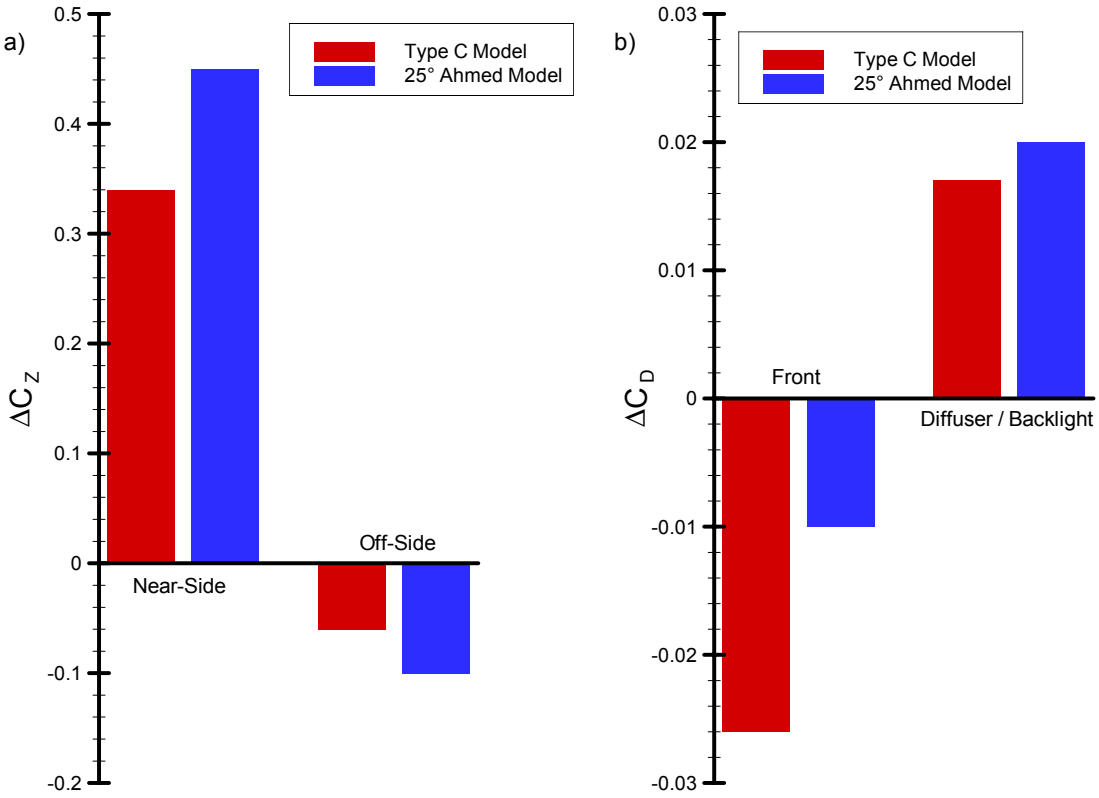

Figure 8.13 - Variation in side force and drag from isolated case on sections of the 25° Ahmed and Type C models at wall separations of z_w=0.048L (Ahmed) and z_w=0.045L (Type C) - CFD data (a) Sideforce coefficient variation - ΔC_Z (b) Drag coefficient variation - ΔC_D

8.2 Summary of Results

• Lift is found to increase at most wall separations measured in the case of the Ahmed model, both as a result of the increased suction near the backlight and over the top of the front end. The opposite is found to be the case for the Type C model, mainly as a result of increased suction near the underbody diffuser. This continues to a minimum point after which the suction caused by the diffuser is found to drop rapidly, with the subsequent increase in ΔC_L. The maximum variations in C_L from the respective isolated model values were found to be -0.58 for the 2° wing, 11mm ride height Type C model case, and 0.26 for the 30mm ride height Ahmed model case.

• Drag is also found to increase with decreasing wall separation on the Ahmed model, predominantly a result of the continuing pressure drop on the 25° backlight. The pressure drop caused by the diffuser on the Type C model also results in a drag increase, but where the diffuser downforce is found to fall rapidly, causing an increase in ΔC_L, there is a corresponding decrease in ΔC_D not consistent with the Ahmed model results.

• Side force acts towards the near-side on the Type C and Ahmed model configurations tested. As the pressure drop on the near-side, and subsequently ΔC_Z, is influenced by the increased suction on either the backlight (Ahmed) or diffuser (Type C), there is found to a be a greater maximum C_Z value measured on the Type C model, with a value of 0.5 for the 2° wing, 39mm ride height Type C model case, and 0.38 for the 30mm ride height 25° Ahmed model case.

• Pitching moment change is most significantly influenced by the front-end pressure drop over the Ahmed model, resulting in an increase in ΔC_M with decreasing wall separation for each model configuration tested. Pitching moment on the Type C model is, however, determined mainly by the variation in downforce with wall proximity produced by the diffuser. Subsequently, the Type C model experiences a maximum ΔC_M at the wall separation where the greatest increase in diffuser downforce occurs, after which there is, as in the case of both ΔC_D and ΔC_L, a significant drop. The maximum recorded values of ΔC_M were found to be 0.16 and 0.05 for the 25°, 50mm ride height Ahmed model and the 2° wing, 11mm ride height Type C model respectively.

• Yawing moment was found to be influenced mainly by the pressure increase over the front end of the Ahmed model. In the Type C model, however, the comparatively large pressure drop near the diffuser leading edge leads to a larger ΔC_N than was found on the Ahmed model, with again the expected rapid drop with the decrease in diffuser suction. The maximum recorded values in ΔC_N were found to be 0.045 and 0.21 for the 25°, 50mm ride height Ahmed

model and the 2° wing, 11mm ride height Type C model respectively.

• Rolling moment was found to follow opposite trends on the Ahmed and Type C models. This was an expected result of the model configurations, as in both cases the main contribution to ΔC_R was found to be the pressure drop over the near-side of the model. As this pressure drop was skewed to the top of the model side as a result of the backlight, the Ahmed model experienced a reduction in rolling moment. As the pressure drop on the near-side of the Type C model was skewed towards the bottom as a result of the pressure drop on the under body diffuser with wall proximity, this model experienced an increase in rolling moment. The Type C model also experienced a greater change of C_R in comparison to the Ahmed model, with a value of ΔC_R=0.142 on the 39mm ride height, Type C model case, with a corresponding maximum of ΔC_R=-0.024 on the 50mm ride height 25° Ahmed model.

9. Conclusions and Recommendations

The aims of this investigation, as set out previously, were as follows:

i) To provide a greater understanding of the flow around an isolated Ahmed model, with particular reference to the effects of the current test set-up.
ii) To provide an understanding of the effects of wall proximity on an Ahmed model.
iii) To determine the generality of these near wall effects, and how this knowledge could be utilised in assessing the effects of wall proximity on other body shapes.
iv) To determine the validity and subsequent usefulness of the current numerical simulation, both in predicting isolated Ahmed model flow and the effects of near side wall proximity.

The conclusions drawn relating to each of these objectives will be presented in turn, after which areas identified by the current investigation as targets for future study will be discussed.

Isolated Model

There was found to be a weak interaction between the flow structure and the front and rear of the model, not obvious in previous experimental data. The overhead supporting strut has the expected effect of retarding the flow over the top of the model, and subsequently the backlight, with the effect that weaker longitudinal vortices are formed over the 25° backlight in comparison to previous data. There was also found to be two new circulatory regions in the flow over the 30° and 40° backlights, where the flow is separated. These regions were not previously observed experimentally. The ground simulation in the form of the rolling road was found to have little effect on the backlight flow.

The investigation of a greater range of Ahmed model backlight angles than it has become commonplace to use, in addition to the acquisition of extensive non-intrusive velocity measurements of the resultant flow, has resulted in an expansion of the available knowledge

base in this area. In addition, vortices shed from the underside of the model, not reported in previous experimental work, have been found and analysed.

Ahmed Model Wall Proximity

Wall proximity is found to inhibit the formation of the near-side longitudinal vortices over the 10° and 25° backlights, with a corresponding increase in strength of the off-side longitudinal vortices. It is further found that as wall separation is reduced, the near-side longitudinal vortex is moved upward from the model surface, and that both near and off-side vortices are moved closer to the side wall.

There is found to be a drop in C_L from isolated values with the introduction of a side wall for all Ahmed model configurations tested. As wall separation falls though, there is found to be a large pressure drop over the model top, skewed towards the front end, resulting in a large increase in both C_L and C_M. Model drag is also found to increase with decreasing model-to-wall separation for each of the tested Ahmed model backlight angles and wall separations.

There was found to be a large pressure drop on the near-wall side of the model with decreasing wall separation. This drop in C_p became greater with decreasing wall separation until the boundary layers restricted the flow between the wall and model with the subsequent C_p increase. It was further found that this pressure drop was greater on the top half of the model side, with the level of variation between the top and bottom halves, and overall C_p drop on this section of the model, dependent on the backlight angle. There was subsequently found to be an increase in C_Y and decrease in C_R as wall separation fell, until the wall separation where choking occurred after which these trends were reversed.

Yawing moment was found to be most significantly influenced by the pressure increase over the near wall side of the Ahmed model front end, resulting in a positive yawing moment for each model configuration and wall separation measured.

Near Wall Proximity - General

It is found that detailed understanding of the flow over a model shape in isolation is required before predictions of the effects of wall proximity can be made, as few of these effects are independent of model geometry. The variation in C_p with wall proximity over the near wall side of each of the two tested models was found to follow similar trends, although both the magnitude and distribution of this C_p drop were found to be greatly affected by model geometry, particularly at the back end.

The side wall was also found to affect the longitudinal vortices formed on each of the models

in the same way, with an increase in vortex strength on the off-side and a decrease on the near-side.

The proximity of the wall was further found to reduce the pressure on the top, underside and off-side of each of the models investigated. The magnitudes and distributions of these variations are dependent on model geometry, and as such so are the effects on aerodynamic forces and moments.

Computational Model

The current numerical model has been shown to provide accurate qualitative prediction of the flow structure in comparison to the current experiments, though the following quantitative variations were found. The retardation of the flow over the model top and backlight was not reproduced owing to the lack of inclusion of the overhead strut in the numerical model. This exclusion proved to be necessary in order to model the flow over the backlights, as the computing power available did not allow for the resolution of both this and the strut wake. There was also found to be no computationally predicted interaction between the front and rear-end flows, despite the fact that an interaction of this nature (albeit a weak one) was observed experimentally.

The CFD predicted the formation of weaker longitudinal vortices over the backlight for each of the model geometries, most noticeable for the 25° case where these vortices are strongest. As a result, the wake structure in each numerical case more closely resembled that of an experimental case where these vortices are less energetic, due to the significant effects they have on the wake flow.

As was expected from the nature of the turbulence model employed for the numerical investigation, the simulation over-predicted the drag coefficient on the Ahmed model for all configurations, a significant contribution to this being the over-predicted stagnation pressure on the model front caused by the k-ε turbulence model.

Despite these discrepancies, it was found that the numerical model provided accurate qualitative prediction of the influence of the side wall, at the computed wall proximities. The variation in C_p over the model sections were found to provide important insight into the mechanisms by which the variations in forces and moments recorded by the experiments were produced. Quantitative predictions of the variations in C_p, and subsequently the forces on the model, were not possible from the CFD, as it was found that these variations were consistently under-predicted at a given wall proximity.

9.1 Recommendations for Future Work

It has been shown that the effects of wall proximity are complex, and consequently an experimentally and computationally-challenging area of investigation. The work presented has added significantly to the understanding of the phenomena involved, but has also identified areas where further investigation would serve to extend this knowledge.

It is considered that a more complex geometry should be tested in proximity to a side wall, ideally utilising both pressure and flow visualisation measurements, in order that the generality of the effects of wall proximity presented in the current work could be further analysed. It has been shown that understanding of the isolated model flow is also a prerequisite for analysis of the effects of wall proximity, and as such must form an integral part of any such investigation.

With reference to the Ahmed model, it is suggested that the third velocity component, not available in the presented work, would provide further insight into the effects of wall proximity. This would, in particular, help to quantify the extent to which the flow is inclined toward the side wall and the effects on the backlight longitudinal vortices.

The addition of further pressure tappings around the Ahmed model, in particular at the front and near-side, would also serve to provide greater insight into the effects of wall proximity in these areas, in addition to providing important data with which to validate further the current computational model.

The use of boundary layer control on the side-wall would also be of interest. Although during acquisition of the LDA data in the current experiments it is thought the wall boundary layer has little effect on the flow, the force measurements exhibited clear signs of viscous forces restricting the flow between the wall and the model. It would be useful to perform experiments where the wall boundary layer was removed in order to ascertain the extent of the effect which it has. This would also be more representative of the real-world case, where no boundary layer would exist on the wall.

References

Advantage CFD (2001) *A CFD NASCAR case study into the effects of wall proximity*. Racecar Engineering, June, p48-54

Ahmed, S.R. (1981) *Wake structures of typical automobile shapes.* Journal of Fluids Engineering, Vol 103, 162-169 March

Ahmed, S.R. (1983) *Influence of base slant on the wake structure and drag of road vehicles.* Journal of Fluids Engineering, Vol 105, No.4, 429-434, December

Ahmed, S.R., Ramm G. and Faltin G. (1984) *Some salient features of the time-averaged ground vehicle wake.* Society of Automotive Engineers Technical Paper Series 840300, Detroit, MI, USA, February/March

Aider, J.-L., Dubuc, L., Hulin, G. and Elena, L. (2000) *Experimental and numerical investigation of the flow around a simplified vehicle shape.* 3rd MIRA International Vehicle Aerodynamics Conference, Rugby UK, 18th - 19th October

Alajbegovic, A. (1996) *Digital physics analysis of the Morel model.* MIRA International Vehicle Aerodynamics Conference, Birmingham, UK, 15-16 October

Axelsson, N., Ramnefors, M. and Gustafsson, R. (1998) *Accuracy in computational aerodynamics Part 1: Stagnation pressure.* paper 980037, Society of Automotive Engineers International Congress & Exposition, Detroit, MI, USA, February

Barlow, J.B., Rae W.H., and Pope, A. (1999) *Low-Speed Wind Tunnel Testing.* Wiley, third edition

Basara, B. and Alajbegovic, A. (1998) *Steady state calculations of turbulent flow around morel body.* The 7th Int. Symp. Flow Modelling and Turbulence Measurements, October 5-7, Taiwan

Bayraktar, I., Landman, D. and Baysal, O. (2001) *Experimental and computational Investigation of Ahmed body for ground vehicle aerodynamics.* paper 2001-01-2742, Society of Automotive Engineers International Truck & Bus Meeting & Exhibition, Chicago, IL, USA, November

Baysal, O. and Bayraktar, I. (2000) *Computational simulations for the external aerodynamics of heavy trucks.* Journal of Commercial Vehicles 109, 813-819

Bearman, P.W., De Beer, D., Hamidy, E. and Harvey, J.K. (1988) *The effect of a moving floor on wind tunnel simulation of road vehicles.* paper 880245, Society of Automotive Engineers International Congress & Exposition, Detroit, MI, USA, February/March

Benedict, L. H. and Gould, R. D. (1996) *Uncertainty estimates for any turbulence statistics.* In Proc. of the 8th Int. Symp. of Applications of Laser Techniques to Fluid Mechanics, Instituto Superior Técnico, Lisbon, Portugal

Berndtsson, A., Eckert, W. and Mercker, E. (1988) *The effect of ground plane boundary layer control on automotive testing in wind tunnels.* paper 880248, Society of Automotive Engineers International Congress & Exposition, Detroit, MI, USA, February/March

Buchave, P., George, W. K. Jr and Lumley, J. L. (1979) *The measurement of turbulence with the laser-Doppler anemometer.* Ann. Rev. Fluid. Mech., 11:443–503

Brown, J. (2005) *Racecar Aerodynamics in Close Proximity to a Retaining Wall.* MSc Aerospace Dynamics Individual Thesis, Cranfield University, Cranfield

Carr, G.W. (1988) *A comparison of the ground-plane-suction and moving-belt ground representation techniques.* paper 880249, Society of Automotive Engineers International Congress & Exposition, Detroit, MI, USA, February/March

Carr, G.W. and Eckert, W. (1994) *A further evaluation of the ground plane suction method for ground simulation in automotive wind tunnels.* paper 940418, Society of Automotive Engineers International Congress & Exposition, Detroit, MI, USA, February/March

Dantec Dynamics (2004) A/S. *Statistical stop criteria in BSA flow software.* Product Information 189, Denmark

Duell, E. and George, A. (1999) *Experimental study of a ground vehicle body unsteady near*

wake. paper 1999-01-0812, Society of Automotive Engineers International Congress & Exposition, Detroit, MI, USA, March

Dring, R. P. (1982) *Sizing criteria for laser anemometry particles.* ASME Journal of Fluids Engineering, 104:15–17, March

Fleming, J., Simpson, R.L. and Davenport, W.J. (1991) *An experimental study of a turbulent wing-body junction and wake flow.* VPI & SU Report VPI-AOE-179, Virginia Polytechnic Institute & State University, Blacksburg, VA, Dept. of Aerospace and Ocean Engineering

Fox, R.W. and McDonald, A.T. (1994) *Introduction to fluid mechanics.* Wiley, fourth edition

Gaylard, A.P., Baxendale, A.J. and Howell, J.P. (1998) *The use of CFD to predict the aerodynamic characteristics of simple automobile shapes.* paper 980036, Society of Automotive Engineers International Congress & Exposition, Detroit, MI, USA, February

Gaylard, A.P., Bickerton, J.E. and Howell, J.P. (1998) *Current issues in the use of CFD to predict aerodynamic characteristics of car shapes.* 2nd MIRA International Conference on Vehicle Aerodynamics, UK, 20th - 21st October

Gharib, M. (1996) *Prospective: The experimentalist and the problem of turbulence in the age of supercomputers.* Journal of Fluids Engineering 118, pp 233-242, June

Gosse, K., Patte-Rouland, B., Gonzalez, M. and Paranthoen, P (2006) *Scalar dispersion in the near wake of a simplified model car.* Experiments in Fluids 40: 135–140

Graysmith, J.L. and Baxendale, A.J. (1995) *Further CFD analysis of flow around the Ahmed body.* Institute of Mechanical Engineering. Autotech 95 paper C498/36/160, Birmingham, UK, 1995

Graysmith, J.L., Baxendale, A.J., Howell, J. P. and Haynes, T. (1994) *Comparisons between CFD and experimental results for the Ahmed reference model.* proc Royal Aeronautical Society Conference on vehicle aerodynamics, Loughborough, pp30.1-30.11

Gillieron, P. and Chometon, F. (1999) *Modelling of stationary 3-D separated air flows around an Ahmed reference model.* European Series in Applied and Industrial Mathematics: Proceedings, Vol. 7, 173-182

Hetherington, B and Sims-Williams, D. B. (2004) *Wind tunnel model support strut*

interference. Technical Paper 2004-01-0806, Society of Automotive Engineers, Warrendale, PA, February

Houghton, E.L. and Carpenter, P.W. (1993) *Aerodynamics for Engineering Students*. Butterworth Heinemann, fourth edition

Howell, J. and Hickman, D. (1997) *The influence of ground simulation on the aerodynamics of a simple car model.* paper 970134, Society of Automotive Engineers International Congress & Exposition, Detroit, MI, USA, February

Hucho, W.H. editor. (1998) *Aerodynamics of Road Vehicles.* Society of Automotive Engineers International, fourth edition

Jameson, A. (1995) *The present status, challenges and future developments in computational fluid dynamics.* 12th Australian Fluid Mechanics Conference, University of Sydney, 10th-15th December, pp 423-459

Kapadia, S., Roy, S. (2003) *Detached Eddy Simulation over a reference Ahmed car model.* American Institute of Aeronautics and Astronautics 41st Aerospace Sciences Meeting and Exhibit, Reno, NV, USA, January 6-9th, AIAA Paper 2003-0857

Katz, J. (1995) *New Directions in Racecar Aerodynamics - Designing for Speed*. Bentley, 1st Edition

Knowles, R.D. (2005) *Monoposto racecar wheel aerodynamics: Investigation of near-wake structure and support sting interference.* Ph.D. Thesis, Cranfield University, Shrivenham, UK

Krajnovic, S. and Davidson, L. (2002) *Development of Large-Eddy Simulation for vehicle aerodynamics.* ASME International Mechanical Engineering Congress & Exposition, New Orleans, Louisiana, November 17th-22nd, Paper 32833

Krajnovic, S., Davidson, L. (2004) *Large-Eddy Simulation of the flow around simplified car model.* paper 2004-01-0227, Society of Automotive Engineers World Congress & Exhibition, March, Detroit, MI, USA

Lawson N. J. and Davidson M. R. (1999) *Crossflow characteristics of an oscillating jet in a thin slab casting mould.* Journal of Fluids Engineering 121, p588-595

Le Good, G.M. and Garry, K.P. (2004) *On the use of reference models in automotive*

aerodynamics. paper 2004-01-1308, Society of Automotive Engineers World Congress, Detroit, Michigan, March 8-11

Lienhart, H. and Becker, S. (2002) *LDA measurements of the flow structure in the wake of a simplified car model.* 11th International Symposium on Applications of Laser Techniques to Fluid Mechanics, Lisbon, Portugal, July

Lienhart, H. and Becker, S. (2003) *Flow and turbulence structures in the wake of a simplified car model.* paper 2003-01-0656, Society of Automotive Engineers World Congress & Exhibition, Detroit, MI, USA, February

Lienhart, H. and Soots, C. (2000) *LDA measurements of the flow and turbulence structures in the wake of a simplified car model.* Institute of Fluid Mechanics (LSTM) University Erlangen-Nuremberg

Lienhart, H., Soots, C. and Becker, S. (2002) *Flow and turbulence structures in the wake of a simplified car model (Ahmed Model).* In Proc. DGLR Fach. Symp. der AG STAB Stuttgart Univ.

McCutcheon, G., McColgan, A.H., Grant, I. and Hurst, D. (2002) *Wake studies of a model passenger car using PIV.* Society of Automotive Engineers Motorsports Engineering Conference and Exhibition, Indianapolis, IN, USA, paper 2002-01-3335

Makowski, F.T. (1997) *FLUENT/UNS simulation of the Ahmed model body with 30° base-slant angle.* Fluent Deutschland GmbH Internal Report, June 9th

Makowski, F. and Kim, S. (2000) *Advances in external aero simulation of ground vehicles using the steady RANS equations.* paper 2000-01-0484, Society of Automotive Engineers World Congress, Detroit, MI, USA

Milliken, W. F. and Milliken, D. L. (1995) *Racecar Vehicle Dynamics.* Society of Automotive Engineers, Warrendale, PA

Morel, T. (1978) *Aerodynamic drag of bluff body shapes characteristic of hatch-back cars.* paper 780267, Society of Automotive Engineers World Congress & Exhibition, Detroit, MI, USA, February/March

Nobach, H. (2000) *A global concept of autocorrelation and power spectral density estimation from LDA data sets*. In Proc. of the 10th Int. Symp. of. Applications of Laser Techniques to Fluid Mechanics, Instituto Superior Técnico, Lisbon, Portugal

Olcmen, M.S. and Simpson, R.L. (1994) *Influence of wing shapes on surface pressure fluctuations at wing-body junctions.* AIAA Journal vol.26 no.4 pp494-496

Pearson, W.E., Manners, A.P. and Passmore M.A. (1994) *Prediction of the flow around a bluff body in close proximity to the ground.* proc Royal Aeronautical Society Conference on Vehicle Aerodynamics, Loughborough, pp29.1-29.12

Perzon, S., Sjogren, T. and Jonson, A. (1998) *Accuracy in computational aerodynamics Part 2: Base pressure*. paper 980038, Society of Automotive Engineers International Congress & Exposition, Detroit, MI, USA, February

Perzon, S., Janson, J. and Hoglin, L. (1999) *On comparisons between CFD methods and wind tunnel tests on a bluff body.* paper 1999-01-0805 Society of Automotive Engineers International Congress & Exposition, Detroit, MI, USA, March

Ramnefors, M., Bensryd, R., Holmberg, E. and Perzon, S. (1996) *Accuracy of drag predictions on cars using CFD - Effect of grid refinement and turbulence models.* paper 960681, Society of Automotive Engineers International Congress & Exposition, Detroit, MI, USA, February

Romberg, G.F., Chianese, F. and Lajoie R.G. (1971) *Aerodynamics of race cars in drafting and passing situations.* paper 71-0213, Society of Automotive Engineers Automotive Engineering Congress and Exposition, Detroit, Michigan, USA, January

Simpson, R.L. (2001) *Junction Flows*. Annual review of fluid mechanics 33: 415-443

Sims-Williams, D.B. and Dominy R.G. (1998) *Experimental investigation into unsteadiness and instability in passenger car aerodynamics*. paper 980391, Society of Automotive Engineers International Congress & Exposition, Detroit, MI, USA, February

Sims-Williams, D.B. and Duncan, B.D. (2003) *The Ahmed model unsteady wake: Experimental and computational analyses.* paper 2003-01-1315, Society of Automotive Engineers World Congress & Exhibition, Detroit, MI, USA, March

Spohn, A. and Gillieron, P. (2002) *Flow separations generated by a simplified geometry of an automotive vehicle.* Produced by Laboratoire d'Etudes Aerodynamiques, ENSMA and Laboratoire d'Etudes Aerodynamiques, CNRS

Strachan, R. K., Knowles, K. and Lawson, N. (2004) *A CFD and experimental study of an Ahmed reference model.* paper 2004-01-0442, Society of Automotive Engineers World Congress & Exhibition, Detroit, MI, USA, March

Strachan, R. K., Knowles, K. and Lawson, N. (2005) *Comparisons between CFD and experimental results for a simplified car model in wall proximity.* Proc. Integrating CFD and Experiments in Aerodynamics, Cranfield University, Shrivenham, September

Wright, P. (2001) *Formula 1 Technology.* Society of Automotive Engineers, Warrendale, PA

Wright, P. (2004) *Ferrari Formula 1: Under the Skin of the Championship-Winning F1-2000.* Society of Automotive Engineers, Warrendale, PA, 2004.

Wallis, S.B. and Quinlan, W.J. (1988) *A discussion of aerodynamic interference effects between a race car and a race track retaining wall (a wind tunnel NASCAR case study).* paper 880458, Society of Automotive Engineers International Congress and Exposition, Detroit, Michigan, USA, February/March

FLUENT® Users' Guide - Various sections

GAMBIT® Users' Guide - Various sections

Appendix A: Experimental Programme

LDA Testing

Isolated Model Testing

Tables A.1 - A.3 show the y-z, x-y and x-z planes investigated during the isolated model testing. The number of individual points taken for some of the cases has been marked as variable, due to their exact dimensions being dependent on the geometry of the backlight. Figures A.1 - A.3 plot a graphical representation of the planes, though planes 1,2,4 and 5 are omitted from Figure A.1 for clarity. All numbers in the following tables are in mm.

Plane	x	Min y	Max y	Min z	Max z	# Points	0°	5°	10°	15°	20°	25°	30°	40°
1	-220	var	var	-230	230	var	✓	✓						
2	-210	var	var	-230	230	var			✓	✓				
3	-200	var	var	-230	230	var					✓	✓		
4	-190	var	var	-230	230	var							✓	
5	-170	var	var	-230	230	var								✓
6	-150	var	var	-230	230	var	✓	✓	✓	✓	✓	✓	✓	✓
7	-100	var	var	-230	230	var	✓	✓	✓	✓	✓	✓	✓	✓
8	-50	var	var	-230	230	var	✓	✓	✓	✓	✓	✓	✓	✓
9	0	var	var	-230	230	var	✓	✓	✓	✓	✓	✓	✓	✓
10	80	0	360	-200	200	759	✓	✓	✓	✓	✓	✓	✓	✓
11	522	0	360	-200	200	759			✓			✓		✓
12	1044	0	360	-200	200	759			✓			✓		✓
13	0	10	130	174.5	254.5	59			✓			✓		
14	50	10	130	174.5	254.5	59	✓							✓
15	100	10	130	174.5	254.5	59	✓							✓
16	150	10	130	174.5	254.5	59	✓							✓
17	200	10	130	174.5	254.5	59	✓		✓			✓		✓
18	250	10	130	174.5	254.5	59	✓							✓
19	300	10	130	174.5	254.5	59	✓							✓
20	350	10	130	174.5	254.5	59	✓							✓
21	400	10	130	174.5	254.5	59	✓		✓			✓		✓
22	600	10	130	174.5	254.5	59			✓			✓		
23	800	10	130	174.5	254.5	59			✓			✓		

Table A.1 - LDA y-z Planes tested - Isolated cases

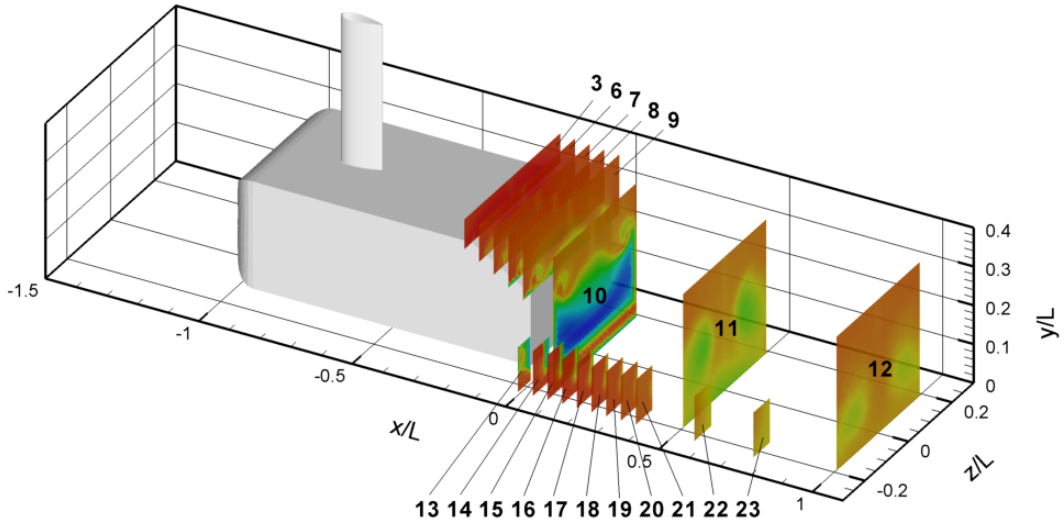

Figure A.1 - LDA y-z Planes tested

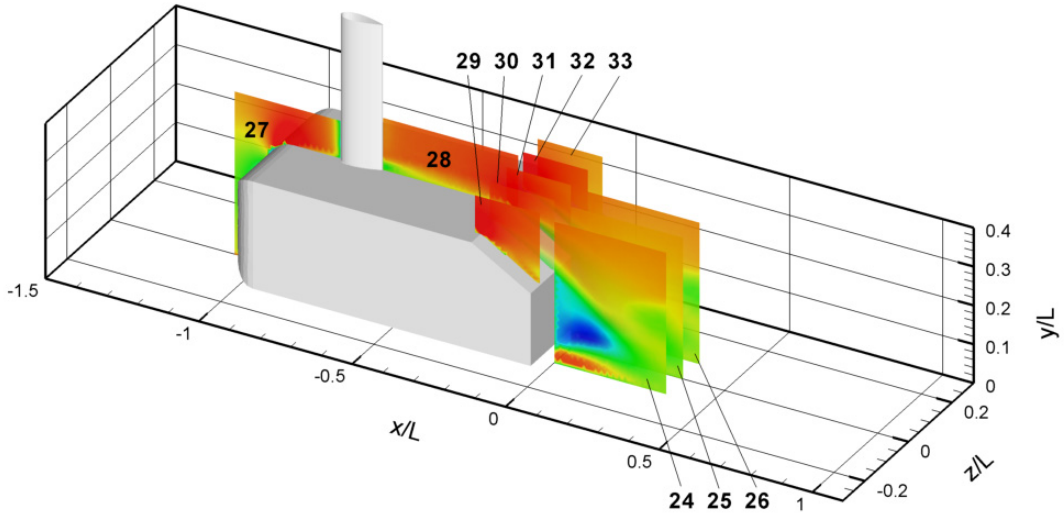

Figure A.2 - LDA x-y Planes tested

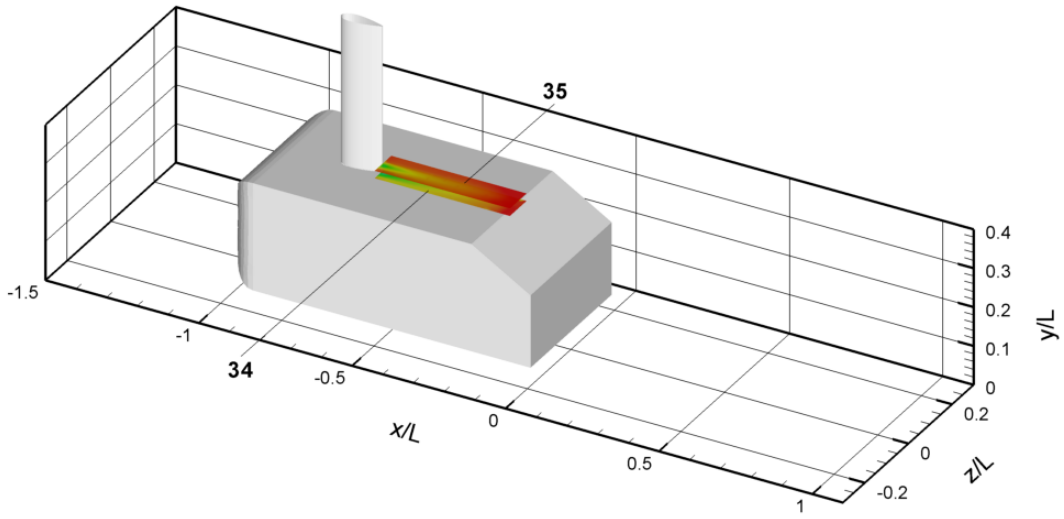

Figure A.3 - LDA x-z Planes tested

Plane	z	Min x	Max x	Min y	Max y	# Points	0°	5°	10°	15°	20°	25°	30°	40°
24	-80	0	380	0	380	761						✓		
25	0	0	380	0	380	761	✓	✓	✓	✓	✓	✓	✓	✓
26	80	0	380	0	380	761			✓			✓		
27	0	-1144	-784	0	438	536			✓			✓		
28	0	-640	-180	338	478	353			✓			✓		
29	-150	-220	0	var	438	var			✓			✓		
30	-80	-220	0	var	438	var			✓			✓		✓
31	0	-220	0	var	438	var	✓	✓	✓	✓	✓	✓	✓	✓
32	80	-220	0	var	438	var			✓			✓		✓
33	150	-220	0	var	438	var			✓			✓		

Table A.2 - LDA x-y Planes tested - Isolated cases

Plane	y	Min x	Max x	Min z	Max z	# Points	0°	5°	10°	15°	20°	25°	30°	40°
34	340	-640	-180	40	-40	212			✓			✓		
35	360	-640	-180	40	-40	212			✓			✓		

Table A.3 - LDA x-z Planes tested - Isolated cases

Near - Wall Model Testing

Tables A.4 - A.6 show the y-z, x-y and x-z planes investigated during the near-wall model testing. Again Figures A.1 - A.3 plot a graphical representation of the planes, though planes 36-41, which are equivalent to planes 14-19 on the opposite side of the model, are omitted from Figure A.1 for clarity.

	10°				25°				40°			
Plane	300mm	200mm	100mm	50mm	300mm	200mm	100mm	50mm	300mm	200mm	100mm	50mm
2	✓	✓	✓	✓								
3					✓	✓	✓	✓				
5									✓	✓	✓	✓
6	✓	✓	✓	✓	✓	✓	✓	✓	✓	✓	✓	✓
7	✓	✓	✓	✓	✓	✓	✓	✓	✓	✓	✓	✓
8	✓	✓	✓	✓	✓	✓	✓	✓	✓	✓	✓	✓
9	✓	✓	✓	✓	✓	✓	✓	✓	✓	✓	✓	✓
10						✓		✓				
14												✓
15												✓
16												✓
17												✓
18												✓
19												✓
36												✓
37												✓
38												✓
39												✓
40												✓
41												✓

Table A.4 - LDA y-z Planes tested - Near-Wall cases

	10°				25°				40°			
Plane	300mm	200mm	100mm	50mm	300mm	200mm	100mm	50mm	300mm	200mm	100mm	50mm
24		✓		✓		✓		✓				✓
25		✓		✓		✓		✓		✓		✓
26		✓		✓		✓		✓				✓
27					✓	✓		✓				
28					✓	✓	✓	✓				
29	✓	✓	✓	✓	✓	✓	✓	✓	✓	✓	✓	✓
30	✓	✓	✓	✓	✓	✓	✓	✓	✓	✓	✓	✓
31	✓	✓	✓	✓	✓	✓	✓	✓	✓	✓	✓	✓
32	✓	✓	✓	✓	✓	✓	✓	✓	✓	✓	✓	✓
33	✓	✓	✓	✓	✓	✓	✓	✓	✓	✓	✓	✓

Table A.5 - LDA x-y Planes tested - Near-Wall cases

	10°				25°				40°			
Plane	300mm	200mm	100mm	50mm	300mm	200mm	100mm	50mm	300mm	200mm	100mm	50mm
34					✓	✓	✓	✓				
35					✓	✓	✓	✓				

Table A.6 - LDA x-z Planes tested - Near-Wall cases

Laser Doppler Anemometer	
Probe Orientation	
u-component (nm)	514.5
v-component (nm)	488
Probe Settings	
Focal Length (mm)	2500
Beam Diameter (mm)	2.2
Expander Ratio	2.97
Beam Spacing	40
Alignment pinhole (μm)	25
Seeding	
Generator	Jem Hot2000
Fluid	Jem Long-Lasting
Mean Particle Diameter (μm)	1.3
Position in Tunnel	Between 3rd & 4th Corners

Table A.7 - LDA Testing Specifications - Isolated and Near-Wall cases

Force and Moment Testing

Tables A.8 and A.9 outline the experimental set-up employed to record the forces and moments on the Ahmed model for both the isolated and near-wall cases.

Measurements Taken	
Backlights tested	0°, 5°, 10°, 15°, 20°, 25°, 30°, 40°
Measurements Recorded	C_L C_D C_Y C_M C_R C_N
Ride Heights Tested (mm)	50
Measurement Rate (Hz)	10
Test Configuration	
Wind Tunnel	D.S. Houghton
Wind & Road Speed (ms^{-1})	25
Re (based on model length)	1.7×10^6
Model / Nozzle Area - Blockage (%)	2.9
Boundary Layer Suction (%)	
Primary	33.6
Secondary	53.5
Belt Suction	45.3

Table A.8 - Force and Moment Testing Specifications - Isolated cases

Measurements Taken	
Backlights tested	10°, 25°, 40°
Measurements Recorded	C_L C_D C_Y C_M C_R C_N
Ride Heights Tested (mm)	30, 40, 50, 60, 70
Distances from the Wall Tested (mm)	300, 200, 100, 50, 40, 30, 20, 10
Measurement Speed (Hz)	10
Test Configuration	
Wind Tunnel	D.S. Houghton
Wind & Road Speed (ms^{-1})	25
Re (based on model length)	1.7×10^6
Model + Wall / Nozzle - Blockage (%)	4.7
Boundary Layer Suction (%)	
Primary	33.6
Secondary	53.5
Belt Suction	45.3

Table A.9 - Force and Moment Testing Specifications - Near-Wall cases

Static Pressure Measurements

Figure A.4 is a drawing of the backlight plate used to measure the static pressures over this region of the model, and table A.10 outlines the specifications of the pressure tests.

Measurements Taken	
Backlights tested	25°
Measurements Recorded	Static Pressure
Ride Heights Tested (mm)	50
Distances from the Wall Tested (mm)	Isolated Case, 200, 100, 50
Measurement Speed (Hz)	500
Measurement time (each tapping) (s)	16
Test Configuration	
Wind Tunnel	D.S. Houghton
Wind & Road Speed (ms^{-1})	25
Re (based on model length)	1.7×10^6
Model (+Wall) / Nozzle - Blockage (%)	2.9 (4.7)
Boundary Layer Suction (%)	
Primary	33.6
Secondary	53.5
Belt Suction	45.3

Table A.10 - Static Pressure Testing Specifications - Isolated and Near-Wall cases

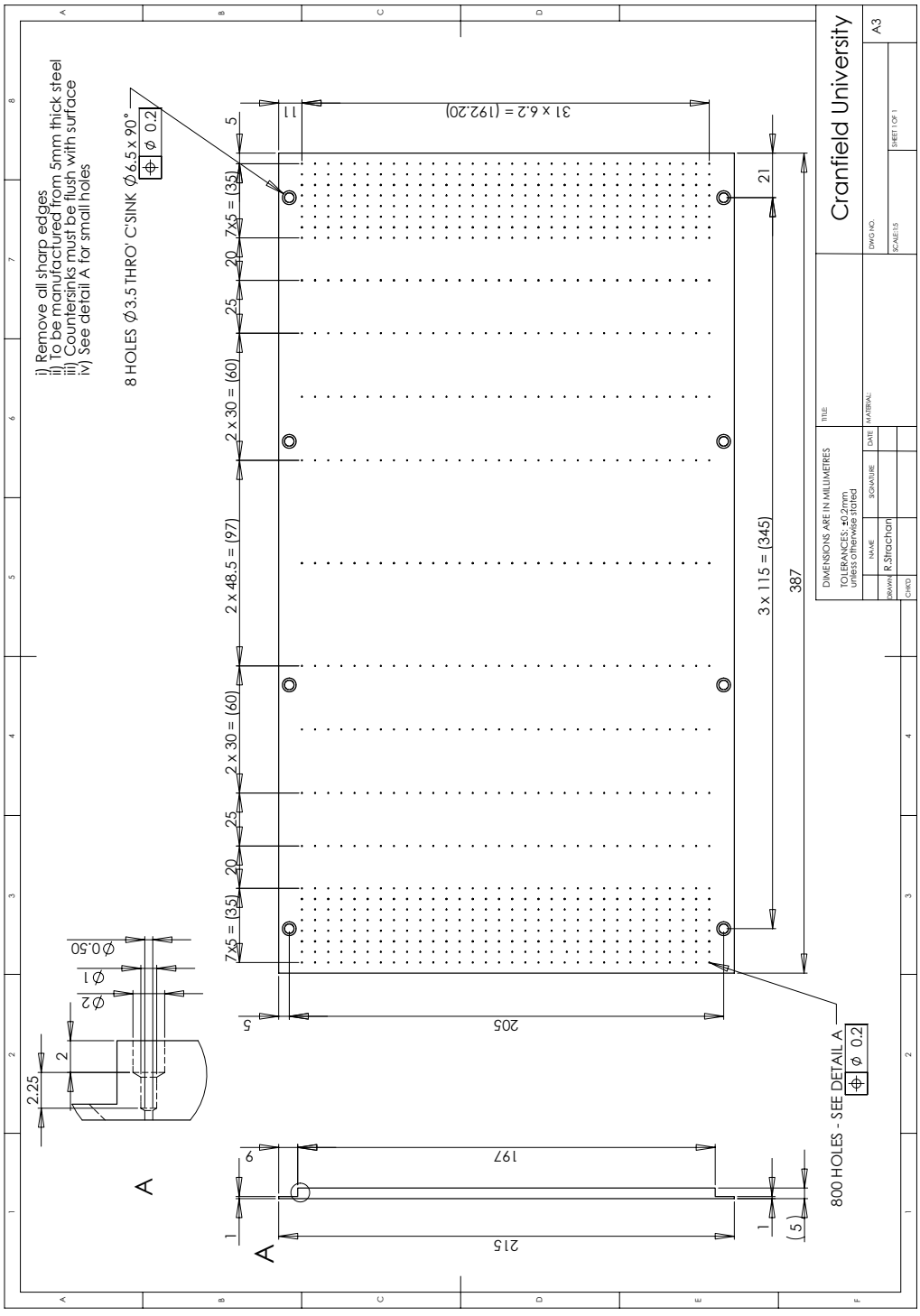

Figure A.4 - CAD Drawing of pressure-tapped plate.

Appendix B: Wind Tunnel Specifications

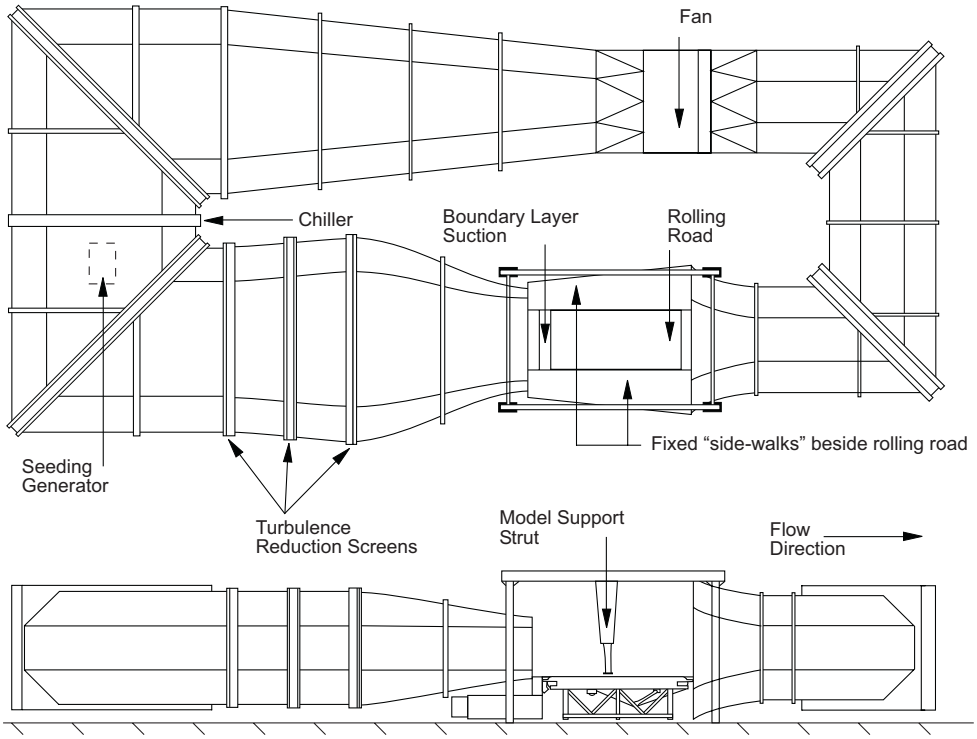

D. S. Houghton Wind Tunnel

Type		Closed Circuit, 3/4 Open-Jet with Rolling Road
Contraction Ratio		3.31:1
Nozzle Dimensions		2.75m×1.4m
Max. Flow Speed		42ms^{-1}
Boundary Layer Thickness		1.5mm @ wheel test location
Wind Speed Error		< 0.2%
Turbulence Intensity		0.25%
Turbulence Reduction Screens		3× 53%-Open Area, Wire Mesh
Max. Rolling Road Speed		50ms^{-1}
Temperature Control	Air	±0.5C via 400kW Cooling Circuit
	Road	±0.5C via 150kW Cooling Circuit
Force Balance		6-Component, Internal-to-Model

Appendix C: Preliminary Experimental Investigations

Support Strut Interference

In order to perform the current experiments employing a rolling road ground simulation, the model had to be suspended with an overhead supporting strut. The testing of the Ahmed model in this manner requires quantification of any influence of the strut on the air flow around the model. This is important not only from the point of view of obtaining accurate experimental results, but also in the comparison between experimental values and CFD predictions, as in the CFD model the strut was not included. Ascertaining the effect of the supporting strut is not a simple task, as it is impossible to test the model without the strut (or some supporting mechanism) in order to quantify any effect its inclusion may have. LDA analysis of the effect of the strut on the flow over the model backlight is discussed in the relevant chapter, presented here is analysis of the effect on the overall model drag force.

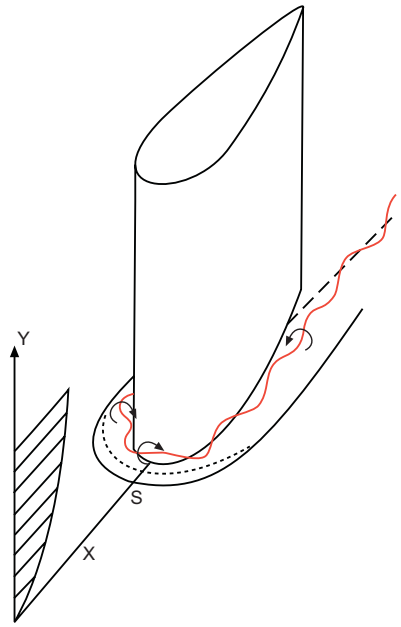

Figure C.1 - Horseshoe vortex system around a streamlined obstacle - after Simpson [2001]

There exists previous work on junction flows between supporting struts and models [Simpson (2001), Hetherington, (2004)]. Generally these flows are simplified to an aerofoil intersecting a flat plate. Figure C.1 shows the approaching boundary layer separating and forming a horseshoe vortex due to the adverse pressure gradient at the leading edge of the aerofoil. The vortices continue downstream of the aerofoil trailing edge. The flow also separates from the aerofoil at the trailing edge.

The additional drag produced by the inclusion of the aerofoil (interference drag) consists of the increased pressure drag of the two separations and the added friction drag produced by the horseshoe vortices pulling the high speed freestream air into the junction area [Hetherington, 2004]. The strength of these vortices is dependent on the geometry of the aerofoil, and a bluntness factor (B.F.) was developed by Fleming [1991] to calculate the vortex formation:

$$B.F. = \frac{1}{2}\frac{R_o}{X_T}\left[\frac{T}{S_T} + \frac{S_T}{X_T}\right] \qquad C.1$$

Where R_o is the aerofoil leading-edge radius, X_T is the chordwise position of the aerofoil's maximum thickness T, and S_T is the distance from the leading edge along the aerofoil surface to the maximum thickness.

It has been shown previously that vortices are formed for B.F.s greater than 0.045 [Olcmen, 1994] with vortex strength increasing with B.F. For the strut used in the current experiments the values in the above equation are:

R_o = 10.416mm
X_T = 45mm
T = 34.5mm
S_T = 50.93mm

Therefore B.F = 0.209

This is above the threshold value of 0.045, and as such strong horseshoe vortices are expected to be formed in the manner described around the supporting strut.

Equation C.2 was derived empirically by Hoerner [1965] for aerofoil sections of t/c = 0.1-0.75 and X_T/c = 0.3-0.35, to quantify the change in drag coefficient as a result of the effects of the horseshoe vortices:

$$\Delta D = q.t^2\left[0.75\left(\frac{t}{c}\right) - 0.0003\left(\frac{c^2}{t}\right)\right] \qquad C.2$$

or in non-dimensionalised form:

$$\Delta C_D = \frac{t^2}{A}\left[0.75\left(\frac{t}{c}\right) - 0.0003\left(\frac{c}{t}\right)^2\right] \qquad C.3$$

Where t = aerofoil thickness, q = freestream dynamic pressure, c = aerofoil chord, ΔC_D= change in drag force and A = model and strut frontal area.

From Equation C.3 the supporting strut used for the current experiments gives a value of ΔC_D=0.00017, a negligible amount in comparison to the overall drag experienced by the model.

Ground Simulation Effects

In order to assess the effects of the supporting strut, the effect of the rolling road ground simulation, must be isolated. To this end profiles of vertical velocity taken above the backlight at x/L=-0.096 and at the model trailing edge, both with and without ground simulation are shown in Figures C.2 (a) and (b). Initial inspection of these figures reveals that the inclusion of the rolling road has little, if any significant effect on the strength and structure of the longitudinal vortices. Indeed the maximum and minimum recorded v velocities between the two cases at both plotted positions were found to be within $0.01u_\infty$ of each other, and there

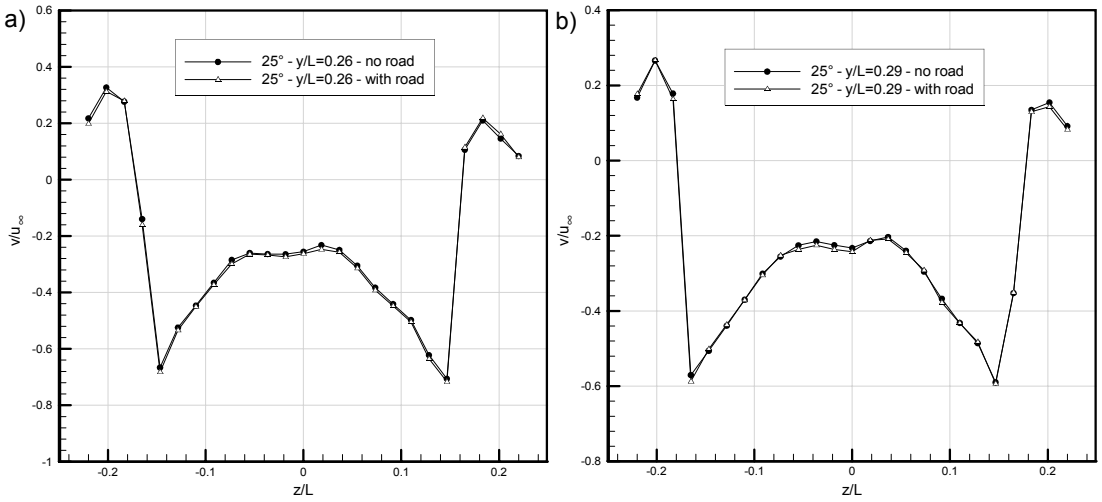

Figure C.2 - Profiles of normalised vertical velocity at (a) x/L=0 (b) x/L= -0.1 above 25° Ahmed model backlight, with and without ground simulation - LDA data

was found to be no variation in the positions of the maxima and minima. This reinforces the belief that it is the strut which causes the discrepancies in longitudinal vortex formation between the current experiments and those of Lienhart et al., as was discussed in Chapter 5.

Side-Wall Boundary Layer

The extent of the boundary layer on the side-wall must be quantified in order that its influence on the measurements taken during the near-wall phase of the investigation can be assessed. To this end LDA data were taken 1mm downstream of the side-wall trailing edge without the Ahmed model present. Contours of streamwise velocity from this position are shown in Figure C.3.

It is clear that at the plotted streamwise position (0.5L downstream of the where the Ahmed model trailing edge would be if included), the flow has recovered to $0.9u_\infty$ by 20mm (0.02L) from the side wall. It is therefore assumed that the side-wall boundary layer will have a negligible effect on the LDA results, for which the minimum tested wall separation was 50mm

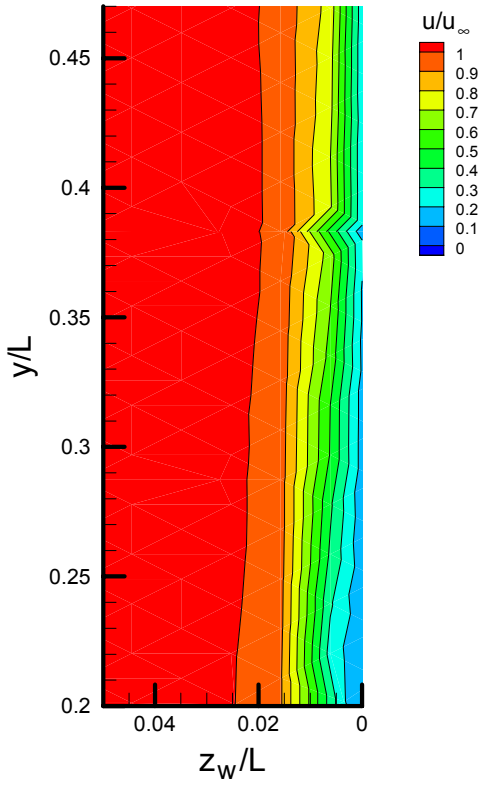

Figure C.3 - Contours of normalised streamwise velocity 1mm downstream of model wall trailing edge

(z_w=0.048L). During force and moment measurements, however, the smallest tested wall separation was 10mm (z_w=0.01L), so the side-wall boundary layer must be considered.

Appendix D: Computational Summary

Ahmed model - Isolated cases	
Fluent Release	6.0.12
Version	3D, Segregated, Steady
Mesh Type	Viscous-Hybrid
Number of cells (no refinements)	1,160,308 (0°) - 1,262,151 (40°)
Number of cells (final)	≈1,900,000 in each case
Solver Controls	
Turbulence model	RNG k-ε
Material	Air
Near-Wall treatment	Standard Wall Functions
Discretisation	
Pressure	Second-Order
Momentum	Second-Order Upwind
Turbulence	Second-Order Upwind
Pressure-Velocity Coupling	SIMPLE
Boundary Conditions	
Inlet: Velocity Inlet	
Velocity (ms^{-1})	$25ms^{-1}$
Direction Vector	(1,0,0)
Outlet: Pressure Outlet	
Ground: Symmetry	
Sides: Symmetry	

Table D.1 - Isolated Ahmed model cases - computational parameters

Ahmed model - Near-Wall Cases	
Fluent Release	6.0.12
Version	3D, Segregated, Steady
Mesh Type	Viscous-Hybrid
Number of cells (no refinements)	1,339,748 (10°) - 1,442,781 (40°)
Number of cells (final)	≈1,900,000 in each case
Solver Controls	
Turbulence model	RNG k-ε
Material	Air
Near-Wall treatment	Standard Wall Functions
Discretisation	
Pressure	Second-Order
Momentum	Second-Order Upwind
Turbulence	Second-Order Upwind
Pressure-Velocity Coupling	SIMPLE
Boundary Conditions	
Inlet: Velocity Inlet	
Velocity (ms^{-1})	$25ms^{-1}$
Direction Vector	(1,0,0)
Outlet: Pressure Outlet	
Ground: Symmetry	
Sides: Symmetry	

Table D.2 - Near-Wall Ahmed model cases - computational parameters

Type C model - Near Wall and Isolated Case	
Fluent Release	6.0.12
Version	3D, Segregated, Steady
Mesh Type	Viscous-Hybrid
Number of cells (no refinements)	1,632,559 (iso.) - 1,726,012 (near-wall)
Number of cells (final)	≈1,900,000 in each case
Solver Controls	
Turbulence model	RNG k-ε
Material	Air
Near-Wall treatment	Standard Wall Functions
Discretisation	
Pressure	Second-Order
Momentum	Second-Order Upwind
Turbulence	Second-Order Upwind
Pressure-Velocity Coupling	SIMPLE
Boundary Conditions	
Inlet: Velocity Inlet	
Velocity (ms^{-1})	$23ms^{-1}$
Direction Vector	(1,0,0)
Outlet: Pressure Outlet	
Ground: Symmetry	
Sides: Symmetry	

Table D.2 - Near-Wall and Isolated C Type model cases - computational parameters

The Type C model computation was performed without the inclusion of the rear wing assembly. It was considered that in order to more accurately model the flow both near the diffuser and over the front end, the available level of computing power did not allow modelling of this section of the model.

Appendix E: Preliminary Numerical Studies

Inlet Distance Investigation

The investigation was performed only for the 10° case, as the backlight angle has been shown to have little or no effect on the pressure distribution over the front end. The distance marked x in Figure E.1 is the only parameter altered for each case, and the results are shown in Table E.1. It can be seen that for the shortest distance investigated, there is a significantly larger calculated value of C_{D_f}. There is, however, only around a 1% change in C_{D_f} between $2088 \leq x \leq 4176$. As such an inlet distance of 2L (2088mm) was chosen, in order to keep the overall cell count as small as possible whilst maintaining sufficient inlet distance.

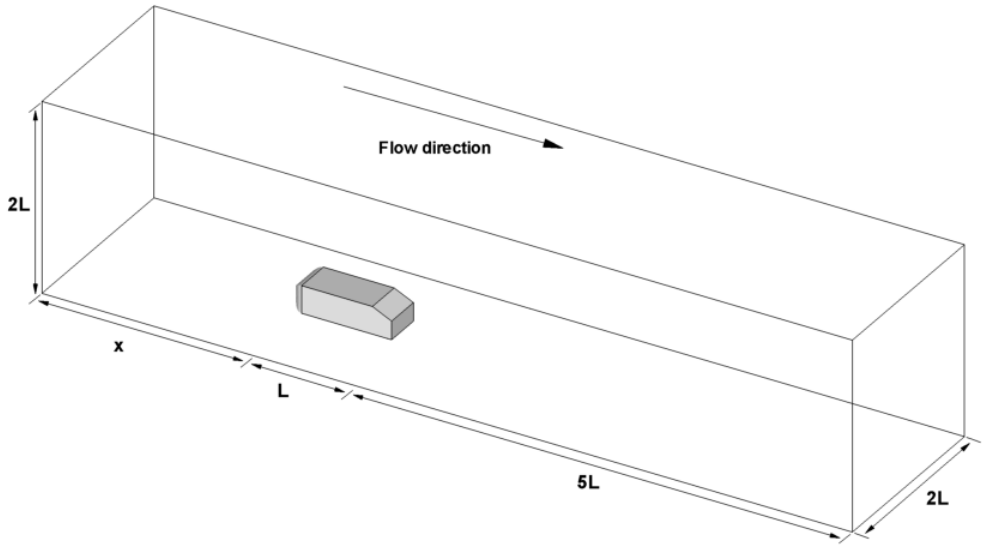

Figure E.1 - Inlet distance investigation set-up

Inlet Distance (x) (mm)	Mesh Size	C_{D_f}
1044	1,366,049	0.106
1566	1,390,765	0.092
2088	1,424,027	0.090
2610	1,454,205	0.090
3132	1,437,754	0.089
4176	1,494,409	0.089

Table E.1 - Inlet distance investigation results

Support Strut Investigation

The experimental investigation employed an overhead supporting strut to mount the model above a moving ground plane. In order to model this support mechanism accurately in the computational model, however, required a significant number of the available grid cells being used to mesh the region around the strut. This allowed fewer cells to be used in the region of the model backlight. In order to ascertain the validity of the computational model with the support strut inclusion the 25° backlight angle was tested. This backlight angle was chosen owing to the greatest complexity of backlight flow experienced over this model configuration. Figure E.2 plots contours of normalised streamwise velocity and in-plane velocity vectors at the trailing edge of the 25° model backlight for both the with and without-strut CFD cases.

If these results are compared to the experimental 25° model trailing edge data presented previously (Chapter 5, Figures 5.13 and 5.14), the shortcomings of the with-strut CFD model (Figure E.2 (b)) become immediately apparent. It was therefore concluded that the inclusion of the supporting strut served only to reduce the accuracy of the computational model, as a result of the necessity to relocate grid cells from the backlight. As such, the overhead strut was not included in further CFD analysis.

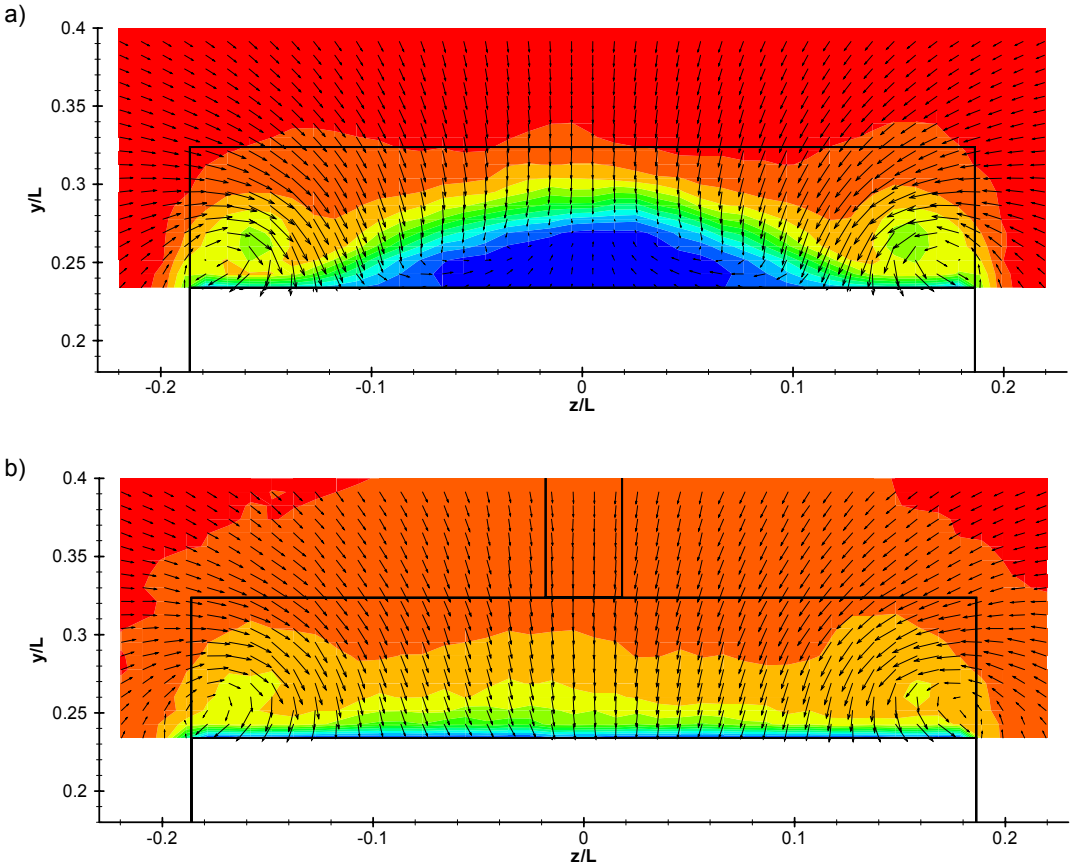

Figure E.2 - Calculated contours of normalised streamwise velocity and in-plane velocity vectors above the trailing edge of the 25° Ahmed model (a) without overhead strut (b) with overhead strut

Appendix F: Experimental Error Analysis

LDA Error

Seeding Response

The variation in density between the seeding used for the LDA and the flow itself introduces a seeding response error into the LDA measurements. The inability of the seeding to follow the flow was assessed using the following method, as described by Dring {1982]. The response of a particle to an acceleration of the fluid is related to the Stokes number, S_t, of the particle:

$$S_t = \frac{\rho_p D_p^2}{18 \mu T_c} \qquad F.1$$

Where ρ_p is the density of the seeding particles, D_p is the seeding particle diameter, μ is the absolute viscosity of the freestream fluid and T_c is the characteristic time taken for the acceleration.

It can be seen from equation F.1 that the particle size of the seeding used must be small enough to ensure a low seeding response error. This criteria must be balanced with the fact that the particle size must be large enough to ensure sufficient light is scattered when it enters the measurement volume.

Taking the seeding particle density and diameter as 1019kgm^{-3} and 1.3x10^{-6}m respectively, air viscosity as 1.75x10^{-5}kgm^{-1}s^{-1}, and the characteristic time as 8.6x10^{-3}s (in line with previous analysis [Knowles, 2005]), the Stokes number is found to be 6.4x10^{-4}.

It was stated by Dring [1982] that for Stokes numbers less than 0.01 the maximum speed error

is equal to the Stokes number. Seeding response error was therefore considered negligible in the current investigation.

Velocity Bias

As LDA measurements are made on the seeding in the flow, this random sampling means that the flow and samples recorded are not statistically independent. At any given point in a uniformly seeded flow a velocity fluctuation above the mean value would lead to an increased number of seeding particles passing through the measurement volume, with the opposite being true for fluctuations below the mean value. Therefore, if the mean velocity was calculated from raw samples , the result would be biased toward the higher velocities. This velocity bias can be removed by weighting the samples by a factor inversely proportional to the velocity of the sample during calculation of the mean value. Buchave et al. [1979] recommended the use of the particle transit time through the measurement volume, t, as the weighting factor. The velocity bias was removed from the mean velocity signals, S, using:

$$S = \frac{\sum_x^N s_x t_x}{\sum_x^N t_x} \qquad F.2$$

Where s is the velocity component measured by the probe and the subscript x refers to the index of the current sample from a population of N samples.

Sampling Error

The rate at which samples are acquired has an effect on the flow statistics which are subsequently calculated, such as population mean and variance. Correct estimation of these statistics requires statistically independent samples. If two samples are less than one integral time scale, τ_i, apart they are considered to be statistically dependent. Thus, to ensure the acquisition of statistically independent data, the sampling interval should be at least twice the integral time scale of the process. As LDA samples are recorded when a particle enters the measurement volume, and therefore not at a predetermined sampling rate, the acquisition of statistically independent samples is difficult. A method known as “dead-time” mode can be employed when using the LDA, whereby the minimum time between the samples can be determined by the user. This, however, requires a priori knowledge of the flow integral time scale.

The outline of the experimental method used in the investigation described that the maximum number of samples and maximum time spent per location were prescribed, with the probe moved to the next location once either of these criteria were fulfiled. The sampling rate varied with location and so did the associated uncertainty.

This uncertainty was estimated using the method of Benedict and Gould[1996] as reported by Dantec Dynamics [2004], whereby it is stated that 95% confidence intervals for a mean value would be:

$$1.96\sqrt{\frac{\overline{u^2}}{N}} \qquad F.3$$

This applies to any population distribution but assumes firstly that N>50, and that the samples, u, are statistically independent. The first of these criteria was easily satisfied for all results taken, however, the second was not and was therefore addressed in the following way. The potential number of statistically-independent samples, N_{eff}, was calculated from the sampling time, T_m, and the integral time scale:

$$N_{eff} = \frac{T_m}{2\tau_i} \qquad F.4$$

If $N_{eff} > N$ then N_{eff} is substituted into equation F.3, else it remained unchanged. The calculation of N_{eff} though required a posteriori estimation of τ_i.

This estimation was made following the method presented by Nobach [2000]. As was stated previously, τ_i is related to the correlation of two samples of the same population, and as such can be found from the autocorrelation function, ACF, of the population. In a dataset where the samples are equi-distant the ACF can be estimated from the inverse Fourier transform of the power spectral density of the data. However, in the case of randomly sampled LDA data, Fourier analysis is not possible unless the data are resampled to be equi-distant, a process which may introduce further error as a result of alaising.

In the method presented by Nobach [2000] the ACF is estimated using slot correction, which does not involve re-sampling the data and thus avoiding aliasing issues. The method also used transit time weighting in order to remove the velocity bias during estimation. Software was written by Knowles [2005] which estimated τ_i at each location in the measurement plane, allowing calculation of N_{eff} and subsequently the confidence intervals for the mean values.

Analysing the u velocity component it was found that to a 95% confidence interval over 50% of the points measured were found to have an error of <1%.

Test Configuration

Measurement	Equipment	Systematic Error	Resultant Error
Traverse Level	Digital Protractor	±0.01°	±0.01°
Traverse Parallel	Steel Rule	±0.1mm	±0.04°
Probe Inclination	Digital Protractor	±0.01°	±0.01°
Model Pitch	Digital Protractor	±0.01°	±0.01°
Model Yaw	Digital Protractor	±0.01°	±0.01°
Model Roll	Digital Protractor	±0.01°	±0.01°
Freestream Velocity	Nozzle Static Pressure	n/a	±0.05ms^{-1}
Rolling Road Velocity	Tachometer	±0.1revs^{-1}	±0.02ms^{-1}
Ride Height	Steel Rule	±0.1mm	±0.5mm
Laser Beam Alignment	25μm pinhole		±12.5μm
Measurement Location	Steel Rule	±0.1mm	see subsection

Table F.1 - Summary of Test Configuration Errors

Measurement Location Uncertainty

The dimensions of the LDA measurement volume introduced a systematic error into the measurement location. As the velocity of a particle could be recorded from anywhere within that volume the maximum location error was half the volumes major dimensions. This results in a measurement location uncertainty of ±0.012mm, ±0.012mm and ±5.1mm for the x, y and z axis as defined previously. This uncertainty was accounted for during design of the measurement planes grid spacing to ensure that each point was unique to within the tolerances specified.